B-Physics

Introduction to B-Physics

1 ATLAS B-physics programme

The ATLAS B-physics programme covers many aspects of beauty flavour physics. First, by measuring production cross-sections of beauty and charm hadrons and of the heavy-flavour quarkonia, J/ψ and Υ, ATLAS will provide sensitive tests of QCD predictions of production in proton-proton collisions at the LHC. Secondly, ATLAS will study the properties of the entire family of B mesons (B_d^0, B^+, B_s^0, B_c and their charge-conjugate states) and B baryons, thereby broadening our knowledge of both the spectroscopic and dynamical aspects of B-physics. However, the main emphasis will be on precise measurements of weak B hadron decays. In the Standard Model, all flavour phenomena of weak hadronic decays are described in terms of quark masses and the four independent parameters in the Cabibbo-Kobayashi-Maskawa (CKM) matrix [1]. Enormous quantities of data collected in the past decade by the experiments BaBar, Belle, CDF and D0 allowed very precise measurements of flavour and CP-violating phenomena. Whilst the analysis of the remaining data of these experiments may still push the boundaries, no evidence of physics beyond the Standard Model, nor any evidence for CP violation other than that originating from the CKM mechanism, has yet been found. At the LHC, thanks to the large beauty production cross-section and the high luminosity of the machine, the sensitivity of B decay measurements is expected to substantially improve. Whilst direct detection of new particles in ATLAS will be the main avenue to establish the presence of new physics, indirect constraints from B decays will provide complementary information. In particular, precise measurements and computations in B-physics are expected to play a key role in constraining the unknown parameters of any new physics model emerging from direct searches at the LHC.

In ATLAS, the main B-physics measurements will be made with an instantaneous luminosity of around 10^{33} cm^{-2} s^{-1}; however, the B-physics potential begins during early data taking at low luminosity (10^{31} cm^{-2} s^{-1}). With an integrated luminosity of 10 pb^{-1} ATLAS will already be able to register about $1.3 \cdot 10^5$ events containing $J/\psi \to \mu^+\mu^-$ selected by the low luminosity trigger menu [2]. Recorded events will contain $J/\psi \to \mu^+\mu^-$ produced both directly in proton-proton interactions as well as indirectly from decays of B hadrons. With these statistics, beauty and quarkonia studies will play an important role in the early data-taking period.

In this document we present studies for several periods of beauty measurements in ATLAS. First, there will be a period of integrated luminosity of order of 10 - 100 pb^{-1} when B-physics and heavy-flavour quarkonia signatures will serve in helping to understand detector properties and the muon trigger, as well as measuring production cross-sections. The physics analyses in this period will deal with prompt J/ψ and Υ events, along with inclusive B hadron decays to muon pairs via J/ψ . Further on, the exclusive decays of $B^+ \to J/\psi K^+$, $B_d^0 \to J/\psi K^{0*}$ and $B_s^0 \to J/\psi\phi$ will be studied.

During the next period, from about 200 pb^{-1} to 1 fb^{-1}, we expect to collect the same or higher statistics as are currently available at the Tevatron. During this period we will start to improve upon current measurements of B hadron properties and set new decay rate limits or possibly give evidence for rates above Standard Model predictions for rare decays (e.g. in the channel $B_s^0 \to \mu^+\mu^-$).

In the most important period for ATLAS B-physics we expect to achieve about 10 - 30 fb^{-1} at an instantaneous luminosity of mostly around 10^{33} cm^{-2} s^{-1}. It is expected that ATLAS can achieve this integrated luminosity in about three years. We are preparing to study a large variety of B-physics topics covering both the production and decay properties of B hadrons. In this document we give examples of performance studies for this period with polarization measurements of heavy-flavour quarkonia and of the baryon Λ_b, by the oscillation phenomena of the $B_s^0 - \overline{B_s^0}$ system, and the rare decay measurement $B_s^0 \to \mu^+\mu^-$. We expect to achieve sensitivities allowing the confirmation of possible contributions of physics beyond the Standard Model.

2 Trigger

All B-physics studies reported in the current document include trigger reconstruction. The ATLAS trigger comprises three levels and the selection of B-physics events is initiated by a di-muon or a single-muon trigger at the first level trigger (L1). At 10^{31} cm^{-2} s^{-1} the lowest possible threshold of about $p_T >$ 4 GeV will be used, rising to 6 - 8 GeV at 10^{33} cm^{-2} s^{-1} for at least one of the L1 muons. The muon is confirmed at the second trigger level (L2), first using muon-chamber information alone, and then combining muon and inner-detector (ID) information. The use of the more precise muon information available at L2 allows rejection of below-threshold muons that passed the L1 trigger. Combining information from the muon chambers and ID track segments gives rejection of muons from π and K decays.

Following the confirmation of the L1 muon(s), cuts on invariant mass and secondary vertex reconstruction of B decay products are used to select specific channels of interest. Channels such as $B^+ \to J/\psi(\mu^+\mu^-)K^+$ and $B_s^0 \to \mu^+\mu^-$ are triggered by requiring two muons fulfilling J/ψ or B_s^0 mass cuts. At 10^{31} cm^{-2} s^{-1} a single muon is required at L1, with the second muon either originating from an additional L1 trigger or found at L2 in an enlarged Region of Interest (RoI) around the trigger muon. At luminosities above about 10^{33} cm^{-2} s^{-1}, a L1 dimuon trigger is used, giving an acceptable rate while keeping a low p_T threshold for both of the two muons.

For hadronic final states such as $B_s^0 \to D_s\pi$, ID tracks are combined to reconstruct first the $\phi \to K^+K^-$, then the $D_s \to \phi\pi$, and finally the B_s^0. Two different strategies are used for finding the tracks, depending on luminosity. Full reconstruction of the whole ID can be performed at 10^{31} cm^{-2} s^{-1}. At higher luminosities, reconstruction will be limited to regions of interest defined by the L1 calorimeter jets.

In all studies reported in the current document the trigger decision was used to accept or reject a given event. The trigger menu used to produce the datasets contained low-p_T L1 muon thresholds of 4, 5 and 6 GeV. These were used to initiate selections at L2 of decays containing $J/\psi \to \mu^+\mu^-$, like $B^+ \to J/\psi(\mu^+\mu^-)K^+$, and $B_s^0 \to \mu^+\mu^-$. The lowest thresholds for J/ψ or B_s^0 required two 4 GeV muons. In addition there were selections for $B_s^0 \to D_s\pi$ based either on full ID reconstruction or on a RoI-based reconstruction in L1 Jet RoIs with a 4 GeV threshold. More detailed information on the B-physics trigger is presented in three studies in this document. Specific questions on the L1 di-muon trigger performance for B-physics are addressed in Section 1 of this chapter. L2 triggering on muons and di-muons is presented in Section 2. Finally, triggers for B decays to purely hadronic final states have been studied in the last part of this chapter, Section 8.

If not stated otherwise, the trigger efficiencies in di-muon events were calculated with respect to Monte Carlo samples generated with cuts of $p_T > 6$ GeV and $p_T > 4$ GeV for the first and second muon respectively and with pseudorapidity cuts of $|\eta| < 2.4$ on both muons.

3 Simulation of the events

Some 1 million B hadron events, along with around 400 000 prompt J/ψ and $\Upsilon(1S)$ as well as $c\bar{c}$ events, were produced using PYTHIA 6.4 [3]. The simulations were performed with the CTEQ6L set of parton distribution functions. For quarkonium production, the NRQCD matrix element parameters in PYTHIA were tuned to fit Tevatron data [4]. In the production of non-resonant $b\bar{b}$ and $c\bar{c}$ flavour-creation, PYTHIA models describing flavour-excitation and gluon-splitting were included. The fragmentation of b quarks and c quarks to hadrons was simulated according to the Peterson fragmentation function with parameter 0.006 and 0.05 respectively. The choice of parameters was motivated by Tevatron measurements [5]. Kinematic selections on final state particles from B decays were applied so that most of the generated B events passed the trigger threshold at the reconstruction stage.

The total $b\bar{b}$ or $c\bar{c}$ cross-section is not well defined in PYTHIA when one includes processes other than those of the lowest order for $b\bar{b}$ ($c\bar{c}$) production, since PYTHIA takes the partons to be massless and therefore the cross-section diverges when the transverse momentum approaches zero. However, only part of the cross section is relevant for our studies - in the phase space of events passing B triggers.

Table 3 summarises the predicted single and di-muon cross-sections from charm, beauty and onia production expected at ATLAS from PYTHIA with cuts on the transverse momenta of the muons of 6 or 4 GeV (as appropriate) and pseudorapidity cuts on both muons of $|\eta| < 2.4$. The cuts reflect the trigger thresholds and were selected to allow most of the simulated events to be accepted by the trigger.

Process (μ6 threshold)	Cross-section		Process (μ4 threshold)	Cross-section	
$bb \to \mu 6X$	6.1	μb	$bb \to \mu 4X$	19.3	μb
$cc \to \mu 6X$	7.9	μb	$cc \to \mu 4X$	26.3	μb
$bb \to \mu 6\mu 4X$	110.5	nb	$bb \to \mu 4\mu 4X$	212.0	nb
$cc \to \mu 6\mu 4X$	248.0	nb	$cc \to \mu 4\mu 4X$	386.0	nb
$pp \to J/\psi(\mu 6\mu 4)X$	23.0	nb	$pp \to J/\psi(\mu 4\mu 4)X$	28.0	nb
$pp \to \Upsilon(\mu 6\mu 4)X$	4.6	nb	$pp \to \Upsilon(\mu 4\mu 4)X$	43.0	nb
$bb \to J/\psi(\mu 6\mu 4)X$	11.1	nb	$bb \to J/\psi(\mu 4\mu 4)X$	12.5	nb

Table 1: Predicted PYTHIA cross-sections for various muon and di-muon sources. The numbers following each symbol μ denote the p_T thresholds that were used in generating the events with PYTHIA.

After PYTHIA simulation, the events were passed through detector simulation (based on GEANT4 [6]) which first modelled the behavior of the particles as they passed through the detector, and simulated the response of the active detector components to the energy deposition by these particles. The layout of the detector used by the simulation code was published in Ref. [7]. The output of the simulation was then reconstructed as if it were real data. Following this, reconstructed muons and hadrons were analysed using the dedicated B-physics analysis software.

4 Organization of the B-physics chapter

The following reports on B-physics present our best current understanding of the ATLAS B-physics programme. As the B trigger plays a role in all the studies presented here, the chapter starts with two reports, in Sections 1 and 2, dealing with L1 and L2 muon triggers respectively. There follow three physics studies typical for the early data period: physics of heavy-flavour quarkonia (Section 3), measurements of beauty cross-sections (Section 4) and early physics and performance measurements with decays of B_d^0 and B_s^0 mesons in Section 5. Finally there are Sections 6, 7 and 8, which give typical examples of ATLAS B measurements that can only be achieved during the more advanced data taking period; they are measurements of the polarization of the baryon Λ_b, the rare decay $B_s^0 \to \mu^+\mu^-$ and finally the oscillation measurement of the $B_s^0 - \overline{B_s^0}$ system.

References

[1] N. Cabibbo, Phys. Rev. Lett. 10, p. 531 (1963); M.Kobayashi and T.Maskawa, Prog. Theor. Phys. 49, p. 652 (1973).

[2] ATLAS collaboration, 'Trigger for Early Running', this volume.

[3] T. Sjostrand, S. Mrenna, P. Skands, JHEP 05, 026 (2006).

[4] G. Altarelli, (Ed.), M. L. Mangano, (Ed.) CERN-2000-004, p. 231-304 (2000).

[5] M. Cacciari, S. Frixione , M.L. Mangano, P. Nason, G. Ridolfi, JHEP 07, 033 (2004); M. Cacciari, P. Nason, Phys. Rev. Lett. 89, 122003 (2002).

[6] ATLAS collaboration, Computing Technical Design Report, ATLAS-TDR-017, CERN-LHCC-2005-022 (2005).

[7] ATLAS collaboration, The ATLAS Experiment at the CERN Large Hadron Collider, JINST 3 (2008) S08003.

Performance Study of the Level-1 Di-Muon Trigger

Abstract
An event with two muons in the final state is a distinctive signal and can be triggered efficiently with the use of the level-1 di-muon trigger. Nevertheless triggering is still an issue if these muon tracks are fairly soft and fake di-muon triggers originating from muons that traverse more than one region of the trigger chambers increase the trigger rate. It is important to provide an acceptable trigger rate, while keeping high trigger efficiency to study low-p_T B-physics such as rare B hadron decays or CP violation in the B-events, especially in a multi-purpose experiment like ATLAS. In this note, the level-1 di-muon trigger and its expected performance are described.

1 Introduction

ATLAS is a multi-purpose experiment and its main focus is the direct search for and study of physics beyond Standard Model. However the indirect search for new physics will also play an important role in revealing the (flavor) structure of a non-trivial Higgs sector, which cannot be obtained by direct searches.

The $B^0_{s,d} \to \mu^+\mu^-$ rare decay is one of the interesting signatures which are sensitive to new physics at the TeV energy scale. The precise measurement of the forward-backward asymmetry [1] or branching ratio in the semi-muonic B decay $B \to \mu^+\mu^- X$ requires good understanding of the possible biases introduced by event selection. Also important are precise measurements of Standard Model parameters, including CP-violation in B-events, such as $B_s^0 \to J/\psi\phi$ and $B_d^0 \to J/\psi K_s^0$. The key to the detection of these B signals in ATLAS is to achieve a high trigger efficiency for low-p_T di-muon events, keeping an acceptable trigger rate. It is also essential to understand the acceptance and efficiency using $pp \to J/\psi(\mu^+\mu^-)X$ or $pp \to \Upsilon(\mu^+\mu^-)X$ [2].

First, the level-1 muon trigger is briefly explained in Section 2, then trigger simulation and MC samples used in this note are described in Section 3. The performance of the level-1 single- and di-muon trigger as well as the effect of an algorithm to resolve muons traversing more than one trigger chambers are described in Section 4. Finally, the performance and the impact of various level-1 muon trigger configurations on some example B signal events are discussed in Section 5.

2 Level-1 muon trigger

The ATLAS trigger system architecture is organised in three levels; level-1, level-2 and event filter. The level-2 and event filter triggers provide a software-based event selection after the level-1 trigger and events accepted by this trigger chain are finally reconstructed and analyzed offline.

The ATLAS level-1 muon trigger is based on dedicated, fast and finely segmented muon chambers (RPC and TGC) [3] and a trigger logic implemented in hardware. The muon trigger system provides acceptance in pseudo-rapidity up to $|\eta| \sim 2.4$ and in the full azimuthal angle (ϕ) range. A muon track is triggered by the coincidence of two or three detector stations (consists of chamber doublet or triplet) within a certain road (coincidence window). The transverse momentum of a muon candidate is determined by its deviation from the trajectory of an infinite-momentum track (i.e. a straight line). A three station coincidence is required for any p_T threshold in the endcap and forward regions ($|\eta| > 1.05$) to avoid high trigger rates caused by accidental coincidences due to background.[1] As a result, the acceptance at large $|\eta|$ becomes small for low-p_T muons, as shown in Section 4.

[1]The number of stations used for coincidence is programmable giving the possibility of lowering a p_T threshold at low luminosity if background conditions allow it.

The granularity of the level-1 muon trigger, the size of a Region of Interest (RoI), is $\Delta\eta \times \Delta\phi = 0.1 \times 0.1$ in the barrel region ($|\eta| < 1.05$) and $\sim 0.03 \times 0.03$ in the endcap regions ($1.05 < |\eta| < 2.4$). In short, if two muons leave tracks in the same RoI, they are counted as a single muon candidate by the trigger system. The level-1 muon trigger decisions from different regions are sent to the Muon Central Trigger Processor Interface (MuCTPI) which combines the information and calculates the multiplicity of muon candidates for each p_T threshold over the whole detector. In forming the multiplicities, care is taken to avoid double counting of single-muon tracks, reconstructed separately in adjacent trigger sectors, while retaining a high efficiency for genuine di-muons. The overlap handling is carried out using Lookup Tables (LUT) to give flexibility and programmability. The LUTs are generated based on Monte Carlo simulations of single-muon events, selecting the regions of the level-1 muon system that can be traversed by a single muon.

The overlap handling is mandatory to avoid unacceptably high trigger rates caused by doubly-counted single muons, so called *fake di-muon triggers*. Most of the overlaps are resolved by the MuCTPI, which takes the muon candidate with the higher p_T into account when calculating the muon multiplicity and finding overlapping muon candidates. The MuCTPI consists of independent 16 octant modules and overlap resolving is performed in each module. Therefore, overlapped regions connected to two different octant modules cannot be solved in MuCTPI and should be treated in each subdetector (RPC and TGC) by masking channels or flagging a overlap bit. The parameters used in the overlap handling, such as the combination of RoIs and masked channels are programmable. More details are described in Refs. [3, 4].

3 Monte Carlo samples and trigger configuration

Single-muon Monte Carlo samples with various, fixed p_T values are used for performance tests of the level-1 single muon trigger logic. Single-muon events are generated uniformly over the full azimuthal angle range and $|\eta| < 2.7$ with a fixed p_T value. The detector response is simulated using Geant4 [4] with the ATLAS geometry in the Athena framework [5]. Trigger simulation is performed using the trigger configuration for luminosity of 10^{31}-10^{33}cm^{-2}s^{-1} running, with a set of p_T thresholds of 4, 5, 6, 11, 20 and 40 GeV. The production vertex is smeared with a Gaussian distribution with $\sigma_x = \sigma_y = 15$ μm and $\sigma_z = 56$ mm. The level-1 single- and di-muon trigger menu items are named as MUx (single-muon trigger) and 2MUx (di-muon trigger with the same threshold for both muons) respectively, where x represents the p_T threshold. The exceptions are MU0 and 2MU0, which correspond to completely opened coincidence windows. However, even in this case, the acceptance of the coincidence windows is limited by connectivity as well as by the dimension of the coincidence matrix ASICs [6].

The trigger efficiencies of various level-1 trigger configurations are also studied using B-physics Monte Carlo events. Event generation is done using PYTHIA [7]. Only interesting events associated with at least two muons with $p_T > 6$ GeV (the leading muon) and 4 GeV (the second muon) within $|\eta| < 2.5$ are studied. The B-physics samples used in this note are $B_s^0 \to \mu^+\mu^-\phi$ (47,650 events), $B_s^0 \to \mu^+\mu^-$ (47,450 events) and $B^+ \to J/\psi(\mu^+\mu^-)K^+$ (49,250 events). The last sample is chosen partly as a control sample. The opening angle of the two muons is smaller in this sample than in the other two samples.

In this note, only the level-1 muon trigger is simulated and events triggered by level-1 are studied.

4 Level-1 muon trigger efficiency in single-muon events

Detailed performance studies of the single muon trigger were performed in the barrel and endcap regions separately and the results are described in Ref. [8]. The single muon trigger efficiencies as a function of the transverse momentum of the simulated muon, over the whole muon trigger system are shown in

Figure 1. The single muon trigger efficiency is defined by:

$$\varepsilon(\mathrm{MUx}) = \frac{\text{\# of events triggered}}{\text{\# of single muon events with } |\eta| < 2.5}\,. \tag{1}$$

The range of pseudo-rapidity applied in the efficiency calculation is $|\eta| < 2.5$ and not 2.4 as used in Ref. [8], since $|\eta| < 2.5$ is applied for muons in the B-physics samples (Muons with $|\eta| > 2.4$ can be triggered if their momentum is relatively low and the track is bent towards smaller $|\eta|$). The efficiency, $\varepsilon(\mathrm{MUx})$, includes all contributions from geometrical acceptance and coincidence window coverage. The trigger efficiency of MU5 and MU6 is lower than MU0 even for high p_T muon tracks. This is because all regions don't have full (100 %) acceptance except MU0 which accepts all muons within station coincidence windows. Figures 2 (a) and (b) show the trigger efficiency as a function of the $|\eta|$ of the simulated

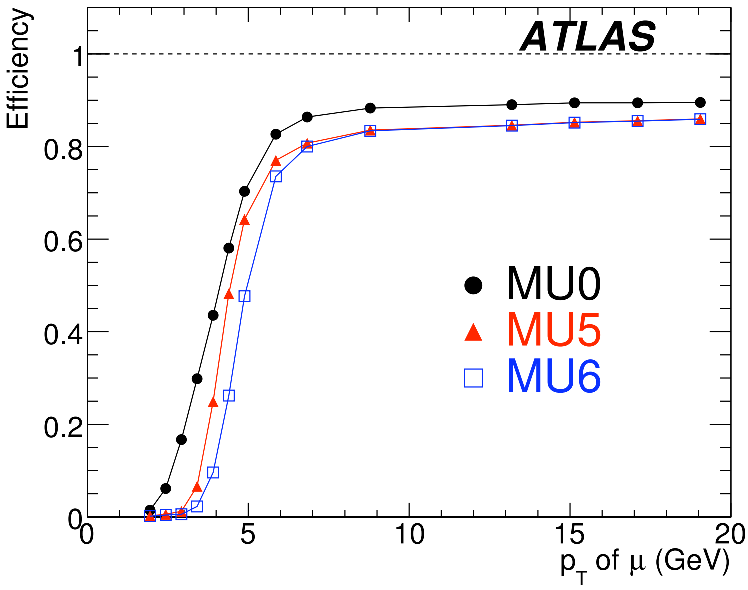

Figure 1: Trigger efficiency as a function of p_T with each low-p_T threshold; MU0 (filled circles), MU5 (filled triangles) and MU6 (open squares) for muons with $|\eta| < 2.5$ at the interaction point.

muon with p_T at threshold and with p_T=19 GeV for MU0 and MU6 trigger selections, respectively. The efficiency at the plateau is predominantly determined by geometrical acceptance. Efficiency losses at $|\eta| \sim 0$, 0.4 and 0.7 are caused by cracks and inactive material, like ribs, detector support structures and the elevator hole. Around the transition region between the barrel and the endcap, $|\eta| \sim 1.05$, some efficiency is lost because the station coincidence cannot be satisfied. A small efficiency gap at the boundary between the endcap and forward regions ($|\eta| \sim 2$) is also due to the station coincidence, since the endcap and forward systems are treated separately. However, this effect is smaller than in the transition region between the barrel and the endcap. Poor MU0 efficiency at p_T =4 GeV is seen in the endcap region due to the requirement of three station coincidence, not two as required in the barrel. The trigger was originally designed for $p_T > 6$ GeV as the lowest threshold, but can be applied below this threshold at very low luminosity.

Figures 3 (a) and (b) show the trigger efficiency as a function of ϕ (ϕ=0 and $\pm\pi$ denote directions perpendicular to the beam axis in the horizontal plane) of the simulated muon with p_T at threshold and with p_T=19 GeV for MU0 and MU6 trigger selections, respectively. The efficiency loss can be clearly

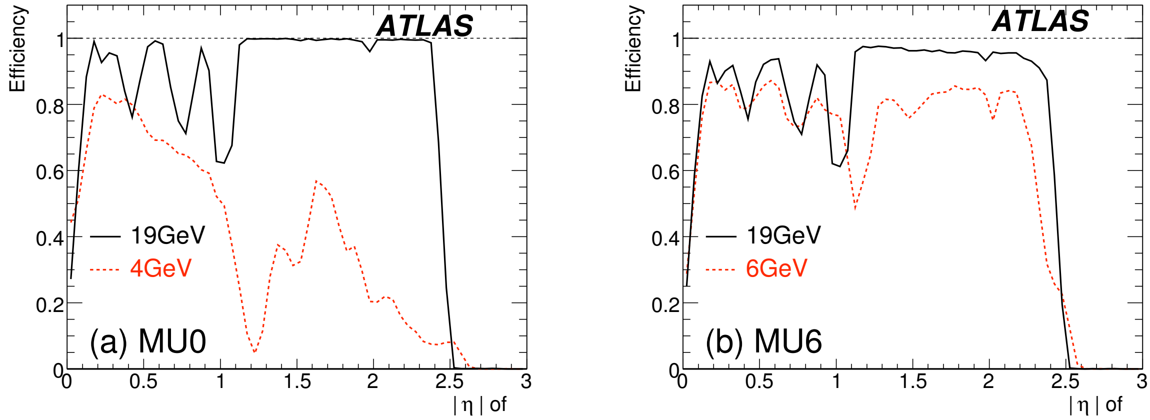

Figure 2: The $|\eta|$ dependency of the trigger efficiency for MU0 (a) and MU6 (b) trigger selections. Solid lines correspond to the simulated muons with p_T=19 GeV, dotted lines are for muons with p_T at threshold (in the case of MU0 this threshold is set to 4 GeV).

seen around $\phi \sim -1.2$ and -2 at the magnet's feet, especially for high p_T muons. The geometrical structure is in general more visible in efficiency using higher p_T muons, as they produce straighter tracks.

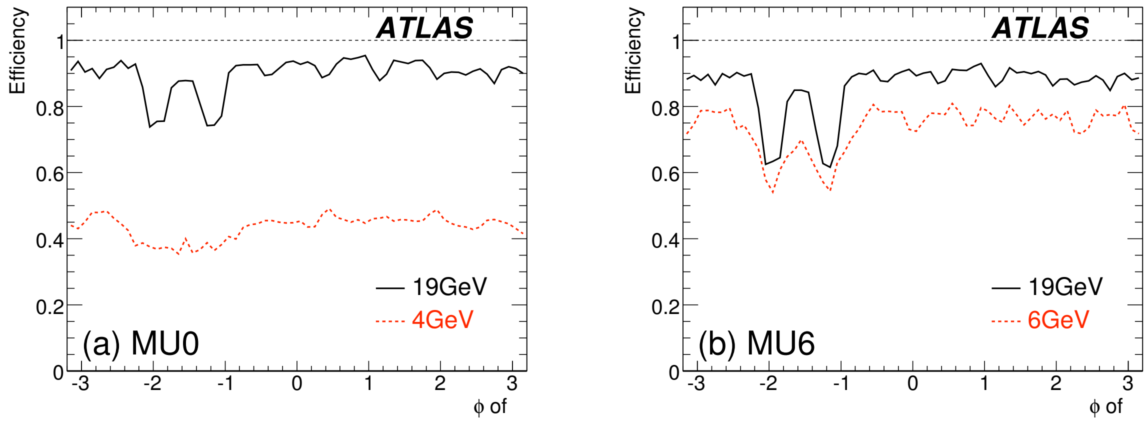

Figure 3: The ϕ dependency of the trigger efficiency for MU0 (a) and MU6 (b) trigger selections. Solid lines correspond to the simulated muons with p_T=19 GeV, dotted lines are for muons with p_T at threshold (in the case of MU0 this threshold is set to 4 GeV).

5 Level-1 muon trigger performance in B-physics events

A detailed level-1 trigger simulation is mandatory to find effective trigger menus and thresholds for certain physics processes and to determine the trigger efficiency and rate as well as to study the trigger bias. In this section, di-muon and single-muon trigger efficiencies with different p_T thresholds and the dependency of di-muon trigger efficiencies as a function of the opening angle between simulated muons are discussed using B-physics Monte Carlo samples.

5.1 Efficiency with various trigger configurations

The efficiency of the level-1 muon trigger for three different B-physics processes, $B_s^0 \to \mu^+\mu^-$, $B_s^0 \to \mu^+\mu^-\phi$ and $B^+ \to J/\psi(\mu^+\mu^-)K^+$ is studied with various trigger configurations. The efficiencies of the single muon triggers (MU0 and MU6) and the di-muon triggers (2MU0 and 2MU6) are summarized in Table 1. The efficiency of the single muon trigger is high, about 95 %, since multiple muons have a higher probability to be triggered by a single muon trigger. The 2MU0 trigger gives better efficiency than 2MU6 by $\sim$ 16 % for di-muon events with p_T above 6 GeV (4 GeV) for the fastest (second fastest) muon. The efficiency loss due to the MuCTPI overlap handling is seen in all physics processes, although the relative efficiency loss is small, $\sim$ 0.5 %.

	Efficiency [%]		
Trigger Menu / Process	$B_s^0 \to \mu^+\mu^-$	$B^+ \to J/\psi(\mu^+\mu^-)K^+$	$B_s^0 \to \mu^+\mu^-\phi$
MU0	97.0±0.1	96.8±0.1	97.0±0.1
MU6	93.0±0.1	92.9±0.1	93.1±0.1
2MU0	67.9±0.2	68.8±0.2	69.0±0.2
2MU6	51.6±0.2	52.9±0.2	53.2±0.2
2MU0 (w/o MuCTPI overlap handling)	68.2±0.2	69.1±0.2	69.4±0.2
2MU6 (w/o MuCTPI overlap handling)	52.0±0.2	53.4±0.2	53.7±0.2

Table 1: The level-1 trigger efficiency of various configurations. The efficiency is calculated with respect to the number of generated events (not to the number of muons) of three different physics processes. The errors are statistical only.

5.2 Opening-angle dependency

In case of measuring some quantity as a function of a certain parameter, one must ensure that the trigger efficiency is independent of that parameter, or correct the measurement to avoid a bias from the trigger. Figure 4 shows the 2MU0 and 2MU6 trigger efficiencies as a function of ΔR ($=\sqrt{\Delta\eta^2+\Delta\phi^2}$) between the two leading muons in $B_s^0 \to \mu^+\mu^-\phi$ events. The η and ϕ are true parameters of muon flight direction at the production vertex. No offline selection is applied in order to see see the bias from the level-1 trigger. The trigger efficiency clearly depends on the opening angle of the two leading muons. The efficiency is lower at large opening angles because in this case the B_s system is not boosted i.e. momenta of the muons are lower. Since overlap removal between the muon candidates doesn't play a role at large opening angles, this effect is purely due to kinematics. Figure 5 (a) shows the p_T distribution of the leading muons for three different ΔR ranges: $\Delta R < 0.1$, $0.2 < \Delta R < 0.4$ and $\Delta R > 0.5$. The muons at large opening angles clearly have a softer p_T spectrum. The effect is even more clearly visible for higher threshold di-muon trigger items, as the probability of having muons at large ΔR with transverse momenta high enough to trigger a high threshold di-muon trigger item is very small, but non-negligible at small opening angles.

The small efficiency loss at very small opening angles ($\Delta R < 0.1$) is however due to the trigger system. In the case that the muons both leave hits in the same RoI, only one muon can be triggered by

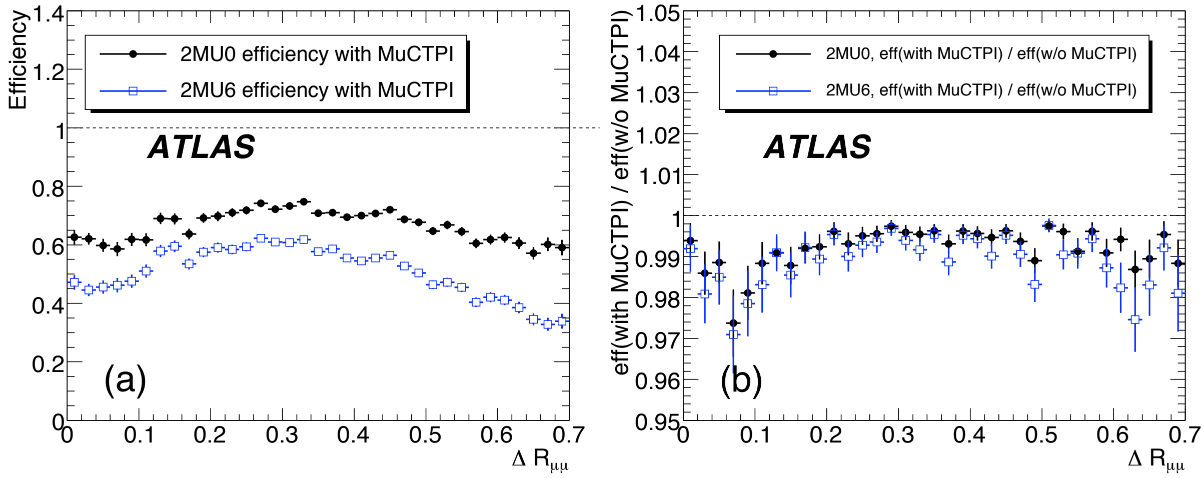

Figure 4: (a) Trigger efficiency as a function of ΔR in the semi-leptonic rare B decay $B_s^0 \to \mu^+\mu^-\phi$ using the 2MU0 (filled circles) and 2MU6 (open squares) with MuCTPI. (b) Effect of MuCTPI as a function of the opening angle, ε(without MuCTPI)/ε(with MuCTPI) for 2MU0 (filled circles) and 2MU6 (open squares).

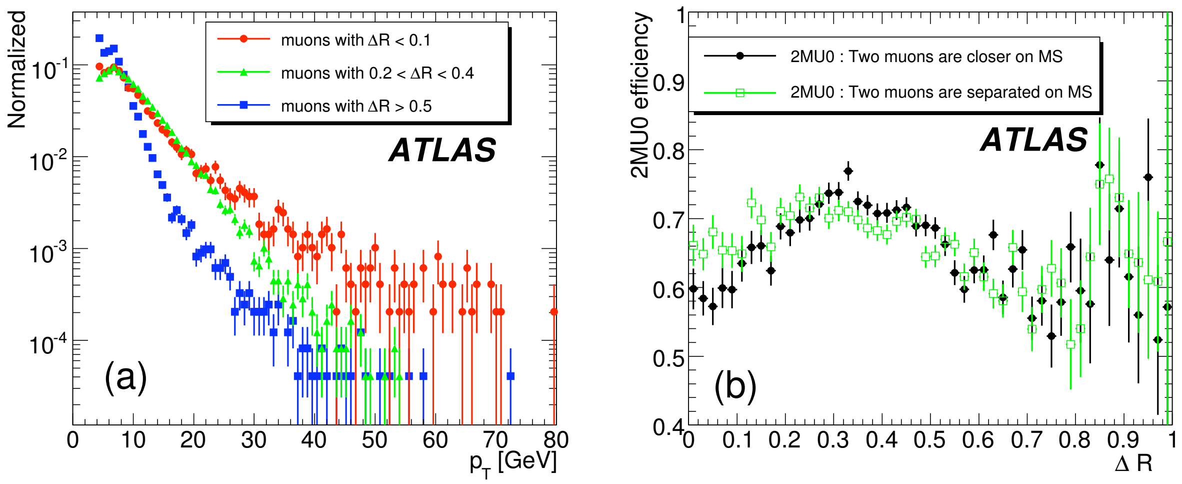

Figure 5: (a) The truth p_T distribution of the two leading muons is different opening angles range in $B_s^0 \to \mu^+\mu^-\phi$ events: $\Delta R < 0.1$ (filled circles), $0.2 < \Delta R < 0.4$ (filled triangles) and $\Delta R > 0.5$ (filled squares). (b) The efficiency of 2MU0 as a function of opening angles for two cases: the ΔR separation of the two muons is either larger (filled circles) or smaller (open circles) at the muon trigger system compared to that at the primary vertex.

the system. Figure 5(b) shows the 2MU0 efficiency as a function of the opening angle, but events are divided into two classes: In one case we select the muon pairs whose separation is expected to shrink when reaching the muon spectrometer (filled circles), while in the other case (open squares) we select the muon pairs whose separation is expected to grow.

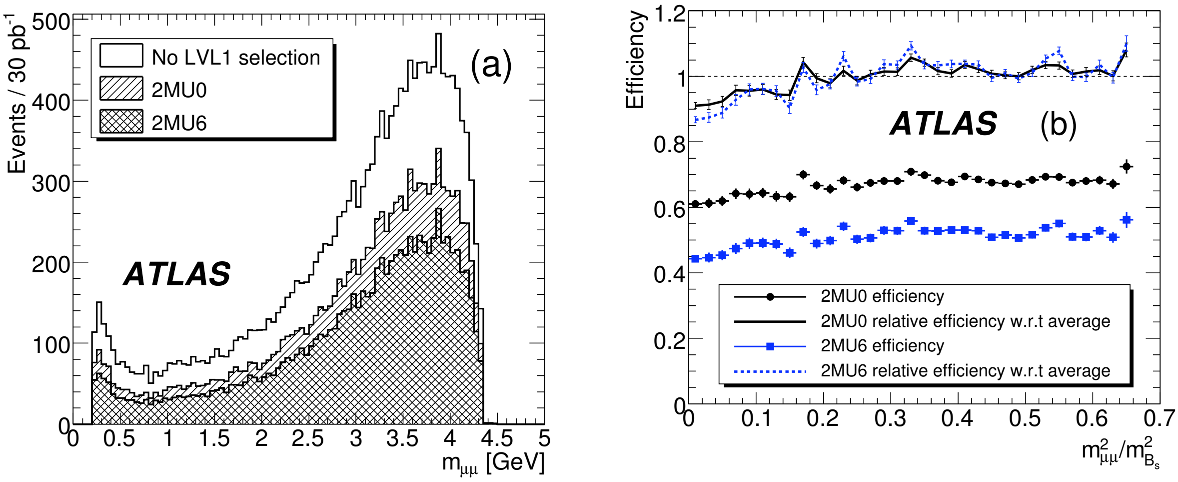

Figure 6: (a) Scaled di-muon invariant mass-squared distribution in $B_s{}^0 \to \mu^+\mu^-\phi$ events: no level-1 selection (open histogram), triggered by 2MU0 (hatched histogram) and by 2MU6(cross hatched histogram). (b) Efficiencies of 2MU0 (filled circles) and 2MU6 (open squares) as a function of di-muon invariant mass-squared. The two lines show the relative efficiency with respect to the corresponding average value for 2MU0 (solid line) and 2MU6 (dotted line).

One example B-physics study is to look at the differential decay rate dBr($B \to \mu^+\mu^-\phi$) / d$\hat{s}$ or forward-backward asymmetry A_{FB} as a function of di-muon invariant mass to discriminate between Standard Model and new physics contributions. The $\hat{s}$ is $m^2_{\mu\mu}/m^2_B$ and the $A_{FB}(\hat{s})$ is defined as

$$\left(\int_0^1 \frac{d\Gamma}{d\hat{s}\hat{z}} d\hat{z} - \int_{-1}^0 \frac{d\Gamma}{d\hat{s}\hat{z}} d\hat{z}\right) / \int_{-1}^1 \frac{d\Gamma}{d\hat{s}\hat{z}} d\hat{z}, \tag{2}$$

where $\hat{z} = \cos\theta$ (θ is the angle between the μ^+ and ϕ in the $\mu^+\mu^-$ rest frame) and $d\Gamma/d\hat{z}$ is the differential event rate of $B_s^0 \to \mu^+\mu^-\phi$.

Figure 6 (a) shows the $\mu^+\mu^-$ invariant mass distribution with and without level-1 triggers in $B_s{}^0 \to \mu^+\mu^-\phi$ events. Trigger efficiency with 2MU0 and 2MU6 are shown as a function of $\mu^+\mu^-$ invariant mass in Figure 6 (b). The relative trigger efficiency, normalized to the efficiency averaged over a whole $m^2_{\mu\mu}/m^2_B$ range, is also shown to illustrate the trigger bias. The invariant mass dependency of the level-1 di-muon trigger efficiency is weak compared to the opening angle dependency and almost independent of the trigger threshold. A efficiency drop can be seen at small $m_{\mu\mu}$, which is also because the two muons are triggered as a single muon by the muon trigger system.

Similarly, the forward-backward asymmetry A_{FB} is shown as a function of $\hat{s}$ in Figure7(a). The difference (A_{FB}[2MUx] - A_{FB}[no selection]) is also shown in Figure 7(b). It should be noted that significant differences between forward and backward samples in terms of momentum, pseudo-rapidity and $\mu^+\mu^-$ opening angle distributions are observed. Nevertheless, as illustrated in Figure 7, the forward-backward asymmetry is more robust to the effects of level-1 di-muon triggering than di-muon mass distributions (see Figure 6).

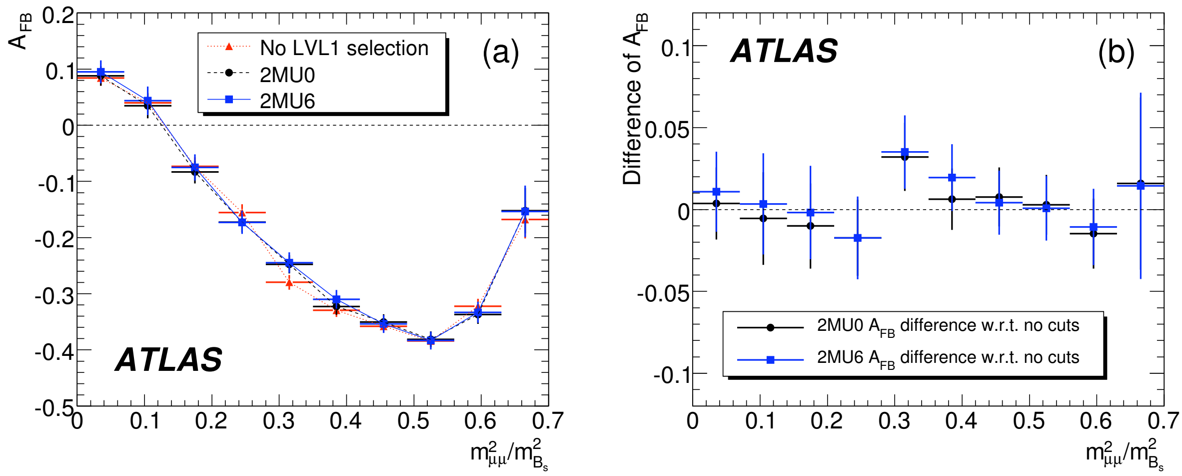

Figure 7: (a) Forward-Backward asymmetry in $B_s^0 \to \mu^+\mu^-\phi$ events: no level-1 selection (filled triangles), triggered by 2MU0 (filled circles) and by 2MU6(open squares). (b) deviation between A_{FB}'s with and without triggers (A_{FB}[`2MUx`] - A_{FB}[`no selection`]: 2MU0 (filled circles) and 2MU6 (open squares).

6 Summary

The level-1 di-muon trigger is essential for selecting rare B decays that have low-p_T muons in the final state. The rate for a single-muon trigger at the relevant thresholds would be unacceptably high. A detailed level-1 muon trigger simulation is implemented and used for the study of the trigger efficiency and its bias for B-physics events. The level-1 di-muon trigger efficiencies of 2MU0 and 2MU6 are high enough (about 70 % and 50 %, respectively) in the interesting B-physics events. The fake level-1 di-muon trigger rate is 2.3 kHz [8] while the genuine di-muon event rate is $\sim$ 600 Hz (muons with $p_T > 4$ GeV from $c\bar{c}$ and $b\bar{b}$) at $\mathscr{L} = 10^{33}\mathrm{cm}^{-2}\mathrm{s}^{-1}$. The efficiency loss from the MuCTPI overlap handling is found to be negligible.

The trigger bias in regard to the opening angle and invariant mass of two muons was also studied. An opening angle dependence is clearly seen, of the order of ±10 % and ±15 % for 2MU0 and 2MU6, respectively. It is explained by the single-muon efficiency curves and muon kinematics in signal events. This dependency is stronger for higher p_T thresholds. No clear bias is seen due to the presence of the MuCTPI overlap handling. The trigger efficiency is rather flat over the invariant mass and less dependent on the trigger threshold since the invariant mass is not as strongly correlated to muon momenta as the opening angle is.

References

[1] A. Policicchio and G. Grosetti, **ATL-COM-PHYS-2007-019** (2007).

[2] The ATLAS Collaboration, *Triggering on Low-p_T Muons and Di-Muons for B-Physics*, this volume.

[3] The ATLAS Collaboration, *The ATLAS experiment at the CERN Large Hadron Collider*, JINST 3 (2008) S08003, 2008.

[4] S. Agostinelli et al., Nucl. Instr. and Meth. **506**, 250 (2003).

[5] The ATLAS Collaboration, CERN-LHCC-2005-022 (2005).

[6] The ATLAS Collaboration, CERN-LHCC-98-14 (1998).

[7] T. Sjöstrand, S. Mrenna and P. Skands, JHEP **05**, 026 (2006).

[8] The ATLAS Collaboration, *Performance of the Muon Trigger Slice with Simulated Data*, this volume.

Triggering on Low-p_T Muons and Di-Muons for B-Physics

Abstract

Muon pairs from J/ψ decay are a clear signature of b hadrons. As a large fraction of b hadrons are produced at low-p_T, a low rate, efficient di-muon trigger for low-p_T muons and a good understanding of the trigger efficiency are essential. Di-muon final states will also play a key role in calibration, alignment and determination of the trigger efficiencies. The performance of the level-2 dimuon trigger algorithms is discussed, together with a method for reducing backgrounds from decays-in-flight. A strategy for calculating the single muon and di-muon trigger efficiencies at level-1 and level-2 using J/ψ from the data themselves is presented.

1 Introduction

B-physics is one of the areas of the physics programme of the ATLAS experiment. It includes the study of production cross sections, searches for rare b decays and measurements of CP violation effects. These studies make use of the large $b\bar{b}$ production cross section at the LHC where $b\bar{b}$ pairs are abundant in the low transverse momentum (p_T) region. On the other hand, one must extract signals from amongst the large QCD background, mostly composed of light quarks. For this purpose, one of the main channels for B physics study involves decay channels with one or more muons in the final state, especially the channel $J/\psi \to \mu^+\mu^-$.

The output rate of the first level trigger at a luminosity of $10^{33}\mathrm{cm}^{-2}\mathrm{s}^{-1}$ is expected to contain 20 kHz of events where one muon passed the p_T threshold of 6 GeV. Early running is envisioned to include even lower p_T thresholds, down to the lowest threshold achievable in the hardware.

At the second level trigger this rate of events must be reduced to 1-2 kHz, of which 5-10% are available for channels of interest only to B-physics. Currently this goal is achieved for level-1 muon triggers by first confirming that a muon over the nominal threshold is reconstructed in the muon spectrometer (MS), and then confirming that there is a matching track in the inner detector (ID). This selection criterion removes many muons from K and π decays, but does not by itself produce the required rate reduction. To achieve the required rate p_T thresholds need to be raised and many interesting b events are likely to be filtered out. We therefore focus also on di-muon final states.

We developed an algorithm, TrigDiMuon, which achieves high efficiency at level-2 for the golden CP channels (J/ψ), using the identification of relatively low-p_T muons from J/ψ decay. TrigDiMuon searches for di-muon pairs from J/ψ or other resonant sources, when only one of the muons passed the level-1 or level-2 single muon selection. The use of TrigDiMuon can enhance J/ψ efficiency at low-p_T compared to the trigger based on two muons found at level-1, with an acceptable increase in the fake rate.

In this note, we present the performance of the TrigDiMuon algorithm, that looks for a second low-p_T muon partner to a single muon triggered at level-1. We compare it to the performance of an algorithm that requires a di-muon level-1 trigger. The comparison is based on a sample of J/ψ which decayed into muons with low-p_T, such that the second muon of each decay may be below the level-1 threshold.

In addition to the foreseen specialised trigger strategies for di-muon signatures, it is important to optimize the rejection of muons from K and π decays for the standard single muon selection in order to have the lowest possible threshold on the inclusive single muon trigger. This is achieved by extrapolating the muon track from the MS back to the interaction vertex and requiring a good match between this track and the associated track from the ID. Muons from light hadron decays do not match accurately the ID track, which in this case is the track produced by the parent hadron (or from a mixture of hits from the parent and the daughter muon) and not by the muon track. This note presents a method implemented at the level-2 trigger for rejecting muons from K and π decays. We summarize the rejection power of this method, show that the efficiency loss is minimal for direct muons and estimate the efficiency loss for low-p_T muons from J/ψ decay.

Cross section measurements or searches for rare decays require a good understanding of the efficiency of the event selection. As we are interested in events with rather low-p_T, the understanding of the trigger efficiency is crucial and we must have a strategy for measuring it from data with high precision. The tag-and-probe method for measuring the single muon trigger efficiency using J/ψ events is presented, and we demonstrate that the obtained trigger efficiency can be applied to calculate the di-muon trigger efficiency. A calibration trigger is proposed to collect an unbiased sample of single muons with an enhanced J/ψ fraction, and the expected performance of the trigger efficiency measurement in the early days of the data-taking is discussed.

Particles from additional collisions in the same bunch-crossing (pile-up) are not simulated in the samples used for this paper, and therefore this additional background is not taken into account in the analysis.

2 Simulated datasets used and production tools

Since the subject of this note is low-p_T muons, we use simulated samples that were produced with especially low-p_T cuts at the event generation level. Samples were generated using the PYTHIA event generator [1]. Except for the minimum bias events, a generator level filter was applied to pre-select efficiently the events in the sample. The di-muons sample passed a filter which required the existence of at least two muons with the appropriate p_T and η cuts. For the inclusive muon samples the filter required the existence of a single muon passing the corresponding selection. Events were processed with the full simulation of the ATLAS detector based on the GEANT package [2]. The level-1 simulation, High Level Trigger (HLT) selection and offline event reconstruction were performed.

The following di-muon samples were used:

- An 8000 event sample of the channel $\Lambda_b \to J/\psi\Lambda$ with $J/\psi \to \mu^+\mu^-$, where one of the muons is required at the event generation level to have $p_T > 4$ GeV and the second muon is required to have $p_T > 2.5$ GeV.
- Simulated samples of direct J/ψ production and $b\bar{b} \to J/\psi$ production, with the generator level filter requiring the existence of at least two muons with $p_T > 6$ GeV for the highest p_T muon and $p_T > 4$ GeV for the second highest p_T muon. For both processes, 150000 events were generated.
- Two samples of inclusive muon from b decays were used. A 200000 event sample of $b\bar{b} \to \mu X$ with a generator level filter requiring one muon with $p_T > 4$ GeV, and a sample of 250000 $b\bar{b}$ events with at least one muon with $p_T > 6$ GeV in the final state.
- Since this note deals specifically with methods of rejecting muons from K and π decays, a large sample of such decays was required. A minimum bias sample where pions and kaons were

forced to decay inside the inner tracker volume was produced for this purpose. The method developed for producing this "forced-decay" sample is described in detail below.

- Events containing a single muon each were used to study the effect on prompt muons of the method for rejecting muons from K and π decays. Some of the single muon samples were simulated with a perfectly aligned detector geometry, while some other samples were simulated with a misaligned detector description.

The trigger and reconstruction software used for some of the samples are of a later version than that used in other notes, because the level-2 and reconstruction software used here have improved significantly in recent version. The software modification will be explained where each package is described. Table 1 summarizes the simulated Monte Carlo samples used in this note.

Samples		Generator level filter	Statistics
Signal samples	Direct $J/\psi \to \mu^+\mu^-$	$p_T^{\mu_{1,2}} > 6,4$ GeV	150 k
	$b\bar{b} \to J/\psi \to \mu^+\mu^-$	$p_T^{\mu_{1,2}} > 6,4$ GeV	150 k
	$\Lambda_b \to J/\psi\Lambda$ ($J/\psi \to \mu^+\mu^-$)	$p_T^{\mu_{1,2}} > 4,2.5$ GeV	7.6 k
Background samples	$b\bar{b} \to \mu + X$	$p_T^{\mu} > 6$ GeV	250 k
	$b\bar{b} \to \mu + X$	$p_T^{\mu} > 4$ GeV	185 k
	Minimum bias (forced K /π)		114 k
	Minimum bias (standard)		500 k

Table 1: Summary of MC samples.

2.1 Production tools and samples employed for K and π decays

Minimum bias events are the most copious source of pions and kaons. These particles are produced mainly with very low-p_T, and typically the muons coming from their in flight decays do not escape the ATLAS hadronic calorimeter. On the other hand pions and kaons with high-p_T have a low probability to decay before the calorimeter because of their high energy. As a consequence it is not efficient to use minimum bias events as a source of decays in flight to muons. Estimates made for this analysis indicated that the simulation of 5000 minimum bias events would be needed to provide one muon from K or π decay capable of passing the 6 GeV threshold of the ATLAS level-1 muon trigger.

To increase the statistics of events with charged pions and kaons decaying in flight, a special simulation tool is applied. Since we are interested in decays which happen inside the detector, the decays cannot be made on generator level but must happen in the GEANT simulation. The program to force the K /π to decay in the detector is an extension to GEANT which runs before the simulation itself.

In each event a list of all charged pions and kaons with $p_T > 2$ GeV is compiled, and one of the particles in the list is randomly selected. Events with no charged pions or kaons with $p_T > 2$ GeV are dropped at this stage, such that the events are not further simulated and nothing is written to output.

The point of decay is selected by first computing the trajectory length from the production vertex to where the particle would exit the ID (neglecting curvature in the magnetic field). The decay position is then determined by taking a random fraction of this maximum track length. Since particles assigned a late decay have a larger probability to be stopped through hadronic interactions, this procedure may introduce a weak bias towards shorter decay lengths.

For this study a minimum bias sample of 114 k events was simulated with forced decays. The transverse momentum cut of 2 GeV applied to the light hadrons reduces the cross section of the sample to $(43.41 \pm 0.07)\%$ of the minimum bias cross section. In addition to this a minimum bias sample of 500 k events, simulated with the standard GEANT simulator, was also employed to provide a cross-check from a single source for both the muons from K/π decay and the prompt muons.

3 The muon trigger

The ATLAS trigger system [3] reduces the event rate from the 40 MHz beam crossing rate to ~200 Hz for mass storage, keeping the events that are potentially the most interesting for physics. The first level trigger [4] selection is performed by custom hardware and identifies a detector region for which a trigger element was found. The second level trigger [5] is performed by dedicated software, making its decision based on data acquired from the Region of Interest (RoI) identified at level-1. Eventually, the event filter [5] uses the complete event data, and algorithms adapted from the offline reconstruction, to refine the selection of level-2 and further reduce the trigger rate by about a factor 10. An event must pass all trigger levels to be kept for analysis.

A detailed description of the ATLAS muon trigger and the estimated trigger rates are presented in [6]. Here we give a very brief summary of the principles of the level-1 and level-2 muon triggers.

3.1 The level-1 muon trigger

The level-1 muon trigger is based on dedicated fast detectors: the Resistive Plate Chambers (RPC) in the barrel and the Thin Gap Chambers (TGC) in the end-caps [7]. The basic principle of the algorithm is to require a coincidence of hits in the different trigger stations within a predefined angular region, called a "road", from the interaction point through the detector. The width of the road is related to the bending of the muon in the magnetic field and thus to the p_T threshold to be applied.

The trigger in both the barrel and the end-cap regions is based on three trigger stations at different distances from the interaction point [4]. The low-p_T triggers (4 to 10 GeV) are derived from a coincidence in two stations, while the high-p_T triggers (over 10 GeV) require an additional coincidence with the third station. In the end-cap, there is an option to use all three stations also for the low-p_T trigger. This option is the one used in the trigger performance studies in Reference [6].

The level-1 trigger provides for each muon candidate the region where it was found, called the region of interest (RoI). For the muon trigger, the size of the level-1 RoI is $\Delta\eta \times \Delta\phi = 0.1 \times 0.1$ in the barrel and $\Delta\eta \times \Delta\phi = 0.03 \times 0.03$ in the end-cap region, respectively.

3.2 The level-2 single-muon trigger

The level-2 trigger is a software-based trigger and uses the information of the Region of Interest provided by the level-1 trigger. Level-2 algorithms only process data around the RoI, using the full granularity of the detector readout within the RoI.

The HLT trigger selection proceeds in "trigger chains". A chain consists of a series of reconstruction and decision (hypothesis) algorithms that process the data in a RoI identified by level-1. The role of the level-2 muon trigger is to confirm muon candidates flagged by the level-1 and to give more precise track parameters for the muon candidate.

The level-2 muon selection is performed in two stages. The first stage is performed by the muFast algorithm [8], which starts from a level-1 muon RoI and reconstructs the muon in the spectrometer, using the more precise Monitored Drift Tubes (MDT) to perform a new p_T estimate for the muon candidate and creating a new trigger element. The hypothesis algorithm cuts on the estimated p_T and passes the validated trigger elements to the next algorithm.

Track finding in the inner detector is based on the region of the candidate found by muFast. The muFast candidate and ID tracks are passed to the next algorithm, muComb, which matches an ID track with the trigger element from the muon spectrometer and refines the p_T estimate [5].

3.2.1 muFast

For level-1 RoI's flagged by the RPC (barrel region) and the TGC (end-cap region), muFast performs global pattern recognition, a local segment fit in each muon station and a fast p_T estimation. The global pattern recognition is designed to select clusters in MDT tubes belonging to a muon track without using the drift time measurements. It is divided into two steps, firstly the pattern recognition in the trigger chambers seeded by the level-1 RoI, and the subsequent MDT pattern recognition seeded by the result of the previous step. In the MDT pattern recognition muon roads are opened in selected MDT chambers, and the loactions of hit tubes are collected. A contiguity algorithm is applied on the selected hits to remove the background.

The track reconstruction approximates a muon track as a series of segments built separately in each MDT chamber. Segments are reconstructed using the drift time measurements and an approximate calibration to obtain hit radii from them. The fitted segments provide a precision measurement of the point where the fitted line crosses the middle of the MDT chamber, called the super-point.

The track bending is measured in a different way in the barrel and the end-cap. In the barrel, the sagitta is computed from the three super-points found in the three stations. In the end-cap, the track bending is measured by the angle α between the track direction measured by the muon chambers in the middle and outer stations of the muon spectrometer, and the direction obtained by connecting the nominal interaction vertex with the mean hit position in the middle station.

The muon transverse momentum is estimated using an inverse linear relationship between the measured sagitta (in the barrel) or α (in the end-cap) and p_T. The detector region is divided into bins in η and ϕ and the parameters of this inverse linear function are estimated in each bin.

3.2.2 muComb

The muComb algorithm matches the muon track found by muFast to ID tracks reconstructed at level-2 citeID-CSC. In reconstructing the level-2 ID tracks, only hits from the pixel and SCT detectors were used, for speed.

The matching between muFast and ID track segments proceeds as follows. First, a preselection of ID tracks is made based on the difference in η and ϕ between muFast and ID track segments. In the barrel, this preselection also makes use of the difference in the Z of the extrapolated track segments at the radius of the barrel calorimeter. A weighted combined p_T, and a matching χ^2, are calculated for each ID track passing the preselection in combination with the muon track information, and the ID track giving the lowest χ^2 is selected as the best match to the muFast track.

The version of the algorithm used in this study is improved with respect to that used in [6]. The resolution of muFast tracks assumed in combining with the ID tracks have been retuned, using the correct p_T resolutions for the different end-cap regions, and for the misaligned detector geometry. A specific tuning of the matching windows is used to improve the resolution for very low p_T muons. This algorithm will be referred to as "the baseline muComb selection" in Section 5, where a modified algorithm with better rejection for muons from K and π decays is also described, and the performance of the two algorithms is compared.

3.2.3 Level-2 muon hypotheses

The p_T cuts corresponding to each nominal threshold are set so that 90% of the muons at the nominal threshold would pass the selection. The actual cuts used depend on the resolution of the p_T estimation. Therefore the cuts are different for different regions of the detector as well as different between muFast and muComb. Thus for a nominal threshold of 6 GeV the muFast hypothesis cuts at estimated p_T values between 4.5 and 5.4 GeV in the different η regions, while the muComb hypothesis cuts at estimated p_T of 5.8 GeV in the barrel and end-cap and 5.6 GeV in the forward region. Since the p_T resolution of muComb is better than that of muFast, the cuts are closer to the nominal thresholds, and reject more muons with p_T below the threshold. A special case is the 4 GeV nominal threshold which is meant to accept lower p_T muons and the cuts are set at 3 GeV in the barrel and 2.5 GeV in the end-cap for both muFast and muComb.

3.3 The level-2 di-muon triggers

There are two approaches at level-2 for selecting di-muon events from a resonance such as J/ψ and Υ. The first approach is to start from a di-muon trigger at level-1 which produces two muon regions of interest. In this approach, reconstruction of a muon is confirmed separately in each RoI as described above and the two muons are subsequently combined to form a resonance and to apply a mass cut. We will refer to this trigger as the "topological di-muon trigger".

An alternative approach is to start with a level-1 single muon trigger and search for two muons in a wider η and ϕ region. This approach starts from reconstructing tracks in the inner detector and extrapolating the track to the muon spectrometer to tag muon tracks. Since this method does not explicitly require the second muon at level-1, it has an advantage for reconstructing J/ψ at low-p_T. This is implemented in the TrigDiMuon algorithm. The two approaches using either two or one muon RoI are illustrated in Figure 1.

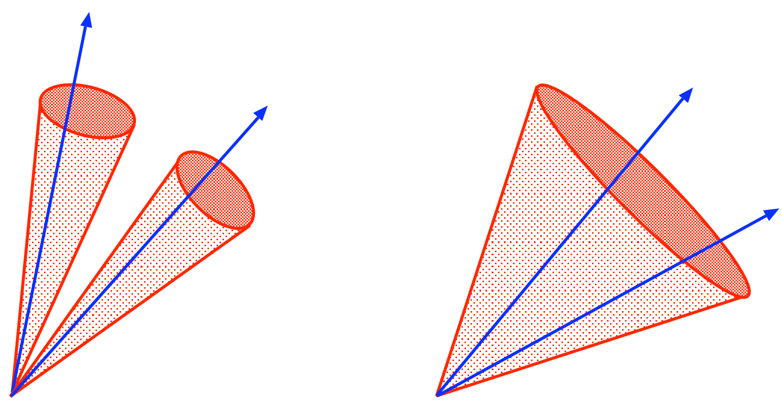

Figure 1: A schematic picture of RoI based di-muon trigger, using two RoI's (left) and seeded by a single muon RoI (right).

3.3.1 The TrigDiMuon algorithm

TrigDiMuon is a level-2 trigger algorithm based on associations established between ID tracks and MS hits. Each time a pair of oppositely charged ID tracks, above a minimal invariant mass, is successfully associated with the MS hits, a muon pair object is created with the parameters of these ID tracks. Later, in the hypothesis step, an additional invariant mass selection can be applied, thus selecting interesting physics objects such as J/ψ or B.

The motivation for developing this algorithm comes from the fact that while di-muon final states exist in many interesting B-physics channels, the cross sections for di-muon final states are orders of magnitude smaller than those for single muons of the same p_T. An additional advantage is that resonant final states can also be used to calibrate trigger efficiencies as will be shown in Section 5.

First, the initial muon RoI is extended in order to search for a second muon, which was not triggered by level-1. The input muon may be from a region of interest identified at level-1, but the input rate to the algorithm can be reduced if, prior to the RoI extension, the level-1 RoI would be confirmed in the level-2 trigger by the muFast and (possibly also) the muComb algorithms. The performance of these options is studied in Section 4. The size of the extended RoI is based on the distribution of angular distance in η and ϕ between two muons from J/ψ decay. Figure 2 shows the probability of including the second muon from J/ψ decays RoI as a function of the extended RoI size for different samples. The current default region size in TrigDiMuon is $\Delta\eta \times \Delta\phi = 0.75 \times 0.75$.

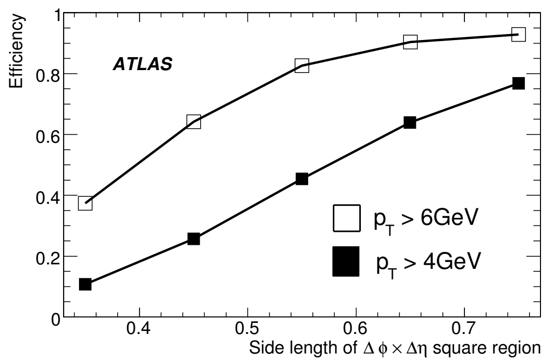

Figure 2: Probability of including the second muon from J/ψ decays RoI as a function of the extended RoI size for different samples. Open squares are from J/ψ decays where one muon has $p_T > 6$ GeV and the other $p_T > 3$ GeV. Full squares are from J/ψ decays where one muon has $p_T > 4$ GeV and the other $p_T > 2.5$ GeV.

The ID tracks in the search region are found using the trigger-tracking program IdScan or SiTrack [9], and are selected if they form a pair of oppositely charged tracks with invariant mass $M > 2.8$ GeV. Each selected track is extrapolated to the different stations of the MS using a formula parameterizing the expected track bending in the magnetic field. The bending parameterization is calculated separately for different regions of the muon spectrometer to account correctly for the inhomogeneous toroidal field in the end-cap region. Figure 3 shows the difference, $\Delta\eta$, between η measured in the inner detector and that measured in the middle station of the muon spectrometer. The lines indicate the choice of η regions for the parameterization. The parameterization was also subdivided in ϕ.

The algorithm then searches for muon hits within a road around the extrapolated track. The road size also differs for different η regions. If a sufficient number of muon hits are found in the MS, the

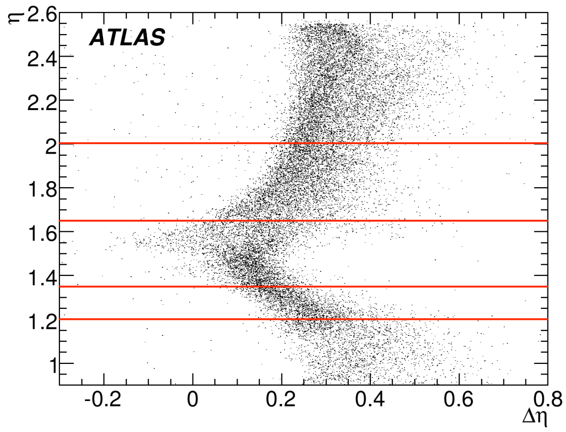

Figure 3: The η direction of muons at the intercation point vs. the difference in η position between the inner detector and the middle station of the muon spectrometer, for muons with $p_T = 6$ GeV. The lines indicate the choice of η regions for the parameterization.

track is identified as a muon. If both tracks from the pair are identified as muons, a muon pair object is created. The two tracks are fit to a common vertex, and the vertex χ^2 is calculated to allow a later selection of only the pairs with a good quality vertex.

4 Performance of the level-2 di-muon triggers for J/ψ

In this Section the efficiency and fake rates resulting from the two approaches to selecting di-muons at level-2 will be presented and compared. For the TrigDiMuon algorithm we calculate the efficiency and fake rates in three different trigger chains.

In the first configuration, TrigDiMuon runs directly after the level-1 trigger based on the RoI produced by level-1. The performance of this trigger is compared to the efficiency and fake rate of the level-1 di-muon trigger.

The other two trigger chains confirm a single level-2 muon before calling TrigDiMuon. The purpose of these chains is not to reduce the fake di-muon trigger rate, but rather to reduce processing time by reducing the input rate to TrigDiMuon. Since TrigDiMuon starts from ID track reconstruction in an extended region around the muon region of interest, the tracking in the inner detector requires three times longer than if only reconstructing ID tracks in the narrow road used by muComb. Thus, this time consuming process can be avoided for candidates for which the level-1 trigger is not confirmed at level-2.

In the second chain TrigDiMuon runs after muFast. The input to TrigDiMuon in this case is a muon confirmed in the MS, with a cut on the p_T estimated at this stage. The efficiency of this trigger is compared with that of a topological di-muon trigger based on a level-1 di-muon with two oppositely charged muons confirmed in the MS at level-2.

In the third chain TrigDiMuon runs after muComb. The input to TrigDiMuon in this case is a muon confirmed in the MS and the ID, with a cut on the p_T estimated at this stage. The efficiency of this trigger is compared with that of the topological di-muon trigger with two oppositely charged level-2 combined muons, within the same invariant mass window. The invariant mass window can be applied in this chain, and not the second chain, because only after muComb the momentum resolution is sufficient for a reasonable selection on invariant mass.

The efficiency and fake rates of these trigger sequences were studied for two different trigger thresholds, a 4 GeV threshold that is envisioned to run at initial luminosity, and a 6 GeV threshold that will be the lowest threshold for running at a luminosity of $10^{33}\text{cm}^{-2}\text{s}^{-1}$.

A selection requiring the two muons to be oppositely charged, and the pair to have invariant mass between 2.8 GeV and 3.4 GeV was applied to both TrigDiMuon and the topological di-muon trigger. For the topological algorithm the invariant mass selection was only applied after muComb. The fake rates were calculated as follows: the probability of each of the level-2 strategies to find a di-muon pair in events which contain only a single muon was estimated separately for the b events and the minimum-bias events. This probability was multiplied by rates which were estimated independently from [6], but are consistent with it. The fake probability in b events was taken to be representative of that in all events with prompt muons. For the topological di-muon trigger, the probability was calculated relative to the number of di-muon level-1 triggers, and multiplied by the level-1 fake di-muon trigger rate from [6].

4.1 Efficiency relative to events accepted at level-1

Table 2 gives the efficiency, relative to level-1, for the two di-muon trigger algorithms for a trigger threshold of 4 GeV. Table 3 gives the efficiencies, relative to level-1, for a trigger threshold of 6 GeV. The efficiencies in these tables are calculated with respect to the J/ψ events accepted by the corresponding level-1 single muon trigger. In parenthesis we give the efficiency relative to J/ψ events at the starting point of the di-muon algorithm.

One can see that the TrigDiMuon efficiency is significantly higher than the topological di-muon trigger in all cases. As a matter of fact, the topological di-muon trigger, which applies p_T cuts on both muons, can have only a limited acceptance for J/ψ events passing a single muon trigger because the second muon is very frequently below the trigger threshold. To pass the topological di-muon trigger the second, lower p_T muon also has to pass the level-2 selections.

Because TrigDiMuon can reconstruct muons below the level-1 thresholds, the TrigDiMuon efficiency, shown in brackets, remains nearly the same with the different chains. However, the total efficiency is reduced when starting from the single muons accepted by muFast or muComb, because of the p_T cut imposed by those algorithms. In particular, in Table 3 muFast and muComb reject successively more of the muons below the nominal threshold and this explains the big drop from row to row for TrigDimuon and even bigger drop for the topological trigger.

The loss of efficiency in the single muon triggers is smaller for the 4 GeV threshold, because the level-2 cuts for the 4 GeV threshold are quite loose, as mentioned above. When calculating the 4 GeV trigger efficiency using only muons from J/ψ with generated p_T above the 4 GeV threshold, TrigDiMuon has an efficiency of 90% and the topological trigger has an efficiency of 64%.

As discussed earlier, in spite of some loss of efficiency, the trigger chains with TrigDiMuon running after a level-2 confirmed muon might be more suitable to an overall planning of the ATLAS trigger menu due to the reduced input rate they have to sustain.

4.2 Fake rates

Table 4 gives the expected fake rates for TrigDiMuon with the different chains described above, for a trigger threshold of 4 GeV at a luminosity of $10^{31}\text{cm}^{-2}\text{s}^{-1}$. Table 5 gives the rates for a trigger threshold of 6 GeV at a luminosity of $10^{33}\text{cm}^{-2}\text{s}^{-1}$.

Chain starting from	TrigDiMuon (%)	Topological trigger (%)
level-1	73 (73)	51
muFast	71 (73)	43
muComb	70 (74)	33

Table 2: Efficiency, relative to level-1, of the two di-muon trigger algorithms for a trigger threshold of 4 GeV. In parenthesis is the efficiency calculated relative to J/ψ events that passed the single muon trigger that selects the input to TrigDiMuon. To estimate the efficiency we used a sample of $\Lambda_b \to J/\psi\Lambda$, where $J/\psi \to \mu(p_T > 2.5 \text{ GeV})\mu(p_T > 4 \text{ GeV})$.

Chain starting from	TrigDiMuon (%)	Topological trigger (%)
level−1	75 (75)	56
muFast	67 (77)	25
muComb	60 (78)	15

Table 3: Efficiency, relative to level-1, of the two di-muon trigger algorithms for a trigger threshold of 6 GeV. In parenthesis is the efficiency calculated relative to J/ψ events that passed the single muon trigger that selects the input to TrigDiMuon. To estimate the efficiency we used a sample of $\Lambda_b \to J/\psi\Lambda$, where $J/\psi \to \mu(p_T > 2.5 \text{ GeV})\mu(p_T > 4 \text{ GeV})$.

Source	Chain starting from	Input rate (Hz)	Fake acceptance (%)	Fake rate (Hz)
	level−1	460	0.42	1.9
$b+c$	muFast	380	0.42	1.6
	muComb	340	0.43	1.5
	level−1	620	0.07	0.43
K/π	muFast	270	0.11	0.29
	muComb	170	0.09	0.15
	level−1	1080	0.22	2.3
Total	muFast	650	0.29	1.9
	muComb	510	0.32	1.6

Table 4: Fake rate of the TrigDiMuon algorithm for muons from different sources and total fake rate using a trigger threshold of 4 GeV, at a luminosity of $10^{31}\text{cm}^{-2}\text{s}^{-1}$. The b and c components were estimated from a sample of $b\bar{b} \to \mu + X$ with $p_T^{\mu} > 4$ GeV and the K/π component from the minimum bias sample with forced decays

Fake rates can be further reduced by reconstructing the J/ψ decay vertex from the two muon tracks. Selecting J/ψ with a good quality vertex fit will reduce fake rates from unrelated track combinations. Figure 4 shows the distribution of the vertex χ^2 for true J/ψ decays and for fake di-muon triggers. A cut of $\chi^2 < 30$ reduces the fake rate by 20-30% and only reduces the trigger

Source	Chain starting from	Input rate (Hz)	Fake acceptance (%)	Fake rate (Hz)
	level-1	21500	0.48	103
$b+c$	muFast	12500	0.60	76
	muComb	10300	0.75	76
	level-1	15800	0.22	34
K/π	muFast	5000	0.30	15
	muComb	3500	0.41	14
	level-1	37400	0.37	137
Total	muFast	17500	0.51	91
	muComb	13700	0.66	90

Table 5: Fake rate of the TrigDiMuon algorithm for muons from different sources and total fake rate using a trigger threshold of 6 GeV, at a luminosity of $10^{33}\mathrm{cm}^{-2}\mathrm{s}^{-1}$. The b and c components were estimated from a sample of $b\bar{b} \rightarrow \mu + X$ with $p_T^{\mu} > 4$ GeV and the K/π component from the minimum bias sample with forced decays

efficiency by 1-2%. The vertex position can also be used to reject J/ψ produced at the primary interaction and accept only J/ψ from b hadron decays, but a study of this is outside the scope of this note.

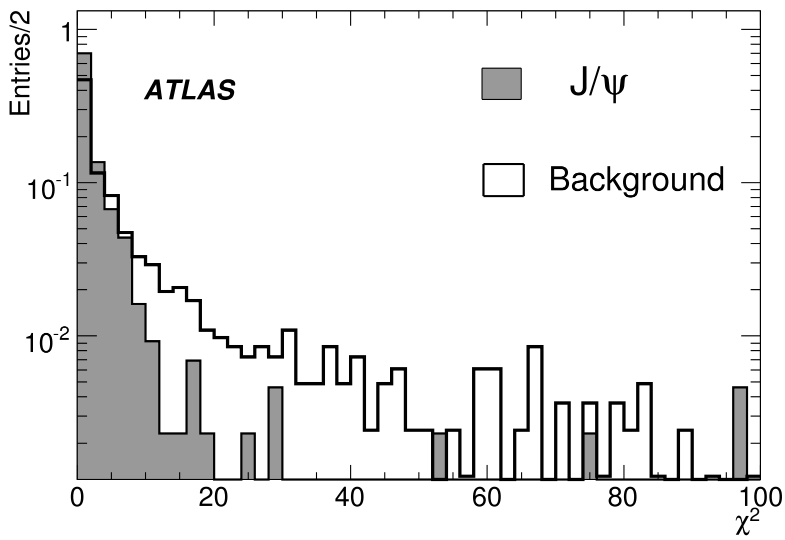

Figure 4: Distribution of the vertex χ^2 for true J/ψ decays (shaded) and for fake di-muon triggers (open histogram).

Finally Table 6 compares the total rates and efficiencies of the two level-2 di-muon algorithms. When TrigDiMuon runs after muComb, the signal to background ratio is worse than when it runs after muFast. Using the input rates from Table 4 and 5, one can calculate that the time needed to reconstruct the ID tracks is also the smallest when TrigDiMuon runs after muFast, reduced by 1/3 for the 4 GeV threshold and by 1/2 for the 6 GeV threshold with respect to running after L1.

It can be seen from this table that the fake rate for the topological di-muon trigger is small. The fake rate from the TrigDiMuon algorithm is much higher but these output rates from level-2 should be acceptable for the gain in efficiency, at the initial low luminosity.

Threshold (Luminosity)	Chain starting from	TrigDiMuon			Topological		
		Efficiency (%)	J/ψ rate (Hz)	Total rate (Hz)	Efficiency (%)	J/ψ rate (Hz)	Total rate (Hz)
4 GeV	level−1	71	1.17	3.1	51	0.8	24
(10^{31}cm^{-2}s^{-1})	muFast	70	1.15	2.7	43	0.7	-
	muComb	69	1.14	2.4	33	0.5	0.6
6 GeV	level−1	74	43	151	56	32.5	357.5
(10^{33}cm^{-2}s^{-1})	muFast	66	38	114	25	14.5	-
	muComb	59	34	109	15	8.7	9.3

Table 6: Total rate and efficiency relative to level-1 of the TrigDiMuon algorithm including the vertex cut $\chi^2 < 30$, and of the topological di-muon trigger. The efficiency is estimated from a sample of $\Lambda_b \to J/\psi\Lambda$, where $J/\psi \to \mu(p_T > 2.5\text{ GeV})\mu(p_T > 4\text{ GeV})$.

The b-physics trigger rate from TrigDiMuon requires further reduction for $L = 10^{33}$. This can be achieved by introducing an additional trigger with a cut on the J/ψ decay length. Then the trigger without decay length cut will be prescaled to an acceptable rate for calibration and alignment purposes, as for example in Section 6. An event filter algorithm will further reduce the rates for a luminosity of 10^{33}cm^{-2}s^{-1}.

4.3 Efficiency relative to reconstructed events

Our goal is to maximize trigger efficiency at the level-2 trigger for the muons that can later be identified offline. The efficiencies for the two algorithms and thresholds were re-estimated with respect to the J/ψ events reconstructed with the muon identification program MuGirl [10], which is efficient for low-p_T muons. The resulting efficiencies are given in Table 7 for a trigger thresholds of 4 GeV and 6 GeV respectively. Figure 5 shows the efficiency of TrigDiMuon relative to muons identified by MuGirl for the higher p_T muon (left) and the second muon (right).

Threshold (Luminosity)	Chain starting from	TrigDiMuon Efficiency (%)	Topological Trigger Efficiency (%)
4 GeV	level−1	84	58
(10^{31}cm^{-2}s^{-1})	muComb	81	42
6 GeV	level−1	81	45
(10^{33}cm^{-2}s^{-1})	muComb	66	17

Table 7: Efficiency of the TrigDiMuon and Topological di-muon algorithms for J/ψ reconstructed by MuGirl. To estimate the efficiency we used a sample of $\Lambda_b \to J/\psi\Lambda$, where $J/\psi \to \mu(p_T > 2.5\text{ GeV})\mu(p_T > 4\text{ GeV})$.

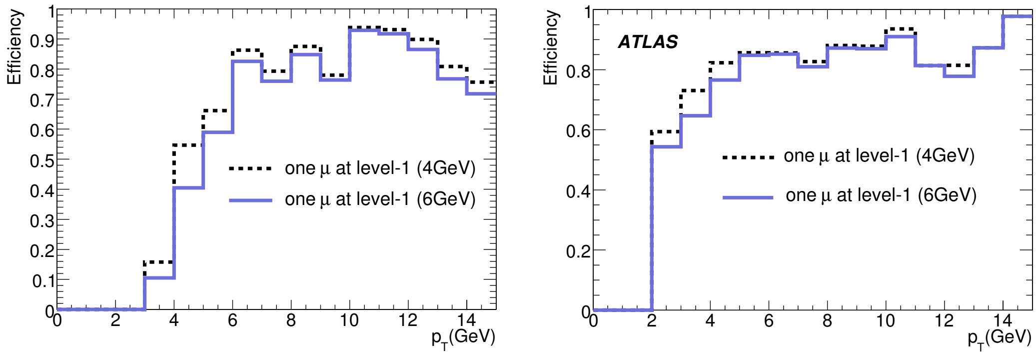

Figure 5: Efficiency of TrigDiMuon relative to muons identified by MuGirl for the higher p_T muon (left) and the second muon (right).

5 Rejection of muons from K and π decays

The lowest single muon p_T threshold in the original ATLAS HLT design [5] was chosen to be 6 GeV. This is because below this p_T value the rate of muons from K and π decays becomes higher than that from b and c decays. Nevertheless, during the low luminosity phase, it is desirable to collect muons with lower p_T, both for detector and trigger calibration and for initial physics studies. If thresholds are lowered, K and π decays become the dominant source of single muon triggers. These decay muons must be rejected as early as possible so as not to dominate the single muon trigger rate, thus ensuring we can achieve the physics and calibration studies with prompt muons.

5.1 Description of the method

The method we describe rejects K and π decays based not on their p_T but on the topology of the decay. The track position of a prompt muon, extrapolated from the MS to the interaction vertex, is a gaussian distributed around the ID track position. The corresponding distribution of a decay muon around the light hadron from which it decayed is broader because of the contribution of the decay kink in addition to the multiple scattering effect. Thus if the track seen in the inner detector is that of the K or π, this discrepancy with prompt muons can be used to reject some of the muons from light hadron decays.

With this method, we can reject the muons from K and π decays by using a matching window tuned for prompt muons, with the window width varying according to the track p_T. Due to time constraints, a precise propagation of tracks in the magnetic field can not be done at level-2, so instead the muon track from the MS is extrapolated back to the interaction vertex using a parameterization that is a function of measured η, ϕ and p_T (exploiting the linear relationship between the bending and $1/p_T$). Multiple scattering effects can be parameterized in the same way to estimate the corresponding errors of the back extrapolation, which determine the window size.

Three main regions are identified for the field parameterization used to propagate the muon tracks, one in the barrel and two in the end-cap. To account for the relative inhomogeneity of the magnetic field inside each region, the parameters of the back extrapolation are computed as a function of η, ϕ, muon charge and spectrometer side (z or $-z$). A different tuning is used for high and low-p_T tracks, to take into account the fluctuations of the energy loss in the calorimeter which are important for the propagation of the latter. In the end-cap, the innermost station of the MS does not provide a complete geometric coverage, thus for the muons with no hits in the innermost station, a seed from the middle station is used to extrapolate the track back. This is the most difficult case since an extrapolation through the toroids must be performed and the resulting precision is spoiled by a factor of two with respect to the other cases. Therefore the back extrapolation in the end-cap is treated separately for regions with inner station coverage and region without inner station coverage.

The strategy for the level-2 combined muon reconstruction described in [5] is to use only the pixel and the SCT data. With this setup, the decays in flight happening near or after the last SCT layer are reconstructed using mainly the hits of the decaying K or π. Some rejection of these events can be achieved by checking the η and ϕ position of the extrapolated MS track relative to the ID track with a matching window whose size is based on the position spread coming out from the muon multiple scattering. Some of the decays between the pixel and the SCT can be rejected by applying a cut on the χ^2 of the Inner Detector fit.

The cuts studied, ordered in terms of increasing rejection are:

- A loose-window cut, using the muon track position from muFast, and the track position from the ID reconsrtruction. The window size was tuned to recover almost 100% of the multiple scattering for a muon p_T equal to the threshold value (4 GeV and 6 GeV);
- A tight-window cut, refining the muon back-extrapolation by exploiting the measurement of the interaction vertex from the ID reconstruction. The window size was tuned to 2.7 σ of the multiple scattering spread for that muon p_T; the combined p_T estimation is used to tune the window width;
- The normalized χ^2 of the ID track fit is required to be less than 3.2.

5.2 Performance of the method

5.2.1 Rejection results for K and π decays

The 6 GeV threshold is used as a benchmark to estimate the K and π rejection achieved by the various cuts. The forced-decay minimum bias sample has been used to study and tune the cuts to reject muons from K and π decays. The results shown in Table 8 are expressed in terms of trigger rate, computed using the cross section of these events.

Cut	π/K rate (Hz)
Baseline muComb	3470 ± 380
Loose window cut	2920 ± 430 (-16%)
Tight window cut	2800 ± 440 (-20%)
Tight window + χ^2 cut	2550 ± 440 (-26%)

Table 8: Expected rate with a 6 GeV single muon threshold from the muComb algorithm for the π and K decays. The rejection with respect to the baseline muComb algorithm is shown in parenthesis. These rates were estimated from the forced-decay minimum bias sample

Figure 6 shows the trigger efficiency for muons from K and π decays as a function of p_T for the baseline muComb selection, compared to the tight window selection described above.

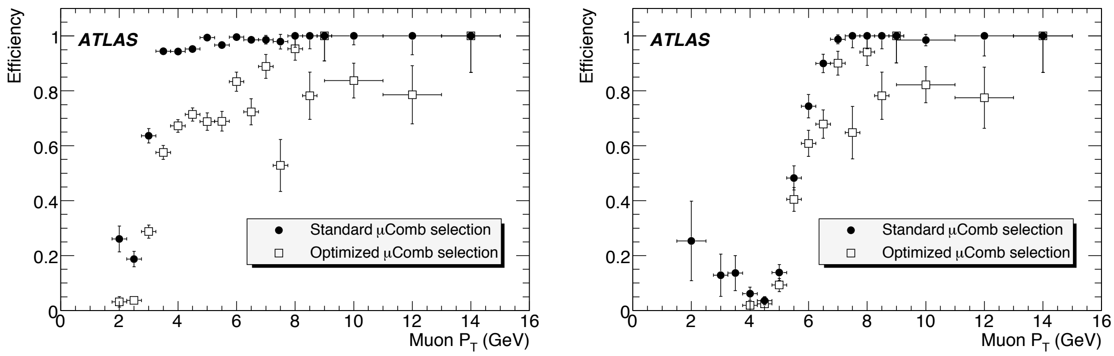

Figure 6: Efficiency for muons from K and π decays as a function of p_T for the baseline muComb selection, compared to the optimized muComb selection described in Section 5.1 for the 4 GeV threshold (left) and the 6 GeV threshold (right).

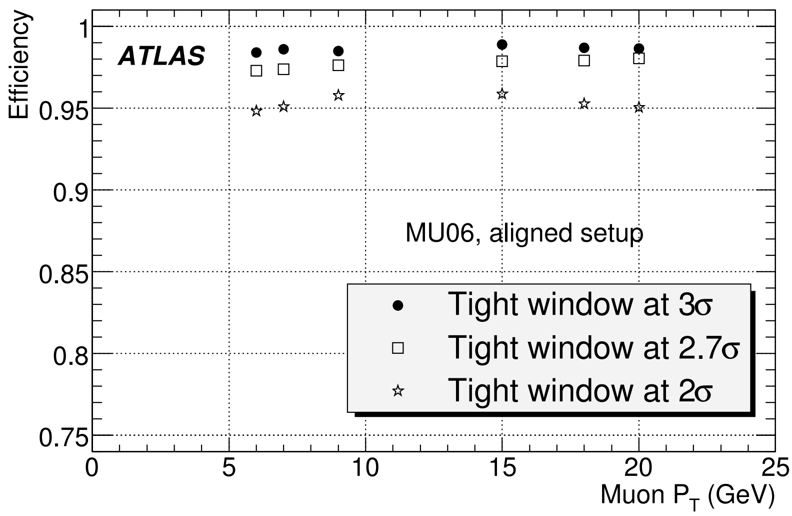

Figure 7: Efficiency of the tight window match on single muons simulated with the aligned detector setup. The efficiency drop for the 6 GeV threshold is shown according to different σ cuts.

5.2.2 Efficiency loss for prompt muons

The efficiency loss for prompt muons due to the matching window cuts has been estimated with a single muon sample. Figure 7 shows the relative efficiency obtained for the aligned detector setup. The relative efficiency is seen to be almost constant in the p_T range of 4-40 GeV and its value for the cut at 2.7 σ is about 98%. The detector misalignment reduces the efficiency plateau to 95% as shown in Figure 8, but the relative efficiency can be recovered by 1% with a specific tuning of the back extrapolator.

The rate reduction for b decays is calculated reliably from the $b \to \mu(4) + X$ sample. The results are shown in Table 9. A good agreement between b events and single muons is found for the efficiency

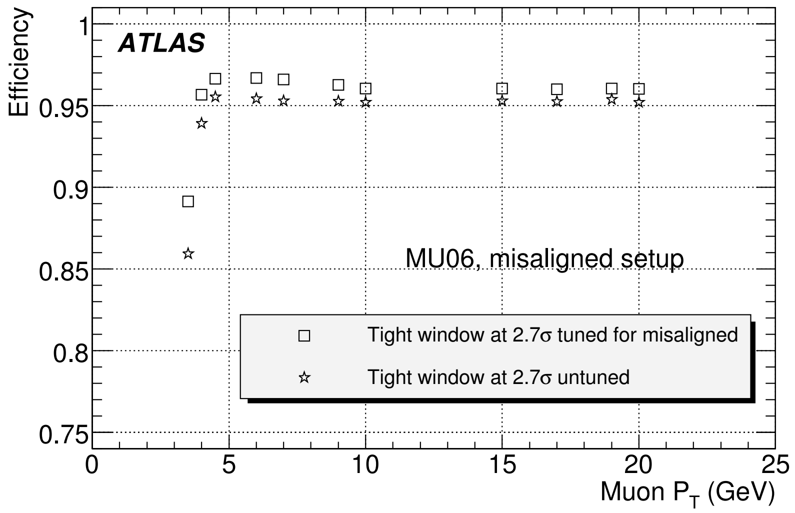

Figure 8: Efficiency of the tight window match at 2.7 σ on single muons simulated with the misaligned detector setup. The relative efficiency is shown for the 6 GeV threshold.

loss due to the tight window match.

Cut	b$\rightarrow \mu(4)+X$ rate (Hz)
Baseline muComb	4850 ± 20
Loose window cut	4780 ± 20 (-1.5%)
Tight window cut	4710 ± 20 (-3%)
Tight window + χ^2 cut	4560 ± 20 (-6%)

Table 9: Expected rate with a 6 GeV single muon threshold from the muComb algorithm for the b component. In parenthesis is the percentage rejection with respect to the baseline muComb.

5.2.3 Resulting muon trigger rates

A coherent description of the full trigger rate after the muComb algorithm is obtained using the standard minimum bias sample and is shown in Table 10 and in Table 11. All the cuts mentioned were applied. A very good agreement is found with both the forced sample for the K /π component, and the $b \rightarrow \mu + X$ sample for the b component.

The optimized version of muComb improves the rejection of muons from decays in flight by about 30% at the 4 GeV threshold and of about 20% at the 6 GeV threshold with respect to the baseline muComb algorithm. The rejection of muons from b events is 20% at the 4 GeV threshold and 7% at the 6 GeV threshold. Thus while the total trigger rate is reduced the purity of the sample increases. Given the uncertainties on the estimation of the production cross section for K and π this optimization is crucial for the low-p_T single muon trigger.

Sample	muFast rate (Hz)	muComb rate (Hz)	muComb + π/K cuts rate (Hz)
π/K	224 ± 15	210 ± 9	145 ± 9
b	145 ± 7	140 ± 6	114 ± 6
c	234 ± 8	200 ± 8	168 ± 8

Table 10: Expected output rate of muFast and muComb for a 4 GeV threshold at the $10^{31}\mathrm{cm}^{-2}\mathrm{s}^{-1}$ Luminosity.

Sample	muFast rate (Hz)	muComb rate (Hz)	muComb + π/K cuts rate (Hz)
π/K	5050 ± 760	3530 ± 380	2860 ± 410
b	5550 ± 600	4900 ± 400	4550 ± 430
c	6900 ± 700	5390 ± 420	5050 ± 450

Table 11: Expected output rate of muFast and muComb for a 6 GeV threshold at the $10^{33}\mathrm{cm}^{-2}\mathrm{s}^{-1}$ Luminosity.

Checking the effect of this method to reject muons from K and π decays on the two level-2 di-muon strategies showed that both efficiency and trigger rates are reduced. There is no significant gain in purity from this method for the di-muon selections, because the rejection is achieved by using the J/ψ reconstruction and mass cuts, and most of the fake rate comes from b and c decays.

6 Measuring trigger efficiency for low-p_T muons from ATLAS data

6.1 Method description

Cross section measurements require a good understanding of the efficiency of the event selections. A precise understanding of the trigger efficiency is crucial and we must have a strategy for measuring it from data with high precision. We study the performance of measuring the trigger efficiency from data with the tag-and-probe method which uses di-muon final states for measuring the single muon trigger efficiency. In this method, a single triggered muon from a reconstructed di-muon decay of a specific particle identified by mass cuts provides the tag that allows us to probe the trigger efficiency of the second muon.

For B physics we are interested in events with rather low-p_T muons, so the tag-and-probe method for measuring the single muon trigger efficiency using J/ψ events is presented. We demonstrate that the obtained trigger efficiency can be applied to calculate the di-muon trigger efficiency. This principle can also be applied to Z decays to calibrate the high-p_T trigger efficiency [11].

6.1.1 Measuring single muon efficiency

We use the tag-and-probe method to measure the muon trigger efficiency, using as the calibration sample events collected by a single muon trigger where the J/ψ is found in the offline reconstruction. In this sample, one of the muons forming the J/ψ is triggered, while the other one may or may not be triggered, thus providing an unbiased sample of muons to study the single muon trigger efficiency.

First, the triggered muon is matched to one of the reconstructed muons from an identified J/ψ. This muon is called the *tagged*-muon. Once the tagged-muon is identified, the other muon, the *probe-*

muon is used to check whether it is also triggered or not. A matching between the reconstructed muon and the one found at the trigger level is needed here too.

At the high level trigger, the position of the muon found at the trigger level is stored, and can be compared precisely to the reconstructed muon. However, at level-1 the position granularity is that of the RoI. Due to the limited precision of the location of the RoI, care must be taken when matching a muon RoI to the reconstructed muon. The bending of the muon tracks in the magnetic field and the fact that high-p_T decay muons have small opening angles between them also introduces an ambiguity in the matching.

The single muon trigger efficiency, $\varepsilon_{1\mu}$, is calculated as the ratio between the number of probe muons which were triggered ($N_{probe\&triggered}$) to the total number of probe muons (N_{probe}),

$$\varepsilon_{1\mu} = \frac{N_{probe\&triggered}}{N_{probe}}. \tag{1}$$

The single muon efficiency can be obtained in detail as a function of kinematic variables (p_T, η, ϕ) of the muons using as fine a binning as the statistics allows. A fine binning is, in fact, necessary since the efficiency depends on these variables, especially at level-1 where there are sharp changes in the efficiency due to structural features such as the experiment's support structures. Because of this the overall efficiency depends on the distribution of the muons produced. We call the detailed *map* of efficiencies in each region of the phase space a trigger efficiency map.

Our primary goal is to demonstrate that it is possible to obtain the trigger efficiency map from data alone. The di-muon trigger efficiency can then be calculated from it, given the distribution of the parent particles and the decay angular distribution.

6.1.2 Calculating di-muon trigger efficiency

The di-muon trigger efficiency can be calculated using the obtained single muon efficiencies, taking into account the dependence on kinematic variables of the muons. For example, the efficiency of J/ψ particles are different depending on the kinematic distribution of the two decay muons. The J/ψ efficiency, $\varepsilon^{J/\psi}$ can be calculated using the single muon trigger efficiency map as

$$\varepsilon_{J/\psi}(p_T^{J/\psi}, \eta^{J/\psi}, \phi^{J/\psi}) = \frac{1}{2\pi} \iint \varepsilon_{1\mu}(p_T^{\mu_1}, \eta^{\mu_1}, \phi^{\mu_1}) \varepsilon_{1\mu}(p_T^{\mu_2}, \eta^{\mu_2}, \phi^{\mu_2}) f(\cos\theta^*) d\cos\theta^* d\phi^*. \tag{2}$$

Here, $f(\cos\theta^*)$ is the angular distribution of the decay muon from the J/ψ where θ^* represents the decay angle of the muon in the J/ψ rest frame with the z-axis taken as the direction of the J/ψ in the laboratory frame. The variable ϕ^* is the azimuthal angle of the decay muon in the J/ψ rest frame, normalized as $\int f(\cos\theta^*) d\cos\theta^* = 1$. Kinematic variables of the decay muons ($p_T^{\mu_1}$, $p_T^{\mu_2}$,η^{μ_1}, η^{μ_2}, ϕ^{μ_1}, ϕ^{μ_2}) are functions of the J/ψ variables, $\cos\theta^*$ and ϕ^*. To get the overall efficiency of J/ψ events, the integration of J/ψ variables must be performed in the kinematic region of the cross-section definition.

Note that this formula is universal and can be applied to other resonances such as $B_{s,d} \to \mu\mu X$ using the same single muon efficiency map. The $\cos\theta^*$ distribution depends on the polarization state of the J/ψ which reflects the J/ψ production mechanism. For the unpolarized case, this distribution is flat. In certain analysis, the production mechanism of the parent particle could be of interest, so we cannot assume the distribution to be flat. In such cases, it is necessary to be able to calculate the efficiency as a function of $\cos\theta^*$ as well. In these cases, Equation 2 would become,

$$\varepsilon_{J/\psi}(p_T^{J/\psi}, \eta^{J/\psi}, \phi^{J/\psi}, \cos\theta^*) = \frac{1}{2\pi} \int \varepsilon_{1\mu}(p_T^{\mu_1}, \eta^{\mu_1}, \phi^{\mu_1}) \varepsilon_{1\mu}(p_T^{\mu_2}, \eta^{\mu_2}, \phi^{\mu_2}) d\phi^* \tag{3}$$

without the $\cos\theta^*$ integration. Equation 3 is simply expressing the efficiency of events where J/ψ is produced with a fixed momentum and the decay angle is also fixed, so the decay muon momenta are also fixed. Some variables could be integrated out, but the important thing is that the efficiency with respect to $\cos\theta^*$ can also be obtained from the single muon efficiency map, $\varepsilon_{1\mu}(p_T^\mu, \eta^\mu, \phi^\mu)$.

6.2 Performance studies

In order to emulate the efficiency measurement from data, we use J/ψ events with two muons in the offline reconstruction passing the single muon threshold of 6 GeV and a di-muon invariant mass between 2.88 GeV and 3.3 GeV.

6.2.1 Matching of muons at trigger and reconstruction

The first step of the tag-and-probe method is to find out which of the two offline muons was triggered. This is done by finding the best match using $\Delta R = \sqrt{\Delta\eta^2 + \Delta\phi^2}$, where $\Delta\eta$ and $\Delta\phi$ are the difference of η and ϕ between the offline muon and the triggered muon. For the matching with level-2 muons, track parameters at the perigee are used. On the other hand, for level-1, the position of the triggered muon is taken as the center of the RoI. In this case, the matching must be done carefully as the opening angle of the two muons from the J/ψ is small and the bending, of the rather low-p_T muons, in the magnetic field is non-negligible. The offline muon tracks are extrapolated to the plane of the RPC or TGC chamber which defines the RoI.

Figure 9 shows the ΔR distrbution between the level-1 RoI and offline track with and without using the extrapolation. The improvement obtained by the extrapolation is significant and as a result a good matching is established by requiring $\Delta R < 0.15$. To further reduce the possibility of having a wrong match, in this study we only use events where the opening angle between the two muons is $\Delta R > 0.4$.

Figure 10 shows the ΔR distribution between the level-2 muon and the offline track. The resolution of ΔR becomes an order of magnitude better than at level-1 since the level-2 muon tracks use the measurements from the ID. The condition $\Delta R < 0.005$ is used for the matching between the offline track and the level-2 track.

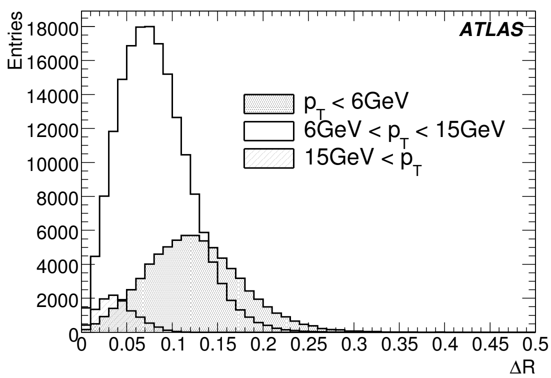

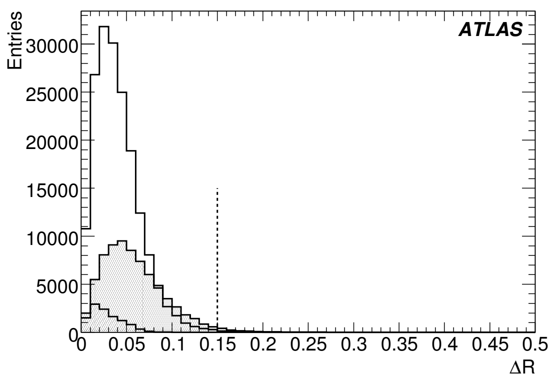

Figure 9: The distribution of ΔR between the level-1 RoI and the offline muon track, (a) using the offline track parameters at the perigee and (b) by extrapolating the offline track to the RoI position. The dashed line shows the value where the cut was applied for the matching.

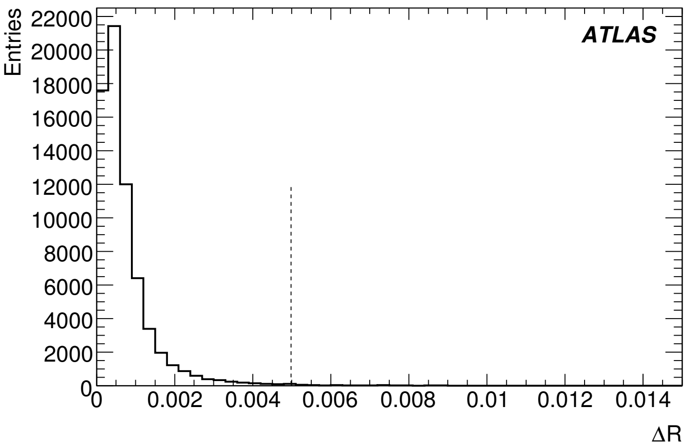

Figure 10: The distribution of ΔR between the level-2 muon and the offline muon track. The dashed line shows the value where the cut was applied for the matching.

6.2.2 Level-1 efficiency

Using the method described in Section 6.1 and the matching criteria, we obtain the single muon efficiency as a function of the p_T of the muon. Figure 11 shows the single muon efficiency as a function of p_T by evaluating how often the probe-muon was triggered. The points are fitted with the function

$$\varepsilon(p_T) = \frac{A}{1+\exp(-a\times(p_T-b)))}. \quad (4)$$

Also shown in Figure 11 is the efficiency measured directly in the single muon Monte Carlo sample which provides an unbiased value of the efficiency. The agreement of the efficiencies obtained by the two methods is around 5% in the turn-on region (4 GeV $< p_T <$ 8 GeV) and becomes smaller as the p_T increases, becoming within a few percent at $p_T >$ 10 GeV.

To calculate the di-muon trigger efficiency using Equation 2, the efficiency curve must be measured in each η and ϕ region. For this, we divided the detector into 10×10 regions for the barrel ($-1.05 < \eta < 1.05$). For the end-cap region ($1.05 < |\eta| < 2.4$), we assumed that there is a complete symmetry between octants and divided one octant into 8×6 regions. Efficiency curves as a function of p_T are obtained in each of the regions. Figure 12 shows the three fit parameters, A, a and b in Equation 4 as a function of η and ϕ. The figure shows that the efficiency curve behaves differently for different regions but in a smooth way, except for a small region around $\eta = 0.725$ and $\phi = -1.6$. In this region the efficiency is very low due to the MS layout and as a result the fit is unreliable. These results are used to calculate the di-muon efficiency.

Distributions of offline J/ψ variables, $p_T^{J/\psi}$, $\eta^{J/\psi}$ and $\cos\theta^*$ are shown in Figure 13 after applying the selection criteria of muons ($p_T^{\mu} >$ 6 GeV and $|\eta^{\mu}| <$ 2.4). The open histograms are for all J/ψ in the MC sample and the filled histograms are for events where the level-1 di-muon trigger, requiring at least two muons with $p_T >$ 6 GeV, has fired. The generator level filter with the p_T cut for the highest (second highest) p_T muon of $p_T >$ 6(4) GeV was applied for the MC sample.

The $\cos\theta^*$ distribution reflects the polarization state of the J/ψ and is flat for the non-polarized case. Since the $\cos\theta^*$ distribution is an interesting quantity to measure in its own right, we do not make any assumptions about this distribution but instead try to measure the efficiency as a function

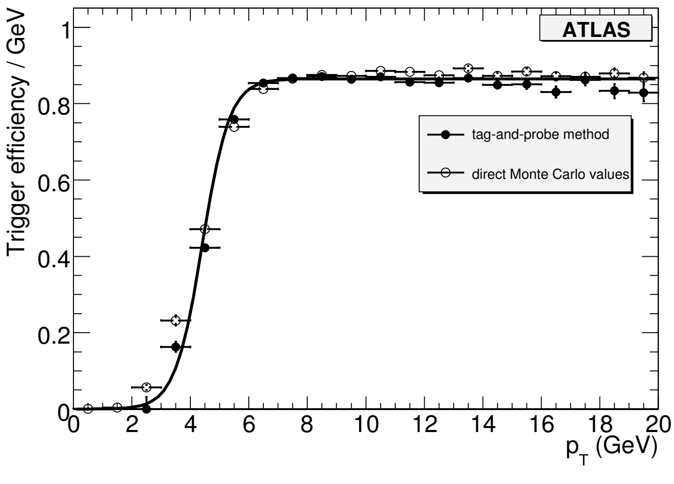

Figure 11: The overall efficiency of the level-1 single muon trigger with respect to the offline selection obtained by the tag-and-probe method (filled circles) and the efficiency estimated from a single muon Monte Carlo sample (open circles). The curve is a fit to the efficiency obtained by the tag-and-probe method from Equation 4.

of $\cos\theta^*$. Although the generated $\cos\theta^*$ distributions were flat, reconstructed distributions will be biased by the p_T^μ cuts applied at the generator level. At $|\cos\theta^*| = 1$, one of the decay muons flies in the opposite direction to the J/ψ and has low transverse momentum, therefore these events are more likely to be rejected by the p_T cut for the highest (second highest) p_T muon of $p_T > 6(4)$ GeV requirement.

Figure 14 shows the di-muon trigger efficiencies calculated in two methods. The open circles are obtained by checking the decision of the level-1 di-muon trigger for each event. The efficiencies calculated using the parameterization in Figure 12 are shown by the filled circles. They are calculated by assigning an efficiency for each event according to the kinematics of the two muons in the final state using Equation 3. The same technique may be used once data are collected by the experiment. The effect of the systematic uncertainty of the method has been estimated by changing the procedure to obtain the trigger efficiency map, namely by using 16×16 bins in η–ϕ in the barrel and 15×10 in the endcap. In addition, the fitting function has been changed by adding a linear function $c(p_T - d)$ to the original function for $p_T > d$. This was done to better describe a drop of efficiency for higher p_T. c and d are additional fit parameters. Both statistical and systematic errors are a few % in most of the region, but the systematic uncertainty increases where the change of efficiency is rapid. In Figure 14, the statistical and systematic errors are added in quadrature.

Results of the two methods agree within a few % in most regions. Efficiency losses at $\eta^{J/\psi}$ around -1, 0 and +1 are due to the layout of the muon trigger chambers. These plots confirm that the requirement of $p_T^\mu > 6$ GeV on two muons introduces an effective cut of $p_T > 12$ GeV for the J/ψ and the efficiency with respect to $\cos\theta^*$ is flat across the region between $-0.8 < \cos\theta^* < 0.8$. The overall efficiencies calculated in the kinematic region of $p_T^{J/\psi} > 12$ GeV and $|\eta^{J/\psi}| < 2$ are 76.1% and 77.0% using the trigger decision and the trigger efficiency map, respectively, which is in agreement within the statistical and systematic errors. The size of the systematic errors may be improved by creating the efficiency map with finer granularity, which requires more statistics.

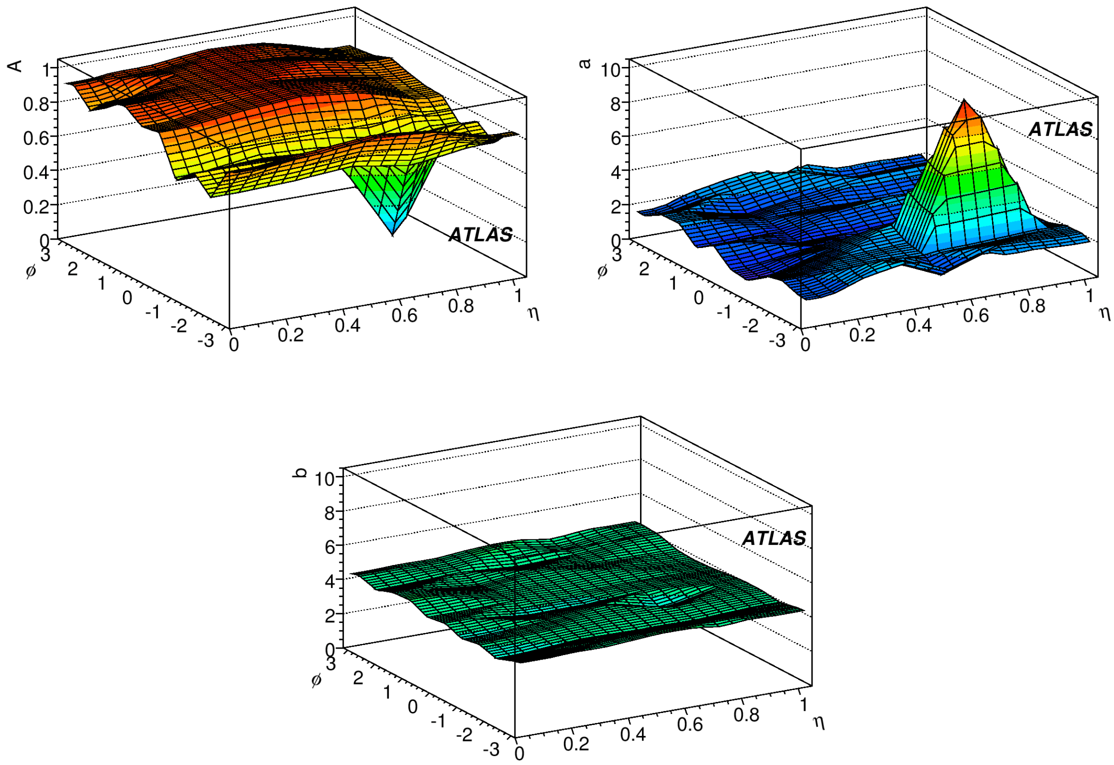

Figure 12: Fit parameters (A, a and b in Equation 4) of the efficiency curve in different η and ϕ regions.

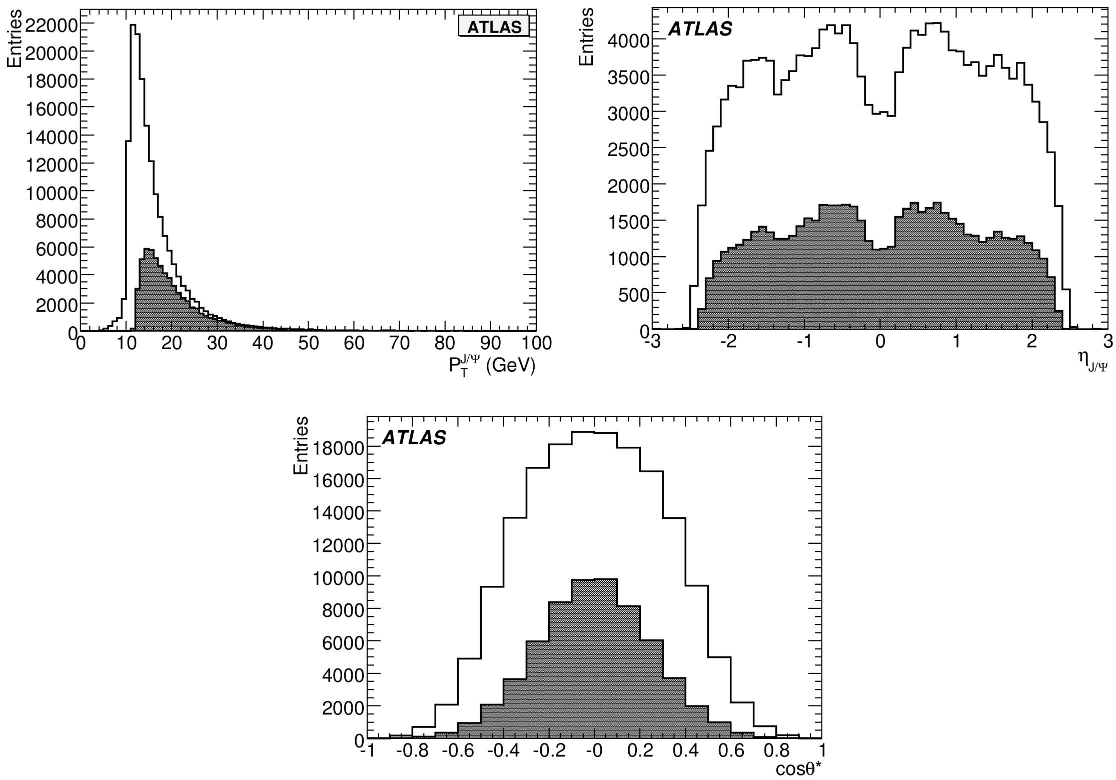

Figure 13: Distributions of J/ψ variables, p_T , η and $\cos\theta^*$. The open histograms are for all reconstructed J/ψ s with the generator level cut of $p_T^{\mu_1} > 6$ GeV and $p_T^{\mu_2} > 4$ GeV. Filled histograms are distributions of events passing the level-1 di-muon trigger.

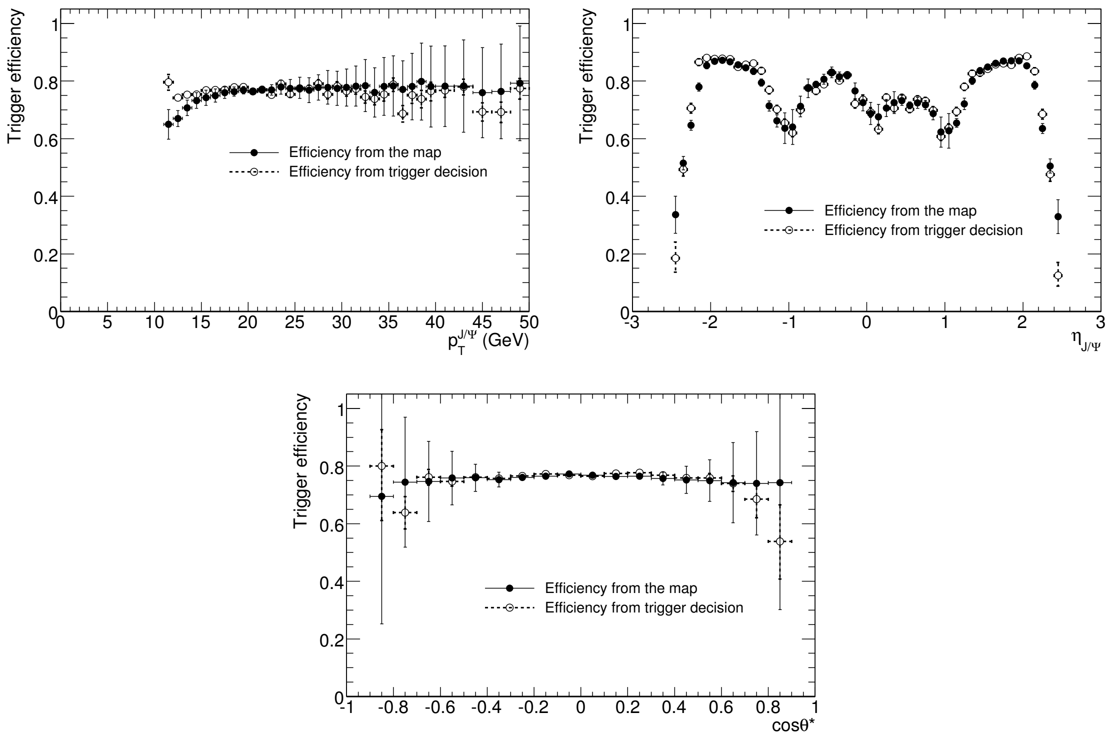

Figure 14: Di-muon trigger efficiency with $p_T^{\mu} > 6$ GeV. Open circles are the result obtained from decision of the level-1 di-muon trigger and filled circles are the efficiency obtained using the parameterization shown in Figure 12.

6.2.3 Level-2 efficiency

The single muon level-2 efficiency can be defined in two ways: level-2 efficiency with respect to offline reconstruction (*L2/rec*) and level-2 efficiency with respect to level-1 (*L2/L1*). The *L2/rec* efficiency is obtained in the same way as the efficiency with respect to level-1. The only difference is that the probe muon must have both level-1 and level-2 trigger objects associated to be considered as triggered.

For the calculation of the *L2/L1* efficiency the set of probe muons is restricted to only those that have an associated level-1 RoI. This way the efficiency with respect to level-1 is obtained. Overall efficiencies as a function of p_T are shown in Figure 15. The points were fitted with the functional form of Equation 4. Efficiency curves calculated using all offline muons matched to generated muons are plotted in the same figure to check that the selection of probe muons is unbiased. It is clear that there is a good agreement between the measured efficiency and the direct Monte Carlo efficiency.

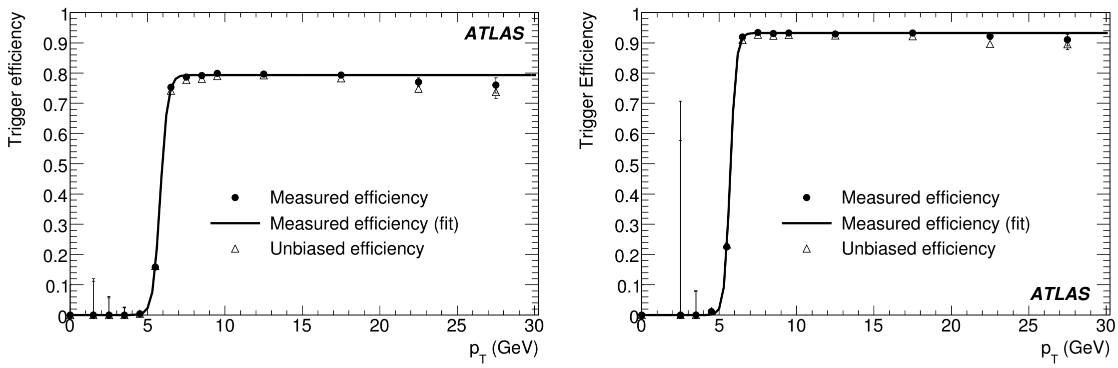

Figure 15: The overall efficiency of the level-2 single muon trigger, (a) with respect to offline reconstruction, (b) with respect to level-1.

To calculate level-2 di-muon efficiency the *trigger efficiency map* was created in the same way as for level-1. The η–ϕ plane was divided into regions as described in Section 6.2.2 and in each region an efficiency curve was constructed and fitted with Equation 4. This was done for *L2/rec* as well as for *L2/L1* efficiencies.

Using the trigger efficiency map for the *L2/rec* efficiency, we can calculate the level-2 trigger efficiency. To check that the map was created correctly, the single-muon efficiency curves were constructed using level-2 muons associated to the offline muons with the ΔR matching criteria explained in Section 6.2.2. To get an agreement between the two methods one must use the same data sample. In Figure 16, open triangles represent a straightforward calculation of the efficiency using matched trigger objects while the solid circles are the efficiencies calculated using the map. To each offline muon from the sample the probability that it would be triggered was assigned using the map. In each p_T bin the efficiency was calculated as an average of these probabilities. Systematic uncertainties were estimated in the same way as the level-1 efficiency by changing the procedure to calculate the trigger efficiency map. The same method was used for other two variables η and ϕ. The two methods give an agreement within 6% in most regions while the difference gets as large as 15% at some regions ($\phi \simeq -1, -2$) where the efficiency is low and therefore the precision of the fit to create the trigger efficiency map was poor. Also, since the average efficiency is calculated in each bin of the map this causes discrepancies in the regions where efficiency changes rapidly.

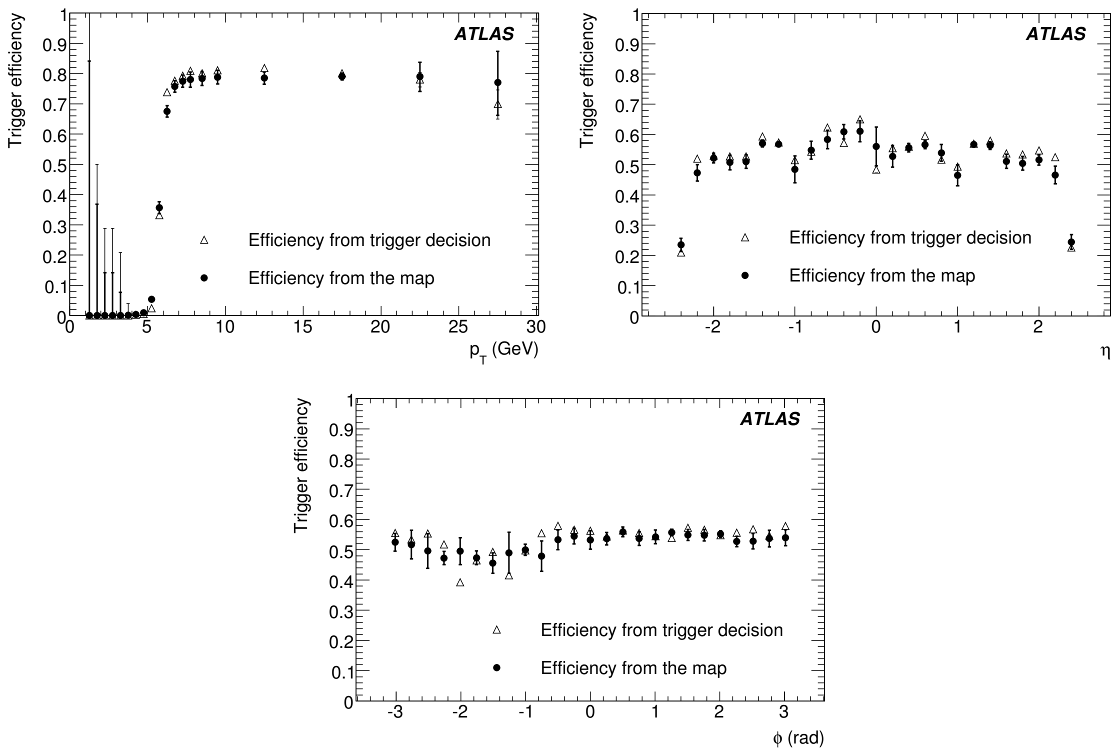

Figure 16: The overall *L2/rec* single-muon trigger efficiency as a function of p_T , η and ϕ. Efficiency is calculated using the *trigger efficiency map* (black circles) and it is compared to the one calculated using matched level-1 and level-2 trigger objects (open triangles).

The efficiency of the level-2 di-muon trigger for J/ψ was calculated in the same way as for level-1. Again two methods were used: firstly direct calculation using the trigger decision for the di-muon trigger and secondly using the efficiency map. Since a simple di-muon trigger without any cut on invariant mass was used, all the muons in the sample must be used in calculation of the efficiency (not just those from J/ψ). To each offline muon in the event the probability ε_i that it would be triggered was assigned. The probability that the whole event will be triggered by the di-muon trigger is then

$$\varepsilon^{2\mu} = 1 - \prod_i (1-\varepsilon_i) - \sum_i \varepsilon_i \prod_{j\neq i} (1-\varepsilon_j) \tag{5}$$

where the products and sums run over all decay muons used in the measurement.

The di-muon efficiency is calculated in the same way as the single-muon efficiency, as an average of probabilities $\varepsilon^{2\mu}$ in each bin of a given variable. In our case it is either the p_T , η, ϕ or the $\cos\theta^*$ of the J/ψ reconstructed in the event. Figure 17 shows a comparison of the J/ψ efficiency curves. Like the single muon efficiency results, the agreement between the two methods is within 6% in most regions except for some regions where the available statistics was low. The overall J/ψ efficiency (*L2/rec*) in the kinematic region, $p_T^{J/\psi} > 15$ GeV, $|\eta^{J/\psi}| < 2$ with the cuts on the muons ($p_T^{\mu} > 6$ GeV, $|\eta^{\mu}| < 2.4$) is 69.2% and 69.4% using the trigger decision and the trigger efficiency map, respectively. We have a good agreement on the overall efficiency integrated in the above phase space.

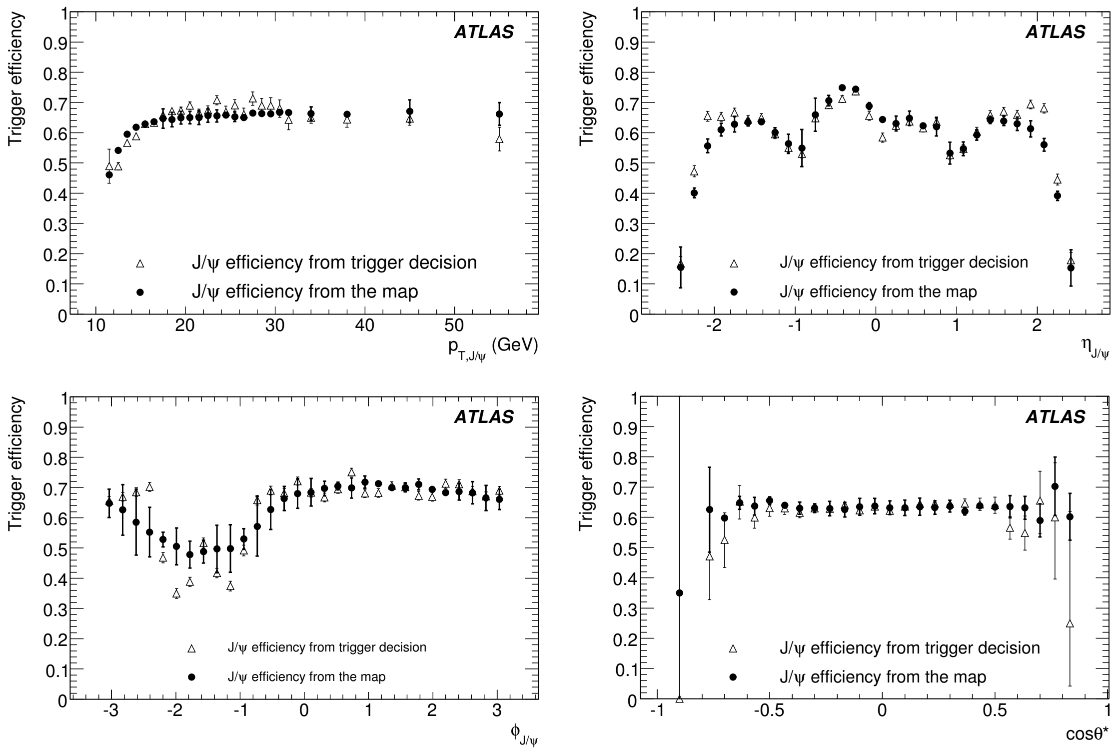

Figure 17: The overall di-muon J/ψ trigger efficiency as a function of p_T , η, ϕ and $\cos\theta^*$. Efficiencies from the trigger decision bit (open triangles) and the ones calculated from the trigger efficiency map (black circles) are shown.

In Figure 18 the efficiency as a function of the distance, ΔR, in the η–ϕ plane between the two

J/ψ muons is shown.

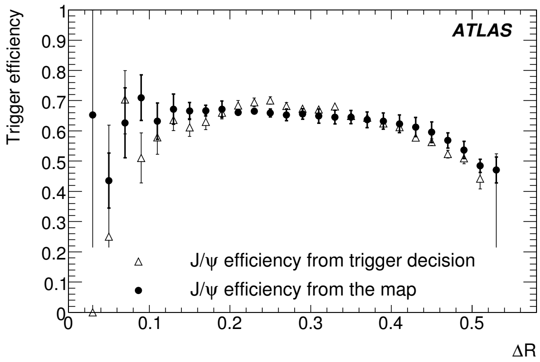

Figure 18: The overall di-muon J/ψ trigger efficiency as a function of ΔR. Efficiencies from the trigger decision bit (open triangles) and the ones calculated from the trigger efficiency map (black circles) are shown.

6.3 Requirements on the trigger menu

In order to use the method developed here for real data, we need a large sample of J/ψ events with at least one muon unbiased by the trigger selection. The following selection criteria at each trigger level will satisfy this requirement:

Level-1 Single muon trigger above a certain threshold;

Level-2 J/ψ reconstruction within one RoI using the TrigDiMuon algorithm to enhance J/ψ events;

Event Filter (EF) No further selection is imposed so as to avoid biasing the sample;

In this Section, we give some estimates of the statistics of the J/ψ sample using this trigger selection and show the precision on the trigger efficiency with a certain luminosity. Taking into account the limit on the EF output rate of 200 Hz it is plausible to use a few Hz of the bandwidth for this calibration trigger. The parameters to optimize are the prescale factor, to reduce the rate when it is too high, and the threshold value.

The level-1 single muon trigger rate has been studied in detail taking into account contributions from different sources. At low-p_T , the main contribution is from K /π in-flight decay and muons from b and c quarks. The rejection of these non-J/ψ events by the topological di-muon trigger at level-2 has been studied using a genererated sample of $b\bar{b} \to \mu + X$, where the efficiency of non-J/ψ events to be selected was found to be 0.8%. This factor is used to estimate the rate reduction by the level-2 selection.

Table 12 shows the expected rate of the level-1 single muon trigger and the contribution of the $J/\psi \to \mu^+\mu^-$ to the rate assuming a luminosity of 10^{31} cm^{-2}s^{-1}. The rate of J/ψ events is the sum of J/ψ direct production and from $b\bar{b}$ production. If we could allocate a bandwidth of 1 Hz to this trigger chain with 6 GeV level-1 threshold, we must apply a prescale factor of 3 to reduce the rate down to around 1 Hz. Given the fraction of $J/\psi \to \mu^+\mu^-$ events among this rate is 6%, we get a rate of 0.06 Hz for collecting the calibration sample.

	rate (Hz)	J/ψ fraction
level-1	380 (0.21)	0.05%
level-2	3 (0.19)	6%

Table 12: The rates after level-1 and level-2 using the proposed calibration trigger for a luminosity of 10^{31} cm^{-2}s^{-1} with the threshold of $p_T > 6$ GeV. The contribution of $J/\psi \to \mu^+\mu^-$ process to the rate is also shown in parentheses.

With one year of data, we expect to collect about 300 k J/ψ events according to this triggering strategy, which is comparable to the statistics used in this study (150 k direct J/ψ and 150 k $b\bar{b} \to J/\psi$). Therefore, we expect a similar performance (for $\simeq 1$ Hz calibration trigger rate) to that shown in Section 6.2 after the first year of data-taking. The number of events may increase if we allocate more than 1 Hz for the calibration trigger.

7 Conclusions

In this note we presented methods to efficiently select J/ψ events at the second level trigger, reject muons from K and π decays and measure the trigger efficiencies from the ATLAS data.

TrigDiMuon is a second-level trigger algorithm that selects efficiently at level-2 events which include J/ψ or other di-muon states, starting from a single level-1 muon trigger. The efficiency of TrigDiMuon for events accepted by level-1 and the level-2 single muon trigger is between 73% for the 4 GeV trigger threshold and 60% for the 6 GeV threshold. This may be compared with the topological di-muon trigger efficiencies of 33% for the 4 GeV threshold and 15% for the 6 GeV threshold. The fake trigger rates of TrigDiMuon are estimated to be 2 Hz for a trigger threshold of 4 GeV at a luminosity of 10^{31}cm^{-2}s^{-1}, and 90 Hz for a trigger threshold of 6 GeV at a luminosity of 10^{33}cm^{-2}s^{-1}. For the B-physics trigger at $L = 10^{33}$cm^{-2}s^{-1} the rate will have to be further reduced by means of a decay length cut on the J/ψ decay vertex.

Extrapolating the muon track from MS back to the interaction vertex improves the single muon trigger selection at the level-2 stage and allows increased rejection of muons from K and π decays without a significant loss of efficiency for b events. The back extrapolator provides a further reduction factor of about 20% at the trigger threshold of 4 GeV and of about 10% at the trigger threshold of 6 GeV with respect to the output trigger rate of the baseline muComb selection. Despite this good performance, its use for triggering on low p_T di-muon objects is not recommended, since the background to TrigDiMuon is dominated by muons from b and c rather than by muon from K and π decays. However, because the rate of muons from K and π decays may be even higher than in our simulation, it is important to have it available for the single muon triggers.

The J/ψ trigger efficiency can be measured from ATLAS data using the tag-and-probe method. As the efficiency of the single muon trigger depends on the η and ϕ regions, it is necessary to measure the efficiency as a function of these variables. With 300k J/ψ events, it is possible to measure the efficiency at level-1 and level-2 with better than 5 % precision for each region. The uncertainty comes mainly from the lack of statistics to measure the efficiencies for each region of η and ϕ and will improve as more J/ψ events become available. To collect an unbiased J/ψ sample which can be used for the trigger efficiency measurement, we plan to use a level-1 single muon trigger with a J/ψ reconstruction using the inner detector at level-2. With this trigger we can collect around 300k events for an integrated luminosity of 100 pb^{-1} while keeping the rate of this calibration trigger around 1 Hz.

With the methods provided it is possible to collect a large number of J/ψ events at luminosities of around $10^{31}\text{cm}^{-2}\text{s}^{-1}$, without an overly high rate from K and π decays. Furthermore, these low-p_T J/ψ events can also be used to calibrate trigger efficiencies from the actual ATLAS data, and provide the trigger efficiencies for analyses that use low-p_T muons.

References

[1] T. Sjostrand, S. Mrenna and P. Skands, *PYTHIA 6.4: Physics and manual*, JHEP, **05**, 026 (2006).

[2] S. Agostinelli et al., Nucl. Inst. and Meth. **506** 250 (2003).

[3] ATLAS Collaboration, *ATLAS Technical Proposal*, CERN/LHCC 94-43, LHCC/P2, (1994)

[4] ATLAS Level-1 Trigger Group, *Level-1 Technical Design Report*, ATLAS TDR 12, (1998).

[5] ATLAS HLT/DAQ/DCS Group, *High-Level Trigger, Data Acquisition, and Control Technical Design Report*, ATLAS TDR 16, (2002).

[6] ATLAS Collaboration, *Performance of the Muon Trigger Slice with Simulated Data*, this volume.

[7] ATLAS Muon Collaboration, *ATLAS Muon Spectrometer Technical Design Report*, CERN/LHCC 97-22, (1997)

[8] A. Di Mattia et al., *A Level-2 trigger algorithm for the identification of muons in the ATLAS Muon Spectrometer*, ATL-DAQ-CONF-2005-005, (2005)

[9] ATLAS Collaboration, *The Expected Performance of the Inner Detector*, this volume.

[10] S. Tarem et al, *MuGirl - Muon identification in ATLAS from the inside out*, Nuclear Science Symposium Conference Record, IEEE **Volume 1**, 617 (2007).

[11] ATLAS Collaboration, *In-Situ Determination of the Performance of the Muon Spectrometer*, this volume.

Heavy Quarkonium Physics with Early Data

Abstract
Results are reported on an analysis on simulated data samples for production of heavy quarkonium states $J/\psi \to \mu\mu$ and $\Upsilon \to \mu\mu$, corresponding to an integrated luminosity of 10 pb^{-1}. It is shown that the p_T dependence of the cross-section for both J/ψ and Υ should be measured reasonably well in a wide range of transverse momenta, $p_T \simeq 10-50$ GeV. The precision of J/ψ polarisation measurement is expected to reach $0.02-0.06$, while the projected error on Υ polarisation is around 0.2. Observation of radiative decays of χ_c states, and the feasibility of observing $\chi_b \to J/\psi J/\psi$ decays are also discussed.

1 Introduction and theoretical motivation

The number of $J/\psi \to \mu^+\mu^-$ and $\Upsilon \to \mu^+\mu^-$ decays produced at the LHC is expected to be quite large. Their importance for ATLAS is threefold: first, being narrow resonances, they can be used as tools for alignment and calibration of the trigger, tracking and muon systems. Secondly, understanding the details of the prompt onia production is a challenging task and a good testbed for various QCD calculations, spanning both perturbative and non-perturbative regimes. Last, but not the least, heavy quarkonium states are among the decay products of heavier states, serving as good signatures for many processes of interest, some of which are quite rare. These processes have prompt quarkonia as a background and, as such, a good description of the underlying quarkonium production process is crucial to the success of these studies.

This note mainly concentrates on the capabilities of the ATLAS detector to study various aspects of prompt quarkonium production at the LHC. The methods of separating promptly produced J/ψ and Υ mesons from various backgrounds are discussed, and strategies for various measurements are outlined.

1.1 Theory overview

Quarkonium production was originally described in a model where the quark pair was assumed to be produced endowed with the quantum numbers of the quarkonium state that it eventually evolved into [1]. This approach, subsequently labelled as the Colour Singlet Model (CSM), enjoyed some success before CDF measured an excess of direct J/ψ production [2], more than an order of magnitude greater than predicted (see Figure 1(a)).

The Colour Octet Model (COM) [5] was proposed as a solution to this quarkonium deficit. COM suggests that the heavy quark pairs produced in the hard process do not necessarily need to be produced with the quantum numbers of physical quarkonium, but could evolve into a particular quarkonium state through radiation of soft gluons later on, during hadronisation. This approach isolates the perturbative hard process from the non-perturbative long-distance matrix elements, which are considered as free parameters of the theory. However, their universality means that their values can be extracted independently from a number of different processes, such as deep inelastic scattering, hadro- and photoproduction.

Hence the good description of the Tevatron data by the Colour Octet Model shown in Figure 1(a) is, at least in part, due to the fact that the values of some parameters were determined from the same data. Tests of other COM predictions have not been so successful: Figure 1(b) shows the polarisation coefficient in $\Upsilon \to \mu\mu$ decay as a function of its transverse momentum, where the COM prediction disagrees with the data.

A model based on k_T factorisation in QCD showers [6] claims to be able to describe both the lack of transverse polarisation in J/ψ decays [4, 7] and the high cross-section of J/ψ production. Another

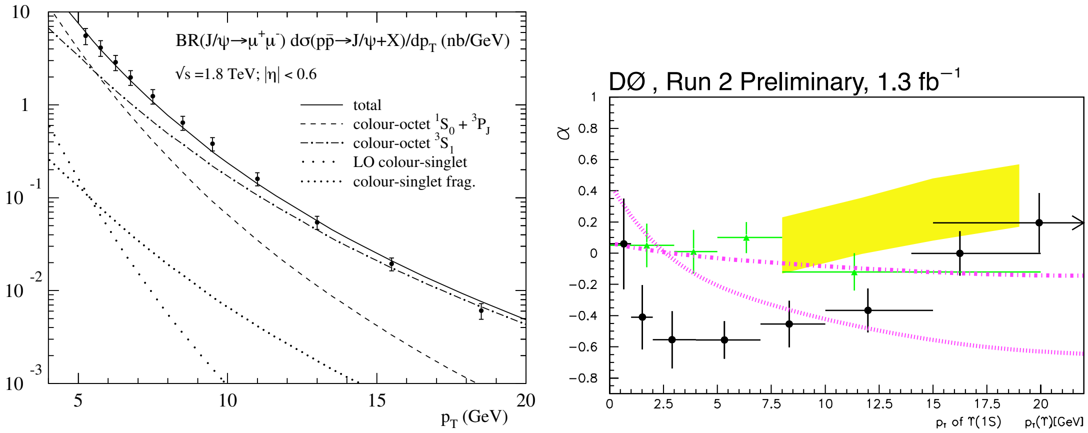

(a) (b)

Figure 1: (a) Differential cross-section of J/ψ production at CDF, with predictions from CSM and COM mechanisms (from [3]). (b) Υ polarisation measured as a function of p_T at DØ (black dots) and CDF (green triangles), compared to the limits of the k_T factorisation model (dashed and dotted curves [6]) and COM predictions [5], depicted by a shadowed band (from [4]).

model [8] argues that the deficit in the cross-section as predicted by CSM can be largely explained by the production of a quarkonium state in association with an additional heavy quark, and also predicts lower levels of polarisation.

In the following, we show that ATLAS is capable of detailed checks of the predictions of various models by measuring not only p_T and η distributions of onium states in a wide range of these variables, but also the degree of polarisation and the production of C-even states. In the absence of a comprehensive Monte Carlo generator capable of simulating all aspects of all theoretical models, we used the PYTHIA 6.403 generator [9] incorporating the Colour Octet Mechanism, with model parameters fixed through a combination of theoretical and experimental constraints [10]. Inevitably, this simulation is unable to reproduce adequately some features of the data, notably the polarisation angle distributions and hadronic accompaniment of the quarkonium states. However, the simulated samples allowed us to study the acceptance and efficiency of ATLAS to detect all required particles and measure their parameters, across the whole range of the accessible phase space.

1.2 Classification of production mechanisms in the simulation

In the following, we will use a simple classification of the quarkonium production mechanisms based on the model implemented in the PYTHIA generator.

A sample diagram describing the leading colour-singlet subprocess $g+g \rightarrow J/\psi+g$ is shown in Figure 2(a). In the accessible range of transverse momenta of J/ψ its contribution is expected to be small. The dominant contribution at the lower p_T comes from the subprocess shown in Figure 2(b), where both singlet and octet $c\bar{c}$ states with various quantum numbers contribute to J/ψ production, through $\chi_{cJ} \rightarrow J/\psi+\gamma$ decays and/or soft gluon emission.

At high p_T, the gluon fragmentation subprocess shown in Figure 2(c) becomes increasingly dominant. According to COM, this is unlikely to produce anything other than $^3S_1$ quarkonium states. Hence, the fraction of J/ψ mesons produced from χ_{cJ} decays should decrease with increasing p_T. The production mechanisms for the radially excited $\psi'(3686)$ meson follows the same pattern, except for the absence of respective χ'_{cJ} contributions, thus one should expect different p_T distributions for J/ψ and

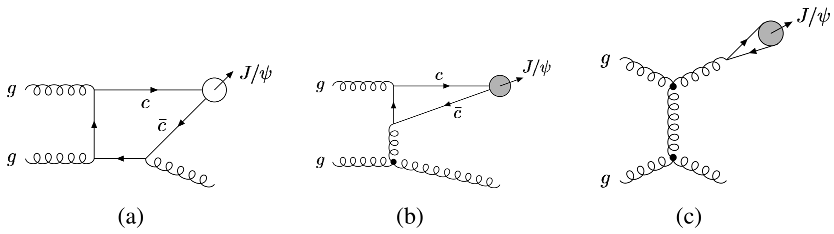

Figure 2: Some example diagrams for the singlet and octet J/ψ production mechanisms implemented in PYTHIA.

ψ'.

The overall picture is expected to be similar for bottomonium production, except the number of radial excitations below the open beauty threshold is now three, and many more radiative transitions are possible between the various n^3P_J and n^3S_1 state. However, compared to J/ψ, the accessible range of p_T for Υ is significantly extended towards smaller transverse momenta. This opens up the range of p_T dominated by the colour singlet contribution, which may make it directly observable for Υ.

1.3 $\chi_b \to J/\psi J/\psi$ decay

Despite much higher production cross-sections, C-even states of quarkonia are far more difficult to observe than their vector counterparts. The usual way of studying $\chi_{c,b}$ (and $\eta_{c,b}$) states has been so far through radiative decays of or into respective vector states. However, in the high energy hadronic collision environment, observation of the photon in $\chi_b \to \Upsilon + \gamma$ may be problematic (see Section 5.1).

We have performed a feasibility study to assess the capability of ATLAS to observe $\chi_b \to J/\psi J/\psi \to \mu^+\mu^-\mu^+\mu^-$ decay with the standard di-muon trigger. The results are presented in Section 5.2. The observation and measurement of these final states will give a valuable insight into the heavy quark bound state dynamics from several separate viewpoints.

2 Trigger considerations

Details of the triggers to be used in ATLAS B physics programme can be found in [11]. This section discusses the trigger signatures relevant for quarkonium production at ATLAS, the implications they have on the measured cross-section, and the expected effects they have on our ability to make various physics measurements.

Two specific types of di-muon triggers dedicated to quarkonium are: the topological di-muon triggers, which require two level-1 regions of interest (RoIs) corresponding to two muon candidates with p_T thresholds of 6 and 4 GeV, and di-muon triggers that only require a single level-1 RoI above a threshold of 4 GeV and searches for the second muon of opposite charge in a wide RoI at level-2. They are discussed in Section 2.1. An additional trigger scenario is based on a single muon trigger with a higher p_T threshold of 10 GeV, discussed in Section 2.2.

2.1 Di-muon triggers

Being able to determine the trigger efficiency of measured J/ψ and Υ is crucial to correctly infer the production cross-section of quarkonium at the LHC. Indeed, using J/ψ and Υ (as well as the Z boson) to construct a trigger efficiency map is a necessary step in order to perform cross-section measurements in ATLAS.

Studies are being conducted in ATLAS into developing a calibration method to obtain the low-p_T single muon trigger efficiency, and henceforth the di-muon trigger efficiency of events using real data by virtue of the so-called tag-and-probe method (see Ref. [11] for details). In the absence of data, we have performed our own studies of trigger efficiencies, based on Monte Carlo simulation.

If not stated otherwise, the quoted trigger efficiencies have been calculated with respect to the Monte Carlo samples, generated with the cuts $p_T(\mu_1) > 6$ GeV, $p_T(\mu_2) > 4$ GeV, where μ_1 (μ_2) is the muon with the largest (second largest) transverse momentum in the event.

The level-1 trigger is a hardware trigger that uses coarse calorimeter and muon spectrometer information to identify interesting signatures to pass to the level-2 and Event Filter stage. Figure 3 shows the various individual level-1 trigger efficiencies as a function of the p_T of the di-muon system. The total trigger efficiency at level-1, running over direct J/ψ events, is 87%.

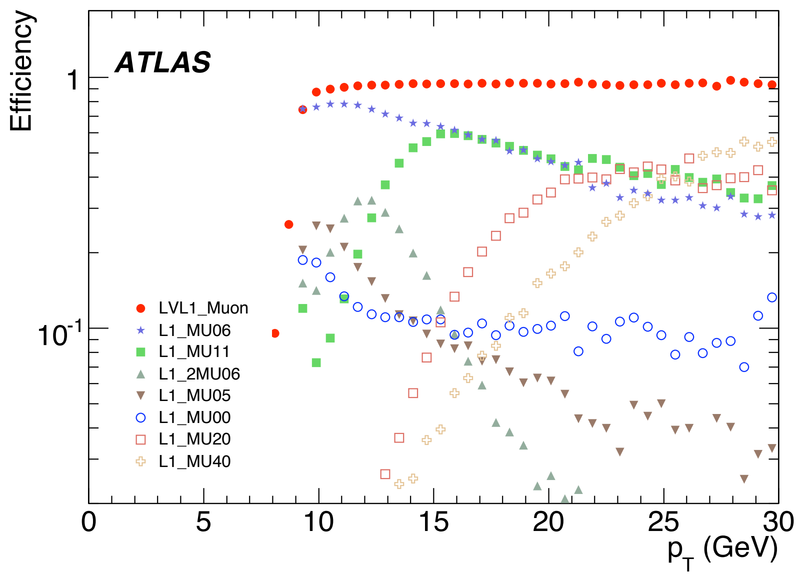

Figure 3: Efficiency of various level-1 triggers for prompt J/ψ events versus p_T of the di-muon system. Only the triggers with efficiencies greater than 2% in some region of p_T are displayed. The relevant triggers are the single muon p_T threshold triggers labelled `L1_MUXX` (where `XX` indicates the p_T threshold in GeV) and the di-muon trigger `L1_2MU06`. Each p_T range of these triggers is exclusive. The efficiency curve labelled `LVL1_Muon` is the sum of all level-1 single muon efficiencies (excluding the di-muon trigger `L1_2MU06`).

The level-2 trigger is software-based and is designed to reduce the output rate of the data, passed to it from level-1, by two orders of magnitude. Within regions of interest defined by the level-1 trigger, full granularity of the detector is accessible. The efficiency of the level-2 triggers for prompt J/ψ events is plotted in Figure 4 as a function of di-muon p_T. The total level-2 trigger efficiency in the reconstructed prompt J/ψ events (relative to level-1) is 97%. The di-muon trigger scenario $\mu6\mu4$, considered in the majority of this note, uses all the above trigger signatures.

2.1.1 Effect of di-muon trigger cuts on quarkonium rates

Figures 5(a) and 5(b) illustrate the distribution of cross-sections across the values of the p_T of the harder and softer muon from the quarkonium decay without any muon cuts applied at generator level. The lines

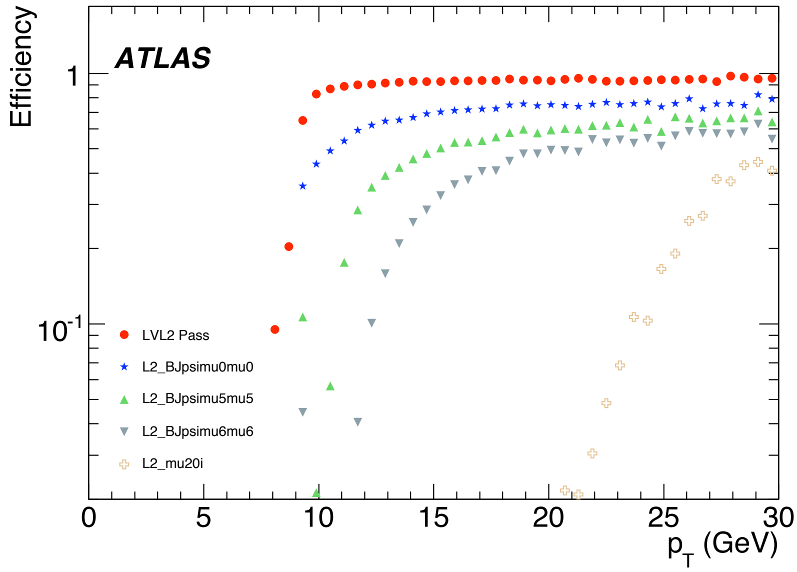

Figure 4: Efficiency of various level-2 triggers for prompt J/ψ events versus p_T of the di-muon system. Only the triggers with efficiencies greater than 2% in some region of p_T are displayed. The level-2 trigger signatures of interest include single muon p_T threshold triggers `L2_MUXX` and 'TrigDiMuon' triggers `L2_BJpsimuXmuY` which are specialised for searching for J/ψ [11]. The efficiency curve labelled `LVL2_Pass` in (b) is the sum of all level-2 efficiencies.

overlaid on the plots represent various nominal muon p_T thresholds: (6 GeV, 4 GeV) and (4 GeV, 4 GeV), as well as the nominal thresholds (10 GeV, 0.5 GeV) corresponding to the single muon trigger $\mu 10$ (see below).

For J/ψ the bulk of the cross-section lies near the (4 GeV, 1 GeV) region, far from the low-p_T muon trigger thresholds proposed for ATLAS, and we see only a small increase in accessible cross-section by lowering the cut on the harder muon from 6 GeV to 4 GeV (although this reduction in the effective J/ψ p_T threshold is useful from a physics standpoint). The situation for Υ is significantly different however, as the relatively large mass of the Υ shifts the bulk of the production to the region near muon p_T thresholds of (5 GeV, 4 GeV). This means that by lowering the di-muon trigger cuts from (6 GeV, 4 GeV), which sits just above the highest density area of Υ production, to (4 GeV, 4 GeV), a much higher fraction of the produced Υ can be recorded, leading to a predicted order-of-magnitude increase in the accessible cross-section. The predicted cross-sections for the processes $pp \to J/\psi(\mu^+\mu^-)X$ and $pp \to \Upsilon(\mu^+\mu^-)X$ (before incorporating trigger and reconstruction efficiencies) for a number of trigger scenarios are presented in Table 1. Although no higher ψ and Υ states have been simulated for this analysis, their expected cross-sections are also shown in Table 1, as estimated using Tevatron results on their relative yields [12]. Numbers include feed-down from χ states and higher radial excitations to lower ones. Due to the expected ATLAS mass resolution for the Υ states, however, it is unlikely that the higher state resonances will be separable. These predictions have been obtained by extrapolating the Colour Octet Model, tuned to describe the Tevatron results, to the LHC energy. Although every care have been taken to ensure stability of this extrapolation, inevitably there is an uncertainty in the overall scale of the predicted cross-sections (linked to the uncertainties in the parton distribution functions at small x), which we estimate at the level of $\pm 50\%$.

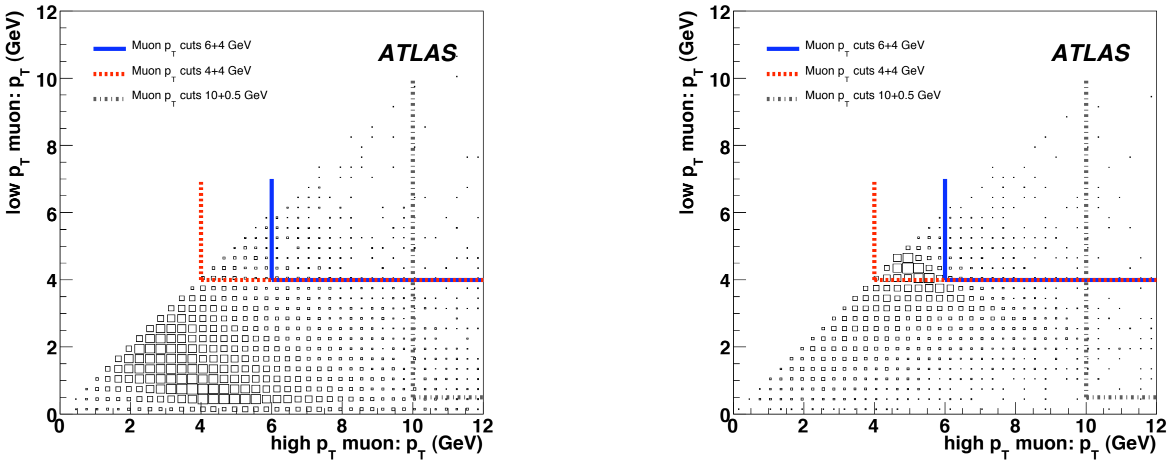

(a) J/ψ

(b) Υ

Figure 5: Densities of $J/\psi \to \mu\mu$ (a) and $\Upsilon \to \mu\mu$ (b) production cross-section as a function of the two muon transverse momenta. No cut was placed on the generated sample. The overlaid lines represent the nominal thresholds of observed events with various trigger cuts applied: $\mu6\mu4$ (solid line), $\mu4\mu4$ (dashed line) and $\mu10$+track (dash-dotted line).

It is likely that the cross-section accessible by ATLAS will be higher than the values quoted in Table 1, as during early running the low p_T muon trigger will run with an open coincidence window in η at level-1 and no requirement of an additional level-2 di-muon trigger. This trigger item has a turn-on threshold at around 4 GeV, giving the (4 GeV, 4 GeV) trigger scenario described above, but in practice there is a non-zero trigger efficiency below 4 GeV, which, combined with the large rate of low p_T onia, may add a significant extra contribution to the overall observed cross-section. Even including this contribution, the overall rate of signal events from all quarkonium states is likely to remain below the rate of 1 Hz at a luminosity of 10^{31} cm^{-2}s^{-1}, which is a small fraction of the available trigger bandwidth.

Quarkonium	Cross-section, nb			
	$\mu4\mu4$	$\mu6\mu4$	$\mu10$	$\mu6\mu4 \cap \mu10$
J/ψ	28	23	23	5
ψ'	1.0	0.8	0.8	0.2
Υ(1S)	48	5.2	2.8	0.8
Υ(2S)	16	1.7	0.9	0.3
Υ(3S)	9.0	1.0	0.6	0.2

Table 1: Predicted cross-sections for various prompt vector quarkonium state production and decay into muons, with di-muon trigger thresholds $\mu4\mu4$ and $\mu6\mu4$ and the single muon trigger threshold $\mu10$ (before trigger and reconstruction efficiencies). The last column shows the overlap between the di-muon and single muon samples.

2.1.2 Effect of trigger cuts on analysis of octet states

As discussed above, the quarkonium cross-section is composed of three main classes of processes: direct colour singlet production, colour octet production and singlet/octet production of χ states. Figure 6 illustrates the contributions of these three classes to the overall production rate for Υ, once the p_T trigger cuts of 6 and 4 GeV are applied to the muons. Lower p_T trigger cuts will strongly enhance the Υ rate and

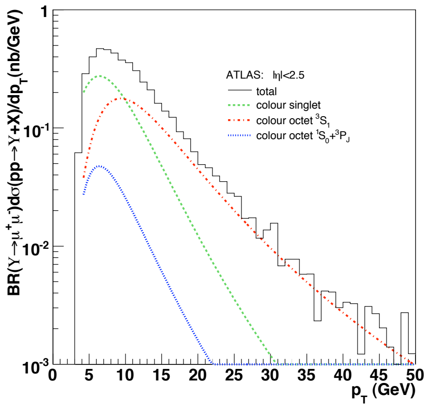

Figure 6: Expected p_T-distribution for Υ production, with contributions from direct colour singlet, singlet χ production and octet production overlaid.

allow for analysis of colour singlet production, which is expected to dominate for Υ with $p_T < 10$ GeV. Lower trigger cuts available during early running, such as the $\mu 4 \mu 4$ trigger described above, will allow the opportunity to extend the low-p_T region down to $p_T \simeq 0$ in the case of Υ and help separate octet and singlet contributions.

2.1.3 Acceptance of $\cos\theta^*$ with di-muon triggers

An important consideration for calculating the di-muon trigger efficiencies of J/ψ and Υ is the angular distribution of the decay angle θ^*, the angle between the direction of the positive muon (by convention) from quarkonium decay in the quarkonium rest frame and the flight direction of the quarkonium itself in the laboratory frame (Figure 7).

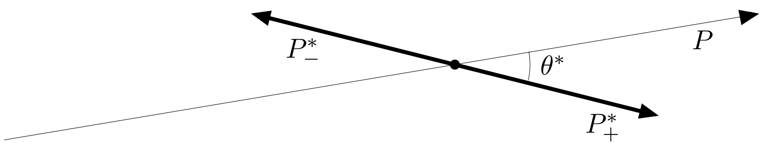

Figure 7: Graphical representation of the θ^* angle used in the spin alignment analysis. The angle is defined by the direction of the positive muon in the quarkonium decay frame and the quarkonium momentum direction in the laboratory frame.

The distribution in $\cos\theta^*$ may depend on the relative contributions of the various production mechanisms, and is as of yet not fully understood. Crucially, Monte Carlo studies have shown that different production mechanisms (and thus different angular distributions) can have significantly different trigger acceptances, and without the measurement of the spin-alignment of quarkonium it will be difficult to be sure that the full trigger efficiency has been calculated correctly.

It is clear that $\cos\theta^* \simeq 0$ corresponds to events with both muons having roughly equal transverse momenta, while in order to have $\cos\theta^*$ close to ± 1 one muon's p_T needs to be very high while the other's p_T is very low. In the case of a di-muon trigger, both muons from the J/ψ and Υ decays must have relatively large transverse momenta. Whilst this condition allows both muons to be identified, it also severely restricts acceptance in the polarisation angle $\cos\theta^*$, meaning that for a given p_T of J/ψ or Υ a significant fraction of the total cross-section is lost.

Examples of the polarisation angle distributions for the $\mu 6\mu 4$ trigger are shown by solid lines in Figure 8. Here, the samples for both J/ψ and Υ were generated with zero polarisation, so with full acceptance the corresponding distribution in $\cos\theta^*$ should be flat, spanning from -1 to $+1$. Clearly,

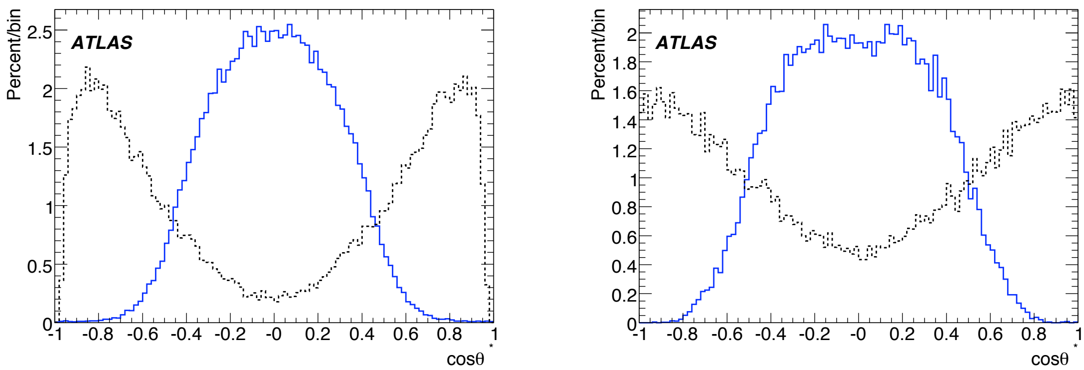

(a) J/ψ (b) Υ

Figure 8: Reconstructed polarisation angle distribution for $\mu 6\mu 4$ di-muon triggers (solid line) and a $\mu 10$ single muon trigger (dashed line), for J/ψ (a) and Υ (b). The distributions are normalised to unit area. The generated angular distribution is flat in both cases.

narrow acceptance in $|\cos\theta^*|$ would make polarisation measurements difficult.

2.2 Single muon trigger

Another possibility for quarkonium reconstruction is to trigger on a single identified muon. The non-prescaled level-1 single muon trigger `L1_MU10` with a 10 GeV p_T threshold is expected to produce manageable event rates at low luminosities [11]. Once this muon triggers the event, offline analysis can reconstruct the quarkonium by combining the identified muon with an oppositely-charged track in the event. In Figure 5 this trigger corresponds to the dash-dotted lines, with the predicted cross-sections also shown in Table 1. With this trigger (referred to as $\mu 10$ in the following) one removes the need for the other muon to have a large p_T, i.e. one has a fast muon, which triggered the event, and one track, whose transverse momentum is only limited by the track reconstruction capabilities of ATLAS, with the threshold around 0.5 GeV.

Thus, the onium events with a single muon trigger typically have much higher values of $|\cos\theta^*|$, as illustrated by the dotted lines in Figure 8, complementing the di-muon trigger sample. So, the single- and di-muon samples may be used together to provide excellent coverage across almost the entire range of $\cos\theta^*$ in the same p_T range of onia.

It's worth noting that the di-muon and single muon samples have comparable cross-sections and similar p_T dependence. They are not entirely independent: at high transverse momenta the two samples have significant event overlap (see Table 1 for more details), which could be useful for independent calibration of muon trigger and reconstruction efficiencies.

3 Reconstruction and background suppression

3.1 Quarkonium reconstruction with two muon candidates

In each event which passes the di-muon trigger, all reconstructed muon candidates are combined into oppositely charged pairs, and each of these pairs is analysed in turn. The invariant mass is calculated and, if the mass is above 1 GeV, the two tracks are refitted to a common vertex. If a good vertex fit is achieved, the pair is accepted for further analysis. If the invariant mass of the refitted tracks is within 300 MeV of the nominal mass in the case of J/ψ , or 1 GeV in the case of Υ, the pair is considered as a quarkonium candidate. The values quoted by the Particle Data Group [13], 3097 MeV and 9460 MeV for J/ψ and Υ respectively, are used throughout this paper, and the widths of the mass windows are chosen to be about six times the expected average mass resolution (see Table 2).

For those pairs for which the vertex fit is successful (more than 99% for both J/ψ and Υ), the invariant mass is recalculated. The invariant mass resolution depends on the pseudorapidities of the two muon tracks. To illustrate this effect, all accepted onia candidates are divided into three classes depending on η of the muons, and Gaussian fits are performed to determine the resolutions and mass shifts. The results are presented in Table 2. It is found that the mass resolution is the highest when both tracks are

Quarkonium	$M_{\text{rec}} - M_{\text{PDG}}$, MeV	Resolution σ, MeV			
		Average	Barrel	Mixed	Endcap
J/ψ	$+4 \pm 1$	53	42	54	75
Υ	$+15 \pm 1$	161	129	170	225

Table 2: Mass shifts and resolutions for di-muon invariant mass distributions after the vertex fit, for J/ψ and Υ candidates.

reconstructed in the barrel area, $|\eta| < 1.05$, degrades somewhat if both tracks are reconstructed in the endcap regions, $|\eta| > 1.05$, and is close to its average value for the mixed η events, with one muon in the barrel and the other in the endcap. It should be noted that no significant non-gaussian tails are observed in either of these mass distributions, and the fit quality is good. Also shown in the table are the shifts of the mean reconstructed invariant mass from the respective nominal values. The observed mass shifts are due to a problem with simulation of material effects in the endcap, which has since been understood and corrected.

The reconstructed muon pairs that remain after vertexing cuts are considered to be good quarkonium candidates, and further analysis is done using these pairs only. The transverse momentum distributions of these candidates are shown in Figure 9.

As can be seen from the Figure 9(a), prompt J/ψ are mainly selected with p_T above around 10 GeV, due to the di-muon trigger cuts applied to the events. The decay kinematics of Υ is somewhat different due to its larger mass, thus allowing Υ to be selected with p_T as low as 4 GeV. Even at these, relatively low, statistics one expects to see significant numbers of both types of quarkonia at large p_T, which will allow statistically significant high-p_T analyses beyond the reach of the Tevatron.

Figure 10(a) presents the J/ψ acceptance as a function of the J/ψ transverse momentum, relative to the Monte Carlo generated dataset, which requires the two muons to be within $|\eta| < 2.5$ and have transverse momenta greater than 6 and 4 GeV, respectively. Geometric acceptance of the detector and

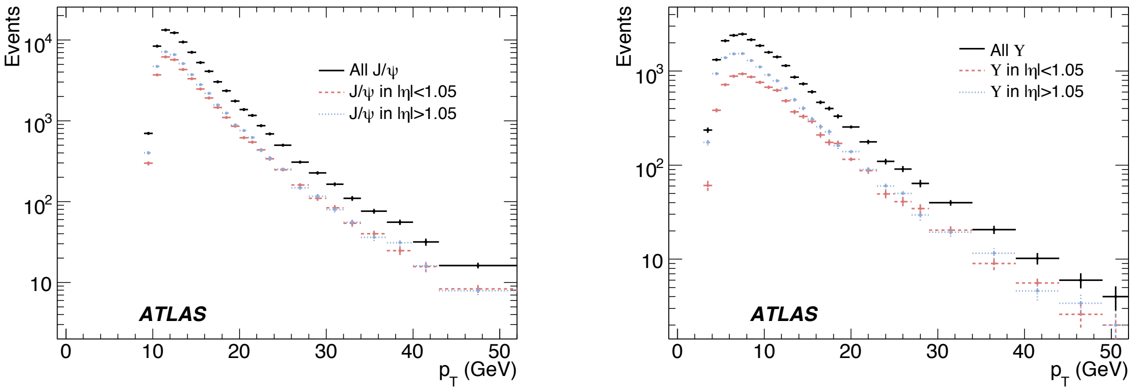

(a) J/ψ

(b) Υ

Figure 9: Transverse momentum distribution of triggered reconstructed quarkonium candidates, also shown separately for quarkonia found in the barrel and endcap regions of the detector. Statistics shown in the figures correspond to integrated luminosities of about 6 pb^{-1} and 10 pb^{-1} for J/ψ and Υ, respectively.

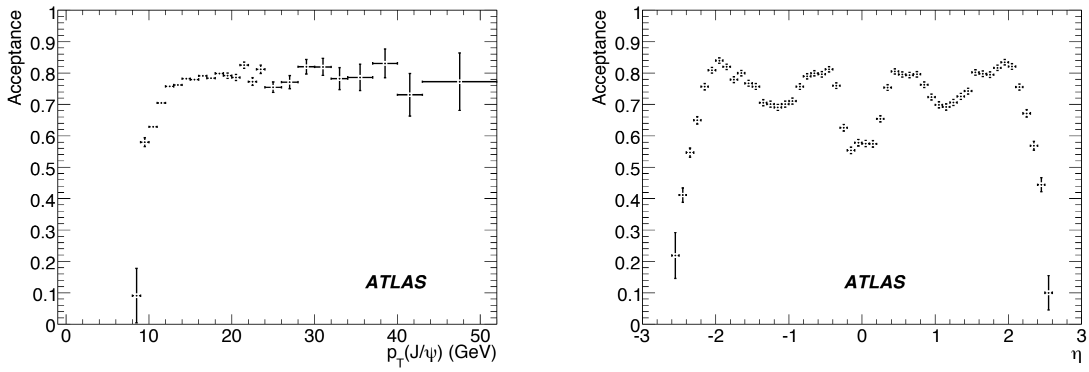

(a) J/ψ acceptance with p_T

(b) J/ψ acceptance with η

Figure 10: Acceptance of reconstructed prompt J/ψ as a function of J/ψ transverse momentum and pseudorapidity (relative to the MC generated dataset with $\mu6\mu4$ cuts).

reconstruction efficiency losses due to vertexing, as well as trigger efficiencies have been taken into account. When J/ψ are produced with a transverse momentum above 10 GeV, we see a sharp rise in the acceptance as J/ψ above this threshold are able to satisfy the muon trigger requirements within a certain kinematic configuration.

The structure in the plot of the η-dependence of J/ψ reconstruction efficiency, shown in Figure 10(b), highlights the configuration necessary in order for muons from the J/ψ to be able to pass the di-muon trigger, described below. The distribution of reconstructed quarkonium candidates with the angular separation of the two muons, described by the variable $\Delta R = \sqrt{\Delta\phi^2 + \Delta\eta^2}$, is shown in Figure 11. On average, muons from reconstructed J/ψ ($\mu6\mu4$) candidates are separated by $\Delta R \simeq 0.47$, and are restricted from being detected with separations larger than around 0.7.

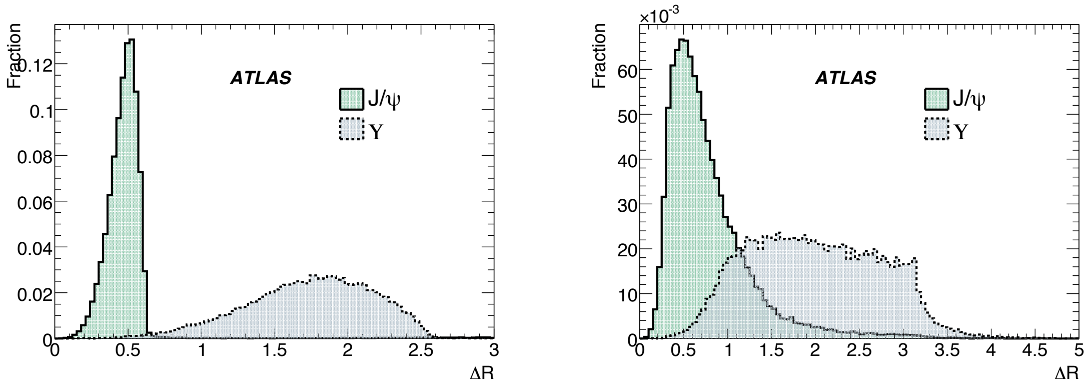

(a) ΔR with $\mu 6\mu 4$ cuts

(b) ΔR with $\mu 10$ cuts

Figure 11: Distribution of ΔR separation of the two muons from J/ψ and Υ candidates with di-muon $\mu 6\mu 4$ generator-level cuts (left) and single muon $\mu 10$ cuts (right) applied.

In comparison, the higher mass of Υ requires the muons in the $\mu 6\mu 4$ case to have a much larger opening angle, with a broad distribution in ΔR peaking at around 1.8 and spanning up to 2.6. One can see that for the single $\mu 10$ case in Figure 11(b) the distributions are much broader, and generally with smaller separation in ΔR, reflecting the lower p_T constraint on the second muon.

The small separation of muons in ΔR for the J/ψ ($\mu 6\mu 4$) case has consequences for the J/ψ reconstruction efficiency as a function of pseudorapidity, shown in Figure 10(b). Significant dips in efficiency are seen near $\eta \pm 1.2$ and $\eta = 0$, due to the muon spectrometer layout [14]. As the muons from J/ψ are on average separated by only $\Delta R = 0.47$, they are subject to similar material and detector effects, and so these effects are carried over into the J/ψ reconstruction with very little smearing. Hence, this distribution has a similar shape to the individual muon reconstruction efficiency distribution in ATLAS.

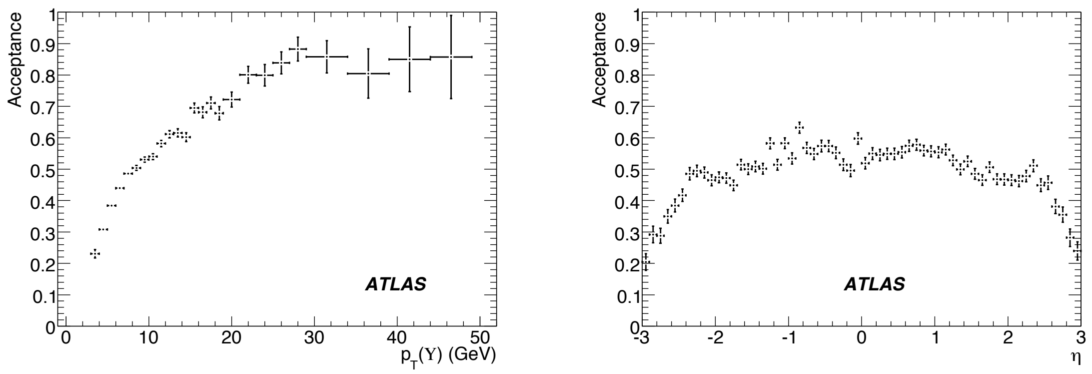

(a) Υ acceptance with p_T

(b) Υ acceptance with η

Figure 12: Acceptance of reconstructed prompt Υ as a function of transverse momentum and pseudorapidity of the quarkonium state (relative to the Monte Carlo generated dataset with $\mu 6\mu 4$ cuts).

This contrasts with the Υ reconstruction efficiency dependence on pseudorapidity, shown in Figure 12(b), which is much smoother than in J/ψ case: the two muons have large angular separation and the detector layout effects are smeared over a broader range of η values. Figure 12(a) shows the variation of acceptance with the Υ transverse momentum, and reflects the fact that with the $\mu6\mu4$ trigger Υ can be reconstructed with a lower p_T threshold. In the absence of a dedicated topological trigger for Υ, trigger efficiency at low p_T suffers due to the differing decay kinematics between J/ψ and Υ as only specialised J/ψ triggers exist in reconstruction software used in this analysis. At larger p_T both acceptances reach a plateau at around 80–85%.

3.2 Offline monitoring using quarkonium

The di-muon decays of J/ψ and Υ will be used in both online and offline monitoring at ATLAS. Mass shifts for the reconstructed quarkonium states, plotted versus a number of different variables, have been proposed to monitor detector alignment, material effects, magnetic field scale and its stability, as well as to provide checks of muon reconstruction algorithm performance. The CDF collaboration extensively and successfully used this method, although it took many years at the Tevatron to collect sufficient statistics to allow for the disentanglement of various detector effects [15].

The expected rate of quarkonium production at ATLAS is such that we can expect to be able to perform meaningful monitoring and corrections online. There are many examples of where monitoring of quarkonium mass shifts can be useful in data-taking. Mass shifts in quarkonia as a function of transverse momentum can reveal problems with energy loss corrections and the muon momentum scale. As a function of pseudorapidity this can be a good probe of over- or under-correction of material effects in the simulated detector geometry and of magnetic field uniformity. J/ψ mass shifts in Monte Carlo simulations have already helped to improve muon reconstruction algorithms in ATLAS.

An example of a reconstructed J/ψ mass shift measurement at ATLAS with the statistics corresponding to 6 pb^{-1} is presented in Figure 13. This is the dependence of ΔM on the difference in curvatures

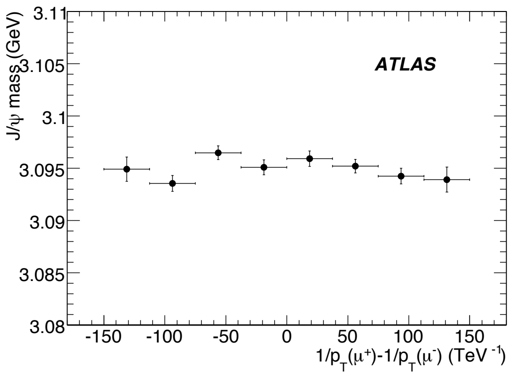

Figure 13: J/ψ mass shift plotted versus the difference of curvature between the positive and negative muons. Statistics corresponds to the integrated luminosity of about 6 pb^{-1}.

of positive and negative muons, which allows for checks of a potentially important effect seen at CDF: horizontal misalignments in some detector elements may result in a constant curvature offset that can lead to significant charge-dependent tracking effects. A misalignment may be such that a negative track has a higher assigned curvature (and hence lower momentum) than is truly the case, whilst a positive track would be affected in the opposite way. The sample shown in the figure is simulated with ideal geometry and does not show any significant effects of this kind.

For detector alignment and data monitoring purposes, quarkonium provides a low p_T point for calibration, complementary to the Z boson sample, and allows for the possibility to identify any systematic variations that may develop at higher p_T.

In order to be able to analyse mass shifts due to two-variable correlations and disentangle various detector effects, significant statistics of J/ψ and Υ di-muon decays have to be accumulated. A dedicated study is being performed in ATLAS to optimise the strategy of real time and offline monitoring using this method, but these results lie beyond the scope of this note.

3.3 Background suppression in di-muon case

The expected sources of background for prompt quarkonium with a di-muon $\mu6\mu4$ trigger are:

- indirect J/ψ production from $b\bar{b}$ events;
- continuum of muon pairs from $b\bar{b}$ events;
- continuum of muon pairs from charm decays;
- di-muon production via the Drell-Yan process;
- decays in flight of $\pi^{\pm}$ and $K^{\pm}$ mesons.

The most important background contributions are expected to come from the decays $b \to J/\psi + X$, and the continuum of di-muons from $b\bar{b}$ events. Both of these have been simulated and analysed. The estimated total contribution from charm decays is higher than that from $b\bar{b}$ events. However, this background has not been simulated, as it is not expected to cause problems for prompt quarkonium reconstruction because the transverse momentum spectrum of the muons falls very steeply and the probability of producing a di-muon with an invariant mass within the range of interest is well below the level expected from $b\bar{b}$ events. Only a small fraction of the Drell-Yan pairs survive the di-muon trigger cuts of $\mu6\mu4$ in the $J/\psi - \Upsilon$ mass range, which makes this background essentially negligible, as estimated from generator-level simulation. Muons from decays in flight also have a steeply falling muon momentum spectrum, and in addition require random coincidences with muons from other sources in the quarkonium invariant mass range. This is estimated to be at the level of a few percent of the signal rate, spread over a continuum of invariant masses.

All background di-muon sources mentioned above, apart from Drell-Yan pairs, contain muons which originate from secondary vertices, which makes it possible to suppress these backgrounds by removing such di-muons whenever a secondary vertex has been resolved, based on the pseudo-proper time measurement. The pseudo-proper time is defined as

$$\text{Pseudo-proper time} = \frac{L_{xy} \cdot M_{J/\psi}}{p_T(J/\psi) \cdot c}, \tag{1}$$

where $M_{J/\psi}$ and $p_T(J/\psi)$ represent the mass and the transverse momentum of the J/ψ candidate, c is the speed of light in vacuum, and L_{xy} is the measured radial displacement of the two-track vertex from the beamline. Once the two muons forming a J/ψ candidate are reconstructed, the pseudo-proper time is used to distinguish between the prompt J/ψ, which have a pseudo-proper time of zero, and J/ψ coming from B-hadron decays and hence having an exponentially decaying pseudo-proper time distribution, due to the non-zero lifetime of the parent B-hadrons.

The dependence of the resolution in radial decay length L_{xy} on di-muon pseudorapidity η is shown in Figure 14, while the variation of the expected resolution in the pseudo-proper time with di-muon p_T is shown in Table 3. An improvement in the resolution is seen with increasing p_T of the J/ψ and

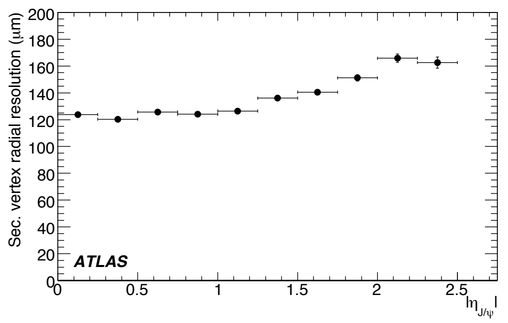

Figure 14: Radial position resolution of secondary vertex for J/ψ decays as a function of the J/ψ pseudorapidity.

J/ψ transverse momentum (GeV)	$9-12$	$12-13$	$13-15$	$15-17$	$17-21$	>21
Pseudo-proper time resolution (ps)	0.107	0.103	0.100	0.093	0.087	0.068

Table 3: Pseudo-proper time resolution of direct J/ψ events as a function of J/ψ p_T.

decreasing $|\eta|$. Here a perfect detector alignment is assumed, with the resulting average resolution estimated at around 0.1 ps.

Figure 15(a) illustrates the pseudo-proper time distribution for both the prompt and indirect J/ψ samples. By making a cut on the pseudo-proper time, one can efficiently separate most of the indirect J/ψ from a prompt J/ψ sample (or vice-versa). The efficiency and purity of the pseudo-proper time cuts for prompt J/ψ are presented in Figure 15(b). A pseudo-proper time cut of less than 0.2 ps allows to retain prompt J/ψ with the efficiency of 93% and the purity of 92%. Note that the distribution shown in Figure 15(a) is, in a sense, self-calibrating: the part to the left of the maximum can be used to determine the resolution σ, and an appropriate cut of 2σ can be applied to remove the 'tail' of secondary J/ψ candidates on the right hand side.

The background levels of beauty and Drell-Yan production under the Υ peak are similar to those for the J/ψ , except that here one does not have to contend with sources of non-prompt quarkonia from B-decays. However, the $bb \to \mu6\mu4$ background continuum under the Υ is more problematic: higher invariant masses around the Υ mean that the two triggered muons will necessarily come from two separate decays, meaning that the pseudo-proper time cut is far less effective.

Fortunately, flags associated to individual reconstructed muon tracks provide further vertexing information, which could be used for suppressing of the $bb \to \mu6\mu4$ continuum background. Reconstructed tracks are assigned to either come from the primary vertex, a secondary vertex, or are left undetermined. By requiring that both of the muons combined to make a J/ψ or a Υ candidate are determined to have come from the primary vertex, background from the $bb \to \mu6\mu4$ continuum can be reduced by a factor of three or more, whilst reducing the number of signal events by around 5% in both cases.

Figure 16 illustrates the quarkonium signal and main background invariant mass distributions in the mass range $2-12$ GeV, for those events which satisfy the $\mu6\mu4$ trigger requirements, with reconstruction efficiencies and background suppression cuts taken into account. Peaks from the J/ψ and $\Upsilon(1S)$ clearly dominate the background. As no higher ψ and Υ states were simulated for this analysis, their peaks are

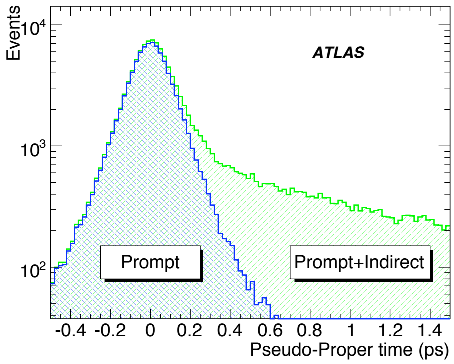

(a)

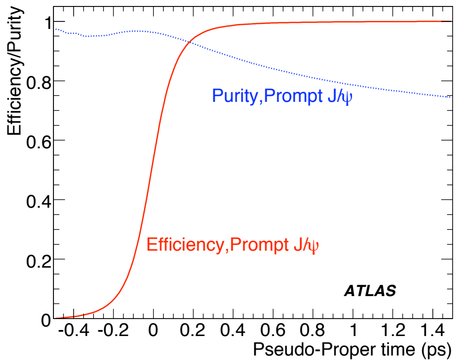

(b)

Figure 15: (a) Pseudo-proper time distribution for reconstructed prompt J/ψ (dark shading) and the sum of prompt and indirect J/ψ candidates (lighter shading). (b) Efficiency (solid line) and purity (dotted line) for prompt J/ψ candidates as a function of the pseudo-proper time cut. Statistics correspond to the integrated luminosity of 6 pb^{-1}.

not shown. The dotted line indicates the level of the background continuum before the vertexing cuts.

In conclusion, we find that the level of the backgrounds considered for both J/ψ and Υ do not represent any serious problem for reconstruction and analysis of direct quarkonia with the di-muon $\mu6\mu4$ trigger.

3.4 Reconstruction and background suppression with a single muon candidate

By using the $\mu10$ trigger, one selects events with at least one identified muon candidate with p_T above 10 GeV. In this part of the analysis, each reconstructed single muon candidate is combined with oppositely-charged tracks reconstructed in the same event. For both J/ψ and Υ reconstruction, we insist that any other reconstructed track to be combined with the identified trigger muon has an opposite electric charge and is within a cone of $\Delta R = 3.0$ around the muon direction, so as to retain over 99% (91%) of the signal events in the J/ψ (Υ) case. As in the di-muon analysis, we require that both the identified muon and the track are flagged as having come from the primary vertex. In addition, we impose a cut on the transverse impact parameter d_0, $|d_0| < 0.04$ mm on the muon and $|d_0| < 0.10$ mm on the track, in order to further suppress the number of background pairs from B-decays.

The invariant mass distribution for the remaining pairings of a muon and a track is shown in Figure 17(a) for J/ψ with p_T larger than 9 GeV and in Figure 17(b) for J/ψ with p_T larger than 17 GeV. The distributions are fitted using a single gaussian for the signal and a straight line for the background. Clear J/ψ peaks can be seen, with statistically insignificant mass shifts and the resolution close to that in the di-muon sample. It's worth noting that the signal-to-background ratio around the J/ψ peak improves slightly with increasing transverse momentum of J/ψ. At higher p_T the $\cos\theta^*$ acceptance also becomes broader, which should help independent polarisation measurements.

For Υ the situation is less favourable, due to the combination of a lower signal cross-section and a higher background. Although the Υ peak can be seen above the smooth background, its statistical significance is rather low. Hence, with this statistics, the use of the single muon sample for Υ cannot be justified, and in the following we will only rely on the di-muon sample.

In conclusion, we expect that the single muon trigger with a 10 GeV threshold can be successfully

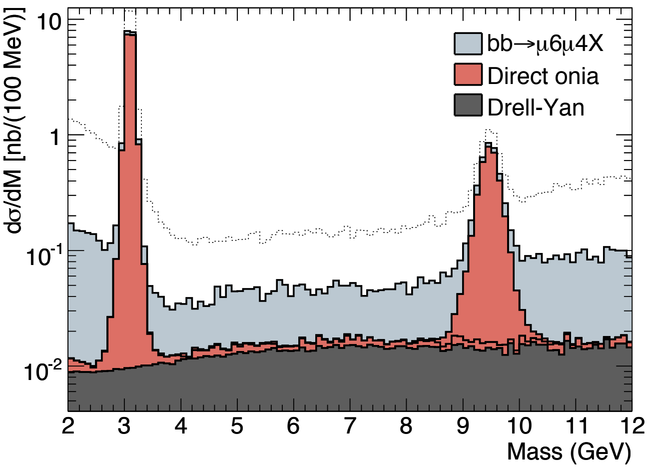

Figure 16: The cumulative plot of the invariant mass of di-muons from various sources, reconstructed with a $\mu 6 \mu 4$ trigger, with the requirement that both muons are identified as coming from the primary vertex and with a pseudo-proper time cut of 0.2 ps. The dotted line shows the cumulative distribution without vertex and pseudo-proper time cuts.

used to select prompt J/ψ events. The expected background here, although much larger than in di-muon case, is well under control. For Υ however, the single muon sample is only likely to be useful at significantly higher statistics and higher transverse momenta.

3.5 Summary of cuts and efficiencies

Table 4 summarises the efficiencies of all the selection and background suppression cuts described above, for both the di-muon and single muon trigger samples. Not all cuts are applicable to all samples; those which are not are labelled accordingly. Numbers in italics are estimates in cases where no adequate fully simulated sample was available. The efficiencies for $\mu 6 \mu 4$ samples are calculated relative to the Monte Carlo sample with generator-level cuts on the two highest muon transverse momenta of 6 and 4 GeV. For the $\mu 10$ samples, the generator-level cut of 10 GeV was applied to the p_T of the highest-p_T muon. Expected yields N_S of quarkonia for 10 pb^{-1} are given at the bottom of the table, along with background yields N_B within the invariant mass window of ± 300 MeV for J/ψ and ± 1 GeV for Υ, and the signal-to-background ratios at respective J/ψ and Υ peaks for each sample.

For higher, excited quarkonium states with vector quantum numbers the efficiencies are expected to be similar, but not necessarily identical. The biggest differences are expected for ψ', where the production mechanisms as well as decay kinematics are significantly different.

4 Polarisation and cross-section measurement

The Colour Octet Model predicts that prompt quarkonia produced in pp collisions are transversely polarised, with the degree of polarisation increasing as a function of the transverse momentum. Other production models predict different p_T dependencies of the polarisation and so this quantity serves as an important measurement for discrimination of these models (see Figure 1(b)).

Quarkonium polarisation can be assessed by measuring the angular distribution of the muons produced in the decay. The relevant decay angle θ^* is defined in Figure 7. The spin alignment of the parent

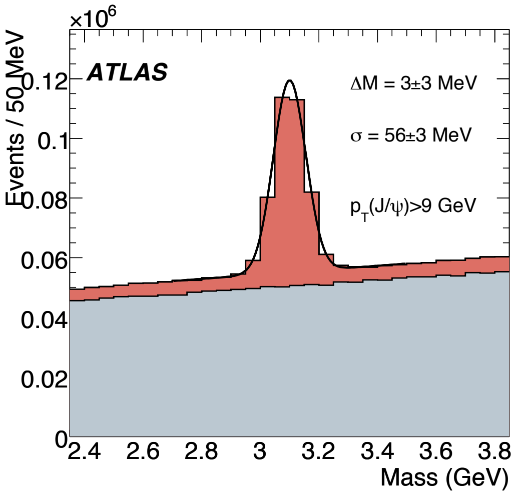

(a) J/ψ with $p_T > 9$ GeV

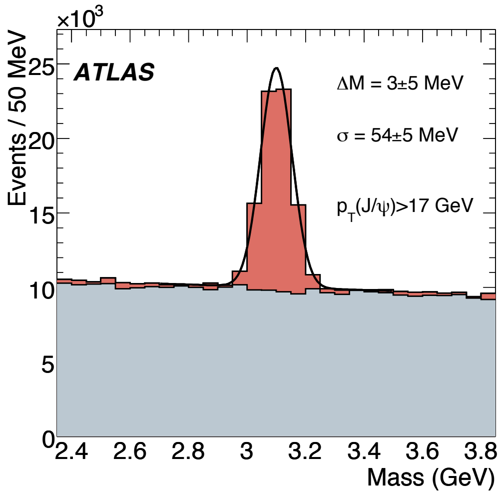

(b) J/ψ with $p_T > 17$ GeV

Figure 17: Prompt quarkonium signal and $bb \to \mu X$ background events selected with the $\mu 10$ trigger, in the mass range around J/ψ with (a) p_T above 9 GeV, and (b) p_T above 17 GeV, corresponding to 10 pb^{-1} of data. The background from B decays is shown in light grey. Cuts described in the text have been applied. The distributions were fitted using the sum of a linear background and a gaussian peak centered at $M = 3097$ MeV $+\Delta M$ with resolution σ.

vector quarkonium state can be determined by measuring the polarisation parameter α in the distribution

$$\frac{dN}{d\cos\theta^*} = C\,\frac{3}{2\alpha+6}\left(1+\alpha\cos^2\theta^*\right). \tag{2}$$

The choice of parameters in Equation 2 is such that the distribution is normalised to C. The parameter α, defined as $\alpha = (\sigma_T - 2\sigma_L)/(\sigma_T + 2\sigma_L)$, is equal to $+1$ for transversely polarised production (helicity $= \pm 1$). For a longitudinal polarisation (helicity $= 0$), α is equal to -1. Unpolarised production consists of equal fractions of helicity states $+1$, 0 and -1, and corresponds to $\alpha = 0$.

The difficulty of quarkonium polarisation measurements is evidenced by the discrepancies between DØ and CDF results shown in Figure 1(b). The problem can be traced to the limited acceptance at high $|\cos\theta^*|$, and hence difficulties in separating acceptance corrections from spin alignment effects (see, e.g., [7]).

Note that the feed-down from χ state and b-hadron decays may lead to a different spin alignment and hence to a possible effective depolarisation which is hard to estimate. In addition, due to the limited statistics, the polarisation measurements at the Tevatron cannot reach the region of high p_T, where theoretical uncertainties are expected to be smaller.

At ATLAS we aim to measure the polarisation of prompt vector quarkonium states, in the transverse momentum range up to ~ 50 GeV and beyond, with extended coverage in $\cos\theta^*$ which will allow for improved understanding of efficiency measurements and thus reduced systematics. The promptly produced J/ψ mesons and those that originated from B-hadron decays can be separated using the displaced decay vertices, as explained above. With a high production rate of quarkonia at LHC, it will be possible to achieve a higher degree of purity of prompt J/ψ in the analysed sample and reduce the depolarising effect from B-decays, whilst retaining high statistics.

As explained in Section 2.1.3, with the di-muon trigger signature such as $\mu 6\mu 4$, the acceptance at large values of $|\cos\theta^*|$ (where the difference between various polarisation states is the biggest)

	Quarkonium Trigger type	J/ψ $\mu6\mu4$	J/ψ $\mu10$	Υ $\mu6\mu4$	Υ $\mu10$
	MC cross-section	23 nb	23 nb	5.2 nb	2.8 nb
ε_{L1}	Level-1 trigger	87%	96%	84%	96%
ε_{L2}	Level-2 trigger	97%	>99%	66%	>99%
ε_{Rec}	Reconstruction	89%	96%	93%	96%
ε_{Vtx}	Vertex fit	99%	99%	99%	99%
ε_1	$\varepsilon_{L1}\cdot\varepsilon_{L2}\cdot\varepsilon_{Rec}\cdot\varepsilon_{Vtx}$	75%	90%	51%	90%
ε_{t0}	Pseudo-proper time cut	93%	93%	n/a	n/a
ε_{Flg}	Only primary vertex tracks	96%	92%	95%	92%
$\varepsilon_{\Delta R}$	Second track inside cone	n/a	99%	n/a	91%
ε_{d0}	Impact parameter cut	n/a	90%	n/a	90%
ε_2	$\varepsilon_{t0}\cdot\varepsilon_{Flg}\cdot\varepsilon_{\Delta R}\cdot\varepsilon_{d0}$	90%	76%	95%	75%
ε	Overall efficiency $\varepsilon_1\cdot\varepsilon_2$	67%	69%	49%	68%
	Observed signal cross-section	15 nb	16 nb	2.5 nb	2.0 nb
	N_S for 10 pb^{-1}	150 000	160 000	25 000	20 000
	N_B in mass window for 10 pb^{-1}	7000	700 000	16 000	2 000 000
	Signal/Background at peak	60	1.2	10	0.05

Table 4: Predicted and observed cross-sections for prompt vector quarkonia, and efficiencies of various selection and background suppression cuts described in Section 3.

is strongly reduced, especially at low transverse momenta of quarkonium. The kinematic acceptance $\mathscr{A}(p_T,\cos\theta^*)$ of the $\mu6\mu4$ cuts applied at generator level, with respect to the full generator-level sample with no cuts on muon transverse momenta, is shown by the solid lines in Figure 18 for various p_T slices of J/ψ. The acceptance is seen to be quite low at J/ψ p_T below 12 GeV, but in higher p_T slices there is an area in the middle of $\cos\theta^*$ range with essentially 100% acceptance, which becomes broader with increasing p_T of the J/ψ, but does not go beyond $|\cos\theta^*|\simeq 0.5$.

The acceptance for the single muon trigger sample, shown with the dashed lines in Figure 18, is different: here the areas of 100% acceptance are at high $|\cos\theta^*|$, and the dip in the middle gradually fills up with increasing p_T. This sample essentially has a full acceptance at $p_T > 20$ GeV, apart from the drop at $|\cos\theta^*| > 0.95$ due to the cut of 0.5 GeV on the p_T of the track of the second muon.

The plots in Figure 18 were obtained using a dedicated generator-level Monte Carlo sample. The error bars shown in the figure reflect both statistical errors and the uncertainties due to possible dependence on η coverage.

The simulated 'raw' measured distributions $dN^{\mathrm{raw}}/d\cos\theta^*$, for the same slices of J/ψ transverse momenta, are shown in Figure 19. Again, solid and dashed lines represent the events selected by the di-muon $\mu6\mu4$ and the single muon $\mu10$ triggers, respectively. The sample was generated with zero polarisation. The raw numbers of measured events in the $\mu10$ sample were obtained by fitting the invariant mass distributions with a gaussian peak and a linear background, for each bin of $\cos\theta^*$ in each p_T slice. With the estimated signal-to-background ratios shown in Figure 17(a), this causes an increase in the statistical errors, typically by a factor of 2.

The corrected distributions $dN^{\mathrm{cor}}/d\cos\theta^*$ are calculated according to the following formula:

$$\frac{dN^{\mathrm{cor}}}{d\cos\theta^*} = \frac{1}{\mathscr{A}(p_T,\cos\theta^*)\cdot\varepsilon_1\cdot\varepsilon_2}\cdot\frac{dN^{\mathrm{raw}}}{d\cos\theta^*} \tag{3}$$

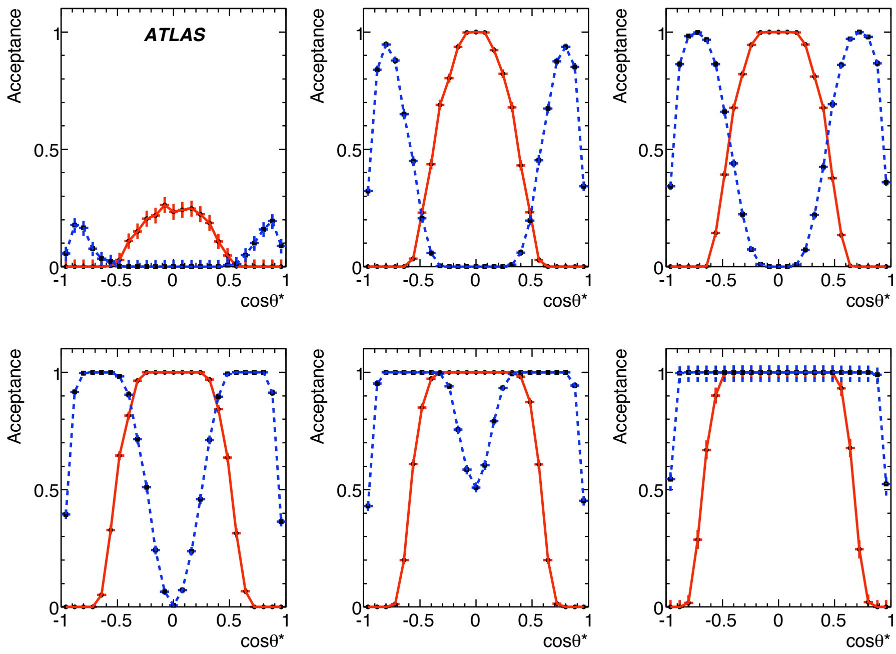

Figure 18: Generator-level kinematic acceptances of the $\mu6\mu4$ (solid lines) and $\mu10\mu0.5$ (dashed lines) cuts, calculated with respect to the sample with no muon p_T cuts, in slices of J/ψ transverse momentum: left to right, top to bottom $9-12$ GeV, $12-13$ GeV, $13-15$ GeV, $15-17$ GeV, $17-21$ GeV, above 21 GeV.

Here ε_1 stands for the trigger and reconstruction efficiency, while ε_2 denotes the efficiency of background suppression cuts for each sample, as defined in Table 4. Their values have been averaged over the accessible phase space within the relevant p_T slice. Studies have shown that while ε_1 depend on p_T (cf. Figure 10(a)), ε_2 remain essentially constant over the phase space of interest. The efficiencies ε_1 and ε_2 for both samples are listed in Table 5, while the acceptances $\mathscr{A}(p_T, \cos\theta^*)$ are shown in Figure 18.

p_T, GeV	$9-12$	$12-13$	$13-15$	$15-17$	$17-21$	>21
$\varepsilon_1(\mu6\mu4)$, %	67 ± 1	75 ± 1	77 ± 1	78 ± 1	79 ± 1	80 ± 1
$\varepsilon_2(\mu6\mu4)$, %	90 ± 1	90 ± 1	90 ± 1	90 ± 1	90 ± 1	90 ± 1
$\varepsilon_1(\mu10)$, %	86 ± 1	89 ± 1	90 ± 1	90 ± 1	90 ± 1	90 ± 1
$\varepsilon_2(\mu10)$, %	76 ± 1	76 ± 1	76 ± 1	76 ± 1	76 ± 1	76 ± 1

Table 5: Efficiencies for the $\mu6\mu4$ and $\mu10$ samples, averaged over each of the six p_T slices.

At high p_T the two samples increasingly overlap, thus allowing for a cross-check of acceptance and efficiency corrections. However, for measurement purposes the $\mu6\mu4$ samples are used whenever possible, complemented by $\mu10$ samples at high $\cos\theta^*$. In order to achieve this, the distributions shown in Figure 19 were appropriately masked and combined. The combined distributions $dN^{\text{cor}}/d\cos\theta^*$, corrected according to Equation 3, are shown in Figure 20. The errors shown in the plots include the statistical errors on the raw data, as well as the uncertainties on the acceptance and efficiencies. These $\cos\theta^*$ distributions are fitted using the Equation 2, with α and C as free parameters for each p_T slice. The fit

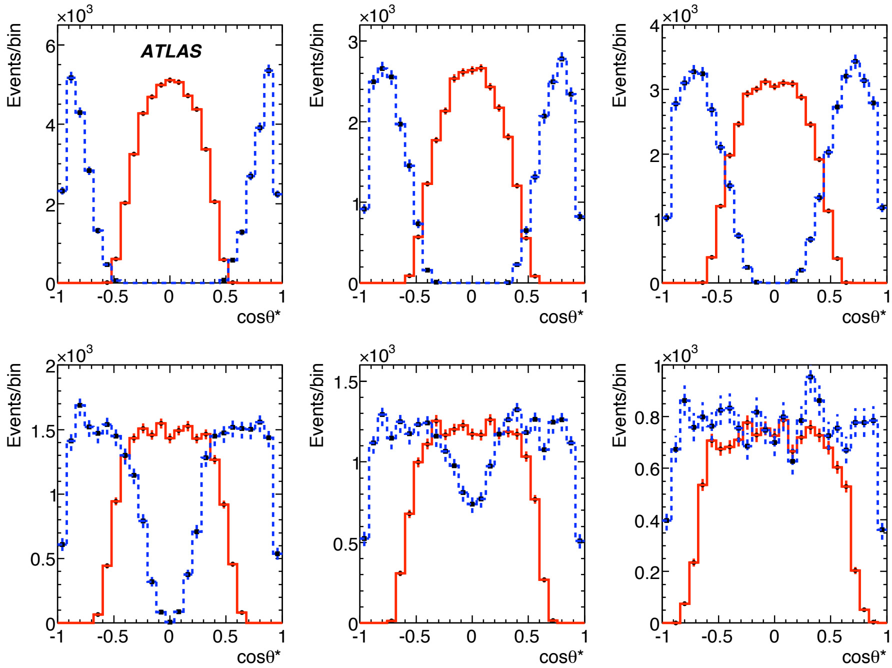

Figure 19: Measured distributions for $\mu6\mu4$- (solid lines) and $\mu10$- (dashed lines) triggered events, in the same p_T slices of the J/ψ candidate as in Figure 18. The simulated data sample is unpolarised. Statistics correspond to 10 pb^{-1}.

results are presented in Table 6, with constant C rescaled to the measured cross-section σ, corresponding to the integrated luminosity of 10 pb^{-1}.

To further check our ability to measure the spin alignment of J/ψ , the raw distributions shown in Figure 19 were reweighted to emulate transversely polarised ($\alpha_{\rm gen} = +1$) and longitudinally polarised ($\alpha_{\rm gen} = -1$) J/ψ samples, and the analysis described above was repeated. The results are shown in Figure 21 and in the middle two sections of Table 6.

A similar analysis can be done for measuring the polarisation and cross-section of Υ, but at the integrated luminosity of 10 pb^{-1} these measurements are expected to be far less precise than in J/ψ case. The main reasons are lower Υ cross-sections at high transverse momenta, and higher backgrounds for the $\mu10$ sample. The latter reason, as explained in Section 3.4, means that with these statistics the $\mu10$ sample is essentially unusable, and the limited acceptance of the $\mu6\mu4$ sample at high $|\cos\theta^*|$ makes a precise measurement difficult.

The corrected $|\cos\theta^*|$ distributions for unpolarised Υ from the $\mu6\mu4$ sample are shown in Figure 22. The results of the fit using Equation 2, with normalisation matched to the integrated luminosity of 10 pb^{-1}, are shown in the last section of Table 6. With the integrated luminosity increased by an order of magnitude, the $\mu10$ sample should become useful and the estimated errors on Υ polarisation measurement could be reduced by a factor of 5.

The errors shown in Figures 20 —22 and Table 6 include the statistical uncertainties on the measured numbers of events as well as various systematic errors stemming from the uncertainties on acceptances and efficiencies described above.

The overall uncertainty on the integrated luminosity needs to be added to all measured cross-sections, and is expected to be rather large during the initial LHC runs. This uncertainty will not, however, affect the relative magnitudes of the cross-sections measured in separate p_T slices, or the measured values of

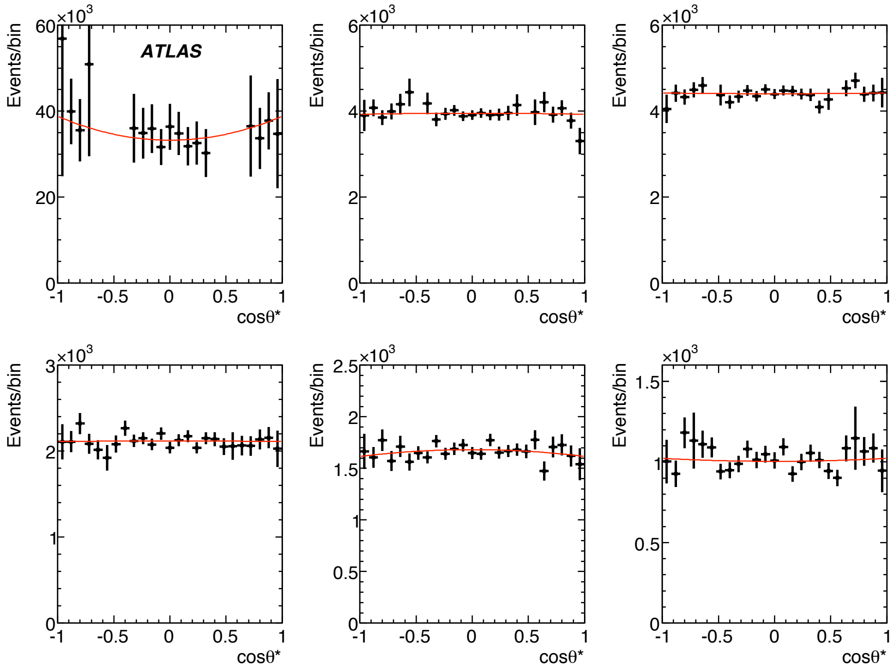

Figure 20: Combined and corrected distributions in J/ψ polarisation angle $\cos\theta^*$, for the same p_T slices as in Figure 18. The data sample is unpolarised ($\alpha_{\text{gen}} = 0$). The lines show the results of the fit using Equation 2, where the fitted values of α are given in Table 6. Statistics correspond to 10 pb^{-1}.

Sample	p_T, GeV	$9-12$	$12-13$	$13-15$	$15-17$	$17-21$	>21
J/ψ, $\alpha_{\text{gen}} = 0$	α	0.156 $\pm$0.166	-0.006 $\pm$0.032	0.004 $\pm$0.029	-0.003 $\pm$0.037	-0.039 $\pm$0.038	0.019 $\pm$0.057
	σ, nb	87.45 $\pm$4.35	9.85 $\pm$0.09	11.02 $\pm$0.09	5.29 $\pm$0.05	4.15 $\pm$0.04	2.52 $\pm$0.04
J/ψ, $\alpha_{\text{gen}} = +1$	α	1.268 $\pm$0.290	0.998 $\pm$0.049	1.008 $\pm$0.044	0.9964 $\pm$0.054	0.9320 $\pm$0.056	1.0217 $\pm$0.088
	σ, nb	117.96 $\pm$6.51	13.14 $\pm$0.12	14.71 $\pm$0.12	7.06 $\pm$0.07	5.52 $\pm$0.05	3.36 $\pm$0.05
J/ψ, $\alpha_{\text{gen}} = -1$	α	-0.978 $\pm$0.027	-1.003 $\pm$0.010	-1.000 $\pm$0.010	-1.001 $\pm$0.013	-1.007 $\pm$0.014	-0.996 $\pm$0.018
	σ, nb	56.74 $\pm$2.58	6.58 $\pm$0.06	7.34 $\pm$0.06	3.53 $\pm$0.04	2.78 $\pm$0.03	1.68 $\pm$0.02
Υ, $\alpha_{\text{gen}} = 0$	α	-0.42 $\pm$0.17	-0.38 $\pm$0.22	-0.20 $\pm$0.20	0.08 $\pm$0.22	-0.15 $\pm$0.18	0.47 $\pm$0.22
	σ, nb	2.523 $\pm$0.127	0.444 $\pm$0.027	0.584 $\pm$0.029	0.330 $\pm$0.016	0.329 $\pm$0.015	0.284 $\pm$0.012

Table 6: J/ψ and Υ polarisation and cross-sections measured in slices of p_T, for 10 pb^{-1}.

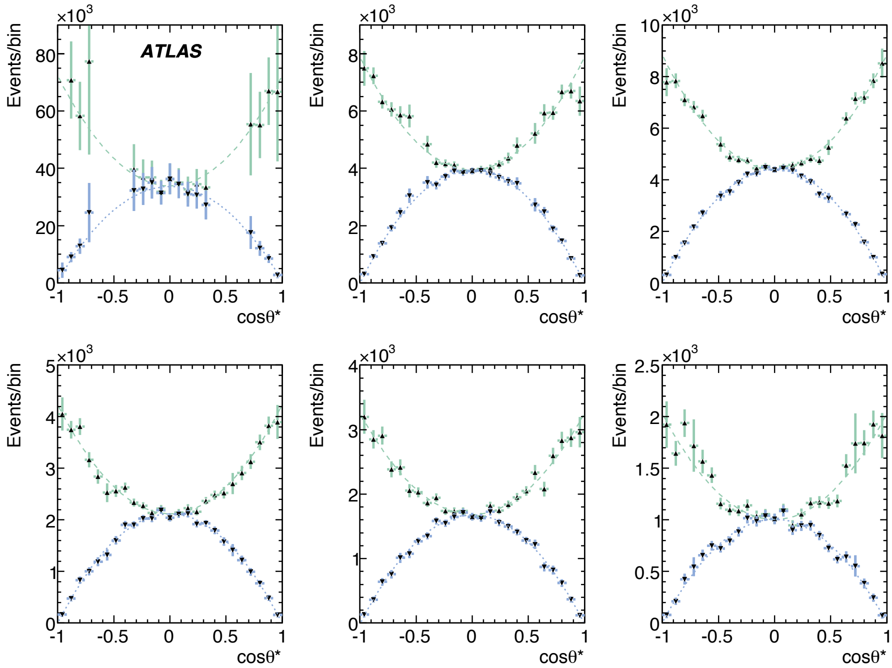

Figure 21: Combined and corrected distributions in polarisation angle $\cos\theta^*$, for longitudinally ($\alpha_{\text{gen}} = -1$, dotted lines) and transversely ($\alpha_{\text{gen}} = 1$, dashed lines) polarised J/ψ mesons, in the same p_T slices as in Figure 18. The lines show the results of the fit using Equation 2, where the fitted values of α are given in Table 6. Statistics correspond to 10 pb^{-1}.

the polarisation coefficient α. Additional systematic effects have also been studied, such as the influence of finite resolution in p_T and $\cos\theta^*$, changes in binning, details of the functions used for fitting the invariant mass distributions, and variations of cuts used for background suppression. Their respective uncertainties on the measured values of α and σ have been found not to exceed a small fraction of the quoted errors, and have thus been deemed negligible.

In conclusion, with the integrated luminosity of 10 pb^{-1} it should be possible to measure the polarisation of J/ψ with the precision of order $0.02-0.06$, depending on the level of polarisation itself, in a wide range of transverse momenta, $p_T \simeq 10-20$ GeV and beyond. In case of Υ, the expected precision is somewhat lower, of order 0.20. In both cases, however, the p_T dependence of the cross-section should be measured reasonably well.

5 Analysis of χ production

Quarkonium states with even C parity, such as $\eta_{c,b}$ and $\chi_{c,b}$, have a strong coupling to the colour-singlet two-gluon state, and hence a significantly higher production cross-section than vector quarkonia. Their dominant production mechanism for the phase space area accessible in ATLAS is via the subprocess shown in Figure 2(b) in Section 1. Their detection, however, is rather more difficult due to the absence of purely leptonic decays.

About 30 to 40% of J/ψ and Υ are expected to come from decays $\chi_c \to J/\psi\gamma$ and $\chi_b \to \Upsilon\gamma$. Unfortunately, the energies of the radiated photons tend to be quite small. The ability of ATLAS to detect these photons and resolve various χ states is analysed in Section 5.1. Another possibility of observing χ_b and possibly η_b states is considered in Section 5.2, where the reconstruction of these states is attempted

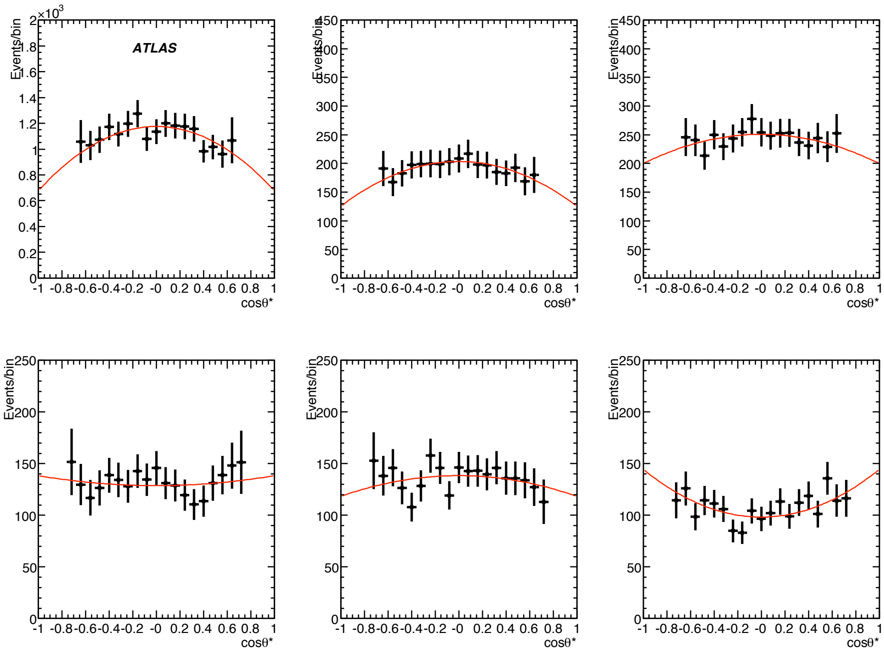

Figure 22: Corrected distributions in polarisation angle $\cos\theta^*$, for unpolarised Υ mesons, in the same slices of Υ transverse momentum as in Figure 18. Only $\mu6\mu4$ sample has been used. Statistics correspond to 10 pb^{-1}.

through their decay into a pair of J/ψ, both of which subsequently decay into $\mu^+\mu^-$.

5.1 Radiative decays of χ_c, χ_b states

Reconstructing χ_c candidates requires associating a reconstructed J/ψ with the photon emitted from the χ_c decay. The transverse momentum distribution for all identified photon candidates in events with a prompt J/ψ, as measured by the ATLAS electromagnetic calorimeter, is shown in Figure 23(a) (light grey histogram).

For χ_c reconstruction, each selected quarkonium candidate is combined with every reconstructed and identified photon candidate in the event, and the invariant mass of the $\mu\mu\gamma$ system is calculated. No explicit cut is applied to the p_T of the photon. The $\mu\mu\gamma$ system is considered to be a χ candidate, if the difference ΔM between the invariant masses of the $\mu\mu\gamma$ and $\mu\mu$ systems lies between 200 and 700 MeV, and the cosine of the opening angle α between the J/ψ and γ momenta is larger than 0.97. The last requirement comes from the observation that for the correct $\mu\mu\gamma$ combinations, the angle α is usually very small (see reconstructed distribution in Figure 23(b)). By analysing Monte Carlo information, it was found that all photons from generated χ decays were found in the peak near $\cos\alpha = +1$, with the long tail in the reconstructed distribution representing the combinatorial background. The transverse energy distribution for those photon candidates which satisfy the above requirements is presented in Figure 23(a) by the dark histogram. With these cuts, the combinatorial background is strongly reduced.

Figure 24 shows the distribution in ΔM for the selected χ_c decay candidates. The expected mean positions of the peaks corresponding to χ_0, χ_1 and χ_2 signals (318, 412 and 460 MeV, respectively) are indicated by arrows. The grey histogram shows the contribution from the background process of J/ψ production from B-hadron decays, some of which survive the pseudo-proper time cut.

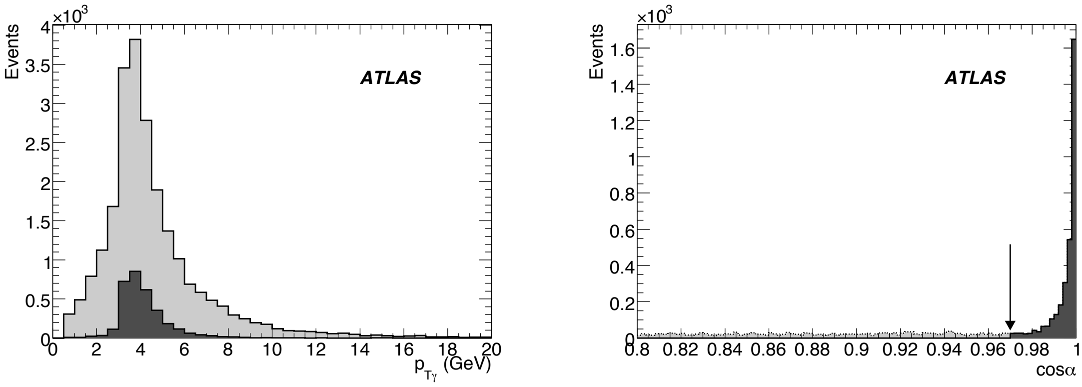

(a) (b)

Figure 23: (a) Transverse momentum distribution of photons reconstructed in prompt J/ψ events. (b) Distribution of $\cos\alpha$ for each reconstructed γ in an event. On both plots, the light grey (dark grey) histograms show the distributions before (after) the cut on the opening angle α between the photon and the J/ψ momentum direction. All photons from $\chi \to J/\psi\gamma$ decays have $\cos\alpha > 0.97$, while the vast majority of background combinations fall outside the range shown in plot (b). The sample corresponds to the integrated luminosity of 6 pb^{-1}.

The solid line in Figure 24 is the result of a simultaneous fit to the measured distribution, with the three peak positions fixed at their expected values, and the common resolution function $\sigma(\Delta M)$. The resolution in $\sigma(\Delta M)$ is expected to increase with increasing ΔM, and was empirically parameterised as $\sigma(\Delta M) = a \cdot \Delta M + b$. The dashed lines show the shapes of individual peaks and of the background continuum. The fit parameters are the heights of the three gaussian peaks h_0, h_1, h_2, the constants a and b, and the three parameters describing the smooth polynomial background. The systematic studies include the variation of the background parameterisation and the introduction of a mass shift common for the three resonances. The true amplitudes of the peaks (15, 123 and 87, respectively) are reproduced reasonably well:

$$\begin{aligned} h_0 &= 15 \pm 3(\text{stat.}) \pm 10(\text{syst.}), \\ h_1 &= 101 \pm 4(\text{stat.}) \pm 12(\text{syst.}), \\ h_2 &= 103 \pm 4(\text{stat.}) \pm 9(\text{syst.}), \end{aligned} \tag{4}$$

with a strong negative correlation between the last two. The resolution is found to increase from about 35 MeV at χ_0 to about 48 MeV at χ_2, while the overall reconstruction efficiency of χ_c states is estimated to be about 4%. It may be possible to significantly improve the resolution by using photon conversions, but this is unlikely to yield a big increase in efficiency.

The procedure of reconstructing χ_b decays into $\Upsilon + \gamma$ is the same as in the charmonium case, except the di-muon pair is required to be an Υ candidate. However, the higher di-muon mass and hence smaller expected boost makes the photon much softer and hence more difficult to detect. With the available simulated statistics (50 000 events corresponding to 10 pb^{-1}), only 20 χ_b candidates have been found in the appropriate mass window, which gives an efficiency estimate of 0.03%. In order to reliably observe $\chi_b \to \Upsilon + \gamma$ decays, an integrated luminosity of at least 1 fb^{-1} will be needed.

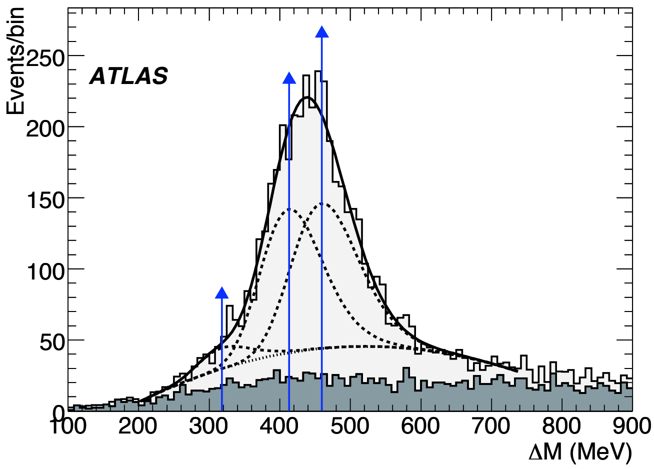

Figure 24: Difference in invariant masses of $\mu\mu\gamma$ and $\mu\mu$ systems in prompt J/ψ events (light grey) with $bb \to \mu6\mu4X$ background surviving cuts (dark grey). The arrows represent the true signal peak positions, and the lines show the results of the fit described in the text. Event yields correspond to an integrated luminosity of 10 pb^{-1}.

5.2 Analysis of $\chi_b \to J/\psi J/\psi$

Another possibility for measuring χ_b production is through the decay $\chi_b \to J/\psi J/\psi \to \mu\mu\mu\mu$. The use of this decay for χ_b detection was proposed in [16], while in [17] the corresponding branching fraction was calculated to be $Br(\chi_{b0} \to J/\psi\ J/\psi) = 2 \times 10^{-4}$.

The predicted total inclusive cross-section of χ_{b0} production at LHC is estimated at around 1.5 μb [17], yielding the following theoretical estimate (without any momentum cuts on muons):

$$\sigma(pp \to \chi_{b0} + X) Br(\chi_{b0} \to J/\psi\ J/\psi) = 330\,\text{pb} \tag{5}$$

We use this cross-section in our study. It should, however, be considered as a lower bound, with higher order QCD corrections expected to increase it significantly, especially within the COM approach. This cross-section also does not include other C-even states (η_b, χ_{b2} and radial excitations), meaning that the overall combined cross-section of resonant $J/\psi\ J/\psi$ production in the Υ mass region can be at least an order of magnitude higher.

The PYTHIA Monte Carlo generator, used to simulate this process, was modified to include this particular decay. Events for this study are triggered with a di-muon trigger $\mu6\mu4$, as for the J/ψ and Υ di-muon analysis. Out of 50 000 generated $\chi_b \to J/\psi(\mu\mu)J/\psi(\mu\mu)$ events 815, or 1.6%, passed the $\mu6\mu4$ trigger cuts. Taking into account di-muon branching fractions of the two J/ψ mesons, this corresponds to the cross-section $\sigma = 20$ fb after trigger.

The two triggered muons have the highest p_T of the four. The two remaining muons, in many cases, have transverse momenta too low to be identified as muons (i.e. below 2.5 GeV), and sometimes too low to be even reconstructed (below 0.5 GeV).

Two classes of events, remaining after the trigger cuts, have been considered to be useful:

a) events where the two trigger muons came from the same J/ψ . Then, the third muon has to be identified by the muon system, while the fourth must at least be reconstructed as a track (124 events);

b) events where each trigger muon came from a different J/ψ . The remaining two muons may or may not be identified, but their tracks still need to be reconstructed (330 events).

Thus, taking the trigger, muon identification and track reconstruction efficiencies into account, one expects about 50% of triggered $\chi_b \to J/\psi(\mu\mu)J/\psi(\mu\mu)$ decays to be observed, which amounts to 0.8% of the generated sample, corresponding to the cross-section of 10 fb. Hence, the observed statistics is expected to be around 100 events for the integrated luminosity 10 fb^{-1}.

Once the two J/ψ candidates in the event have been reconstructed, a simultaneous fit of the four muon tracks to the common vertex is performed, with J/ψ mass constraints applied to the respective di-muon invariant masses. The resulting distribution is presented in Figure 25(a). The resolution on the χ_b

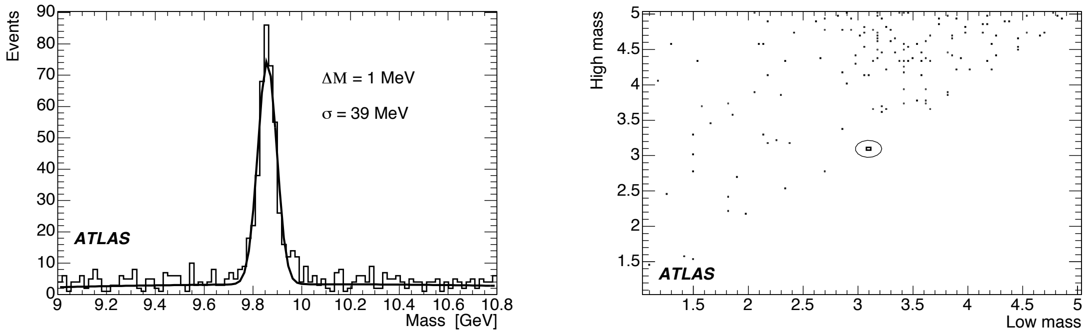

(a)

(b)

Figure 25: (a) Reconstructed χ_b invariant mass, with J/ψ mass constraints applied on the respective di-muon pair masses. (b) Higher di-muon invariant mass plotted versus the lower di-muon invariant mass in $\chi_b \to J/\psi(\mu\mu)J/\psi(\mu\mu)$ events.

mass is estimated to be as good as 40 MeV. Similar resolution should be expected for the reconstructed invariant mass in the decays of other χ_{bJ} states, while the resolution for $\eta_b \to J/\psi(\mu\mu)J/\psi(\mu\mu)$ should be slightly better.

With two pairs of muons in each signal event, there are two possible pairings of oppositely charged muons. The plot of the invariant mass of one di-muon pair versus the invariant mass of the other is shown in Figure 25(b), using generator-level information. All correct pairings, and none of the incorrect pairings of di-muons fall within the circle of radius 200 MeV (about 3-4 σ) from the point with coordinates $M_{J/\psi}, M_{J/\psi}$. The incorrect pairings are scattered over the whole area, so by selecting the pairings from the circle defined above, the combinatorial background can be strongly reduced.

The main expected sources of background to $\chi_b \to J/\psi(\mu\mu)J/\psi(\mu\mu)$ decays are the processes of bottom quark production, $pp \to b\bar{b}X$, with each b either decaying into $J/\psi + X$, or into a muon with additional charged tracks. These backgrounds have been analysed with the same Monte Carlo samples used in our study of backgrounds for single J/ψ and Υ production. Within the available statistics, very few background events have survived the signal selection cuts described above, and the background suppression cuts on pseudo-proper time on secondary vertices. Extrapolating these results to the integrated luminosity of 10 fb^{-1} shows that the statistically significant $\chi_b \to J/\psi(\mu\mu)J/\psi(\mu\mu)$ signal peak (or peaks) should be visible on top of the combinatorial continuum, with the expected signal-to-background ratio of 10-20% or above.

In short, so far we have seen no major obstacles in an attempt to search for narrow resonances in the $J/\psi(\mu\mu)J/\psi(\mu\mu)$ invariant mass distributions. However, dedicated high statistics Monte Carlo samples are needed to draw more reliable conclusions.

6 Physics reach with early data

During the initial run of the LHC, the integrated luminosity of 1 pb^{-1} with the $\mu6\mu4$ trigger would mean about 15 000 $J/\psi \to \mu\mu$ and 2 500 $\Upsilon \to \mu\mu$ recorded events. If the $\mu4\mu4$ trigger is used, these numbers would increase up to 17 000 and 20 000 respectively, with these additional events mainly concentrated at the lower end of the quarkonium transverse momenta.

Additional, largely independent statistics will be provided by the $\mu10$ trigger: 16 000 J/ψ and 2 000 Υ with transverse momenta above about 10 GeV, with distributions similar to those from the $\mu6\mu4$ samples. Quite separate from these, another 7 000 of $J/\psi \to \mu\mu$ events are expected from b-decay events. All these events should be perfectly usable for detector alignment, acceptance and trigger efficiency studies, as well as for understanding tracking and muon system performances.

At the integrated luminosity of about 10 pb^{-1} recorded numbers of $J/\psi \to \mu\mu$ and $\Upsilon \to \mu\mu$ will be roughly equal to the statistics used in this note. With these statistics, the p_T dependence of the cross-section for both J/ψ and Υ should be measured reasonably well, in a wide range of transverse momenta, $p_T \simeq 10-50$ GeV. The precision of J/ψ polarisation measurement can reach $0.02-0.06$ (depending on the level of polarisation itself), while the expected error on Υ polarisation is unlikely to be better than about 0.2. At this stage, first attempts may be made to understand the performance of the electromagnetic calorimetry at low photon energies, and to try and reconstruct χ_c states from their radiative decays.

With an integrated luminosity of 100 pb^{-1}, the transverse momentum spectra are expected to reach about 100 GeV and possibly beyond, for both J/ψ and Υ. With several million $J/\psi \to \mu\mu$ and more than 500 000 of $\Upsilon \to \mu\mu$ decays, and a good understanding of the detector, high precision polarisation measurements, at the level of few percent, should become possible for both J/ψ and Υ. $\chi_b \to \Upsilon\gamma$ decays could become observable, while other measurements mentioned above will become increasingly precise.

Further increase of the integrated luminosity should make it possible to observe the resonant production of J/ψ meson pairs in the mass range of the Υ system. During the future high luminosity running, the need to keep event rates manageable will mean an increase of thresholds of relevant single- and di-muon triggers, and the prescaling of lower threshold triggers. The higher luminosity will further expand the range of reachable transverse momenta and allow further tests of the production mechanisms, as well as make χ_b reconstruction easier.

References

[1] See e.g. V. G. Kartvelishvili, A. K. Likhoded, S. R. Slabospitsky, Sov. J. Nucl. Phys. **28** (1978) 280; M. Gluck, J. F. Owens and E. Reya, Phys. Rev. **D17** (1978) 2324; E. L. Berger and D. L. Jones, Phys. Rev. **D23** (1981) 1521; V. G. Kartvelishvili, A. K. Likhoded, Sov. J. Nucl. Phys. **39** (1984) 298; B. Humpert, Phys. Lett. **B184** (1987) 105.

[2] F. Abe *et al*. [CDF Collaboration], Phys. Rev. Lett. **69** (1992) 3704.

[3] M. Kramer, Prog. Part. Nucl. Phys. **47** (2001) 141 [arXiv:hep-ph/0106120].

[4] V. M. Abazov *et al*. [DØCollaboration], DØ Note 5089-conf.

[5] G. T. Bodwin, E. Braaten and G. P. Lepage, Phys. Rev. **D51** (1995) 1125 [Erratum-ibid. **D55** (1997) 5853] [arXiv:hep-ph/9407339]; E. Braaten and S. Fleming, Phys. Rev. Lett. **74** (1995) 3327 [arXiv:hep-ph/9411365].

[6] S. P. Baranov, Phys. Rev. **D66** (2002) 114003.

[7] A. Abulencia *et al*. [CDF Collaboration], Phys. Rev. Lett. **99** (2007) 132001.

[8] J. P. Lansberg, J. R. Cudell and Yu. L. Kalinovsky, Phys. Lett. **B633** (2006) 301 [arXiv:hep-ph/0507060]; P. Artoisenet, J. P. Lansberg and F. Maltoni, Phys. Lett. **B653** (2007) 60.

[9] T. Sjostrand, S. Mrenna and P. Skands, PYTHIA *6.4: Physics and manual*, JHEP **0605** (2006) 026 [arXiv:hep-ph/0603175].

[10] P. Nason *et al*., *Bottom production*, in CERN report 2000-004 [arXiv:hep-ph/0003142].

[11] ATLAS Collaboration, *Triggering on Low-p_T Muons and Di-Muons for B-Physics*, this volume.

[12] F. Abe *et al*. [CDF Collaboration], Phys. Rev. Lett. **79** (1997) 572; D. E. Acosta *et al*. [CDF Collaboration], Phys. Rev. Lett. **88** (2002) 161802.

[13] W.-M. Yao *et al*., Journal of Physics **G33** (2006) 1.

[14] ATLAS Collaboration, *The ATLAS Experiment at the CERN Large Hadron Collider*, JINST 3 (2008) S08003.

[15] D. E. Acosta *et al*. [CDF Collaboration], Phys. Rev. Lett. **96** (2006) 202001 [arXiv:hep-ex/0508022].

[16] V. G. Kartvelishvili and A. K. Likhoded, Yad. Fiz. **40** (1984) 1273.

[17] V. V. Braguta, A. K. Likhoded and A. V. Luchinsky, Phys. Rev. **D72** (2005) 094018 [arXiv:hep-ph/0506009].

Production Cross-Section Measurements and Study of the Properties of the Exclusive $B^+ \to J/\psi K^+$ Channel

Abstract

In the initial phase of the LHC operation at low luminosity several Standard Model physics analyses will be performed in order to validate the ATLAS detector and trigger system. The $B^+ \to J/\psi K^+$ channel can be observed with the first ATLAS data at LHC and can be used for detector performance studies. This channel will provide a reference in the search for rare B decays. It will also be used to estimate the systematic uncertainties and efficiencies of flavor tagging algorithms, needed for CP violation measurements. The prospects to measure the B^+ mass, its total and differential production cross sections and lifetime with the first ATLAS data, are described in this note.

1 Introduction

The expected large hadronic cross-section for b-quark production and the high luminosity at the LHC leads to copious b-quark production, with the presence of a $b\bar{b}$ pair in about one percent of the collisions. Quantitatively, the expected inclusive production cross-section for $pp \to b\bar{b} + X$ at LHC is estimated to be $\sigma_{b\bar{b}} \approx 500\ \mu$b leading to more than 10^5 $b\bar{b}$ pairs per second at the LHC design luminosity of $\mathscr{L} \approx 10^{33}$ cm^{-2}s^{-1}. However, the extrapolation of the $b\bar{b}$ cross-section measurement from the Tevatron energy of 1.8–1.96 TeV [1, 2] to the LHC energy of 14 TeV suffers from large uncertainties. The theoretical predictions are based on NLO QCD calculations with uncertainties smaller than 20 % [3] in the kinematical region of the LHC, originating mainly from scale uncertainties [4], as well as uncertainties due to the parton density functions and the b-fragmentation.

A precise measurement of the $b\bar{b}$ inclusive cross-section at the LHC can be used to constrain these theoretical uncertainties. In addition, the large production rate allows for exclusive cross-section measurements shortly after the LHC start up, which have different systematic uncertainties and model dependencies (fragmentation models) from the inclusive ones. Furthermore, the $b\bar{b}$ represents the largest physics background for many processes, therefore its measurement is a prerequisite to any discovery.

In this note the exclusive channel $B^+ \to J/\psi K^+$ is studied extensively and the procedure to measure the differential and total cross-sections with the first 10 pb^{-1} is presented, with event selection based on the identification of the J/ψ decay to two muons.

The exclusive $B^+ \to J/\psi K^+$ decay can be measured during the initial luminosity phase of the LHC, because of the clear event topology and rather large branching ratio. It can serve as a reference channel for rare B decay searches, whose total and differential cross-sections will be measured relative to its cross-section, thus allowing the cancelation of common systematic uncertainties. Furthermore, it can be used to estimate the systematic uncertainties and efficiencies of flavour tagging algorithms, which are needed for CP violation measurements. Finally, the relatively large statistics for this decay allow for initial detector performance studies. In particular, the precise measurement of the well-known mass and lifetime [5] can be used for inner detector calibration and alignment studies.

In Section 2 of the note the Monte Carlo data sets used for this study are described. In Section 3 the J/ψ selection procedure is presented. The $B^+ \to J/\psi K^+$ mass, cross-section and lifetime measurements can be found in Section 4. The expected statistics during the early LHC luminosity phase are discussed in Section 5 together with estimates of the systematic uncertainties.

All the following studies have been done for luminosity of $\mathscr{L} = 10^{32}$ cm^{-2}s^{-1}. However, since pile-up does not play any role at this luminosity, it is straightforward to rescale the results of these studies to $\mathscr{L} = 10^{31}$ cm^{2}s^{-1}, in case this will be the luminosity at startup.

2 Monte Carlo Samples

All Monte Carlo (MC) data sets used for the studies presented in this note have been produced using PYTHIA-6.4 [6] without overlaying pileup events.

Process	N_{gen}	$\mathscr{L}$ [pb^{-1}]	$N_{\text{gen}}(B^+ \to J/\psi K^+)$
$b\bar{b} \to J/\psi(\mu6\mu4) + X$	145 500	13.2	7 072

Table 1: Monte Carlo data set used for the B^+ study. The $N_{\text{gen}}(B^+ \to J/\psi K^+)$ events are the ones contained in the whole generated sample.

At the generator level, the ATLAS specific PYTHIA implementation for B-physics which provides an interface to PYTHIA-6 [7] was used. The study of the $B^+ \to J/\psi K^+$ channel is done using the inclusive production cross-section of $\sigma(b\bar{b} \to J/\psi(\mu6\mu4)X)$, where the numbers in the bracket denote the cuts applied on the muons from the J/ψ decay in order for the generated event to be accepted (one muon with $p_T > 6$ GeV and the other with $p_T > 4$ GeV). The cross-section at the generation level, after implementing these cuts to the muons from the J/ψ decay is 11.1 nb. The total number of generated events and the number of the $B^+ \to J/\psi K^+$ decays found in the sample are given in Table 1. All efficiencies presented in this note, are calculated relative to the generated number of events.

3 J/ψ Identification Procedure

A reliable identification of the J/ψ meson in the decay channel $J/\psi \to \mu^+\mu^-$, as well as the reconstruction of the primary and secondary vertices, are the prerequisites for the $B^+ \to J/\psi K^+$cross-section measurement. For the selection of the B^+ candidates a further requirement of a positively charged track (K^+) originating from the J/ψ secondary vertex is imposed.

The distance $\vec{x}$ between the pp interaction vertex and the secondary vertex of the B-decay in the transverse plane is used for the J/ψ identification. In the ATLAS Inner Detector TDR [8], the determination of the position of the primary vertex on an event-by-event basis was demonstrated, and for the $B^+ \to J/\psi K^+$ decay, a vertex resolution of $\sigma_x = 29$ μm and $\sigma_y = 27$ μm was estimated. For up-to-date information on the average primary vertex resolution with the staged ATLAS detector see [9].

The vector $\vec{x} = \vec{x}_{\text{prim}} - \vec{x}_B$ from the primary vertex $\vec{x}_{\text{prim}}$ to the secondary B-decay vertex $\vec{x}_B$ in the plane normal to the incoming proton beam [10] is used to define the transverse decay length L_{xy}, which is actually the projection of $\vec{x}$ onto the direction of the transverse momentum of the B meson:

$$L_{xy} = \frac{\vec{x} \cdot \vec{p}_T}{|p_T|}. \tag{1}$$

The transverse decay length L_{xy} is a signed variable, which is negative if the particle appears to decay before the secondary vertex of its production and positive otherwise. For a zero lifetime sample, a Gaussian distribution peaked at $L_{xy} = 0$ is expected. For exclusive decays, the proper decay length is given by:

$$\lambda = L_{xy} \cdot \frac{m_B}{p_T^B}. \tag{2}$$

For the uncertainty of the transverse decay length L_{xy}, only the contribution arising from the uncertainties on the primary and secondary vertex coordinates are taken into account:

$$\sigma_{L_{xy}}^2 = \frac{1}{(p_T^B)^2} \cdot \left(\sigma_x^2 (p_x^B)^2 + 2\sigma_{xy}^2 p_x^B p_y^B + \sigma_y^2 (p_y^B)^2 + \sigma_{x1}^2 (p_x^B)^2 + \sigma_{y1}^2 (p_y^B)^2 \right), \tag{3}$$

where σ_x, σ_{xy}, and σ_y are the covariance matrix elements of the secondary vertex fit, σ_{x1} is the resolution of the primary vertex in x, σ_{y1} is the resolution of the primary vertex in y, p_T^B is the transverse momentum of the B^+ meson and finally p_x and p_y are the x and y components of B^+ momentum.

Since the J/ψ reconstruction relies on its decay into two muons: $J/\psi \rightarrow \mu^+\mu^-$, the first step in the event selection procedure is the identification of the decay muons, which in general have low p_T.

If a muon track reconstructed by the muon spectrometer has an inner detector track associated to it, it is considered to be a muon and is used to form the J/ψ candidate. An inner detector track may also be declared a muon candidate and used in the J/ψ mass reconstruction, if it is has hits or track segments in the innermost stations of the muon spectrometer. In either case the J/ψ mass is calculated using the momentum of the muon candidate provided by the inner detector, in order to exploit the better momentum resolution of the inner detector in this p_T region. The main J/ψ selection cuts are as follows:

- All possible di-muons with $p_{T,1} \geq 3.0$ GeV and $p_{T,2} \geq 6.0$ GeV are formed;
- The tracks of each muon pair are then fitted to a common vertex;
- From the vertices found, only the ones with $\chi^2/\text{ndf} < 10$ are retained;
- To select J/ψ mesons originating from the decay of a B^+, a cut on the proper decay length, $\lambda > 0.1$ mm, is imposed to reduce combinatorial background from prompt J/ψ. If this cut is not imposed, the algorithm identifies all possible combinations consistent with J/ψ decaying to muons in the event;
- J/ψ candidates inside a mass window of 120 MeV around $m_{J/\psi}$ are retained.

The efficiency for all previously mentioned cuts is presented in Table 2, where the efficiency after each cut is computed with respect to the previous.

Given that the sample used does not contain any prompt J/ψ, the effect of the cut on the proper decay length λ in the table indicates the loss in signal events. As it is explained in the following section, this cut is not applied for the lifetime measurement. The J/ψ reconstruction efficiency is also given for the case of no cut on the J/ψ proper decay length λ.

The J/ψ invariant mass distribution without a cut on λ is shown in Figure 1. The shape can be described by a Gaussian with exponential tails. The J/ψ mass and its resolution, obtained from a Gaussian fit, is 3098 MeV and 57.4 MeV respectively.

cut	with λ cut		no λ cut	
J/ψ cut	$N_{J/\psi}$	$\varepsilon_{J/\psi}$ [%]	$N_{J/\psi}$	$\varepsilon_{J/\psi}$ [%]
after vertexing	123 489	84.8	123 489	84.8
after vtx χ^2 cut	115 156	93.3	115 156	93.3
after λ cut	84 829	73.6	-	-
after mass cut	81 293	95.8	105 827	91.9
Total eff		55.8		72.7

Table 2: J/ψ reconstruction efficiencies with and without λ cut.

In order to study the effect of misalignment, displaced magnetic field and incorrect material map on the J/ψ observed mass position and resolution, a systematic study using different ATLAS geometry configurations was performed, with different combinations of possible misalignments of the calorimeter and the muon spectrometer, as well as a displaced magnetic field map and distorted material in the inner

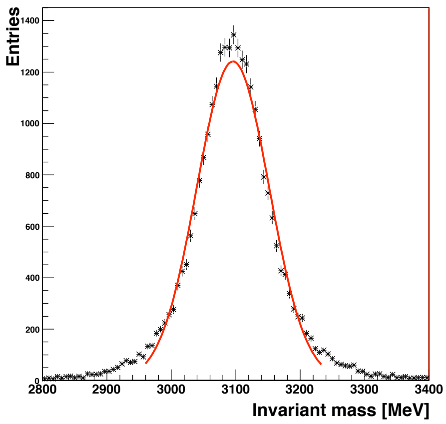

Figure 1: J/ψ invariant mass distribution with a Gaussian fit superimposed.

detector and the calorimeter. These studies were performed using a dedicated $B_s^0 \to J/\psi\phi$ dataset. It was found that the width of the J/ψ mass fit $\sigma(m_{J/\psi})$ is rather stable, varying between 51 and 59 MeV.

The trigger efficiency is about 99 % and was computed from the J/ψ candidates that have at least one muon with $p_T > 6$ GeV in the trigger. This is expected, since at the generation level it is required that both muons from the J/ψ have $p_T > 6$ GeV and $p_T > 4$ GeV.

4 Analysis of the $B^+ \to J/\psi K^+$ Channel

The analysis that follows for the selection of B^+ events can equally well be applied for the charge conjugate state. Negligible direct CP violation is expected in the $B^\pm \to J/\psi K^\pm$ because for $b \to c + \bar{c}s$ transitions the standard model predicts that the leading and higher order diagrams are characterized by the same weak phase. A measurement of the asymmetry is given in [11]. The main source of asymmetry is the different interaction probabilities for K^+ and K^- with the detector material. Other non-CP-violating sources of asymmetry are expected to lead to a lepton energy asymmetry and estimated to be negligible [12].

4.1 Event selection

The B^+ mesons are reconstructed from a J/ψ and a K^+ candidate. The J/ψ selection is described in Section 3 and the K^+ candidates are identified using information from the inner detector. Specifically, the procedure comprises the following steps:

- The original collection of tracks is scanned once again (excluding those already denoted as muons) and those with $p_T > 1.5$ GeV and $|\eta| < 2.7$ are retained;
- From this collection, the tracks with positive charge and inconsistent with coming from the primary vertex at one standard deviation level ($|d_0|/\sigma_{d_0} > 1$, where d_0 is the impact parameter of the track) are considered to be K^+ candidates;
- The $\mu^+\mu^-$ pair considered to be originating from the $J/\psi \to \mu^+\mu^-$ decay and the K^+ candidate are fitted to a common vertex. The vector defined by the sum of the J/ψ and K^+ momentum vectors is required to point to the primary vertex, and the two muon tracks are constrained to $m_{J/\psi}$;

- Only combinations with vertex $\chi^2/\mathrm{ndf} < 6$, $p_T(\mu) > 5$ GeV and $\lambda > 0.1$ mm are retained;
- In case that more than two B^+ candidates were found in the same event, the one with the smallest vertex χ^2/ndf is accepted.

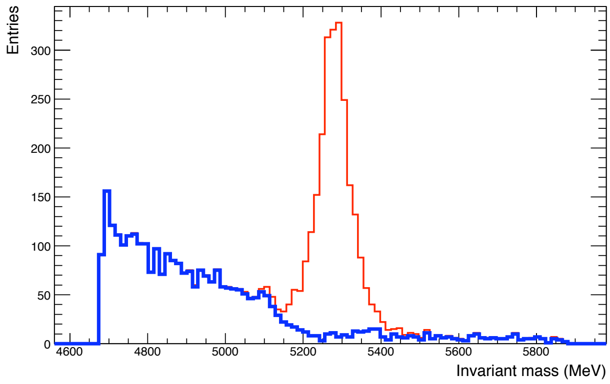

Figure 2: Invariant mass $M(K^+\mu^+\mu^-)$ distribution with the B^+ mass peak for signal (red) and combinatorial $b\bar{b}$ -background (blue).

4.2 Mass fit

The B^+ mass determination has been performed using the sample of $b\bar{b} \to J/\psi X$ decays. The B^+ invariant mass distribution $m(K^+\mu^+\mu^-)$ of the candidates fulfilling all cuts is presented in Fig. 2. In the same figure the signal and background events can be seen separately, where the distinction between them is made using the Monte Carlo truth information. The fit to the mass distribution is done by using the maximum-likelihood method, where the probability density function is a Gaussian for the signal region and a linear function for the background:

$$
\begin{aligned}
L &= \alpha f_{\mathrm{sig}} + (1-\alpha) f_{\mathrm{bkg}} \\
f_{\mathrm{sig}} &= \frac{1}{\sqrt{2\pi}\sigma} e^{-\frac{1}{2}\left(\frac{m_i - m}{\sigma}\right)^2} , \\
f_{\mathrm{bkg}} &= b\left(m_i - \frac{w}{2}\right) + \frac{1}{w} ,
\end{aligned}
\tag{4}
$$

where α is the fraction of signal events in the fitted region, m the B^+ mass, b is the slope of the background distribution and w defines the range of the fit. The mass range of the fit is taken from 5.15 GeV to 5.8 GeV. This is done in order to reduce contributions from partially reconstructed B meson decays that populate the left side of Fig. 2. The background at the right of the mass peak originates from misidentified π^+ from $B^+ \to J/\psi\pi^+$ decays.

The result of the B^+ mass fit is: $M(B^+) = (5279.3 \pm 1.1)$ MeV with a width of $\sigma(B^+) = (42.2 \pm 1.3)$ MeV. The relative errors scaled properly for an integrated luminosity of $10\ \mathrm{pb}^{-1}$ are about 0.02% and 3.5% respectively. The corresponding fit is presented in Fig. 3. The slight shoulder to the left of the mass distribution is due to the background shape.

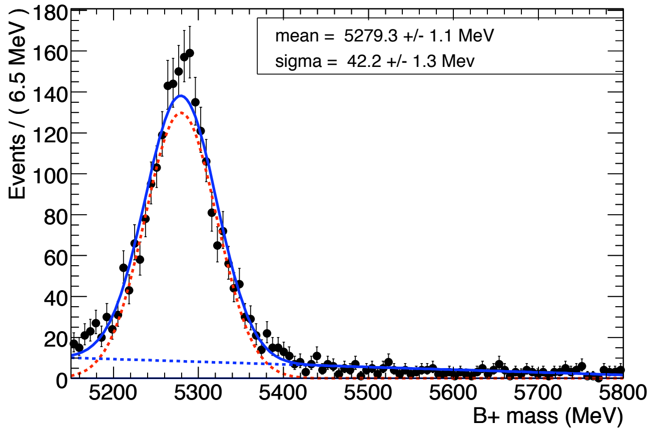

Figure 3: B^+ mass fit with the both signal (red) and background (blue) contributions shown separately.

4.3 Differential and total production cross-section

The feasibility of the measurement of the $B^+ \to J/\psi K^+$ total and differential production cross-sections at LHC, with the first 10 pb^{-1}, is explored in this section. The dataset used is the $b\bar{b} \to J/\psi X$ and the reconstructed $B^+ \to J/\psi K^+$ candidates were selected based on the event selection described in Section 4.1. The B^+ mass fit method described previously was then used to extract the efficiencies in bins of p_T as well as the total efficiency.

The differential cross-section $d\sigma/d\,p_T$ can be obtained from:

$$\frac{d\sigma(B^+)}{d\,p_T} = \frac{N_{\text{sig}}}{\Delta p_T \cdot \mathscr{L} \cdot \mathscr{A} \cdot \text{BR}} \tag{5}$$

where N_{sig} is the number of reconstructed B^+ mesons obtained from the mass fit. The size of the p_T bin is denoted with Δp_T. Furthermore, $\mathscr{L}$ is the total luminosity and $\mathscr{A}$ the overall efficiency. The branching ratio BR is the product of the world average [5] branching ratios of $\text{BR}(B^+ \to J/\psi K^+) = (10.0 \pm 1.0) \times 10^{-4}$ and $\text{BR}(J/\psi \to \mu^+\mu^-) = (5.88 \pm 0.10) \times 10^{-2}$. The invariant mass spectra of the B^+ candidates are fitted in each p_T range using an extended unbinned maximum likelihood fit. The probability density function is a Gaussian for the signal and a linear function for the background region:

$$L = \frac{N_{\text{sig}}}{N_{\text{total}}} \cdot f_{\text{sig}} + \frac{N_{\text{total}} - N_{\text{sig}}}{N_{\text{total}}} \cdot f_{\text{bkg}} \tag{6}$$

where f_{sig} and f_{bkg} are the fit functions as described in Equation 4. For this fit, the B^+ mass has been fixed to the value obtained from the mass fit in the previous Section 4.2, $m = 5279.3$ MeV. The results for the overall efficiencies and the mass widths of the fits, for the individual p_T bins, are summarized in Table 3. The mass fits in the various p_T regions are presented in Figure 4 whereas the fit over the full p_T range is shown in Fig. 3.

To measure the B^+ total cross-section a similar procedure to the one used for the calculation of the differential cross-section is followed, but in this case all B^+ with $p_T > 10$ GeV are used to calculate the total efficiency $\mathscr{A}$. The B^+ mass distribution is shown in Fig. 3. The results of the total efficiency and the mass width from the fit, for the B^+ total cross-section measurement, are presented in Table 4.

p_T range [GeV]	$p_T \in [10,18]$	$p_T \in [18,26]$	$p_T \in [26,34]$	$p_T \in [34,42]$
$\mathscr{A}$ [%]	20.1±1.0	37.3±1.7	45.0±3.1	51.6±4.7
$\sigma(B^+)$ [MeV]	38.5±2.0	42.3±2.1	46.1±3.2	46.6±4.0

Table 3: Efficiency $\mathscr{A}$ and B^+ mass width $\sigma(B^+)$ for the various p_T bins.

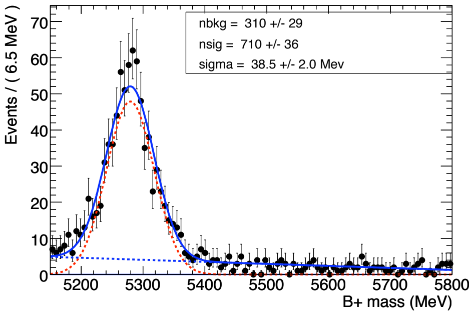

(a) $10 \leq p_T < 18$ GeV

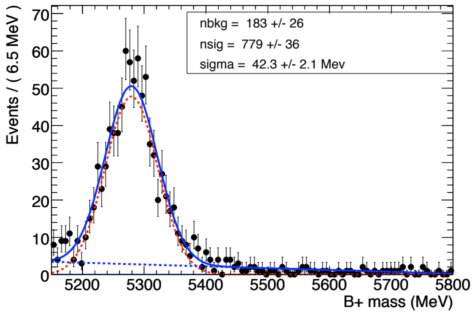

(b) $18 \leq p_T < 26$ GeV

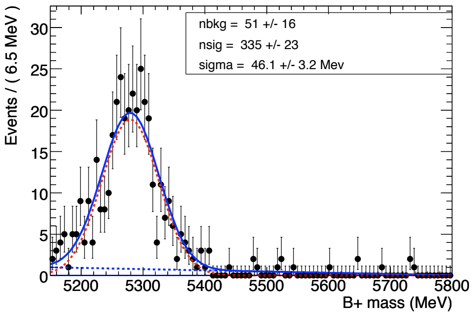

(c) $26 \leq p_T < 34$ GeV

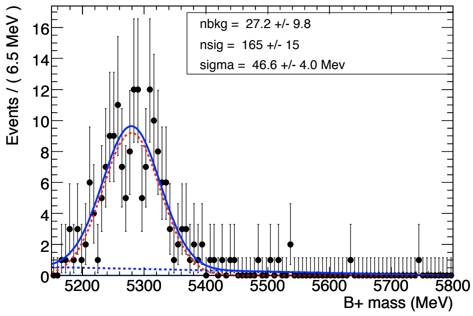

(d) $34 \leq p_T < 42$ GeV

Figure 4: Fit of the B^+ mass in various p_T ranges: $p_T \in [10,18]$ GeV (a), $p_T \in [18,26]$ GeV (b), $p_T \in [26,34]$ GeV (c), $p_T \in [34,42]$ GeV (d).

total cross-section	
$\mathscr{A}$ [%]	29.8±0.8
$\sigma(B^+)$ [MeV]	42.2±1.3

Table 4: Overall efficiency and B^+ mass width for all B^+ with $p_T > 10$ GeV.

4.4 Lifetime measurement

The measurement of the lifetime τ of the selected B^+ candidates is a sensitive tool to confirm the beauty contents in a sample, in particular the number of the reconstructed $B^+ \to J/\psi K^+$ decays obtained in the $b\bar{b} \to J/\psi X$ dataset. The proper decay time is defined as $t = \lambda/c$. For this analysis, no cut on the proper decay length λ (Equation 2) of the J/ψ candidate or the B^+ candidate should be applied.

The proper decay time distribution in the signal region $B^+ \to J/\psi K^+$ can be parametrised as a convolution of an exponential function with a Gaussian resolution function, while the background distribution parametrisation consists of two different exponential functions, where each is convoluted with a Gaussian resolution function. In the $b\bar{b} \to J/\psi X$ no additional zero lifetime events are expected because there are no prompt J/ψ produced. In the realistic case, where zero lifetime events will be present, an extra Gaussian centered at zero is needed in order to properly describe those events. With the model used here, the Gaussian resolution functions depend on the reconstructed uncertainties on an event-by-event basis. In addition, it is assumed, that the distribution of the uncertainties per event are different for the signal and the corresponding background probability density functions (pdf) [13]. The use of conditional pdfs was required in order to take into account the proper decay time error per event. The exponential part of the lifetime distribution has the usual form:

$$F_t(t) = e^{\frac{-t}{\tau}}, \tag{7}$$

where t is the proper decay time and τ is the lifetime. Accordingly, the convoluted function is then

$$F_c(t) = e^{\frac{-t}{\tau}} \otimes G(t, \mu, s \cdot \sigma_i), \tag{8}$$

where μ is the mean value of the Gaussian resolution function which parametrises the average bias in each proper decay time measurement. The scale factor of the error is s and σ_i is the per event proper decay time error. The conditional pdf on the per event uncertainty is then:

$$F_t(t) = F_c(t|\sigma_i) \cdot P(\sigma_i), \tag{9}$$

where $P(\sigma_i)$ is the distribution of the proper decay time error. The distribution of the proper decay time uncertainty is approximated by a superposition of Gaussian functions. In order to separate between the signal and the background, the proper decay time pdf is multiplied with the B^+ mass pdf, described in Section 4.2. A two-dimensional fit to the B^+ proper decay time and B^+ mass is then performed.

The results of the lifetime fit are presented in Table 5 and shown in Figure 5. The background can be best described with the two lifetime components (τ_1 and τ_2) which are also shown in Table 5. For the events in the mass region of the signal within $M(B^+) \in [5.15, 5.8]$ GeV the proper decay time found from the decay length is compared to the generated B^+ lifetime. The result of the comparison is shown in Fig. 5. The differences are well centered at zero with a Gaussian distribution and sigma 0.088 ps. It should be noted that the resolution as well as its σ in η bins of 0.25 is found to be independent of η.

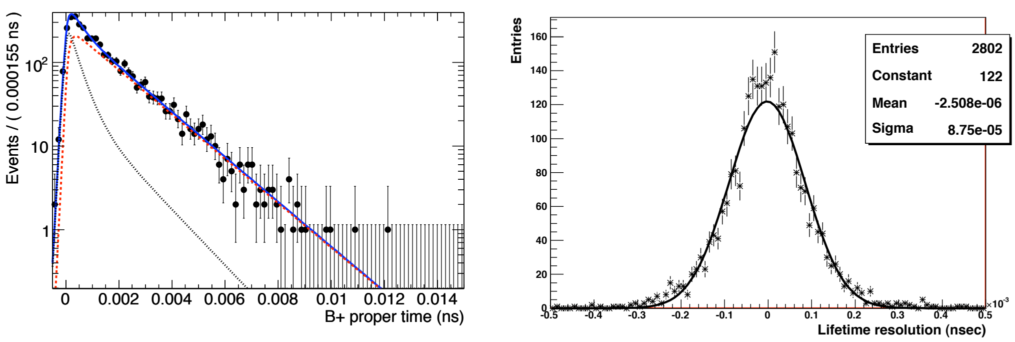

Figure 5: B^+ lifetime fit (left) with the signal (dashed red) and the background (dashed black) contributions shown separately and B^+ lifetime resolution (right).

Signal lifetime τ [ps]	1.637±0.036
BG lifetime τ_1 [ps]	1.320±0.24
BG lifetime τ_2 [ps]	0.370±0.067

Table 5: Results for the lifetime fit.

5 Statistical and Systematic Uncertainties

From the analysis presented above, the expected number of reconstructed B^+ candidates amounts to 160 per pb^{-1} . This implies that sufficient statistics can be collected for a reliable cross-section measurement, after just a few months of data taking at the initial low luminosity phase of the LHC. This scenario is valid for a luminosity less than $\mathscr{L} = 10^{32}$ cm^{-2}s^{-1}, since the analysis was performed without pileup events and contains no special trigger requirements or prescaling other than a single muon with $p_T^\mu > 6$ GeV at level-1.

For the measurements presented in this note the main sources of systematic uncertainties are the same. The uncertainty from the luminosity in the initial phase is estimated to be 10 % and will be reduced to about 6.5 % after 0.3 fb^{-1} of data. The uncertainty from the PDF's is estimated to be 3 %, while the scale uncertainty of the NLO calculations is about 5 %. Finally, the uncertainty originating from the muon identification is about 3 %. Assuming Gaussian distributions for the above mentioned uncertainties, the total systematic uncertainty of the signal varies from 9.2 % to 12 % and is dominated by the uncertainty in the luminosity.

Given that a statistical precision of $\mathscr{O}(1\ \%)$ will be reached with an integrated luminosity of 0.1 fb^{-1}, the contribution of the systematics will dominate the uncertainties of the first measurements. This is the case even for the differential cross-section measurement. Although the statistics in each p_T bin is limited, the total uncertainty is dominated by the systematic uncertainties in the branching ratio of the $B^+ \to J/\psi K^+$ and in the luminosity, which are of the same order. For the exclusive cross-section measurement in the $B^+ \to J/\psi K^+$ channel, the relative uncertainties of the differential and total cross-sections are given in Table 6. Therein, the first row of the table contains the quadratic sum of the statistical uncertainty corresponding to an integrated luminosity of 0.01 fb^{-1} and the uncertainty in the efficiency. The latter is based on the statistics of the Monte Carlo dataset used. The second row is calculated by adding in quadrature the above uncertainty to the systematic uncertainty of the luminosity and the branching ratio for every p_T bin.

For the high statistics p_T bins as well as for the total cross-section, the total relative uncertainty is dominated by systematic errors, originating mainly from the uncertainty in the luminosity, which is assumed to be 10 % for the initial phase, and the 10 % uncertainty in the branching ratio of $B^+ \to J/\psi K^+$. The effect of the assumed background shape on the measurements is estimated to be less than 1 %. Finally, the precision of the lifetime measurement, for the same integrated luminosity is 2.5 %, where no systematic effects are taken into account.

p_T range [GeV]	$p_T \in [10,18]$	$p_T \in [18,26]$	$p_T \in [26,34]$	$p_T \in [34,42]$	$p_T \in [10,\inf)$
stat. + $\mathscr{A}$ [%]	7.7	6.9	10.5	13.9	4.3
total [%]	16.1	15.8	17.6	19.8	14.8

Table 6: Statistical and total uncertainties for the $B^+ \to J/\psi K^+$ differential and total cross-section measurements for an integrated luminosity of 0.01 fb^{-1}. Total uncertainties include luminosity and BR systematic uncertainties.

6 Summary and Conclusions

In this note, the $B^+ \rightarrow J/\psi K^+$ channel using an inclusive $b\bar{b} \rightarrow J/\psi(\mu 6 \mu 4)X$ dataset has been studied by developing the J/ψ selection methods and understanding their efficiencies. A method for measuring the B^+ mass using a likelihood fit, in order to separate signal and background, is established. The B^+ selection efficiency $\mathscr{A}$, both in p_T bins and in the whole p_T region, needed for the calculation of the differential and total cross-sections from real data, is extracted with fit methods similar to those used in the B^+ mass measurement case. Finally a likelihood fit, which takes into account the per-event primary vertex error, is performed for the measurement of the B^+ lifetime.

The total $B^+ \rightarrow J/\psi K^+$ production cross-section can be measured with a statistical precision better than 5% with the first 10pb^{-1} of data. The differential cross-section with precision of the order of 10%. With the same statistics, adequate detector performance studies can be realised using the B^+ mass and lifetime measurements.

References

[1] F. Acosta et al., (CDF Collab.), Phys. Ref. D **71** (2005) 032001.

[2] S. Abbott et al., (D0 Collab.), Phys. Lett. B **487** (2000) 264.

[3] S. Alekhin et al., HERA and the LHC, Workshop Proceedings, Part B., CERN-2005-014, DESY-PROC-2005-01.

[4] S.P. Baranov and M. Smizanska, CERN-ATL-PHYS-98-133.

[5] W. -M. Yao et al, J. of Phys. G **33** (2006) 1.

[6] T. Sjostrand, S. Mrenna and P. Skands, JHEP **0605** (2006) 026.

[7] M. Smizanska,PythiaB an interface to Pythia6 dedicated to simulation of beauty events,ATL-COM-PHYS-2003-038, (2003).

[8] The ATLAS Collaboration, ATLAS Inner Detector Technical Design Report, /CERN/LHCC/97-16, (30 April 1997).

[9] The ATLAS Collaboration, The Expected Performance of the Inner Detector, this volume.

[10] F. Abe et al, Phys. Rev. D **55** (1998) 5382.

[11] B. Aubert et al, (BABAR Collab.), Phys. Rev. D **65** (2005) 091191.

[12] C. Schmidt and M. Peskin, Phys. Rev. Lett. **69** (1992) 410.

[13] G. Punzi, arXiv:physics/0401045v1 [physics.data-an], (2004).

Physics and Detector Performance Measurements with the Decays $B_s^0 \to J/\psi\phi$ and $B_d^0 \to J/\psi K^{0*}$ with Early Data

Abstract
The decay processes $B_d^0 \to J/\psi K^{0*}$ and $B_s^0 \to J/\psi\phi$ are expected to be observed in large numbers with the ATLAS experiment. During the early data taking period, with an integrated luminosity of around $\sim 10-150$ pb^{-1}, it will be possible to measure the masses and proper lifetimes for these decays with sufficient precision to allow them to be used for detector performance checks. Methods for the determination of the mass and lifetime when the performance of the detector and reconstruction software will not be fully understood are presented. A powerful simultaneous fitting technique is used. Understanding the potential for flavour tagging methods will be one of the important goals for B-physics with early data. The performance of the jet charge tagger for the self-calibrating decay, $B_d^0 \to J/\psi K^{0*}$, is presented. The implications for the jet charge tag in the $B_s^0 \to J/\psi\phi$ decay are also discussed.

1 Introduction

The decay $B_s^0 \to J/\psi\phi$ is one of the most promising channels at the LHC due to its rich physics potential. This will begin with the earliest data taken by ATLAS. Due to the high $b\bar{b}$ cross-section [1] and dedicated J/ψ trigger in ATLAS [2], large statistics data will be quickly accumulated. This will allow the channel to be used for basic measurements of the B mass and lifetime, which will provide a sensitive test of the understanding of the tracking system after only 150 pb^{-1} of data. After collecting only 1 fb^{-1} of data, ATLAS will begin to improve world precisions for these measurements. A similar analysis will also be performed for the channel $B_d^0 \to J/\psi K^{0*}$, where the expected statistics are higher by about a factor of 15.

The analysis methods to be used will evolve with increasing statistics and understanding of the detector and backgrounds. This paper concentrates on the early phase of data taking. More advanced studies of the angular dependence of the decays and CP violation are not covered. In the very early data taking period, the low statistics will not allow an investigation of the full list of theoretical parameters, but rather will concentrate on the mass and lifetime. As the backgrounds will not be well understood either, no hard cuts will be made to reject them, but rather backgrounds topologically similar to the signal will be admitted. This will also reduce the dependence on reconstruction algorithms and trigger behaviour, neither of which will be thoroughly tested when ATLAS starts to take data. In particular, no secondary vertex displacement cuts will be applied, and the dominant background admitted will be from direct J/ψ production.

The simulation of the decays and their backgrounds is described in Section 2, and the reconstruction of the events in Section 3. The methods developed to extract the B hadron mass and lifetime as well as the precision expected to be reached with early data are described in Section 4. A study of the possibilities for flavour-tagging with early data, an important initial step for the CP violation measurements to be done later, is presented in Section 5.

2 Monte Carlo production

Table 1 lists the Monte Carlo data samples used in this study. The beauty events were generated by PYTHIA 6.4 [3] using a method described in [4]. For the direct J/ψ decays a special tuning of the

Colour Octet Model was prepared within PYTHIA [5]. In order to make the simulation studies more efficient the initial cuts on the transverse momentum, p_T, and the pseudorapidity, η, were applied at the generator level. To ensure that most of the generated events passed the trigger at the reconstruction stage, only events containing decays of J/ψ into dimuons, with p_T larger than 6 GeV and 4 GeV, both detected within $|\eta| < 2.4$, were retained for detector simulations.

Table 1: Monte Carlo samples used in this study. Cross sections are given by PYTHIA after applying cuts $|\eta| < 2.4$ and p_T larger than 6 GeV and 4 GeV for the first and second muons from J/ψ .

Process	MC Statistics	Cross section
$b\bar{b} \to J/\psi X$	150 000	11.1 nb
$pp \to J/\psi X$	150 000	21.7 nb
$B_s^0 \to J/\psi\phi$	50 000	0.02 nb
$B_d^0 \to J/\psi K^{0*}$	30 000	0.24 nb

3 Analysis of the decays $B_s^0 \to J/\psi\phi$ and $B_d^0 \to J/\psi K^{0*}$

3.1 Strategy for analysis of early data

The strategies deployed during the early period of the experiment will differ from those used later. In particular, the low statistics available will not allow a determination of the complete list of physics variables that can in principle be determined from the $B_s^0 \to J/\psi\phi$ and $B_d^0 \to J/\psi K^{0*}$ decays [6]. During the early phase, the compositions of the backgrounds will not be well understood. Furthermore, at this time, the detector and reconstruction software performance will also not be fully understood, and restrictive selection cuts to remove backgrounds may bias the signal in an uncontrolled way. The strategy in these early stages will therefore be to use loose cuts, which will admit more of the background decays. In particular, omitting vertex selections allows a statistically meaningful contribution from prompt J/ψ events. Most of these events fall outside the signal region of the study, and allow a better determination of the vertex resolution, which in turn allows a better overall B lifetime determination. This approach is consistent with the B trigger strategy for early data where no cut on secondary vertex displacement is required.

3.2 Reconstruction

Monte Carlo events of signal and background processes, as described in Table 1, were passed through full detector simulation and reconstruction. Trigger algorithms were applied during the reconstruction. Only events accepted by the $J/\psi \to \mu^+\mu^-$ trigger [2] (with thresholds of $p_T > 6$ GeV and $p_T > 4$ GeV for the fastest and second fastest muon) were retained for offline analysis. The reconstructed data objects were then processed as follows.

$J/\psi \to \mu^+\mu^-$ candidates were sought by forming all possible pairs of oppositely charged muon tracks passing the cuts $p_T > 4$ GeV and $|\eta| < 2.4$. Pairs containing at least one muon track with $p_T >$ 6 GeV were fitted to a common vertex. Pairs were assumed to be muons from J/ψ decays if the vertex fit resulted in a fit $\chi^2/n.d.f < 6$ and the invariant mass of the muon pair fell within a 3 σ window around the nominal J/ψ mass, with $\sigma = 58$ MeV. This window was chosen by fitting a Gaussian distribution to the invariant mass of the muon pairs in the events $pp \to J/\psi X$ and $bb \to \mu^+\mu^- X$, see Figure 1. The background from non resonant $\mu^+\mu^-$ pairs in the 3 σ window is 10%.

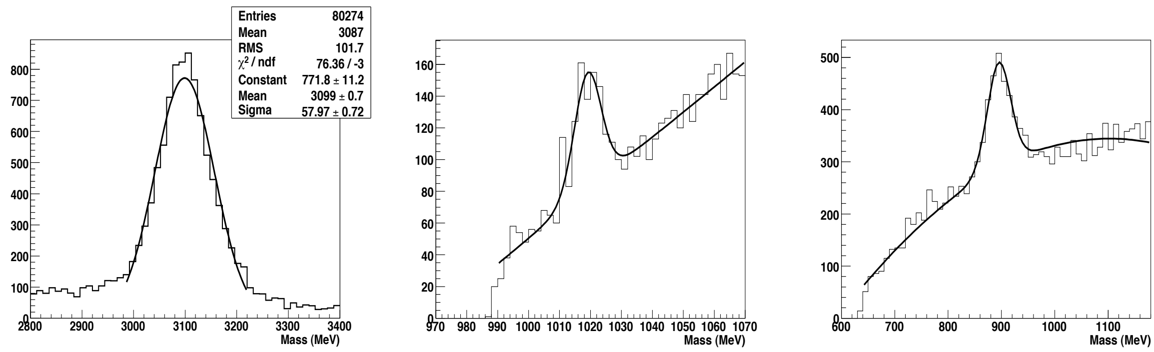

Figure 1: Reconstructed invariant mass distributions of $J/\psi \to \mu^+\mu^-$ (left), $\phi \to K^+K^-$ (middle) and $K^{0*} \to K^\pm\pi^\mp$ (right) candidates.

The $\phi \to K^+K^-$ candidates were reconstructed from all pairs of oppositely charged tracks, not identified as muons, with $p_T > 0.5$ GeV and $|\eta| < 2.5$, which were fitted to a common vertex. These tracks were assumed to be kaons from ϕ decays if the vertex fit resulted in a $\chi^2/n.d.f < 6$, and the invariant mass of the track pairs (under the assumption that they were left by kaons) fell within the interval $1009.2 - 1029.6$ MeV. This interval is based on a fit to the invariant mass distribution of the reconstructed $\phi \to K^+K^-$ decay candidates shown in Figure 1. The signal fit used a Breit-Wigner correctly accounting for phase space convoluted with a Gaussian to represent the detector resolution. The background was approximated by a linear function. (Additional terms up to quadratic have no significant influence on the fit.)

The $K^{0*} \to K^\pm\pi^\mp$ candidates were reconstructed by selecting all tracks that had $p_T > 0.5$ GeV and $|\eta| < 2.5$ that had not been previously identified as muons, forming them into oppositely charged pairs and fitting them to a common vertex. These pairs were assumed to be $K^\pm\pi^\mp$ from K^{0*} decays if the fit resulted in a $\chi^2/n.d.f < 6$, the transverse momentum of the K^{0*} candidate was greater than 3 GeV, and the invariant mass of the track pair fell within the interval 790-990 MeV, under the assumption that they were left by $K^\pm\pi^\mp$ hadrons. In Figure 1, the signal has been fitted to a Breit-Wigner function convoluted with a Gaussian and the background has been fitted to a second degree polynomial function.

To find the $B_d^0 \to J/\psi K^{0*}$ candidates, the tracks from each combination of $J/\psi \to \mu^+\mu^-$ and $K^{0*} \to K^\pm\pi^\mp$ candidates were fitted to a common point. The two muon tracks were constrained to the PDG J/ψ mass. These quadruplets of tracks were assumed to be from $B_d^0 \to J/\psi K^{0*}$ decays if the transverse momentum of the B_d^0 candidate was greater than 10 GeV and the fit resulted in a $\chi^2/n.d.f < 6$. In the case of more than one candidate per event, the candidate with the lowest $\chi^2/n.d.f$ was retained.

$B_s^0 \to J/\psi\phi$ candidates were sought by fitting the tracks from each combination of $J/\psi \to \mu^+\mu^-$ and $\phi \to K^+K^-$ candidates fitted to a common vertex. The two muon tracks were constrained to the PDG J/ψ mass. These quadruplets of tracks were assumed to be from $B_s^0 \to J/\psi\phi$ decays if the transverse momentum of the B_s^0 candidate was greater than 10 GeV and the fit resulted in a $\chi^2/n.d.f < 6$. If there was more than one candidate per event then the candidate with the lowest $\chi^2/n.d.f$ was chosen.

Accepted B_s^0 and B_d^0 candidates contain a negligible background from non-resonant $\mu^+\mu^-$ pairs, 0.1% and 0.2% respectively, and therefore the background from non-resonant bb $\to \mu^+\mu^-$X events are not considered in this analysis.

Events were accepted in a wide invariant mass window of $\pm 12 \cdot \sigma$ around B hadron mass, where the mass resolution σ was determined from recontruction of the B_d^0 and B_s^0 masses for the two signal channels. The mass resolutions were obtained from fitting a single Gaussian to the Monte Carlo signal. Table 2 shows the number of events that can be expected using the above procedure for an integrated

Table 2: Signal and background statistics of B_s^0 and B_d^0 candidates expected with 10 pb^{-1}.

	Selected candidates expected with 10 pb^{-1}
Signal $B_d^0 \to J/\psi K^{0*}$	1024
$pp \to J/\psi X$ background	1419
$b\bar{b} \to J/\psi X$ background	3970
Signal $B_s^0 \to J/\psi\phi$	76
$pp \to J/\psi X$ background	2449
$b\bar{b} \to J/\psi X$ background	1660
All events satifying B_d^0 or B_s^0 selections	10323

luminosity of 10 pb^{-1}.

By the time the LHC reaches a luminosity of 10^{33} cm^{-2} s^{-1} and the detector is better understood, it will be safe to apply displaced secondary vertex cuts, which will remove most of the backgrounds. In the studies of exclusive channels of B decays, vertex displacement selections are replaced by cuts on the B hadron decay time. This method avoids any bias on the proper decay time measurements. Table 3 shows the reconstruction efficiences with and without decay time cuts. In particular, by requiring that the proper decay time of the B_s^0 candidate is greater than 0.5 ps, additional rejection by a factor of 260 for the $pp \to J/\psi X$ can be achieved while losing 25% of the signal.

Table 3: $B_d^0 \to J/\psi K^{0*}$ ($B_s^0 \to J/\psi\phi$) signal and background reconstruction efficiencies before and after the cut on B_d^0 (B_s^0) decay time t. The applied cut was $t > 0.5$ ps.

	efficiency [%]	
	before time cut	after time cut
Signal $B_d^0 \to J/\psi K^{0*}$	42.0	30.4
$pp \to J/\psi X$ background	0.67	0.0064
$b\bar{b} \to J/\psi X$ background	3.05	1.52
Signal $B_s^0 \to J/\psi\phi$	40.5	30.0
$pp \to J/\psi X$ background	1.5	0.0058
$b\bar{b} \to J/\psi X$ background	1.1	0.8

4 Simultaneous fit of mass and lifetime of B_d^0 and B_s^0 with early data

We now turn to methods for extracting physically interesting parameters from the decays of the B_s^0 and B_d^0 mesons. The first measurements with early data will comprise the mean lifetimes and masses of these mesons.

We perform a simultaneous maximum likelihood fit for each B_s^0 and B_d^0 mass and proper decay time distributions. The likelihood function L is defined by:

$$L = \prod_{i=1}^{N} \left[\frac{n_{sig}}{N} \times p_{sig}(t_i, m_i) + \frac{n_{bck1}}{N} \times p_{bkg1}(t_i, m_i) + \frac{N - n_{sig} - n_{bck1}}{N} \times p_{bkg2}(t_i, m_i) \right] \quad (1)$$

where the index i runs over the events, $N = n_{sig} + n_{bck1} + n_{bck2}$ is the total number of reconstructed events in the fit and n_{sig}, n_{bck1} and n_{bck2} are the numbers of signal and background events. The terms p_{sig}, p_{bkg1} and p_{bkg2} are products of two probability density functions that model the mass m and proper decay time t of the signal and the prompt and non-prompt backgrounds respectively (see Section 2). The number of expected events for the prompt background is n_{bck1} and the corresponding probability density function in formula 1 is p_{bkg1}. The probability density function for the non-prompt background is p_{bkg2}.

For the signal, the mass distribution is modeled by a Gaussian distribution, whose mean value is the B hadron mass m(B) and its width σ_m is given by the detector mass resolution. Both m(B) and σ_m are determined from the fit. The reconstructed proper decay time distribution for the signal is parameterised by the function:

$$p_{sig}(t_i) = \frac{\int_0^\infty \mathrm{e}^{-\Gamma t} \rho(t-t_i)\,\mathrm{d}t}{\int_{-\infty}^{\infty} \left(\int_0^\infty \mathrm{e}^{-\Gamma t} \rho(t-t')\,\mathrm{d}t\right) \mathrm{d}t'} \tag{2}$$

where the decay time resolution function $\rho(t-t_i)$ was approximated by a Gaussian of width σ which is a free parameter of the fit.

For the background, the mass distribution of the prompt component is assumed to follow a flat distribution as observed in simulated data (see Figure 2). The non-prompt component is modeled with a second order polynomial function where the coefficient of the linear (quadratic) terms, denoted as c_1 (c_2) in Table 4, are determined from the fit.

The decay time distribution of the prompt background component is parametrised by a Gaussian of width σ. The non-prompt component was modeled by the sum of two exponential functions, convoluted with the decay time resolution function ρ. The two exponential functions are denoted as Γ_1 and Γ_2, the constant coefficient between them is b_1.

$$p_{bck2}(t_i) = \frac{\int_0^\infty \left(\Gamma_1 \mathrm{e}^{-\Gamma_1 t} + \mathrm{b}_1 \times \Gamma_2 \mathrm{e}^{-\Gamma_2 t}\right) \rho(t-t_i)\,\mathrm{d}t}{\int_{-\infty}^{\infty} \left(\int_0^\infty \left(\Gamma_1 \mathrm{e}^{-\Gamma_1 t} + \mathrm{b}_1 \times \Gamma_2 \mathrm{e}^{-\Gamma_2 t}\right) \rho(t-t')\,\mathrm{d}t\right) \mathrm{d}t'} \tag{3}$$

4.1 $B_d^0 \to J/\psi K^{0*}$ decay

The likelihood function, $-2lnL$ is minimised to extract the B_d^0 lifetime $\tau = 1/\Gamma$ and mass m(B) from the reconstructed events containing a $B_d^0 \to J/\psi K^{0*}$ candidates and backgrounds. This fit corresponds to an integrated luminosity of 10 pb^{-1}. The distributions of the reconstructed masses and lifetimes are shown in Figure 2. Table 4 summarises the results of the likelihood fit. The values obtained from the fit agree with the input values used in the simulation (given in the first column) within the statistical errors of the fit. The average lifetime of the B_d^0 can be measured with an uncertainty of 10% for 10 pb^{-1}.

4.2 $B_s^0 \to J/\psi\phi$ decay

The B_s^0 $\overline{B_s^0}$ system exhibits two mass eigenstates with two lifetimes; the lifetime difference $\Delta\Gamma_s/\Gamma_s$ is expected to be $\mathcal{O}(10^{-1})$. However, with early data (a few hundred pb^{-1}), the statistics are insufficient to determine both lifetimes. For the initial period of LHC running, it is assumed that $\Delta\Gamma_s = 0$. The method for the B_s^0 fit is the same as for the B_d^0 case, the main difference being the smaller fraction of signal events, as shown in the mass and lifetime distributions for the reconstructed events after cuts selecting the B_s^0 signal (Figure 3).

Statistics of reconstructed events corresponding to an integrated luminosity of 150 pb^{-1} enables measurements to be made with relative precisions on the B_s^0 lifetime of 10% (Table 5). In the fit the background events are weighted by factor of 15, since Monte Carlo statistics were limited to the equivalent of 10 pb^{-1} for the current study.

Table 4: Results of the fit to reconstructed B_d^0 candidates corresponding to 10 pb^{-1}. The first column shows input values used in simulation.

Parameter	Simulated value	Fit result with statitical error
Γ, ps^{-1}	0.651	0.73 ± 0.07
m(B), GeV	5.279	5.284 ± 0.006
σ, ps		0.132 ± 0.004
σ_m, GeV		0.054 ± 0.006
n_{sig}/N	0.16	0.155 ± 0.015
n_{bck1}/N	0.062	0.595 ± 0.017
b_1		1.08 ± 0.27
Γ_1, ps^{-1}		0.67 ± 0.05
Γ_2, ps^{-1}		2.4 ± 0.3
c_1		-2.75 ± 0.28
c_2		4.7 ± 1.4

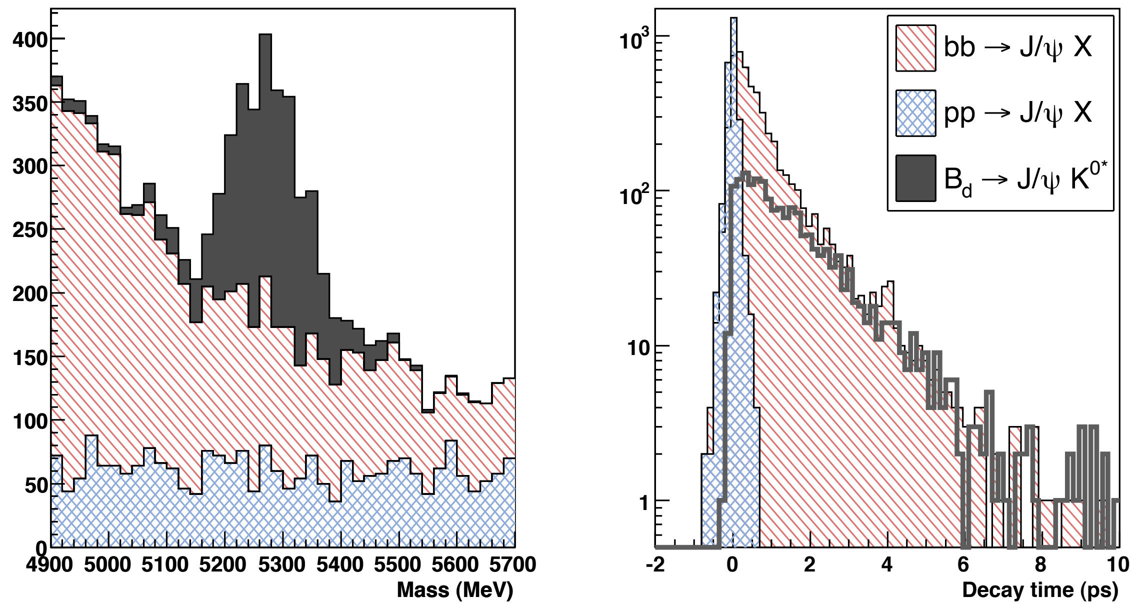

Figure 2: Distributions of the reconstructed B_d^0 mass and decay time expected with integrated luminosity of 10 pb^{-1}.

5 The performance of the jet charge tagger with early data

Most studies of CP-violation and mixing require the identification of the flavour of the neutral B mesons; this is known as *flavour tagging*. Understanding the potential for flavour tagging methods will be one of the important goals with early data. In studies of CP-violation and mixing of neutral B mesons, one must know the flavour of a B meson both at the time of production ($t = 0$) and at the time of decay.

In a small number of cases, the flavour at production can be inferred from the charge of the highest

Table 5: Results from the fit to reconstructed B_s^0 candidates corresponding to 150 pb^{-1}.

	Input	Fit result with statistical error
Γ_s, ps^{-1}	0.683	0.743 $\pm$ 0.051
m(B), GeV	5.343	5.359 $\pm$ 0.006
σ, ps		0.152 $\pm$ 0.001
σ_m, GeV		0.061 $\pm$ 0.006
n_{sig}/N	0.018	0.031 $\pm$ 0.005
n_{bck1}/N	0.397	0.379 $\pm$ 0.006
b_1		0.023 $\pm$ 0.01
Γ_1, ps^{-1}		1.35 $\pm$ 0.02
Γ_2, ps^{-1}		0.44 $\pm$ 0.08
c_1		-1.44 $\pm$ 0.07
c_2		2.14 $\pm$ 0.49

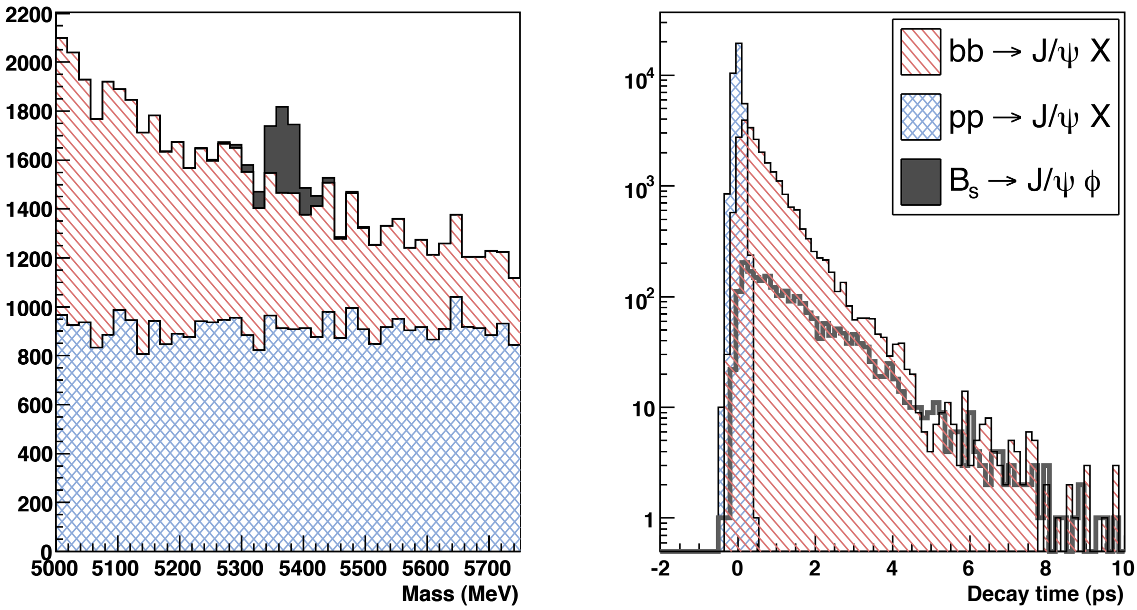

Figure 3: Plots to show the distributions of the reconstructed B_s^0 mass and decay time expected with 150 pb^{-1}. Background distributions constructed from simulated events corresponding to 10 pb^{-1} were scaled by a factor of 15.

p_T lepton unassociated with the signal decay, with the assumption that this tagging lepton originates from a semi-leptonic decay of the other B hadron in the event. For the majority of the events, one must use the jet charge tagging method. According to fragmentation models, the particles are ordered in the momentum component parrallel to the original quark direction, while charge conservation also imposes charge ordering [7]. These two facts may be used to form a jet charge, which is related to the b-quark charge at production. The jet used in this method consists of all tracks that are unassociated with the signal decay with $p_T > 500$ MeV, $|\eta| < 2.5$, inside a cone of opening angle ΔR around the B meson in the laboratory frame. The opening angle of the jet cone, ΔR, is defined:

$$\Delta R = \sqrt{\Delta\eta^2 + \Delta\varphi^2} \tag{4}$$

where $\Delta\eta$ and $\Delta\varphi$ are the differences in pseudorapidity and azimuthal angle between the cone wall and the B meson. The jet charge, Q_{jet}, tends to be positive for $\bar{b}$-jets and negative for b-jets, thus allowing the B^0 meson flavour at production to be inferred. The jet charge is defined as:

$$Q_{\text{jet}} = \frac{\sum_i q_i p_i^\kappa}{\sum_i |p_i|^\kappa} \tag{5}$$

where the q_i is the charge of the i^{th} track in the jet and p_i is a measure of the tracks momentum that can be, for example, the transverse momentum of the track or a projection of the track's momentum along the axis of the B meson's direction. These are referred to as the p_T method and the p_L method respectively. The parameter κ controls the relative contribution of the hard and soft tracks in the jet charge. One possible improvement in the algorithm is to remove ambiguous cases such as events with Q_{jet} close to zero; the smallest allowed value of $|Q_{jet}|$ is called the "exclusion cut". The opening angle of the jet cone, the exclusion cut and κ are free parameters and must be tuned to get the best performance from the tagger.

5.1 Quantifying the performance of a flavour tagger

The effectiveness of the discrimination between B^0 and $\overline{B^0}$ mesons at production time is characterized by two quantities: its *efficiency*, ε_{tag}, and the *dilution*, D_{tag}. The efficiency is the fraction of B mesons that were tagged either correctly or incorrectly and is described by:

$$\varepsilon_{\text{tag}} = \frac{N_r + N_w}{N_t} \tag{6}$$

where N_r and N_w are the numbers of correctly and incorrectly tagged B mesons respectively, and N_t is the total number of reconstructed B mesons. The *dilution*, also known as the *purity*, is given by:

$$D_{\text{tag}} = \frac{N_r - N_w}{N_r + N_w} = 1 - 2w_{\text{tag}} \tag{7}$$

where w_{tag} is the wrong tag fraction:

$$w_{\text{tag}} = \frac{N_w}{N_r + N_w} \tag{8}$$

In a typical CP violation study, where the aim is to identify a difference in some property between a particle and its anti-particle, the relationship between the true asymmetry of this property, A_{true}, and the asymmetry as measured in the data, A_{meas}, will be

$$A_{true} = \frac{1}{D_{\text{tag}}} A_{meas} \tag{9}$$

which is derived in, for instance, [8]. For the small asymmetries expected in the B decays, the statistical uncertainty on A_{true} is, to a good approximation:

$$\sigma_A \approx \frac{1}{\sqrt{\varepsilon_{\text{tag}} D_{\text{tag}}^2 N_t}} \tag{10}$$

The tag algorithm effectiveness is indicated by the *quality factor* or *tagging power*, Q_{tag}:

$$Q_{\text{tag}} = \varepsilon_{\text{tag}} D_{\text{tag}}^2 \tag{11}$$

The quality factor is used as a measure of success when optimising the flavour tagger.

5.2 Understanding the jet charge tagger using $B_d^0 \to J/\psi K^{0*}$ decays

During the early data taking phase, there will be too few $B_s^0 \to J/\psi\phi$ decays reconstructed to allow a detailed comparison between the jet charge distribution obtained from the data and that predicted by the Monte Carlo. However, there will be a sufficient number of the analogous $B_d^0 \to J/\psi K^{0*}$ decays to allow such a comparison to be made. Additionally, the final state of the $B_d^0 \to J/\psi K^{0*}$, with a subsequent decay of K^{0*} to charged mesons, allows the initial flavour to be determined in a statistical way, and therefore the decay mode is considered as self-calibrating. The jet charge tagger thus produced will be important for the CP violation studies with $B_d^0 \to J/\psi K_S$, and the study of $B_d^0 \to J/\psi K^{0*}$ will allow us to gain confidence in the tagging performance for $B_s^0 \to J/\psi\phi$.

For this study, the signal decays were reconstructed as described in the Section 3 for both $B_d^0 \to J/\psi K^{0*}$ and $B_s^0 \to J/\psi\phi$ decays. A reconstructed sample of 15000 decays was used for each channel, corresponding to 150 pb^{-1}for $B_d^0 \to J/\psi K^{0*}$ and 1.5 fb^{-1}for $B_s^0 \to J/\psi\phi$; this defines our working point for the two channels in this study. The quality factor was then maximised by systematically varying the jet charge tagger input parameters ΔR, κ and exclusion cut. It was found that optimal results for both B_s^0 and B_d^0 mesons were obtained using the projection of the track momentum in the direction of the B meson (the p_L method) as the measure of momentum in Equation 5. The other optimal parameters are shown in Table 6. Using these optimised parameters, the jet charge distribution for both $B_d^0 \to J/\psi K^{0*}$ and $B_s^0 \to J/\psi\phi$ are shown in Figure 4.

Table 6: The optimised parameters of the flavour tagging algorithm for both $B_d^0 \to J/\psi K^{0*}$ and $B_s^0 \to J/\psi\phi$.

Parameter	$B_d^0 \to J/\psi K^{0*}$	$B_s^0 \to J/\psi\phi$
κ	0.9	0.8
ΔR cut	0.7	0.6
Exclusion cut	0.05	0.2

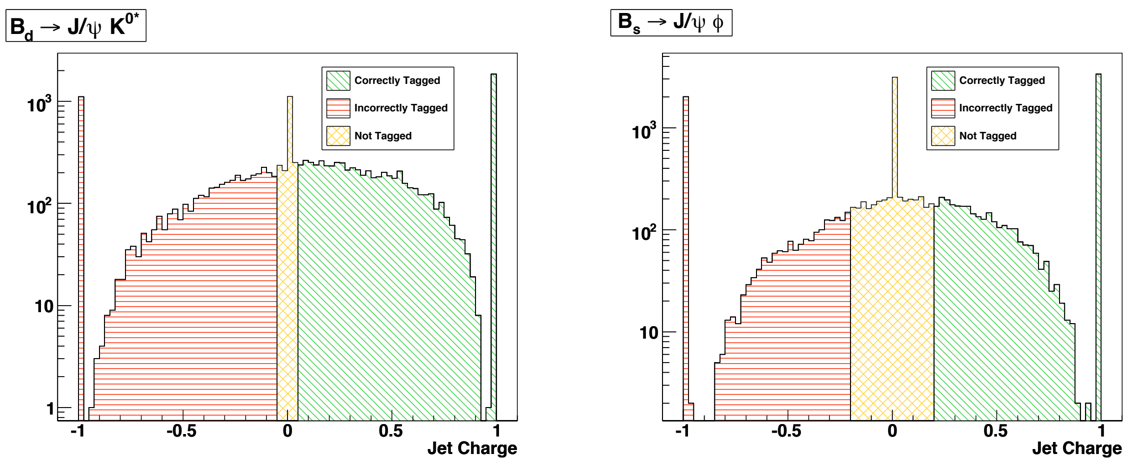

Figure 4: Plots of Q_{jet} for $B_d^0 \to J/\psi K^{0*}$ (left) and $B_s^0 \to J/\psi\phi$ (right) using their optimised parameters of Table 6 and the equivalent luminosity of Table 7.

One might expect that the different flavour content in the formation of the B mesons will result in a different jet charge behavior for $B_d^0 \to J/\psi K^{0*}$ and $B_s^0 \to J/\psi\phi$. This is indeed what is observed, both in the optimisation of these jet charges and their distributions. However, one should also note that both the shapes and the optimised parameters, except the exclusion cut, are similar.

The numbers in Table 7 characterise the expected performance of the jet charge tagger. With an integrated luminosty of 150 pb^{-1}, it will be possible to calibrate the jet charge tagger for the B_d^0, from the data, with an efficiency of $87.0 \pm 0.3\%$ and a wrong tag fraction of $38.0 \pm 0.4\%$. Calibrating with real data for the B_s^0 is more challenging as there is no readily availible and clean self-tagging mode. In this case, the Monte Carlo dependent calibration will be used, but the agreement of the Monte Carlo with real data will be tested indirectly though the $B_d^0 \to J/\psi K^{0*}$ channel.

Table 7: Performance of the flavour tagging algorithm for the optimised values given in Table 6. The errors given in the table are statistical.

Parameter	$B_d^0 \to J/\psi K^{0*}$	$B_s^0 \to J/\psi\phi$
Equivalent luminosity	150 pb^{-1}	1.5 fb^{-1}
Number of Reconstructed Events	13948	15784
Efficiency, $\varepsilon_{\mathrm{tag}}$	0.870 ± 0.003	0.625 ± 0.005
Wrong Tag Fraction, w_{tag}	0.380 ± 0.004	0.374 ± 0.005
Dilution, D_{tag}	0.240 ± 0.009	0.251 ± 0.010
Quality, Q_{tag}	0.050 ± 0.004	0.039 ± 0.003

6 Summary and conclusion

With the early data, the decays $B_d^0 \to J/\psi K^{0*}$ and $B_s^0 \to J/\psi\phi$ can be used to measure B hadron masses and lifetimes with sufficient precision to permit sensitive tests of the detector performance. In particular, the B_d^0 lifetime can be determined with a relative statistical error of 10%, with an integrated luminosity of 10 pb^{-1}, and the same precision will be achieved for the B_s^0 lifetime with 150 pb^{-1}. The proposed method of a simultaneous fit of background and signal events allows a sensitive determination of the masses and decay times of B mesons. With early data, the optimal overall precision will be obtained with no cuts on the secondary vertex displacement. This is appropriate for the early data when the performance of the detector and reconstruction algorithms may not be well understood. This strategy is consistent with that of the early B-physics triggers, where no displacement cuts on the J/ψ will be applied at the trigger level.

In the early data taking phase, the self-tagging decay $B_d^0 \to J/\psi K^{0*}$ will be used to calibrate the jet charge tag for jets containing a B_d^0. This will be of use for physics studies involving B_d^0 decays, but also this good understanding for the tagging performance for $B_d^0 \to J/\psi K^{0*}$ will allow the fragmentation modelling for $B_s^0 \to J/\psi\phi$ decays to be improved.

References

[1] P.Nason, et al., *Bottom Production*, CERN-2000-004, pp.231-304, (2000).

[2] S.Tarem et al., *Triggering on Low-p_TMuons and Di-Muons for B-Physics*, this volume.

[3] T. Sjostrand , S. Mrenna, P. Skands, *PYTHIA 6.4 Physics and Manual*, JHEP 0605:026, (2006).

[4] S.P.Baranov, M.Smizanska, J.Hrivnac, E.Kneringer, *Overview of Monte Carlo simulations for ATLAS B-physics*, ATL-PHYS-2000-025, CERN, (2000); S.P. Baranov, M.Smizanska, *Beauty Production Overview from Tevatron to LHC*, ATL-PHYS-98-133, CERN, (1998).

[5] V. Kartvelishvili for the ATLAS coll, *B physics in ATLAS*, Nucl. Phys. Proc. Suppl. **164**:161-168, (2007).

[6] M. Smižanská for the ATLAS collaboration, *ATLAS: Helicity Analyses In Beauty Hadron Decays*, Nucl. Instrum. Meth. **A446**:138-142, (2000); J. Catmore for the ATLAS collaboration, *LHC sensitivity to new physics in B_s^0 parameters*, Nucl. Phys. Proc. Suppl. **167**:181-184, (2007).

[7] R. D. Field, R. P. Feynman, *A Parameterization of the properties of Quark Jets*, Nucl. Phys. **B 136**, 1 (1978).

[8] CDF Collaboration, *Neural Network based Jet Charge Tagger in Semileptonic Samples*, CDF note 7285, (2005); C. Lecci, *A Neural Jet Charge Tagger for the Measurement of the $B_s^0-\overline{B}_s^0$ Oscillation Frequency at CDF*, Ph.D. thesis, University of Karlsruhe (TH), (2005).

[9] ATLAS Collaboration, *Detector and physics performance Technical Design Report*, CERN/LHCC/99-14, CERN, (1999); R. W. L. Jones for ATLAS collaboration, *High precision measurements of B_s^0 parameters in $B_s^0 \to J/\psi\phi$ decays*. Nucl. Phys. Proc. Suppl. **156**:147-150, (2006); E. Bouhova-Thacker, *Feasibility study for the Measuring of the CKM Phases γ and $\delta\gamma$ in Decays of Neutral B-Mesons with the ATLAS Detector*, Ph.D. thesis, University of Sheffield, (2000).

Plans for the Study of the Spin Properties of the Λ_b Baryon Using the Decay Channel $\Lambda_b \to J/\psi(\mu^+\mu^-)\Lambda(p\pi^-)$

Abstract
This note summarizes the results of a study of the feasibility of measuring certain spin properties of Λ_b baryon in the ATLAS experiment. We present an assessment of approaches for extracting the inclusive Λ_b polarization and the parity violating α_{Λ_b} parameter for the decay $\Lambda_b \to J/\psi(\mu^+\mu^-)\Lambda(p\pi^-)$ from the reconstructed four final state charged particles. As a key test, we generated Monte Carlo samples of Λ_b events of fixed polarization in the ATLAS detector and evaluated our ability to precisely extract the input polarization from the reconstructed events. The physics motivation for the planned measurements in ATLAS include the search for an explanation of the anomalous spin effects in hyperon inclusive production observed at lower energies, tests of various decay models based on HQET, tests of CP in an area not yet directly explored, and the development of Λ_b polarimetry as a possible tool for spin analysis in future SUSY and other studies.

1 Introduction

We report here plans for the measurement of spin parameters of the Λ_b hyperon. We utilize the decay mode $\Lambda_b \to J/\psi(\mu^+\mu^-)\Lambda(p\pi^-)$ to extract the Λ_b signal from what is expected to be a low background environment, given that the final state has four charged particles and a displaced secondary vertex. The polarization and parity violating α_{Λ_b} parameter will be determined from the relevant angular correlations between the final state particles. We expect to accumulate approximately 13000 Λ_b events (and a similar number of $\overline{\Lambda_b}$) with an integrated luminosity of 30 fb^{-1} . This estimation is based on the latest reconstruction software and trigger simulation for the ATLAS experiment.

The Λ_b is the lightest baryon containing a b quark, and since its discovery in 1991 by the UA1 Collaboration [1] it has created a great deal of interest. Besides the so−called Λ_b lifetime puzzle [2], the Λ_b has been the subject of various theoretical studies ranging from proposed tests of CP violation [3], T violation tests and new physics studies [4], measurement of top quark spin correlation functions [5] and the extraction of the weak phase γ of the CKM matrix [6]. Specific physics interest in the Λ_b parity violating α_{Λ_b} parameter studies derives from its ability to serve as a test for various heavy quark factorization models and perturbative QCD (PQCD). Λ_b studies are also of interest because of the continuing mystery of why hyperons have consistently displayed large polarizations when produced at energies even up to several hundred GeV and at large p_T where most models predict zero polarization. It is not known if these effects can be explained by some not yet understood effect of existing physics or if they point to new physics altogether. Λ_b polarization holds the possibility of illuminating just how polarized b quarks are produced and, indeed, it may have relevance to how fermions are produced in all pp induced processes.

Interest in the studies of the Λ_b lifetime parameter derives from the current controversy from Tevatron experiments concerning the question of how much longer the b quark lives in a meson vs. in a hyperon. With an expected increase of a factor of 100 in the statistics at the LHC, we expect to make a definitive statement on this puzzle. Again, this will further constrain the theoretical models which have as their basis PQCD and the Heavy Quark Model. Lifetime measurements will not be examined in this article, since it is not the focus of the current study, though many of the event selection issues, discussed here, might be applicable in the Λ_b lifetime studies.

We have examined the primary technical challenges in the measurement of Λ_b polarization in ATLAS by generating large samples of Λ_b baryons with various known polarizations, allowing them to decay in the detector using model−predicted amplitudes, and then reconstructing these events using standard ATLAS packages. These samples have permitted us to test our ability to reconstruct events and to confirm that we can recover the input polarization and the decay amplitudes. They also have allowed us to compare various polarization extraction methods and to assess the impact of detector corrections and detector resolution effects. We provide here a report on the results of these studies, and on the work we undertook to adapt the EVTGEN [7] decay package to produce polarized Λ_b within the ATLAS software framework.

2 Theoretical overview

In the quark model the Λ_b is a fermion consisting of a b quark accompanied by a di−quark (ud) of total spin zero. In this model the polarization of the Λ_b is thus expected to be totally due to the b quark polarization. QCD calculations suggest that the b quark polarization would be small. However, there are models of quark scattering [8], in which spin effects are expected to scale with the mass of the heavy quark, and where the possibility exists for Λ_b polarizations to be quite large. We further note that QCD has not been able to predict the very large polarizations that have been observed in the inclusive production of Λ hyperons at energies of several hundred GeV. It is hoped that the huge mass difference in the b and s quarks will help elucidate the origin of these unexplained spin effects.

Interest in the α_{Λ_b} parameter for the Λ_b stems from the fact that HQET models [9] purport to calculate this quantity from rather basic principles of PQCD and factorization. We have an interest in comparing our ultimate measurements of this quantity with these predictions and assessing what constraints they can provide for these models. We provide below a brief overview of the theoretical basis for the polarization and α_{Λ_b} measurements.

2.1 Heavy quark polarization in QCD

In the Standard Model heavy quark production is dominated by gluon−gluon fusion and $q\bar{q}$ annihilation processes. A non−zero polarization requires an interference between non−flip and spin−flip helicity amplitudes for the Λ_b production, with the latter containing an imaginary part. In QCD this complex part can only be generated through loop corrections, so that the relevant diagrams for polarized quarks are $\mathscr{O}(\alpha_s^4)$. The polarization expected from all QCD sub−processes ($g-g$ fusion, $q\bar{q}$ annihilation and $q-q$, $q-g$ scattering) have been calculated [10]. The formulae for the polarization for each one of the four processes is directly proportional to α_s, and it depends just on the ratio $x_Q = m_Q/p_Q$ and the scattering angle θ_Q, (all defined in the center of mass frame), and are thus valid for any final−state quark Q. The expected polarization in single b quark production by gluon−gluon fusion and $q\bar{q}$ annihilation has been found to be a maximum of 5% for gluon−gluon fusion, and a maximum 10% for $q\bar{q}$ annihilation. When these predictions are compared to the observed Λ polarization (due to the s quark polarization) [11], they are found to be an order of magnitude too small. One might not be surprised if the Λ_b polarization is, as well, greater than predicted in QCD.

An important result in [10] is the dependence of the polarization on the quark mass. The heaviest quark produced is the most polarized, and the maximum polarization is reached around $x_Q \simeq 0.3$. The b quark polarization is predicted to be an order of magnitude greater than the s quark polarization, which from Λ polarization measurements has been found to reach values over 20% at 400 GeV [12].

The measurement of the Λ_b polarization in ATLAS in the exclusive channel $\Lambda_b \to J/\psi\Lambda$ proposed here would cover $p_T(\Lambda_b) > 8000$ MeV (because of trigger and reconstruction constraints on the transverse momentum of the final−state particles, see Table 2) and $x_F(\Lambda_b) < 0.1$. It could make a significant contribution to testing different models of production of polarized baryons in this new kinematic region.

An idea that the heavy quark pre−exists in the incoming proton before scattering and becomes polarized through a direct scattering from an incoming quark provides another pathway for the Λ_b to be polarized. This possibility has been discussed by Neal and Burelo [13]. If polarizations are observed in inclusive Λ_b production that exceed a few percent, such a mechanism should be given careful attention, since no other existing models can account for such large values.

2.2 $\Lambda_b \to J/\psi(\mu^+\mu^-)\Lambda(p\pi^-)$ decay and angular distributions

The proposed study of Λ_b polarization would probe not only the production process but also explore the decay of Λ_b. Decay models predict values for various quantities that can be experimentally observed, thus providing a test of specific HQET/Factorization model [14] assumptions.

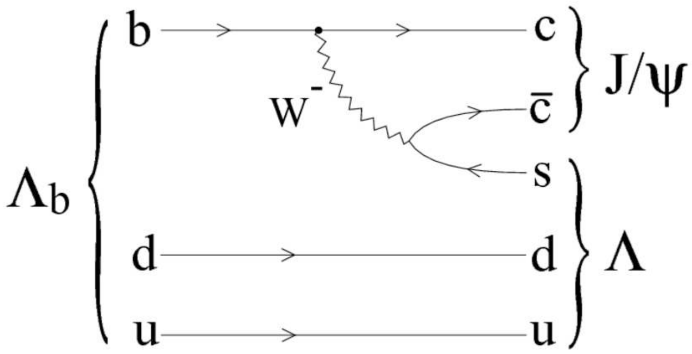

Figure 1: The weak decay of Λ_b: $\Lambda_b \to J/\psi\Lambda$.

The fact that Λ_b has a significant lifetime suggests that it decays weakly. The dominant decay process would involve the emission of a W^- boson, as illustrated in Figure 1. The spin and parity of the particles involved in the $\Lambda_b \to J/\psi(\mu^+\mu^-)\Lambda(p\pi^-)$ decay are well known. The Λ_b with $J^P = \frac{1}{2}^+$ decays to Λ with $J^P = \frac{1}{2}^+$ and J/ψ with $J^P = 1^-$. The general amplitudes for the decay of $\Lambda_b(\frac{1}{2}^+) \to \Lambda(\frac{1}{2}^+)J/\psi(1^-)$ is given by:

$$\mathscr{M} = \overline{\Lambda}(p_\Lambda)\, \varepsilon^*_\mu(p_{J/\psi}) \left[A_1 \gamma^\mu \gamma^5 + A_2 \frac{p^\mu_{\Lambda_b}}{m_{\Lambda_b}} \gamma^5 + B_1 \gamma^\mu + B_2 \frac{p^\mu_{\Lambda_b}}{m_{\Lambda_b}} \right] \Lambda_b(p_{\Lambda_b}), \quad (1)$$

which is parameterized by the four complex decay amplitudes A_1, A_2, B_1, B_2 and where ε_μ is the polarization vector of the J/ψ .

Given the general amplitude, we may compute the helicity amplitudes. We use helicity amplitudes, because they have a direct physical relationship to the spin parameters we wish to study. Four helicity amplitudes are required to describe the decay completely. We will use the notation $H_{\lambda_\Lambda,\lambda_{J/\psi}}$ for the helicity amplitudes of the decay $\Lambda_b \to J/\psi(\mu^+\mu^-)\Lambda(p\pi^-)$, where $\lambda_\Lambda = \pm 1/2$ is the helicity of Λ and $\lambda_{J/\psi}$ = +1, 0, -1 is the helicity of J/ψ . These four helicity amplitudes: $a_+ = H_{1/2,0}$, $a_- = H_{-1/2,0}$, $b_+ = H_{-1/2,1}$, $b_- = H_{1/2,-1}$ are normalized to unity:

$$|a_+|^2 + |a_-|^2 + |b_+|^2 + |b_-|^2 = 1. \quad (2)$$

In this notation, the Λ_b decay asymmetry parameter α_{Λ_b} is given by [15]:

$$\alpha_{\Lambda_b} = \frac{|a_+|^2 - |a_-|^2 + |b_+|^2 - |b_-|^2}{|a_+|^2 + |a_-|^2 + |b_+|^2 + |b_-|^2}. \quad (3)$$

The helicity amplitudes a_+ , a_- , b_+ , b_- are computed directly from the decay amplitudes A_1, A_2, B_1, B_2 according to the following equations:

$$\begin{aligned}
a_+ &= \tfrac{1}{m_{J/\psi}} \left\{ \sqrt{Q_+} \left[(m_{\Lambda_b} - m_\Lambda) A_1 - \tfrac{Q_-}{2m_{\Lambda_b}} A_2 \right] + \sqrt{Q_-} \left[(m_{\Lambda_b} + m_\Lambda) B_1 + \tfrac{Q_+}{2m_{\Lambda_b}} B_2 \right] \right\}, \\
a_- &= \tfrac{1}{m_{J/\psi}} \left\{ -\sqrt{Q_+} \left[(m_{\Lambda_b} - m_\Lambda) A_1 - \tfrac{Q_-}{2m_{\Lambda_b}} A_2 \right] + \sqrt{Q_-} \left[(m_{\Lambda_b} + m_\Lambda) B_1 + \tfrac{Q_+}{2m_{\Lambda_b}} B_2 \right] \right\}, \\
b_+ &= \sqrt{2} \left(\sqrt{Q_+}\, A_1 \mp \sqrt{Q_-}\, B_1 \right), \\
b_- &= -\sqrt{2} \left(\sqrt{Q_+}\, A_1 \mp \sqrt{Q_-}\, B_1 \right),
\end{aligned} \tag{4}$$

where $Q_\pm = (m_{\Lambda_b} \pm m_\Lambda)^2 - m^2_{J/\psi}$ and m_{Λ_b} and m_Λ are the Λ_b and Λ masses respectively [16, 17].

The polarization of the Λ_b can be determined from the angular correlations between the $\Lambda_b \to J/\psi\Lambda$ final decay products. The Λ_b polarization reveals itself in the asymmetry of the distribution of the angle θ. This angle is defined as the angle between the normal to the beauty baryon production plane and the momentum vector of the Λ decay daughter, as seen in the Λ_b rest frame. The decay angular distribution can be expressed as:

$$w \sim 1 + \alpha_{\Lambda_b} P \cos(\theta), \tag{5}$$

where α_{Λ_b} is the decay asymmetry parameter of Λ_b and P is the Λ_b polarization [18].

Using the method described in [17], it can be shown that the full decay angular distribution is:

$$w(\vec{\theta}, \vec{A}, P) = \frac{1}{(4\pi)^3} \sum_{i=0}^{i=19} f_{1i}(\vec{A})\, f_{2i}(P, \alpha_\Lambda)\, F_i(\vec{\theta}) \tag{6}$$

where the $f_{1i}(\vec{A})$ are bilinear combinations of the helicity amplitudes and $\vec{A} = (a_+, a_-, b_+, b_-)$. f_{2i} stands for $P\alpha_\Lambda$, P, α_Λ, or 1, where α_Λ is Λ decay asymmetry parameter. F_i are orthogonal angular functions defined in Table 1. The Λ_b decay asymmetry parameter α_{Λ_b} is related to the helicity amplitudes as defined in Equation 3. The five angles $\vec{\theta} = (\theta, \theta_1, \theta_2, \varphi_1, \varphi_2)$ (see Figure 2) in this probability density function (p.d.f.) have the following meanings:

- θ is the angle between the normal to the production plane and the direction of the Λ in the rest frame of the Λ_b particle;
- θ_1 and ϕ_1 are the polar and azimuthal angles that define the direction of the proton in the Λ rest frame with respect to the direction of the Λ in the Λ_b rest frame;
- θ_2 and ϕ_2, define the direction of μ^+ in the J/ψ rest frame with respect to the direction of the J/ψ in the Λ_b rest frame.

There are nine unknown parameters in Equation 6. They are the polarization P and four complex helicity amplitudes: $a_+ = |a_+|e^{i\alpha_+}$, $a_- = |a_-|e^{i\alpha_-}$, $b_+ = |b_+|e^{i\beta_+}$, $b_- = |b_-|e^{i\beta_-}$. Using the normalization condition (see Equation 2) and using the fact that the overall global phase is arbitrary, we can reduce the number of unknown independent parameters to seven.

3 Monte Carlo samples

In order to determine if it is feasible to detect polarized Λ_b's in the ATLAS experiment and to measure their polarization, Monte Carlo samples of polarized Λ_b particles were generated using the standard ATLAS software packages. The generation of polarized Λ_b particles and the propagation of their polarization in the decay process required a special treatment, and EVTGEN was adapted for this purpose. The next sections describe how this was implemented in the framework of the ATLAS experiment.

i	f_{1i}	f_{2i}	F_i
0	$a_+a_+^* + a_-a_-^* + b_+b_+^* + b_-b_-^*$	1	1
1	$a_+a_+^* - a_-a_-^* + b_+b_+^* - b_-b_-^*$	P	$\cos\theta$
2	$a_+a_+^* - a_-a_-^* - b_+b_+^* + b_-b_-^*$	α_Λ	$\cos\theta_1$
3	$a_+a_+^* + a_-a_-^* - b_+b_+^* - b_-b_-^*$	$P\alpha_\Lambda$	$\cos\theta\cos\theta_1$
4	$-a_+a_+^* - a_-a_-^* + \frac{1}{2}b_+b_+^* + \frac{1}{2}b_-b_-^*$	1	$1/2\,(3\cos^2\theta_2 - 1)$
5	$-a_+a_+^* + a_-a_-^* + \frac{1}{2}b_+b_+^* - \frac{1}{2}b_-b_-^*$	P	$1/2\,(3\cos^2\theta_2 - 1)\cos\theta$
6	$-a_+a_+^* + a_-a_-^* - \frac{1}{2}b_+b_+^* + \frac{1}{2}b_-b_-^*$	α_Λ	$1/2\,(3\cos^2\theta_2 - 1)\cos\theta_1$
7	$-a_+a_+^* - a_-a_-^* - \frac{1}{2}b_+b_+^* - \frac{1}{2}b_-b_-^*$	P,α_Λ	$1/2\,(3\cos^2\theta_2 - 1)\cos\theta\cos\theta_1$
8	$-3Re(a_+a_-^*)$	P,α_Λ	$\sin\theta\sin\theta_1\sin^2\theta_2\cos\varphi_1$
9	$3Im(a_+a_-^*)$	$P\alpha_\Lambda$	$\sin\theta\sin\theta_1\sin^2\theta_2\sin\varphi_1$
10	$-\frac{3}{2}Re(b_-b_+^*)$	$P\alpha_\Lambda$	$\sin\theta\sin\theta_1\sin^2\theta_2\cos(\varphi_1 + 2\varphi_2)$
11	$\frac{3}{2}Im(b_-b_+^*)$	$P\alpha_\Lambda$	$\sin\theta\sin\theta_1\sin^2\theta_2\sin(\varphi_1 + 2\varphi_2)$
12	$-\frac{3}{\sqrt{2}}Re(b_-a_+^* + a_-b_+^*)$	$P\alpha_\Lambda$	$\sin\theta\cos\theta_1\sin\theta_2\cos\theta_2\cos\varphi_2$
13	$\frac{3}{\sqrt{2}}Im(b_-a_+^* + a_-b_+^*)$	$P\alpha_\Lambda$	$\sin\theta\cos\theta_1\sin\theta_2\cos\theta_2\sin\varphi_2$
14	$-\frac{3}{\sqrt{2}}Re(b_-a_-^* + a_+b_+^*)$	$P\alpha_\Lambda$	$\cos\theta\sin\theta_1\sin\theta_2\cos\theta_2\cos(\varphi_1 + \varphi_2)$
15	$\frac{3}{\sqrt{2}}Im(b_-a_-^* + a_+b_+^*)$	$P\alpha_\Lambda$	$\cos\theta\sin\theta_1\sin\theta_2\cos\theta_2\sin(\varphi_1 + \varphi_2)$
16	$\frac{3}{\sqrt{2}}Re(a_-b_+^* - b_-a_+^*)$	P	$\sin\theta\sin\theta_2\cos\theta_2\cos\varphi_2$
17	$-\frac{3}{\sqrt{2}}Im(a_-b_+^* - b_-a_+^*)$	P	$\sin\theta\sin\theta_2\cos\theta_2\sin\varphi_2$
18	$\frac{3}{\sqrt{2}}Re(b_-a_-^* - a_+b_+^*)$	α_Λ	$\sin\theta_1\sin\theta_2\cos\theta_2\cos(\varphi_1 + \varphi_2)$
19	$-\frac{3}{\sqrt{2}}Im(b_-a_-^* - a_+b_+^*)$	α_Λ	$\sin\theta_1\sin\theta_2\cos\theta_2\sin(\varphi_1 + \varphi_2)$

Table 1: The coefficients f_{1i}, f_{2i} and F_i of the probability density function in Equation 6.

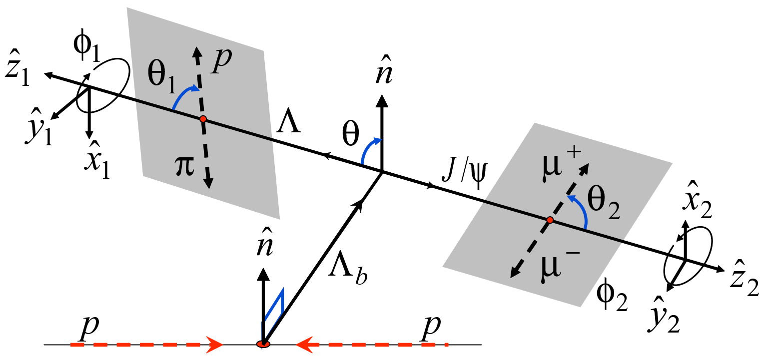

Figure 2: Angles describing the $\Lambda_b \to J/\psi(\mu^+\mu^-)\Lambda(p\pi^-)$ decay.

3.1 The generation of polarized Λ_b particles

To generate Λ_b particles, the PYTHIA 6.4 generator [19] is used. Since PYTHIA does not incorporate polarization information from the decay of Λ_b particles, EVTGEN was used to generate the Λ_b decay. EVTGEN provides a general framework for implementation of B hadron decays using spinor algebra and decay amplitudes. This framework permits the proper management of spin correlations of very complicated decay processes. EVTGEN is a Monte Carlo generation package itself, but in this case it is used only to decay the Λ_b particles produced by PYTHIA.

3.1.1 Re−hadronization process and cuts at PYTHIA level

PYTHIA provides mechanisms to produce b quarks, referred to as gluon−gluon fusion, q-$\bar{q}$ annihilation, flavor excitation, and gluon splitting. If all these processes are taken into account, beauty quark events would constitute only 1% of the total number of generated events. In addition, the fraction of b quarks hadronizing to Λ_b is less than 10%. These make the process of Λ_b generation computationally slow. To optimize the generation process, a re−hadronization step of the same event in the $b\bar{b}$ pairs production is used. In order to avoid repetition of Λ_b events due to the re-hadronization process, a Λ_b pre−selection is implemented at this stage to filter on average only one of the re−hadronized copies of the same event. An additional reason that the Λ_b generation process is slow is that around 95% of final state particles (two muons, a proton, and a pion) of the generated Λ_b events are outside of the η limits ($|\eta| < 2.5$) of the ATLAS detector. In addition, all events must pass the level−1 trigger of the ATLAS trigger system and some pre−reconstruction requirements, such as having a minimum reconstructable transverse momentum. We could not apply these cuts in the PYTHIA step since the kinematics information of the Λ_b children is available only at a later stage, when EVTGEN decays the Λ_b particles. However, by analyzing the p_T and η distributions of Λ_b particles before and after cuts (emulating level−1 and level−2 triggers, and requiring $|\eta| < 2.5$) on the final state particles, we estimated p_T and η limits, below which the Λ_b can not be selected and then applied these cuts in the PYTHIA selection. Figure 3 shows the p_T and η distributions from which the $p_T(\Lambda_b) > 6000$ MeV and $|\eta(\Lambda_b)| < 3$ cuts were selected to filter Λ_b particles in PYTHIA.

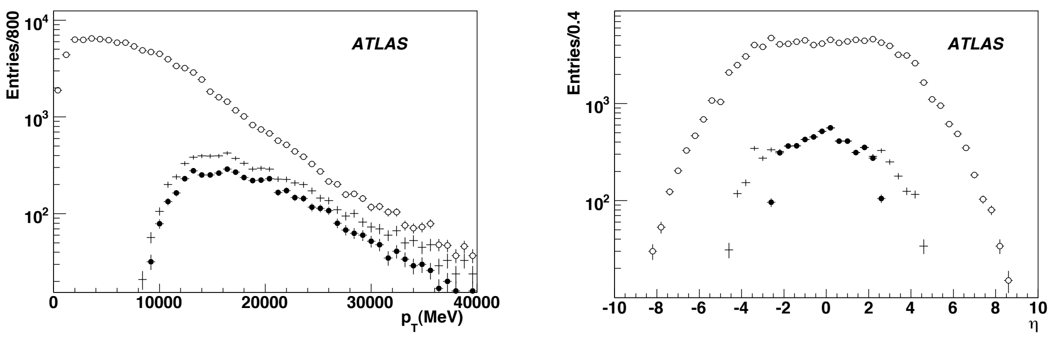

Figure 3: Distributions of p_T (left) and η (right) for Λ_b particles generated using PYTHIA, without cuts (hollow circle), applying η cuts only (cross) and applying all cuts (solid circle) from Table 2.

3.1.2 Setting Λ_b polarization in EVTGEN

To set the polarization of Λ_b particles we used the spin density matrix description of EVTGEN. For the case of spin−1/2 particles like Λ_b the density matrix is defined as:

$$\rho = \frac{1}{2}(I + \vec{P} \cdot \vec{\sigma}) \tag{7}$$

where $\vec{P}$ is the polarization vector, and $\vec{\sigma} = (\sigma_1, \sigma_2, \sigma_3)$, where σ_i is i-th Pauli matrix. In our case $\vec{P}$ is defined as:

$$\vec{P} = P\left(\frac{\hat{z} \times \vec{p}_{lab}(\Lambda_b)}{|\hat{z} \times \vec{p}_{lab}(\Lambda_b)|}\right) \tag{8}$$

where P is the magnitude of the polarization, $\vec{p}_{lab}$ is the momentum of the Λ_b in the laboratory frame, and $\hat{z}$ is the z - axis (along the beam direction) in the ATLAS reference system.

To decay polarized Λ_b we use the HELAMP model of EVTGEN. This model is capable of simulating a generic two body decay with arbitrary spin configuration, taking as input the helicity amplitudes describing the process. In the case of the decay $\Lambda_b \to J/\psi(\mu^+\mu^-)\Lambda(p\pi^-)$, as it has been shown in the previous section, there are four complex helicity amplitudes: a_+, a_-, b_+, and b_-.

The Λ decay into a proton and a pion has been simulated with the same model, using as input parameters the two helicity amplitudes $H_{\lambda_\Lambda,\lambda_p}$ defined in terms of the Λ helicity λ_Λ and the proton λ_p helicity as

$$h_- = H_{-\frac{1}{2},-\frac{1}{2}}, \quad h_+ = H_{+\frac{1}{2},+\frac{1}{2}}. \tag{9}$$

The choice of $h_\pm$ is constrained by the experimentally well known $\Lambda \to p\pi^-$ asymmetry parameter [20]

$$\alpha_\Lambda = |h_+|^2 - |h_-|^2 = 0.642 \pm 0.013. \tag{10}$$

Finally, the decay $J/\psi \to \mu^+\mu^-$ has been described with the EVTGEN VLL (Vector into Lepton Lepton) model [7].

3.1.3 Filtering of $\Lambda_b \to J/\psi(\mu^+\mu^-)\Lambda(p\pi^-)$ events

As a last step in the generation process, we apply kinematic cuts on muons, pion and proton to emulate the fiducial acceptance, level−1 trigger, and pre−reconstruction requirements. These cuts are summarized in Table 2.

Particles	Minimum p_T [MeV]	Maximum $\|\eta\|$
Protons and π's	500	2.7
Most energetic muon	4000	2.7
Other muon	2500	2.7

Table 2: Cuts applied at the particle level.

3.2 Monte Carlo samples and input model for Λ_b decays

As input to the HELAMP class of EVTGEN, the result obtained within the framework of PQCD formalism and the factorization theorem [9] has been used to model the Λ_b decay. From the complex amplitudes calculated in this model, A_1, A_2, B_1, B_2 in Equation 1, the helicity amplitudes a_+ , a_- , b_+ , b_- are calculated by using Equation 4. This is summarized in Table 3. In this model, the Λ_b decay asymmetry parameter, defined in Equation 3, is α_{Λ_b} = -0.457 [1].

$A_1 = -18.676 - 185.036i$	$a_+ = -0.0176 - 0.4229i$
$A_2 = -7.461 - 351.242i$	$a_- = 0.0867 + 0.2425i$
$B_1 = 15.818 - 162.663i$	$b_+ = -0.0810 - 0.2837i$
$B_2 = -4.252 + 266.653i$	$b_- = 0.0296 + 0.8124i$

Table 3: PQCD model amplitudes A_i and B_i, are given in units of 10^{-10} and helicity amplitudes $a_\pm$ and $b_\pm$ are normalized to unity.

By using this decay model as input, two Monte Carlo samples were generated with polarizations of -25% and -75%. These Monte Carlo samples were generated, simulated, and fully reconstructed by using the Athena framework [21].

[1]There is an ERRATA in [9] in the reported value of α_{Λ_b} [14].

To show how the angular distributions behave, fast Monte Carlo samples (see section 3.3) were generated using an accepted−rejected method based on the p.d.f. defined in Equation 6. Figure 4 shows the distributions of the five angles for helicity amplitudes from Table 3 and polarizations of 40%, 0%, -40%.

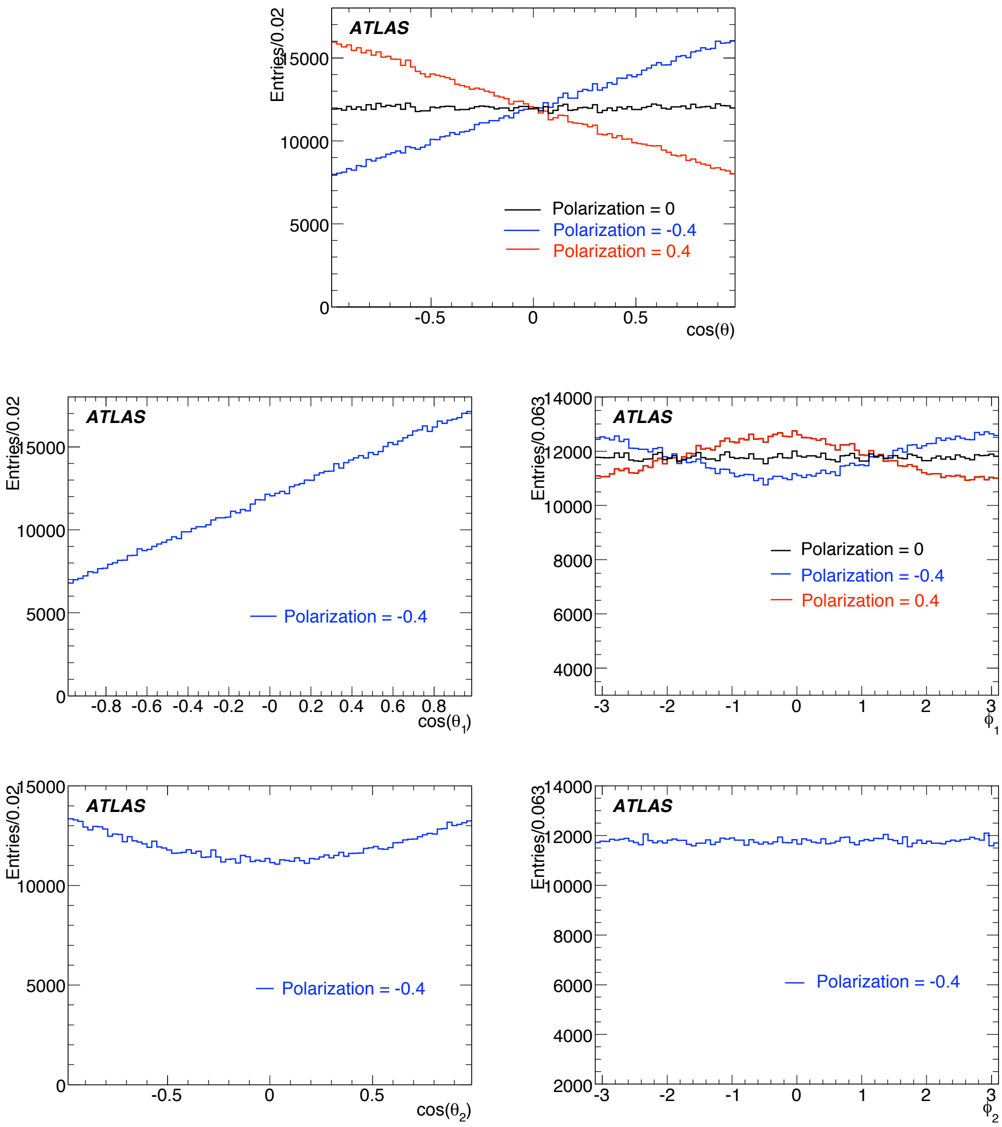

Figure 4: Distributions of the five angles characterizing the decay $\Lambda_b \to J/\psi(\mu^+\mu^-)\Lambda(p\pi^-)$ for different polarization values. For $cos(\theta_1)$, $cos(\theta_2)$, and ϕ_2, all three distributions for the different polarization values look similar, thus only one polarization case is presented.

3.3 Fast Monte Carlo generation

In order to do fast tests of different Λ_b decay models and different polarization values, we need to generate large Monte Carlo samples. This represents a problem due to the computer time required to produce a full chain simulated Monte Carlo data. In order to address this problem a fast Monte Carlo generator was developed. This generator uses Equation 6 to generate angular distributions for the daughters of the Λ_b in the Λ_b rest frame, and then uses a (p,η) distribution derived from phase space of generated events in PYTHIA to compute the kinematic variables of the daughter particles in the laboratory frame. Detector effects are incorporated by using p_T and η cuts on final state particles to mimic di-muon triggers and pre−reconstruction requirements. Figure 5 illustrates the strong agreement between angular distributions produced by using PYTHIA and EVTGEN Monte Carlo events and fast Monte Carlo events.

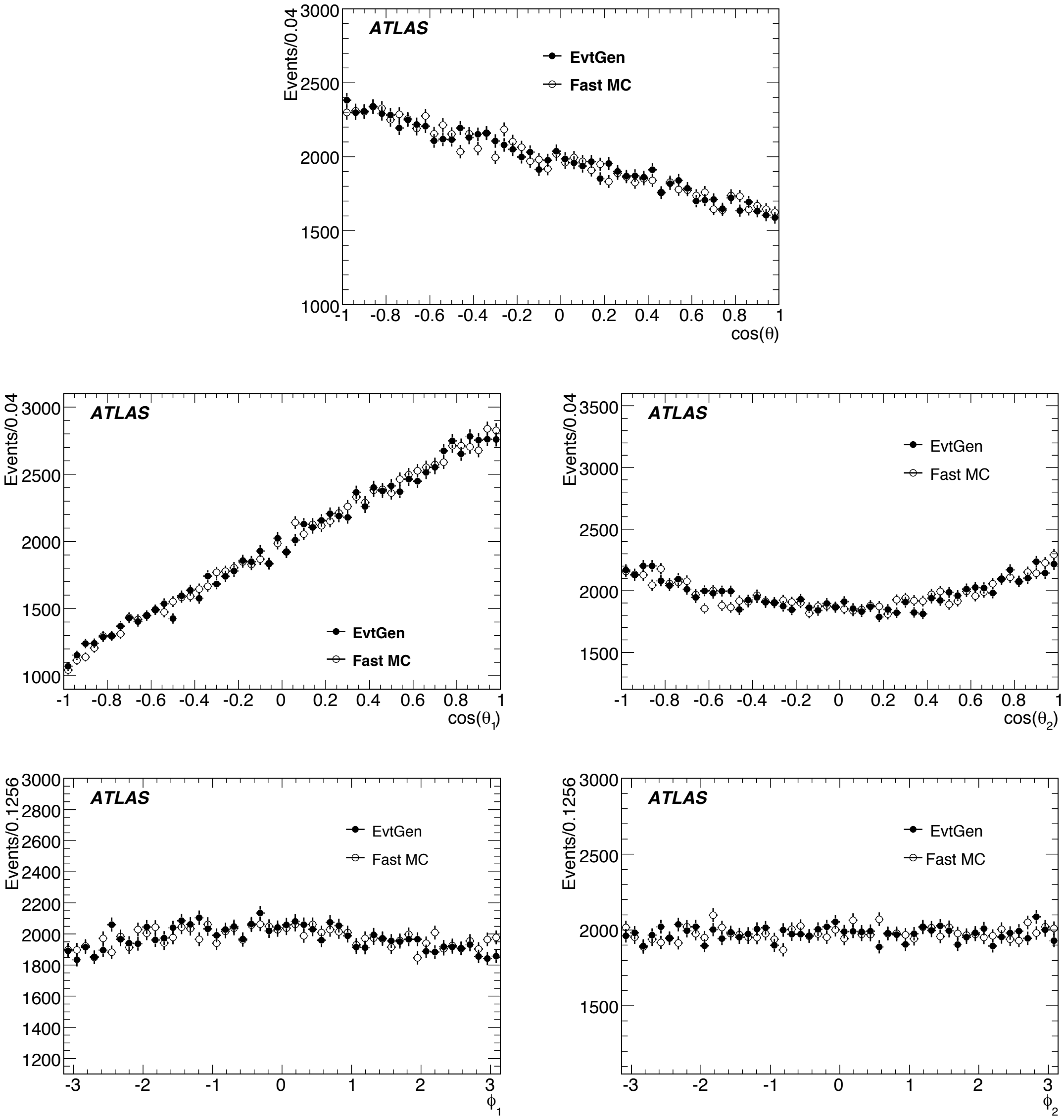

Figure 5: Comparison of Monte Carlo events (PYTHIA + EVTGEN) with fast Monte Carlo generated events. Solid dots represent the Monte Carlo events.

4 Λ_b reconstruction

The reconstruction of Λ_b candidates begins with a search for events with J/ψ candidates. Among these events we search for $\Lambda \to p\pi^-$ candidates, which are then combined with the J/ψ to reconstruct the Λ_b.

4.1 Selection of $J/\psi \rightarrow \mu^+\mu^-$ candidates

We search for J/ψ candidates which satisfy the following selection criteria:

- The $\mu^+\mu^-$ candidates must originate at the same reconstructed vertex and the χ^2 of the vertex must be lower than 20;
- The invariant mass of $\mu^+\mu^-$ candidates M($\mu^+\mu^-$) should be within 2800 MeV and 3400 MeV.

The invariant mass distribution of $\mu^+\mu^-$ candidates before applying the invariant mass cuts to select Λ_b is shown in Figure 6.

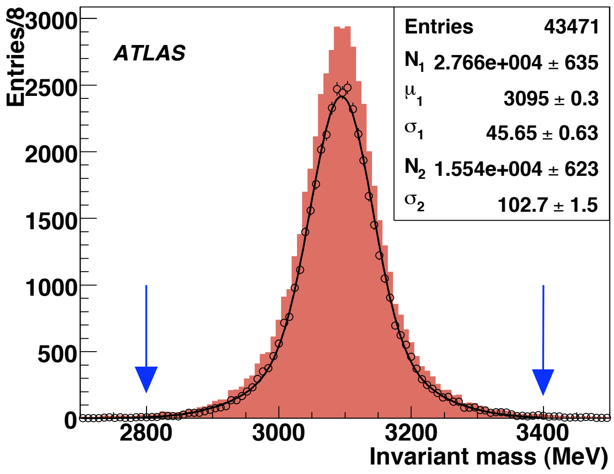

Figure 6: Invariant mass of $\mu^+\mu^-$ candidates. The dark color represents all J/ψ candidates after reconstruction and vertexing requirement. The circles represents J/ψ candidates when level−1 and level−2 trigger signature are required.

4.2 Selection of $\Lambda \rightarrow p\pi^-$ candidates

From the previously selected events containing a J/ψ , Λ candidates are selected by applying the following requirements:

- Two opposite charged tracks originating from the same reconstructed vertex.
- The invariant mass of two tracks M($p\pi^-$) should be within 1105 MeV and 1128 MeV range, where for computing M($p\pi^-$), the track with the highest transverse momentum was assumed to be the proton, as observed in 100% of the times in Monte Carlo generations, while the other track was assumed to be a pion.

Many of the Λ particles decay outside of the high−precision part of the Inner Detector, which covers a radius of about 40 cm from the beam line, and thus are lost in reconstruction. The decay vertex position of Λ's in the *RZ* plane is presented in Figure 8. If the Λ decays outside the 40 cm radius, the number of reconstructed space points (hits in the pixel or silicon layers) is not sufficient for a successful track reconstruction. This effect reduces the fraction of reconstructible Λ to around 60%. Figure 7 presents the invariant mass distribution of the $p\pi^-$ candidates before the invariant mass cuts have been applied.

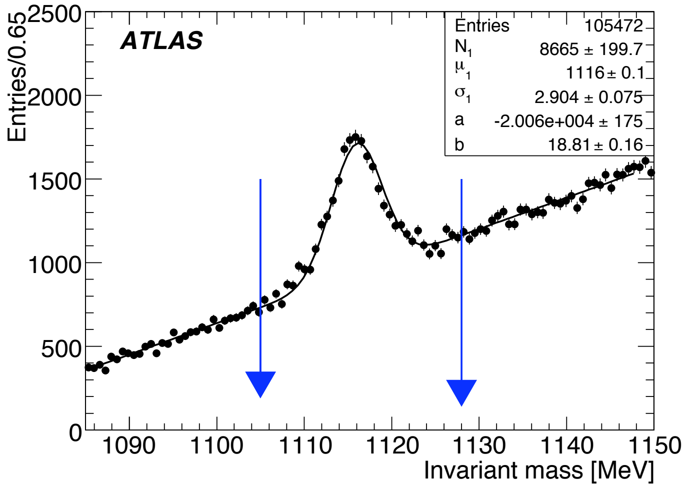

Figure 7: Invariant mass of $p\pi^-$ candidates.

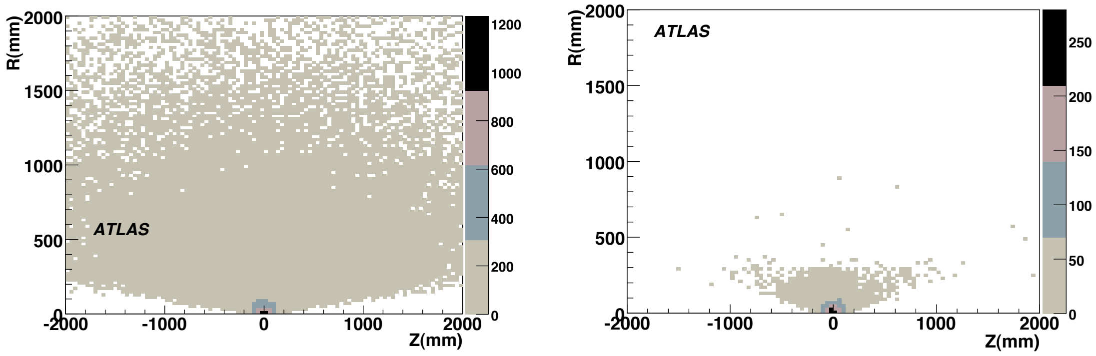

Figure 8: Decay vertex position of Λ's in the RZ plane at the generation level (left) and after reconstruction (right)

.

4.3 Selection of $\Lambda_b \to J/\psi(\mu^+\mu^-)\Lambda(p\pi^-)$ candidates

A previous study [22] based on early ATLAS simulation software estimated that the number of Λ_b and $\overline{\Lambda_b}$ events which we expect to collect for the integrated luminosity of 30 fb^{-1} is 75000. Using the new fully reconstructed sample we made a new estimation. We used the following expression to calculate the number of events:

$$\mathscr{N} = \mathscr{L}\sigma(\Lambda_b)\mathscr{E}, \tag{11}$$

where $\mathscr{L}$ is the integrated luminosity, $\sigma(\Lambda_b)$ = 7.4 pb is the cross section of $\Lambda_b \to J/\psi(\mu(p_T > 4000\text{ MeV})\mu(p_T > 2500\text{ MeV}))\Lambda(p(p_T > 500\text{ MeV})\pi(p_T > 500\text{ MeV}))$, see details of the calculation in Table 4, and $\mathscr{E}$ is an overall Λ_b acceptance, which includes the level-1 and level-2 acceptance for $\Lambda_b \to J/\psi(\mu^+\mu^-)\Lambda(p\pi^-)$.

For selecting events with b hadrons at a luminosity below about $10^{33} cm^{-2}s^{-1}$, the first level trigger will require the presence of a muon with p_T > 6000 MeV within the trigger geometric acceptance of $|\eta| < 2.4$. The effect of the level-1 trigger threshold on muon p_T is not a sharp cut and a fraction of

$\sigma(pp \to \Lambda_b X)$	0.00828113 mb
BR ($\Lambda_b \to J/\psi\Lambda$)	$(4.7 \pm 2.8) \times 10^{-4}$ [20]
BR ($\Lambda \to p\pi^-$)	$(63.9 \pm 0.5) \times 10^{-2}$ [20]
BR ($J/\psi \to \mu^+\mu^-$)	$(5.93 \pm 0.06) \times 10^{-2}$ [20]
Including cuts	0.05
Overall cross-section	**7.4 pb**

Table 4: The cross-section calculation of $\Lambda_b \to J/\psi(\mu^+\mu^-)\Lambda(p\pi^-)$ decay.

muons with p_T lower than 6000 MeV will be collected. Figure 9 shows the efficiency of the level$-$1 simulation with nominal p_T threshold of 6000 MeV as function of p_T. Around 69% of events with $J/\psi \to \mu^+\mu^-$, where one muon has $p_T > 4000$ MeV and the second muon has $p_T > 2500$ MeV, passed the level$-$1 trigger simulation. Therefore a signal dataset with p_T less than 6000 MeV has been chosen to study all possible triggered events with low p_T muons instead of a usual sharp 6000 MeV cut.

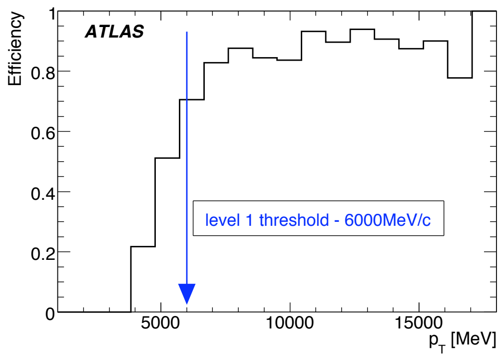

Figure 9: The level$-$1 trigger simulation efficiency as a function of muon p_T, obtained from the Λ_b signal sample over the whole detector volume.

Further selections in the high level trigger are based on the Region of Interest (RoI) identified at level$-$1, as follows: a search for a second muon close to the trigger muon is used to select channels containing two final state muons, for example from J/ψ. It is based on expanding the level$-$1 muon RoI to find a second muon which was not triggered by level$-$1. This increases the efficiency of the di$-$muon trigger by extending the p_T acceptance for the second muon down below 6000 MeV. The size of the increased RoI is based on the distribution of angular distance in η and ϕ between two muons decayed from J/ψ. The Inner Detector tracks which are reconstructed within these RoI, are then extrapolated to the muon system to find the corresponding hits within the window. The Inner Detector tracks associated with the muon spectrometer hits can be identified as muons. The level$-$2 trigger efficiency is found to be around 78% for $\Lambda_b \to J/\psi(\mu(p_T > 4000\text{ MeV})\mu(p_T > 2500\text{ MeV}))\Lambda(p(p_T > 500\text{ MeV})\pi(p_T > 500\text{ MeV}))$.

We reconstruct the Λ_b by performing a constrained fit to a common vertex for the two muon tracks and Λ, with the two muon tracks constrained to the J/ψ mass of 3097 MeV [20]. The reconstruction efficiency depends on the cuts which will be applied on all Inner Detector tracks in the reconstruction stage to reduce the fake rate. The overall efficiency is found to be around 6.1% if the p_T threshold is 500 MeV, see Table 5. Figure 10 shows the invariant mass distribution of Λ_b candidates. Simulation of the level$-$1 trigger with level$-$1 p_T thresholds of 6000 MeV and 4000 MeV and level$-$2 trigger, explained above, included in the analysis. We expect to collect around 13500 (13100) $\Lambda_b \to J/\psi(\mu^+\mu^-)\Lambda(p\pi^-)$ events using 4000 MeV (6000 MeV) level-1 muon threshold for the integrated luminosity of about 30 fb^{-1} .

level-1 trigger: with p_T threshold	one muon 4 GeV	one muon 6 GeV	two muons 4GeV	two muons 6GeV
level-2 trigger:	TrigDiMuon		Topological trigger	
J/ψ reconstruction efficiency including level-1 and level-2 triggers	42%	39%	27.5%	10%
Λ reconstruction efficiency	15%			
Λ_b overall efficiency	6.1%	5.9%	5.4%	3.5%

Table 5: The overall Λ_b efficiency depending on the trigger strategy.

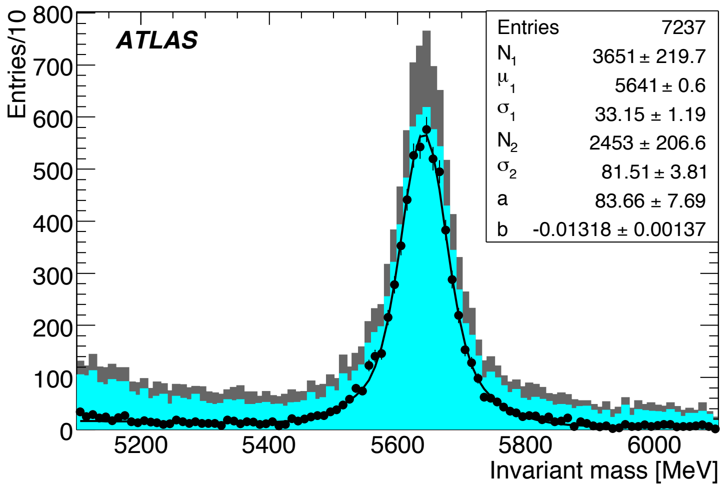

Figure 10: $\mu^+\mu^-$ Λ invariant mass distribution. The dark color represents all Λ_b candidates after reconstruction and vertexing requirement, and the light color represents the case when a level-1 and level-2 trigger signature is required in addition. Filled circles represents data after all selection cuts. The fit is the result of using double Gaussian and Polynomial functions.

We need to acknowledge that there are other inefficiencies that will appear when we analyze the real data. For example, even if the individual track reconstruction efficiency is as high as 98%, we will have an overall reduction in event rate of about 10%. Even if such reductions occur, we still expect the final sample to be sufficient for a meaningful measurement of the Λ_b polarization.

4.4 Angular distributions and angular resolutions

The reconstruction efficiency modifies the angular distributions used in the polarization determination. Figure 11 shows how the angular distributions change due to detector acceptance for a Monte Carlo sample with polarization of -75%.

The angular resolution of the five angles is presented in Figure 12. We used this angular resolution in the statistical uncertainty study.

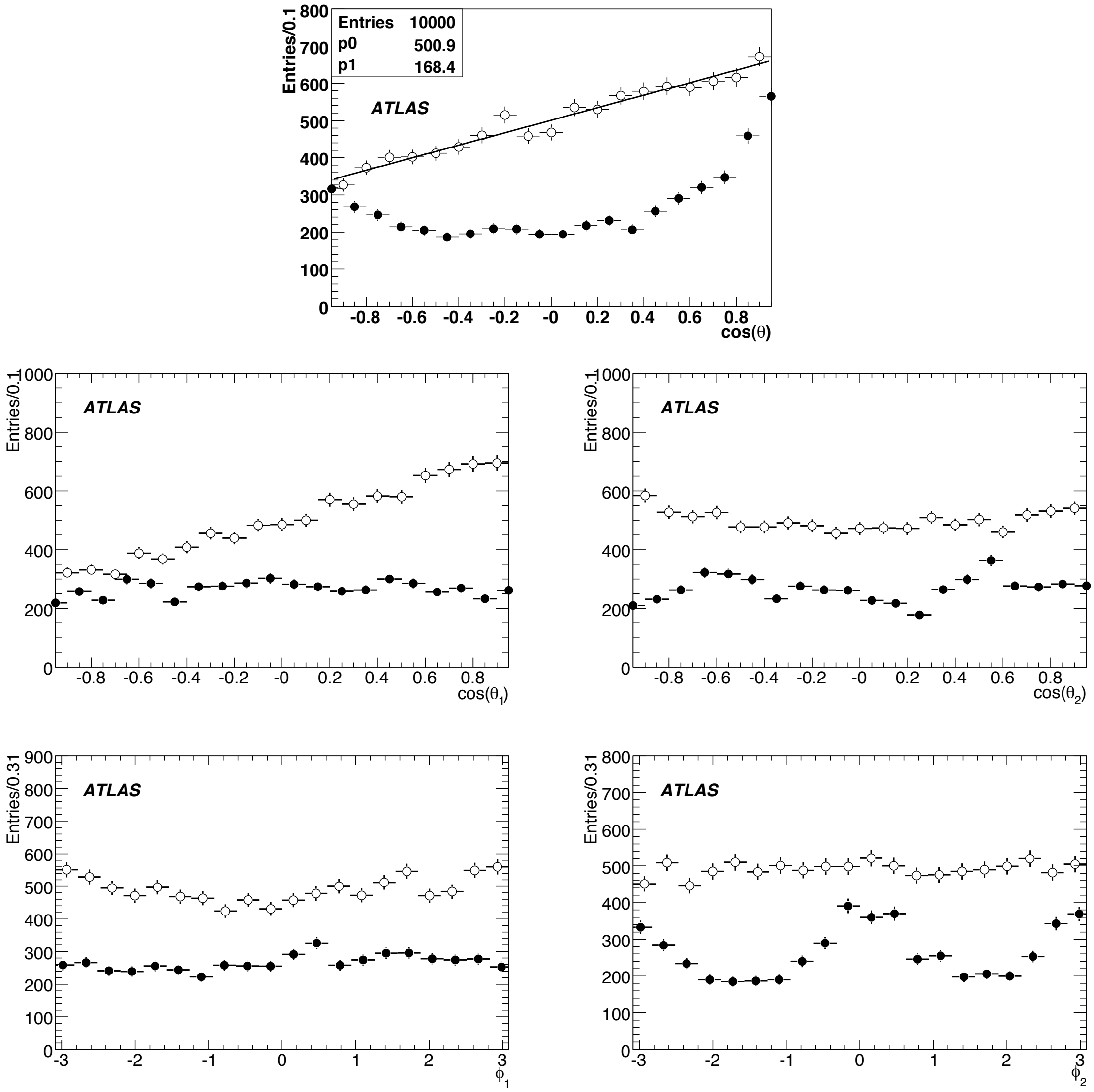

Figure 11: Comparison of fast Monte Carlo events without kinematics and detector acceptance cuts (open circles) and Monte Carlo events after full detector simulation and reconstruction (solid circles).

4.5 Background

Due to its production rate the main background source for our Λ_b reconstruction will be the prompt production and decay of $J/\psi \rightarrow \mu^+\mu^-$ which are then combined with Λ candidates in the event. However, the long lifetime of the Λ_b allows us to reduce significantly this kind of background by applying a lifetime cut. After a Λ_b lifetime cut (a cut of 200 μm on the proper transverse decay length), this background was found to be negligible and it is not considered in this study.

In order to investigate the different contributions of long−lived background particles not removed by the lifetime cut mentioned above, we used a inclusive J/ψ Monte Carlo sample of $b\bar{b} \rightarrow J/\psi X$ requiring in addition to a J/ψ , a Λ in each event ($b\bar{b} \rightarrow J/\psi \Lambda X$). This Λ could be produced along with the J/ψ from a B hadron decay or just be part of the event, and the invariant mass of the $J/\psi + \Lambda$ combination should be within 5100 - 6100 MeV. Figure 13 shows the invariant mass distributions of Λ_b candidates

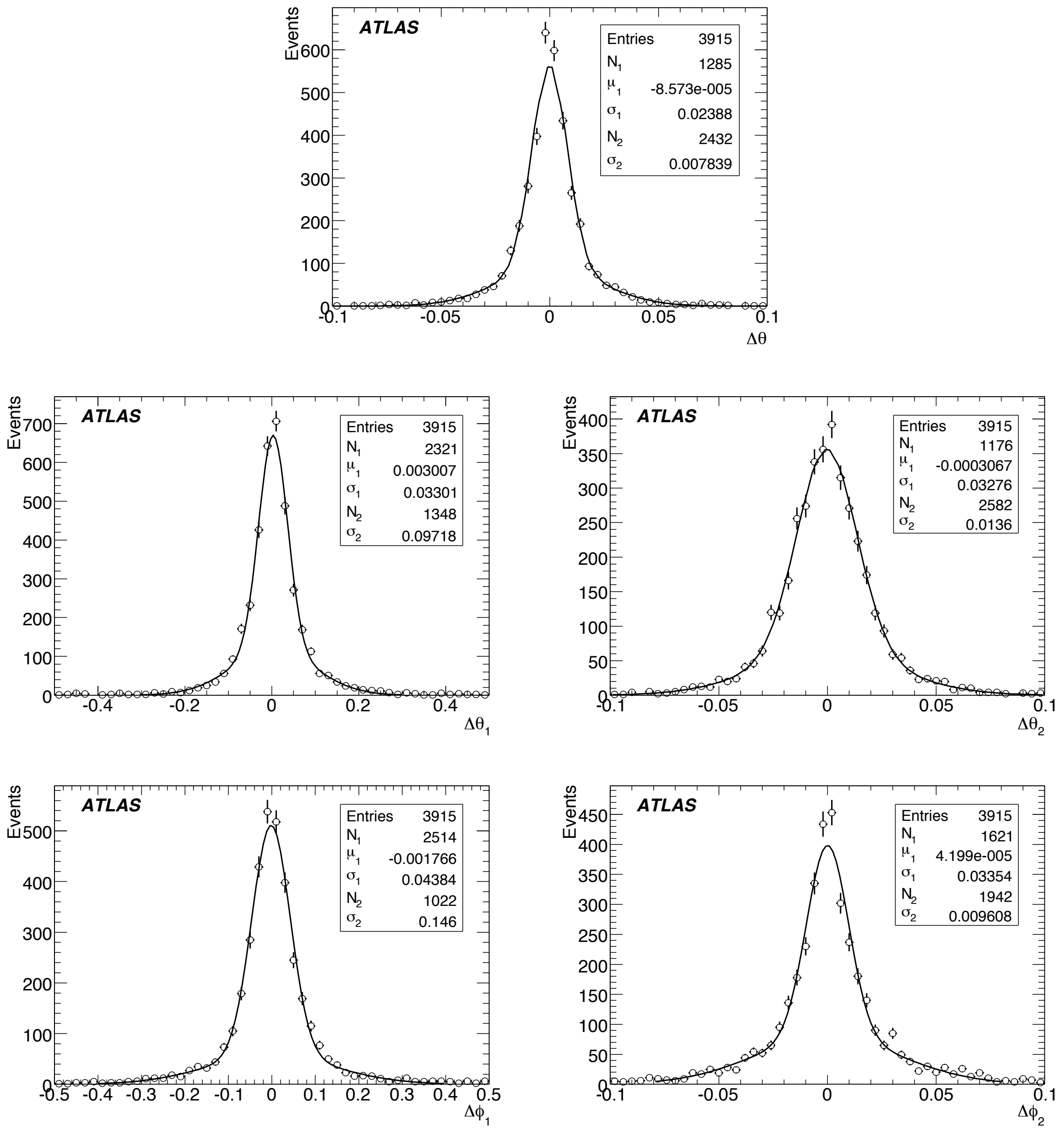

Figure 12: Angular resolution from fully simulated Monte Carlo data. The fit is the result of using double Gaussian distributions.

reconstructed in this Monte Carlo sample. The observed level of background under the Λ_b signal is of few percents, and it is considerably reduced after extra cuts like the lifetime cut mentioned above. In Figure 13 another wider distribution due to $\Lambda_b \rightarrow J/\psi\Sigma^0(\Lambda\gamma)$ is observed very close to our $\Lambda_b \rightarrow J/\psi\Lambda$ signal. This is due to the branching ratios of both decays channels being the same as set by default in PYTHIA. This behavior has not been observed at Tevatron experiments where hundreds of $\Lambda_b \rightarrow J/\psi\Lambda$ events are reconstructed. Therefore we expect the branching ratio of the $\Lambda_b \rightarrow J/\psi\Sigma^0(\Lambda\gamma)$ decay to be considerably smaller than the branching ratio of the $\Lambda_b \rightarrow J/\psi\Lambda$, and that the resulting background will be much smaller than shown.

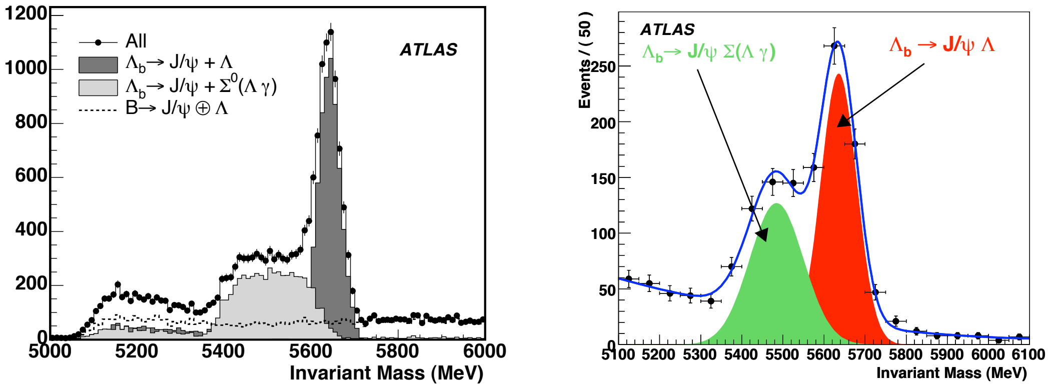

Figure 13: Invariant mass distribution from Λ_b candidates identified in $b \to J/\psi \Lambda X$ Monte Carlo sample. Composition at generation level with smearing from reconstruction (left) and fit to the fully reconstructed events (right) after vertexing requirement are shown.

5 Extracting Λ_b polarization and decay parameters

5.1 Fitting method

5.1.1 Likelihood function

To extract polarization and decay amplitudes we performed an un−binned maximum likelihood fit to the angular distributions. The log−likelihood function $\mathscr{L}$ is defined by:

$$\mathscr{L} = -2 \sum_{j=1}^{N} \log(w_{obs}(\vec{\theta}', \vec{A}, P)), \tag{12}$$

where

$$w_{obs}(\vec{\theta}', \vec{A}, P) = \frac{\int w(\vec{\theta}', \vec{A}, P) T(\vec{\theta}, \vec{\theta}') d\vec{\theta}}{\int \int w(\vec{\theta}', \vec{A}, P) T(\vec{\theta}, \vec{\theta}') d\vec{\theta} d\vec{\theta}'}. \tag{13}$$

$w(\vec{\theta}', \vec{A}, P)$ is the p.d.f defined in Equation 6, $\vec{\theta}'$ are the measured angles, $\vec{\theta}$ are angles without detector effects, and $T(\vec{\theta}, \vec{\theta}')$ is defined as

$$T(\vec{\theta}, \vec{\theta}') = \varepsilon(\vec{\theta}) R(\vec{\theta}, \vec{\theta}'), \tag{14}$$

where $\varepsilon(\vec{\theta})$ is the efficiency function and $R(\vec{\theta}, \vec{\theta}')$ is the resolution function.

In the ideal case the resolution function is:

$$R(\vec{\theta}, \vec{\theta}') = \delta(\vec{\theta} - \vec{\theta}'), \tag{15}$$

then we have

$$w_{obs}(\vec{\theta}', \vec{A}, P) = \frac{w(\vec{\theta}', \vec{A}, P) \varepsilon(\vec{\theta}')}{\sum_{i=0}^{i=19} f_{1i}(\vec{A}) f_{2i}(P\alpha_\Lambda) \mathscr{F}_i}, \tag{16}$$

where $\mathscr{F}_i = \int F_i(\vec{\theta}) \varepsilon(\vec{\theta}) d\vec{\theta}$ are the acceptance corrections values, which have to be calculated in advance to perform the fit.

The final log−likelihood may be re−written as a sum of two terms:

$$L = -2 \sum_{j=1}^{N} [\log(\frac{w(\vec{\theta}', \vec{A}, P)}{\sum_{i=0}^{i=19} f_{1i}(\vec{A}) f_{2i}(P\alpha_\Lambda) \mathscr{F}_i}) + \log(\varepsilon(\vec{\theta}'))]. \tag{17}$$

Since the second term does not depend on the parameters we want to measure, the main challenge is to find the acceptance function.

5.1.2 Detector acceptance corrections

The acceptance corrections integral $\mathscr{F}_i = \int F_i(\vec{\theta})\varepsilon(\vec{\theta})d\vec{\theta}$ can be approximated by the following form, using the Monte Carlo integration techniques

$$\mathscr{F}_i \approx \frac{1}{N_{gen}} \sum_{j=0}^{j=N_{acc}} \frac{F_i(\vec{\theta})}{G(\vec{\theta})}, \tag{18}$$

where N_{gen} is the number of generated events, N_{acc} is the number of accepted events after the simulation of the fiducial acceptance and p_T cut and G is the p.d.f which has been used to generate the θ.

If the generation of the events is done using certain p.d.f (w), the acceptance can be calculated by the simple expression:

$$\mathscr{F}_i \approx \frac{1}{N_{gen}} \sum_{j=0}^{j=N_{acc}} \frac{F_i(\vec{\theta})}{w(\vec{\theta},\vec{A},P)}. \tag{19}$$

We used this expression to calculate the acceptance in the case when w is the p.d.f from Equation 6.

This method can be used under the assumption that the acceptance does not depend on the measured parameters, and that the angular resolutions are close enough to the ideal resolutions. In order to check the first assumption we plotted the ratio

$$\frac{\int w(\vec{\theta},\vec{A},P)\varepsilon(\vec{\theta},\vec{A},P)d\vec{\theta}}{\int w(\vec{\theta},\vec{A},P)\varepsilon(\vec{\theta},\vec{A},P=0)d\vec{\theta}} \tag{20}$$

for the different polarization values (see Figure 14). No significant dependence of the acceptance on the polarization is observed in this test.

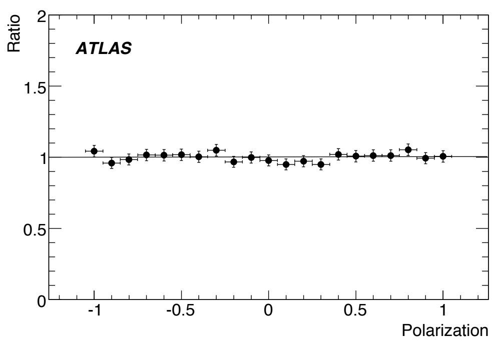

Figure 14: Ratio defined in Equation 20 as a function of polarization.

The angular resolutions are shown in Figure 12. To test the effect of these resolutions, Monte Carlo fits were performed including a smearing of the data based on the Gaussian fits in Figure 12. Fit results with and without smearing are consistent within the statistical uncertainty. Figure 15 shows, as an example, a comparison of fit results for a sample of 2000 events with polarization of -75% when fits are performed on the sample of generated Monte Carlo events.

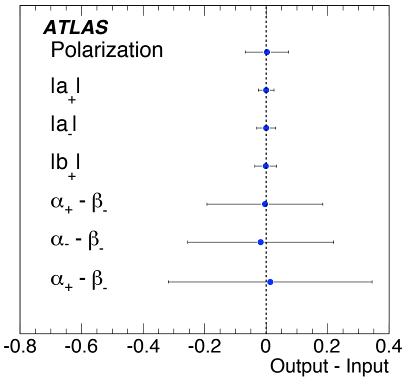

Figure 15: Comparison of fit outputs from generation level Monte Carlo with and without Gaussian smearing due to finite angular resolution. Error bars are statistical uncertainties from the fit with Gaussian smearing included.

5.2 Fits to fully simulated Monte Carlo data

In order to extract polarization and decay parameters from the Monte Carlo data samples, final Λ_b selection cuts were applied. A proper transverse decay length greater than 200 μm is required to remove contamination from prompt produced J/ψ events. The proper transverse decay length for the Λ_b candidate is given by:

$$\lambda = \frac{L_{xy}}{(\beta\gamma)_T^{\Lambda_b}} = L_{xy}\frac{cM_{\Lambda_b}}{p_T}, \tag{21}$$

where $(\beta\gamma)_T^{\Lambda_b}$ and M_{Λ_b} are the transverse boost and the mass of the Λ_b, and L_{xy} is a transverse decay length. The transverse decay length is defined as $L_{xy} = \boldsymbol{L}_{xy}\cdot\boldsymbol{p}_T/p_T$ where $\boldsymbol{L}_{xy}$ is the vector that points from the primary vertex to the Λ_b decay vertex and $\boldsymbol{p}_T$ is the transverse momentum vector of the Λ_b. A minimum p_T of 500 MeV is required for any track used in the Λ_b reconstruction. In addition, a $p_T >$ 4000 MeV is required for the muon with larger p_T, and $p_T > 2500$ MeV for the second muon. These cuts reduce the Λ_b sample by 21%, mainly due to the lifetime cut.

Table 6 shows the results of performing a likelihood fit to our fully simulated Monte Carlo data, for a sample of 2000 Λ_b events, corresponding to around 5 fb^{-1} of collected data. Figure 16 shows the difference between the input values in Monte Carlo and the extracted values of polarization and decay parameters by the likelihood fit. We used as fitting parameters: $|a_+|$, $|a_-|$, $|b_+|$, $\alpha_+ - \beta_-$, $\alpha_- - \beta_-$, $\beta_+ - \beta_-$, and the polarization P.

Detector acceptance corrections in Equation 19 were computed separately from the two Monte Carlo samples with different polarizations which are used in this study. Corrections computed in the Monte Carlo sample of -75% polarization were used in the fit of the Monte Carlo sample of -25% polarization, and vice versa. Due to the limited statistics in the Monte Carlo samples used to calculate the acceptance corrections defined in Equation 19, a bagging (from bootstrap aggregating) technique [23] was used to generate multiple samples in order to avoid the effect of statistical fluctuations. This technique consists of generating replicates of a data set by selecting at random events from the original data set allowing repetition of events. We generated 1000 bootstrap replicates of the fully simulated Monte Carlo data sample. The $\mathscr{F}_i$ factors (Equation 19) were computed from each generated data sample and the average was taken as the value for each of the twenty $\mathscr{F}_i$ correction factors. Systematic uncertainty due to the width of the correction factors distributions in these 1000 generated data sets was estimated by repeating the fit to fully simulated Monte Carlo using the $\mathscr{F}_i$ values from the each of the generated samples, and

Parameter	Value ± Uncertainty (Polarization = -25%)	Value ± Uncertainty (Polarization = -75%)	Value (Input at generation level)
Polarization	-0.213 ± 0.069	-0.882 ± 0.064	-0.25/-0.75
$\|a_+\|$	0.461 ± 0.051	0.413 ± 0.023	0.429
$\|a_-\|$	0.289 ± 0.058	0.161 ± 0.035	0.260
$\|b_+\|$	0.259 ± 0.071	0.370 ± 0.027	0.295
$\alpha_+ - \beta_-$	-0.991 ± 0.640	-2.050 ± 0.134	-1.612
$\alpha_- - \beta_-$	0.856 ± 0.364	0.681 ± 0.342	1.231
$\beta_+ - \beta_-$	-1.442 ± 0.666	-2.624 ± 0.187	-1.849

Table 6: Fit results from fully simulated and reconstructed Monte Carlo events with input polarization of -25% and -75%.

assigning the width of the distribution of fitted parameters as a systematic uncertainty. This systematic error (also shown in Figure 16) can be reduced with more Monte Carlo statistics for the $\mathscr{F}_i$ calculation.

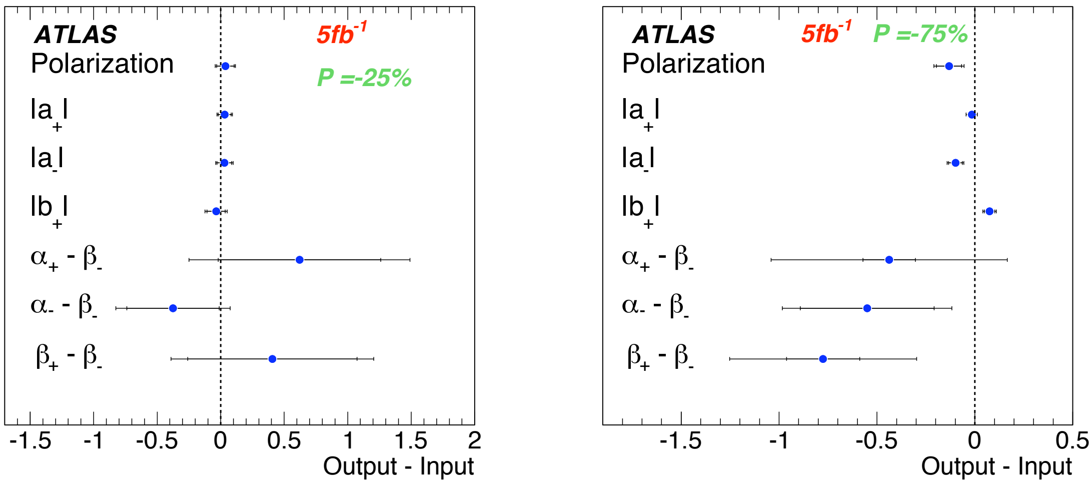

Figure 16: Comparison of fit results for polarization of -25% (left) and -75% (right) with respect to input values from Monte Carlo generation. The statistical and systematic uncertainties are included.

5.3 Estimate of statistical uncertainties

To estimate statistical uncertainties as a function of polarization, we used a fast Monte Carlo probabilistic approach to generate polarized Λ_b particles. The fast Monte Carlo includes angular resolution from the fully reconstructed samples and detector acceptance simulation. We generated a large number of samples with different values of polarization. A maximum likelihood fit was used to extract the decay parameters and the polarization. Detector acceptance corrections were calculated from high statistics fast Monte Carlo data simulated without polarization. Figure 17 presents the expected statistical uncertainty in the polarization P and in α_{Λ_b} as a function of the polarization value for the integrated luminosity of 30 fb^{-1} . The study was done for α_{Λ_b} = -0.457 with the same input model as used in fully simulated Monte Carlo. In Figure 17 also the correlation between α_{Λ_b} and P is shown as a function of polarization. The correlation values were extracted from the Maximum Likelihood fit results.

In our study we used specific set of decay amplitudes, presented in Table 3, to demonstrate our ability to extract these parameters. To insure that the success of our analysis techniques did not depend on the amplitudes chosen, we conducted a fast Monte Carlo study using a different model with α_{Λ_b} = 0.1 [24] to test our procedure in a case of smaller α_{Λ_b} value. We found that it is possible to satisfactorily extract α_{Λ_b} and the polarization even with such a change in the amplitude values.

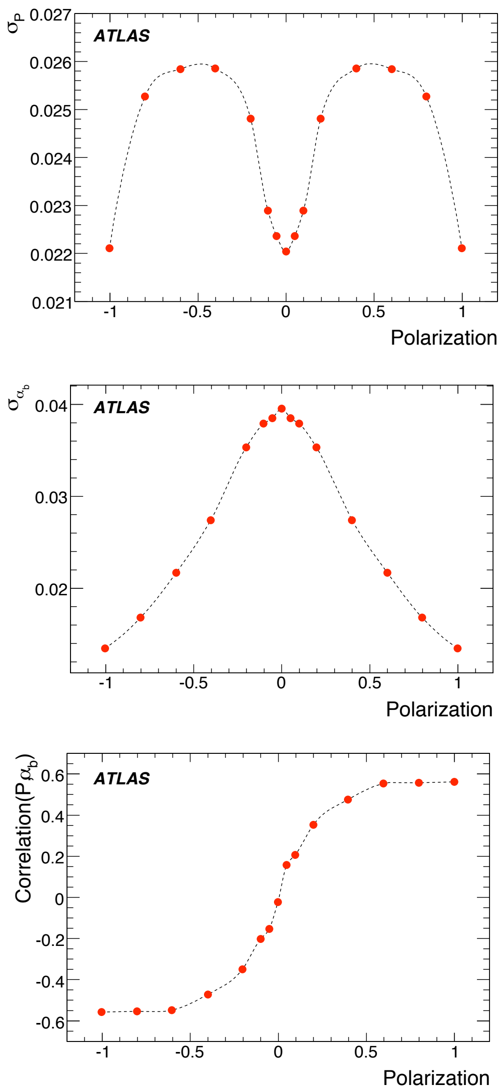

Figure 17: Expected statistical uncertainty on polarization (top) and on α_{Λ_b} (center) as a function of the polarization P. Bottom plot shows the expected correlation between α_{Λ_b} and the polarization P. All plots show results from the fast Monte Carlo study, obtained for the expected number of Λ_b events in data sample of 30 fb^{-1} .

6 Results and conclusions

In this note we have presented the results from a series of studies to determine if polarized Λ_b baryons can be reconstructed in ATLAS and have their polarization and α_{Λ_b} parameter measured. Our results indicate that the answer is affirmative. Λ_b events should be identifiable through the reconstruction of their four charged final state particles, and the angles between these particles can be measured with sufficient accuracy to determine the parent's polarization. With trigger constraints and detector cuts fully specified, our more complete analysis suggests that the number of events we should expect after 30 fb^{-1} of data will only be 13,000, compared to the 37,500 noted in the ATLAS-TDR [22]. Different additional detector and background effects, which are difficult to model at the current level of detector description, can further reduce the signal sensitivity. These effects could include the detector and trigger inefficiency, misalignment, pile-up events and increased combinatorial background due to e.g. the fake tracks. Nevertheless, even with a reduction of 50%, a polarization measurement with a statistical uncertainty of several percent should be possible in a regime where polarization is larger than 25% as experimentally measured at lower energies. Efforts will continue to develop algorithms to improve the various reconstruction and trigger efficiencies and in consequence providing an enhanced yield of reconstructed particles in data samples.

We note that almost all models predict that the Λ_b polarization at the LHC at small Feynman x should be vanishingly small. Measurement of a significant polarization would have to be regarded as a signal of an unexplained effect, either from the domain of existing physics, or of new physics altogether.

We further note that the development of Λ_b polarimetry as a tool for studying spin effects at the LHC could be important. For example, members for the SUSY community are quite interested in knowing what fraction of the b quark polarization ends up in the polarization of a Λ_b, since this could provide a way to test if b quark SUSY partners have the correct handedness. Only a few hundred Λ_b decays would be required to, for example, determine if its polarization were 100% or -100%. Challenges clearly exist, however, in determining the polarization transfer fraction, which requires a source of b's such as from $Z \to b\bar{b}$, and in dealing with the fact that only 10^{-5} of b's generate decay into the Λ_b channel we have described here. Our work on this topic will continue.

Other related studies that should continue include mechanisms for comparing the α_{Λ_b} parameters from Λ_b and its antiparticle as a test of CP. We will accumulate data on both. If CP is conserved, the two parameters should be equal in magnitude but opposite in sign. While the precision of this test will not be high, and while models predict that any CP violation would be small in this sector, nevertheless, such a test would be unique in this domain and should be made.

Finally, as noted in Section 1, the lifetime of the Λ_b remains a topic of significant interest. Such a measurement will be a natural by-product of our efforts to extract the Λ_b spin parameters.

References

[1] C. Albajar *et al*., Phys. Lett. B **243** (1991) 540.

[2] F. Gabbiani *et al*., Phys. Rev. D **68** (2003) 114006.

[3] I. Dunietz, Z. Phys. C **56** (1992) 129.

[4] C. Q. Geng *et al*., Phys. Rev. D **65** (2002) 091502.

[5] C. A. Nelson, Eur. Phys. J. C **19** (2001) 323.

[6] A. K. Giri *et al*., Phys. Rev. D **65** (2002) 073029.

[7] D. J. Lange, Nucl. Inst. Meth. **A462** (2001) 152.
http:://www.slac.stanford.edu/∼lange/EvtGen/

[8] J. Szwed, Phys. Lett. B **105** (1981) 403.

[9] C. Chou *et al*., Phys. Rev. D **65** (2002) 074030.

[10] W. G. D. Dharmaratna and G. R. Goldstein, Phys. Rev. D **53** (1996) 1073.

[11] W. G. D. Dharmaratna and G. R. Goldstein, Phys. Rev. D **41** (1990) 1731.

[12] K. Heller, Proceedings of the 9th International Symposium on High Energy Spin Physics, Bonn, Germany, p. 97, Springer-Verlag (1990).

[13] H. A. Neal and E. De La Cruz Burelo, AIP Conf. Proc. **915** (2007) 449 .

[14] Chung-Hsien Chou *et al*., Phys. Rev. D **65** (2002) 074030; J. C. Collins, Phys. Rev. D **58** (1998) 094002; Chung-Hsien Chou, Int. J. Mod. Phys. A **18** (2003) 1429.

[15] J. Hrivnac *et al*., J. Phys. G: Nucl. Part. Phys **21** (1995) 629.

[16] J. G. Korner and M. Kramer, Z. Phys. C **55** (1992) 659.

[17] P. Bialas *et al*., Z. Phys. C **57** (1993) 115.

[18] R. Lednicky, Jad. Fiz. 43 (1986) 1275.

[19] T. Sjostrand *et al*., Comp. Phys. Comm. **135** (2001) 238, eprint hep-ph/0108264.

[20] W. M. Yao *et al*., J. Phys. G: Nucl. Part. Phys. **33** (2006) 1-1232.

[21] ATLAS-TDR-017; CERN-LHCC-2005-022.

[22] ATLAS TDR, CERNLHC99-15, Vol. II (1999) 614.

[23] A. C. Davison *et al*., Bootstrap methods and their application, Cambridge Univ. Press (1997).

[24] H. Y. Cheng and B. Tseng, Phys. Rev. D **53** (1996) 1457.

Study of the Rare Decay $B_s^0 \to \mu^+\mu^-$

Abstract
We investigate the feasibility of measuring of the rare decay $B_s^0 \to \mu^+\mu^-$ in ATLAS. The contribution of inclusive and of the most important non–combinatorial background is studied.

1 Introduction

The rare decays, $B_s^0 \to \ell^+\ell^-$ with $\ell^\pm = e^\pm, \mu^\pm$, or $\tau^\pm$, are mediated by flavour-changing neutral currents that are forbidden in the Standard Model at tree level. The lowest-order contributions in the Standard Model involve weak penguin loops and weak box diagrams that are CKM suppressed. Examples of the lowest-order diagrams are shown in Figure 1. Since the B_s^0 meson is a pseudoscalar that has positive C parity and the transition proceeds in an $\ell = 0$ state, the electromagnetic penguin loop is forbidden. The two leptons are either both right-handed or both left-handed leading to additional helicity suppression. Thus, branching fractions expected in the Standard Model are tiny.

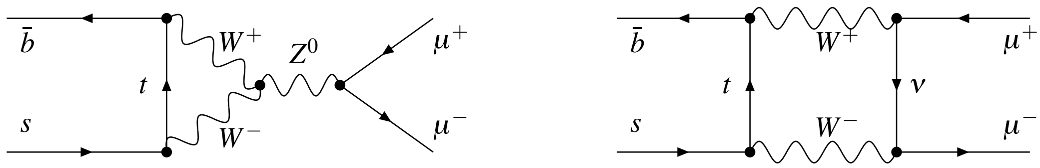

Figure 1: Lowest order Standard Model contributions to $B_s^0 \to \mu^+\mu^-$.

The early searches for rare B meson decays started with radiative penguin decays, first observed by CLEO in 1993, where they presented evidence for the exclusive decay $B \to K^*\gamma$ and for the inclusive decay $B \to X_s\gamma$ a year later [1,2].

The B factory experiments, BaBar and Belle, have measured these decay modes with more precision. The present world average for the inclusive mode is $\mathscr{B}(B \to X_s\gamma) = (3.55 \pm 0.26) \times 10^{-4}$ [3]. BaBar and Belle also observed the decays $B \to K^{(*)}\ell^+\ell^-$ and $B \to X_s\ell^+\ell^-$ that are two orders of magnitude smaller than $B \to X_s\gamma$ [4,5]. The decay $B_s^0 \to \mu^+\mu^-$ is expected to be further reduced by three orders of magnitude.

In extensions of the Standard Model, the $B_s^0 \to \mu^+\mu^-$ branching fraction may be enhanced by several orders of magnitude. Thus, several experiments have searched for these decays. The largest B_s^0 samples have been collected by CDF and D0 corresponding to a luminosity of 2 fb^{-1} but no signal has been observed. The lowest branching fraction upper limit was set recently by CDF yielding $\mathscr{B}(B_s^0 \to \mu^+\mu^-) < 5.8 \times 10^{-8}$@95% confidence level [6]. This is still about an order of magnitude higher than the Standard Model prediction. As ATLAS has an elaborate muon system extended over a large region of the solid angle, the dimuon final state is expected to be reconstructed with high efficiency and good mass resolution. Thus, there are good prospects for observing this decay in the dimuon channel and measuring its branching fraction with reasonable precision.

2 Theoretical description

The Standard Model amplitude for the process $B_{s,d} \to \ell^+\ell^-$ is calculated from the effective Hamiltonian

$$H_{\text{eff}} = -\frac{G_F}{\sqrt{2}}\frac{\alpha}{\pi \sin^2\theta_W} V_{tb}^* V_{tq}(C_{10}(\mu)\mathscr{O}_{10}(\mu) + C_S(\mu)\mathscr{O}_S(\mu) + C_P(\mu)\mathscr{O}_P(\mu)) + h.c., \tag{1}$$

where $C_i(\mu)$ are Wilson coefficients that present the perturbatively calculable short-distance effects and $\mathscr{O}_i(\mu)$ are local operators that describe the non-perturbative long-distance effects of the transition. The scale parameter μ is of the order of the b-quark mass (~ 5 GeV), θ_W is the weak mixing angle, α is the electromagnetic coupling constant and $V_{tb}^* V_{tq}$ are CKM matrix elements for $t \to b$ and $t \to q = s, d$ transitions, respectively.

The dominant contribution results from the axial-vector operator $\mathscr{O}_{10}$, [7]:

$$\mathscr{O}_{10} = (\bar{b}_L \gamma^\mu q_L)(\bar{\ell}\gamma_\mu \gamma_5 \ell). \tag{2}$$

The Wilson coefficient C_{10} has been determined in the next-to-leading order (NLO) of QCD. The NLO corrections are in the percent range and higher-order corrections are not relevant [8]. In NLO an excellent approximation in terms of the $\overline{MS}$ mass of the top quark, $\bar{m}_t$, is given by:

$$C_{10}(\bar{m}_t) = 0.9636 \left[\frac{80.4 \text{ GeV}}{M_W} \frac{\bar{m}_t}{164 \text{ GeV}} \right]^{1.52}. \tag{3}$$

The measurements of the top quark mass at the Tevatron, $m_t^{pole} = 171.4 \pm 2.1$ GeV [9], yield an $\overline{MS}$ mass of $\bar{m}_t = 163.8 \pm 2.0$ GeV and the world average of the W-boson mass is $m_W = 80.403 \pm 0.029$ GeV. The accuracy of this approximation is 5×10^{-4} for masses of 149 GeV $< \mathrm{\bar{m}_t} <$ 179 GeV.

The other two operators represent scalar and pseudoscalar couplings to the leptons:

$$\mathscr{O}_S = m_b(\bar{b}_R q_L)(\bar{\ell}\ell), \mathscr{O}_P = m_b(\bar{b}_R q_L)(\bar{\ell}\gamma_5 \ell). \tag{4}$$

The Wilson coefficients, C_S and C_P, are determined from penguin diagrams that involve the Higgs boson or the neutral Goldstone boson, respectively. Although they are not helicity suppressed, their contributions are tiny in the Standard Model and they may be safely neglected in Standard Model calculations.

The $B_q \to \mu^+\mu^-$ branching fractions including the scalar and pseudoscalar contributions are given by:

$$\begin{aligned} \mathscr{B}(B_q^0 \to \mu^+\mu^-) = \frac{G_F^2 \alpha^2}{64\pi^3 \sin^4 \theta_W} |V_{tb}^* V_{tq}|^2 \tau_{B_q} M_{B_q}^3 f_{B_q}^2 \sqrt{1 - \frac{4m_\mu^2}{M_{B_q}^2}} \\ \times \left[\left(1 - \frac{4m_\mu^2}{M_{B_q}^2}\right) M_{B_q}^2 C_S^2 + \left(M_{B_q} C_P - \frac{2m_\mu}{M_{B_q}} C_{10}\right)^2 \right], \end{aligned} \tag{5}$$

where M_{B_q}, τ_{B_q}, and f_{B_q} respectively are mass, lifetime and decay constants of the B_q meson. The decay constant is determined in different models, including quark models, QCD sum rules and unquenched lattice theory. The accuracy is presently of the order of $10 - 15\%$. Evaluating α at the Z-mass scale, $\alpha(M_Z) = 1/128$, the following predictions were made for the $B_q \to \mu^+\mu^-$ branchings fractions in the Standard Model [8]:

$$\begin{aligned} Br(B_s^0 \to \mu^+\mu^-) &= (3.86 \pm 0.15) \times \frac{\tau_{B_s^0}}{1.527\,\text{ps}} \frac{|V_{ts}^* V_{tb}|^2}{1.7 \times 10^{-3}} \frac{f_{B_s}}{240\,\text{MeV}} \times 10^{-9}, \\ Br(B_d^0 \to \mu^+\mu^-) &= (1.06 \pm 0.04) \times \frac{\tau_{B_d^0}}{1.527\,\text{ps}} \frac{|V_{td}^* V_{tb}|^2}{6.7 \times 10^{-5}} \frac{f_{B_d}}{200\,\text{MeV}} \times 10^{-10}. \end{aligned} \tag{6}$$

In extensions of the Standard Model, such as supersymmetry (SUSY), Higgs doublet models or models with extra gauge bosons, scalar-current, pseudoscalar-current or axial-vector current interactions may arise with new particles in the loop. This yields new contributions in the Wilson coefficients C_{10}, C_S, and C_P. Since the scalar and pseudoscalar operators are not helicity suppressed, they may give rise to a large enhancement of the branching fraction. Furthermore, the contribution of the pseudoscalar operator may produce destructive or constructive interference with the axial vector operator. Thus, new physics may increase or decrease the branching fraction with respect to the Standard Model value. For example, in the minimal supersymmetric Standard Model (MSSM), the $B_s^0 \to \mu^+\mu^-$ branching fractions are proportional to $\tan^6(\beta)$ [1]. The branching fraction of $B_d \to \mu^+\mu^-$ is expected to be a factor of 40 lower than that for $B_s \to \mu^+\mu^-$, hence, the latter is the focus of this note.

3 ATLAS strategy for $B_s^0 \to \mu^+\mu^-$ study

Measurements of the properties of B decays with such extremely low branching fractions in ATLAS is possible namely due to the large beauty cross-section and luminosity of the LHC machine. Thus at luminosity 10^{33} cm^{-2} s^{-1} 10^{12} B hadron pairs will be produced each year. It is expected that ATLAS will record 10^8 events with B decays each year by using B-physics triggers [10]. Triggers dedicated to rare dimuon $B_s^0 \to \mu^+\mu^-$ decays will be described in the Section 4.2 of this document.

Since the branching fraction is so small in the Standard Model, semileptonic B decays and even some rare B decays may yield substantial backgrounds. The key issue for $B_s^0 \to \mu^+\mu^-$ discovery at the LHC is the suppression of the backgrounds. The ATLAS strategy for observing $B_s^0 \to \mu^+\mu^-$ is as follows.

The first step is to trigger on events containing a $B_s^0 \to \mu^+\mu^-$ candidate using dedicated trigger algorithms which are described in this document. In the offline analysis the selections will be refined to reduce backgrounds. To achieve final separation of signal from background we will employ statistical methods based on several variables. Both parts of the offline selection are described in this paper.

Once recorded data are available, the background in the signal region will be estimated using sidebands in the distribution of the muon pair invariant mass. In the current study the background was estimated using simulated events. Two categories of backgrounds were simulated: the so called combinatorial background from $b\bar{b}$ pairs producing two muons in the final state; and the exclusive backgrounds, coming from two-body hadronic B decays and from the process $B_s^0 \to K^-\mu^+\nu$. The exclusive backgrounds contribute to the signal region and the lower mass sideband only. They do not occur in the higher mass sideband, so their contribution to the signal is estimated separately.

After the number of background events in the signal region has been determined, the number of signal events N_B can be determined from a comparison of the total number of events found in the signal region, and the estimated background. For low statistics an upper limit on N_B corresponding to certain confidence level is determined using appropriate statistical methods. Once N_B is determined the $B_s^0 \to \mu^+\mu^-$ branching fraction, $\mathscr{B}(B_s^0 \to \mu^+\mu^-)$, can be calculated using a relative normalisation to the reference channel $B^+ \to J/\psi(\mu^+\mu^-)K^+$.

This document presents a Monte Carlo simulation study which follows the strategy described above. We start from the trigger level in Section 4.2. This is followed by the offline analysis, optimisation of discriminating variables and finally the determination of background and signal contribution in the signal regions, in Section 4.4. Systematic uncertainties are analysed in Section 5, followed by the start-up strategy in Section 6.

It should be stressed that due to large uncertainty in the predictions of the $b\bar{b}$ production cross-section at the LHC energy this paper cannot derive a precise sensitivity to $\mathscr{B}(B_s^0 \to \mu^+\mu^-)$ at ATLAS but rather to show the ATLAS potential for this study and its discovery capability under some assumptions.

[1] $\tan(\beta)$ is the ratio of vacuum expectation values for charged and neutral Higgs bosons.

4 Monte Carlo study

4.1 Simulation and event selection

The Monte Carlo simulation samples used in the analysis have been generated as part of the central ATLAS Monte Carlo data production runs, and details of this simulation have been given in the introduction to this chapter.

The list of generated signal and background events is given in Table 1. To ensure that most of the

Process	# Events
$B_s^0 \to \mu^+\mu^-$	47.5k
$b\bar{b} \to \mu^+\mu^- X$	146.5k
$B_s^0 \to K^-\pi^+$	50k
$B_s^0 \to K^-\mu^+\nu$	50k

Table 1: List of processes and number of events analysed

generated dimuon events passed the trigger, only events containing two muons with p_T larger than 6 GeV and 4 GeV, were retained for detector simulation. For the signal channel $B_s^0 \to \mu^+\mu^-$, multiplying the cross-section reported by PYTHIA with the branching ratio 3.42×10^{-9} gave a cross-section of 15 fb. 47.5k events have been generated and passed through the full detector simulation and reconstruction. Simulation of pileup has not been available, thus it was not simulated for either the signal or the background events.

The sample of dominant background process events, $b\bar{b}$ decaying semileptonically giving two muons in the final state, were simulated with the same versions of the software, and with the same kinematic cuts as for the signal. The PYTHIA cross-section for such a sample is estimated to be 110 nb and a total of 146.5k background events that passed the reconstruction stage were used in the physics analysis.

In addition to the combinatorial background, there are several B backgrounds that may contribute to the signal region. These include two and three body decays where two of the final state particles are $K^\pm$, $\pi^\pm$ or $\mu^\pm$. Although the rate for misidentification of kaons or pions as muons, due to punchthrough or decay in flight, is only of the order 0.5%, the small $\mathscr{B}(B_s^0 \to \mu^+\mu^-)$ requires investigation of the other rare B decays. The decay modes which we consider to be most important are summarised in Table 2.

process	branching fraction	Ref.
$B^0 \to K^+\pi^-$	$(1.82 \pm 0.08) \times 10^{-5}$	[11]
$B^0 \to \pi^+\pi^-$	$(4.6 \pm 0.4) \times 10^{-6}$	[11]
$B^0 \to K^+K^-$	$< 3.7 \times 10^{-7} @ 90\% CL$	[11]
$B_s^0 \to \pi^+\pi^-$	$< 1.7 \times 10^{-4} @ 90\% CL$	[11]
$B_s^0 \to \pi^+K^-$	$< 2.1 \times 10^{-4} @ 90\% CL$	[11]
$B_s^0 \to K^+K^-$	$< 5.9 \times 10^{-5} @ 90\% CL$	[11]
$B_s^0 \to K^-\mu^+\nu$	$\sim 1.36 \times 10^{-4}$	* [2]
$B^0 \to \pi^-\mu^+\nu$	$(1.36 \pm 0.15) \times 10^{-4}$	[11]

Table 2: B meson decays contributing to the non-combinatorial background

[2] An estimation based on isospin symmetry and the measurement of $B^0 \to \pi^-\mu^+\nu$.

We have studied one of the two-body and one of the three-body decays with full simulation, namely $B_s^0 \to K^-\pi^+$ and $B_s^0 \to K^-\mu^+\nu$. Contributions from the other channels were estimated to be similar or smaller. To enable the production of a sizable event sample with decay in flight, a special GEANT simulation option which forces kaons and pions from selected B mesons to decay in the inner detector volume was developed [12].The position of the decay is randomly selected from a uniform distribution between the origin and the exit point from the inner detector.

4.2 Trigger strategy

We describe trigger methods for selection of the $B_s^0 \to \mu^+\mu^-$ channel developed by the B trigger group as part of the project presented in this document. The full description of the ATLAS B-physics triggers is given in the introduction to the B-physics chapter [10]. The first level trigger (L1) performance for dimuon channels can be found in [13] and details of the second level (L2) dimuon trigger implementation in [12].

At the LHC start-up, the luminosity level is expected to be of order $10^{31}\text{cm}^{-2}\text{s}^{-1}$ and a p_T threshold as low as 4 GeV can be used at L1. The dimuon rate after L1 is expected to be only a few Hz. This admits the possibility of applying L2 track reconstruction in the full volume of the inner detector. This detailed approach allows the study of dimuon background features to understand of their composition. With the subsequent rise of luminosity the L1 p_T threshold will increase to 6 GeV. The dimuon rate after L1 is expected to rise to about 360 Hz at $L = 10^{33}\text{cm}^{-2}\text{s}^{-1}$ and the L2 track reconstruction in the full volume of inner detector will be replaced by the Region of Interest (RoI) guided mode, documented in [12].

The simulation of the trigger in the current study is performed by applying the strategies for luminosity $L = 10^{33}\text{cm}^{-2}\text{s}^{-1}$. At L1 the threshold of $p_T > 6$ GeV has been applied and events containing two L1 muon signatures are analysed further using the L2 topological dimuon trigger algorithm with a threshold of $p_T > 6$ GeV. Following the RoI defined at L1, the muon candidates are reconstructed in the muon spectrometer, then matched to the tracks reconstructed in the inner detector (inside the RoI) and combined into one track. The invariant mass of two opposite sign muons is required to be less than 7 GeV. These muons should also be successfully fitted to a common vertex. Only loose selection criteria are used at this step ($\chi^2 < 10$). Implementation of the third level trigger, the event filter (EF), is not finalised yet and the offline reconstruction efficiency is used to estimate the EF efficiency (the same reconstruction algorithms are supposed to be used at EF).

Results on the L1 and L2 efficiencies as well as an estimated EF efficiency for signal $B_s^0 \to \mu^+\mu^-$ are given in Table 3. The L1 efficiency is defined as the ratio of the $B_s^0 \to \mu^+\mu^-$ events passing the L1 trigger and the input events generated with $p_T > 6$ GeV and $|\eta| < 2.5$ for both muons from the $B_s^0 \to \mu^+\mu^-$ decay. The L2 efficiency is defined as the fraction of events accepted by L1 satisfying the above L2 reconstruction and selection cuts. The efficiency of the event filter is estimated as the fraction of events that both satisfy L2 and also are successfully reconstructed at EF. These values of the efficiency have been used in the subsequent analysis.

Various types of trigger algorithms and trigger thresholds will be used in the real experiment depending on the luminosity achieved, dedicated computing resources available for the online event processing and the actual beauty yield at LHC energies.

Table 3: Trigger efficiency of signal $B_s^0 \to \mu^+\mu^-$. The methods of calculating efficiencies at L1, L2 and EF levels are given in the relevant place in the text.

L1*L2 efficiency	EF w.r.t L2	Overall trigger eff.
0.52	0.88	0.46

4.3 Event reconstruction and analysis.

Muon reconstruction quality is of high importance for the $B_s^0 \to \mu^+\mu^-$ channel. The muon candidates produced by the STACO [14] method were used. This method combines the independently reconstructed inner detector and muon spectrometer tracks. Figure 2 shows the muon reconstruction efficiency as a function of a true muon p_T. The efficiency is defined as the number of muon candidates reconstructed and matched to the Monte Carlo particle tracks in the corresponding p_T bin divided by number of generated muons. The p_T spectrum of generated muons is superimposed on the efficiency plot.

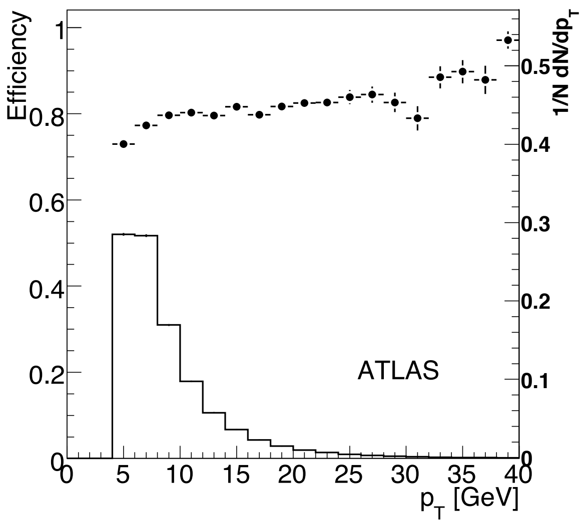

Figure 2: Muon offline reconstruction efficiency as a function of p_T. The superimposed histogram - p_T spectrum of muons in the signal events (right scale).

For the physics analysis, we select events containing identified muon pairs with opposite charges. Aside of the kinematic cuts ($p_T^{\mu_1(\mu_2)} > 6(4)$ GeV and $|\eta_{\mu_1,\mu_2}| < 2.5$) no additional cuts have have been applied. These two muons then constitute a B meson candidate. The VKalVrt vertexing package [15] is used to fit tracks into a vertex. We require the vertex quality to have $\chi^2 < 10$. The momentum resolution is important as a narrow mass search window reduces the background contribution. Figure 3 shows the dimuon mass distribution for the cases when both muons are in the barrel region ($|\eta_{\mu_1,\mu_2}| < 1.1$) or in the end-cap ($|\eta_{\mu_1,\mu_2}| > 1.1$). The Gaussian fit (using bins with contents > 10% of maximum) gives $\sigma = 70$ MeV for the barrel and $\sigma = 124$ MeV for the end-cap. We used 90 MeV as an estimate of the invariant mass resolution for the signal events.

In this document we present a cut-based method for signal extraction and background rejection. For the future, we are investigating another method using a boosted decision tree [16].

In the cut based analysis a set of discriminating variables is chosen and using the signal and background simulated events the optimal set of cuts is determined. The signal events are identified by requiring that the dimuon invariant mass is consistent with the mass of B_s meson. To reduce background events where two muons originate from different sources (e.g. independent semileptonic decays of b and $\bar{b}$ quarks), the following discriminating variables were chosen (values used in the final analysis are given in parentheses):

- Transverse decay length of the B_s candidate L_{xy} (L_{xy} >0.5 mm)

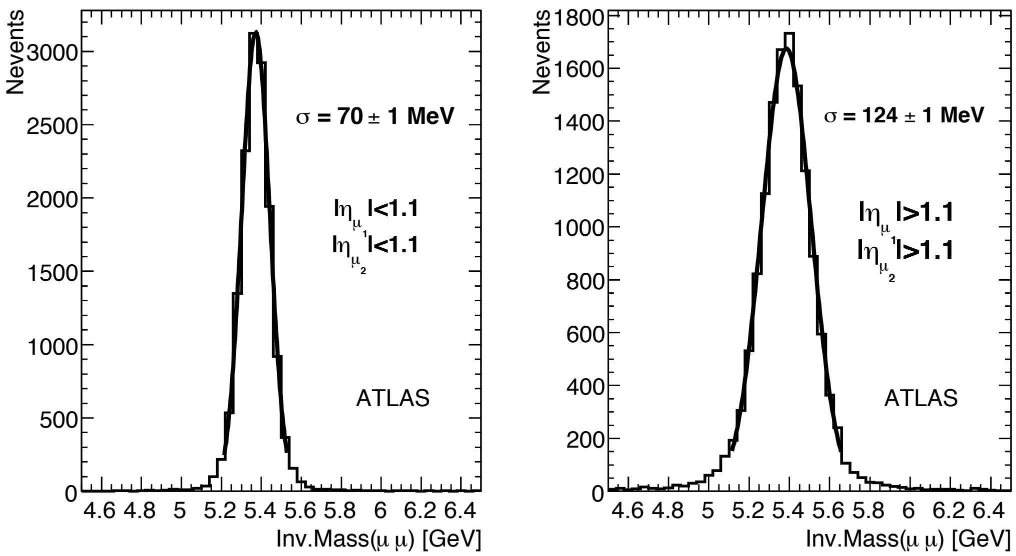

Figure 3: Reconstructed B_s mass in barrel - when both muons have $|\eta| < 1.1$(left) and in the end-cap - both muons have $|\eta| > 1.1$ (right)

- The pointing angle α between the dimuon pair summary momentum and the direction of the decay vertex as seen from the primary vertex (α <0.017 rad)
- Isolation $I_{\mu\mu} = p_T^{\mu\mu}/(p_T^{\mu\mu} + \Sigma_i p_T^i(\Delta R < 1))$, where the sum is over all tracks with $p_T > 1$ GeV (excluding the muon pairs) within a cone of $\Delta R < 1$, where $\Delta R = \sqrt{(\Delta\eta)^2 + (\Delta\phi)^2}$ and $\Delta\eta$ and $\Delta\phi$ are the pseudorapidity and azimuthal angle of track i with respect to the momentum vector of the muon pair ($I_{\mu\mu} > 0.9$).
- An asymmetric search window for $M_{\mu\mu}, \in [M_{B_s^0} - \sigma, M_{B_s^0} + 2\sigma]$, is used to avoid a possible contribution from $B_d^0 \to \mu^+\mu^-$ decay.

Figures 4, 5 and 6 show distributions of discriminating variables for signal and background events. Due to the low Monte Carlo statistics, it is not feasible to perform a cut analysis as in a real experiment (i.e. applying all cuts simultaneously) since this will leave no events for the analysis. However, some of the discriminating variables show no (or small) correlations between each other. This allows the estimation of the rejection power of such variables separately. Then the product of all efficiencies can provide a reasonable estimate of the total rejection. Table 4 shows a correlation matrix for the variables used in this study. The correlation between the pointing angle α and the transverse decay length L_{xy} is higher than among other variables so the pointing angle and the transverse decay length are examined simultaneously to take their correlation into account. The systematic uncertainty due to this correlation is estimated as +50%.

Figure 7 illustrates the rejection power of each cut. One cut is applied at a time to the combinatorial background events and to the $B_s^0 \to K^-\mu\nu$ and $B_s^0 \to K^-\pi^+$ events where one or two hadrons are misidentified as a muon. The combinatorial background is effectively suppressed by these cuts while the non-combinatorial events are less well rejected.

Table 5 summarizes the output of this cut-based analysis. For the $b\bar{b} \to \mu\mu X$ background in the left column the efficiencies are given separately for each cut, whilst in the right column the combined

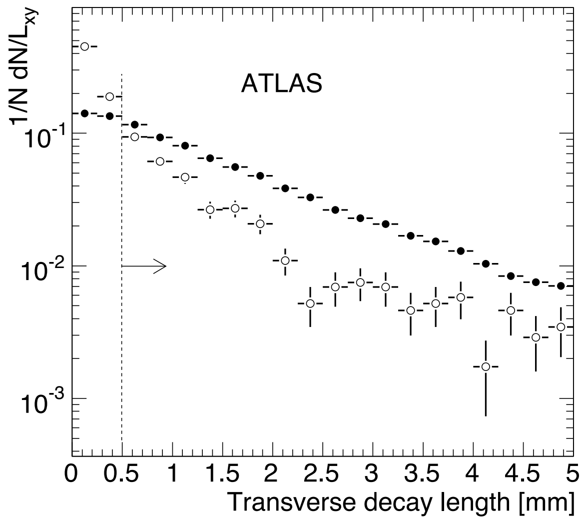

Figure 4: Transverse decay length of reconstructed B_s^0 candidates. The signal is shown as closed circles, background as opened circles. Distributions are normalised to 1. The vertical line indicates the lowest transverse decay length allowed for selected events.

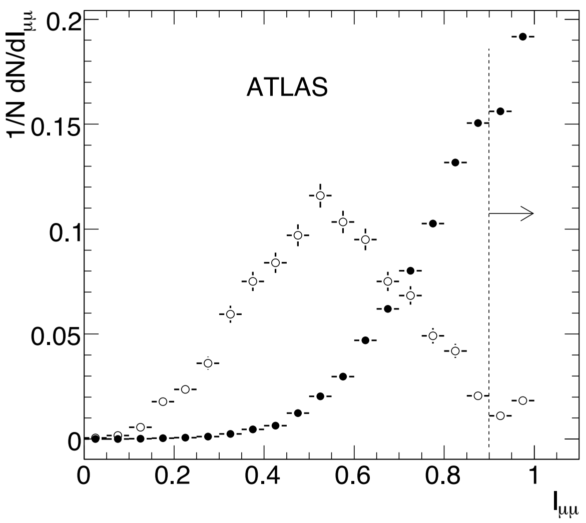

Figure 5: Distribution of isolation variable $I_{\mu\mu}$ for the reconstructed B_s^0 candidates. The signal is shown as closed circles, background as opened circles. Distributions are normalised to 1. The vertical line indicates the lowest values of variable $I_{\mu\mu}$ allowed for selected events.

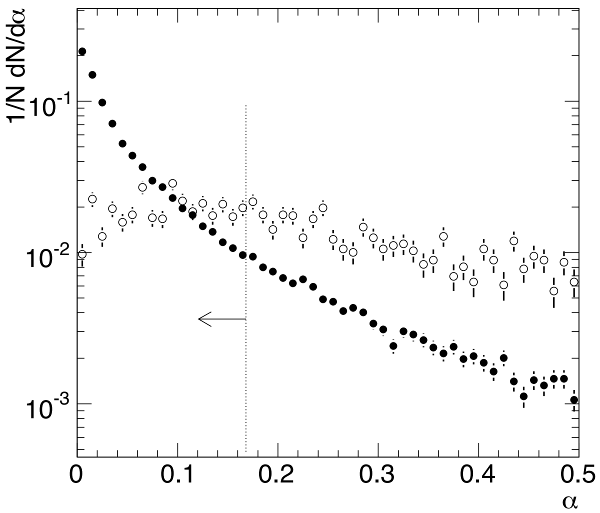

Figure 6: Distribution of pointing angle α for the reconstructed B_s^0 candidates. The signal is shown as closed circles, background as opened circles. Distributions is normalised to 1. The vertical line indicates the highest values of α allowed for selected events.

	$M_{\mu\mu}$	$I_{\mu\mu}$	α	L_{xy}
$M_{\mu\mu}$	1	-0.09	0.04	-0.03
$I_{\mu\mu}$		1	-0.07	-0.03
α			1	-0.17
L_{xy}				1

Table 4: The linear correlation coefficients among the discriminating variables for background events. The statistical uncertainty is about ± 0.05 for each coefficient.

efficiency is given for the cuts on the pointing angle and on the transverse decay length. As one can see the total rejection is largely overestimated if all cuts are treated separately, so the combined value is used to estimate a total yield of background events. The contribution from $B_s^0 \to K^-\mu\nu$ and $B_s^0 \to K^-\pi^+$ is found to be negligible comparing to the combinatorial background contribution. The errors quoted for the efficiencies are statistical only, so they represent only the size of the available Monte Carlo sample, but not the expected accuracy of the experiment where the initial number of background events will be much higher. More details on uncertainties will be given in Section 5.

Figure 8 shows the dimuon mass distribution for signal and background events after all selection cuts have been applied. For the combinatorial background, the contribution for the left and right side of the signal region is estimated in the same way as for the signal region (Table 5).

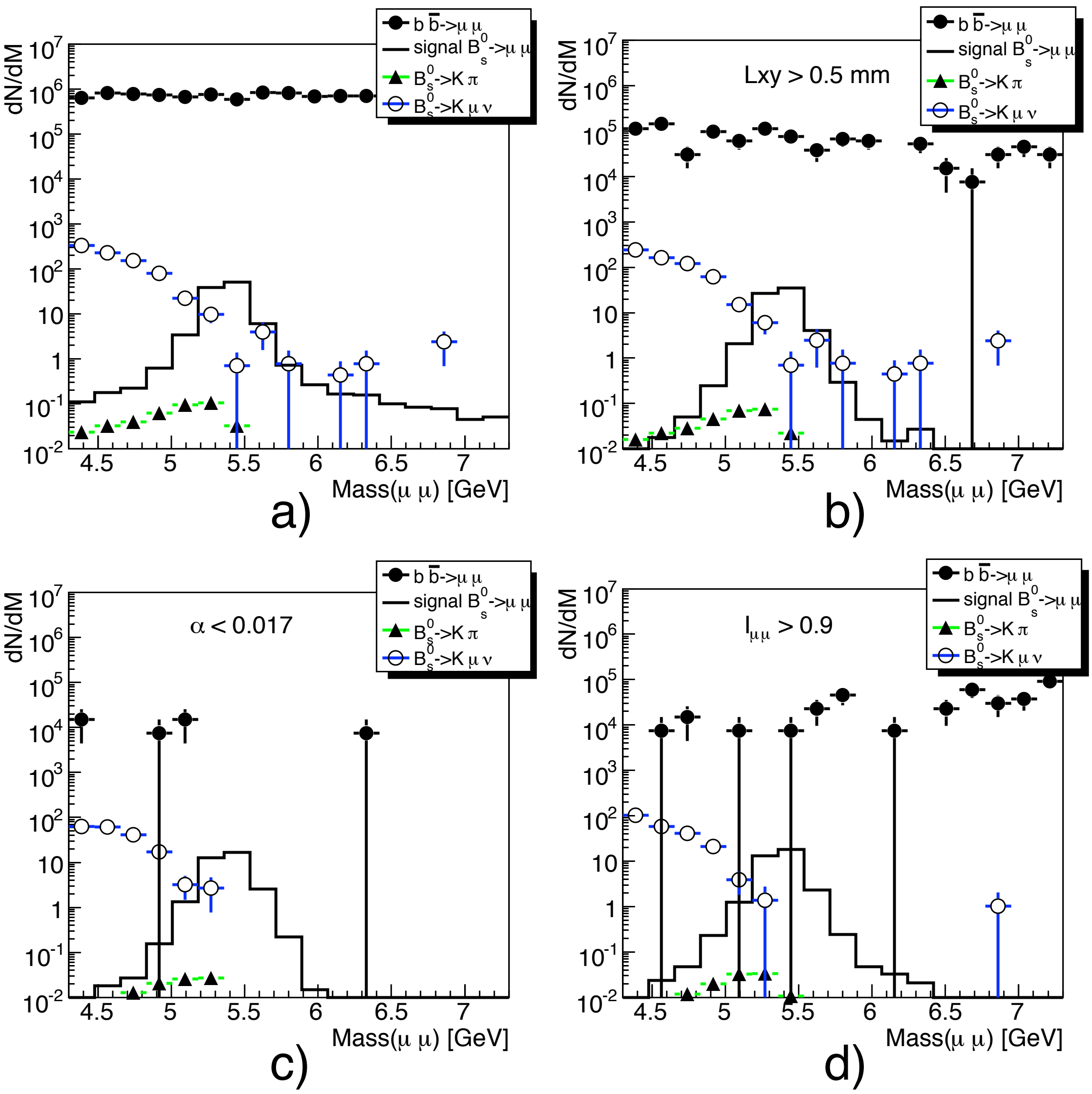

Figure 7: The Monte Carlo di-muon mass distributions for signal $B_s^0 \to \mu^+\mu^-$ (histogram), combinatorial background (closed circles) and non-combinatorial background (open circles and triangles) for (a) preselected events, (b) after cuts on transverse decay length, (c) pointing angle and (d) isolation. The number of events has been scaled to 10 fb^{-1} of integrated luminosity.

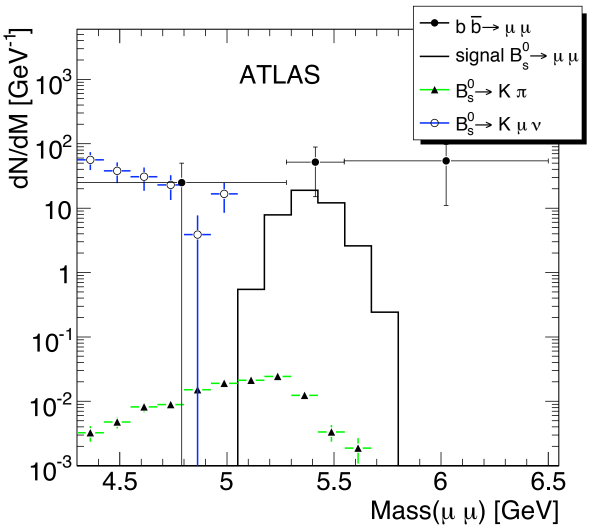

Figure 8: Dimuon mass distribution for surviving events after applying all three cuts. The signal is shown as histogram, combinatorial background by closed circles and non-combinatorial backgrounds by opened circles and triangles. The combinatorial background is estimated assuming a factorisation of applied cuts. Statistics are given for an integrated luminosity 10 fb^{-1}.

Table 5: Selection efficiencies and number of signal and background events for integrated luminosity of 10 fb^{-1}. Preselection criteria used: 4 GeV $< M(\mu\mu) <$ 7.3 GeV , vertex fit $\chi^2 < 10$, transverse decay length $L_{xy} <$ 20 mm. Numbers of expected events are computed according to the Standard Model expectation. In the left column for the $b\bar{b} \to \mu\mu X$ background the efficiencies are given separately for each cut, in the right column the combined efficiency is given for the cuts on the pointing angle and on the transverse decay length.

Selection cut	$B_s^0 \to \mu^+\mu^-$ efficiency	$b\bar{b} \to \mu^+\mu^- X$ efficiency	
$I_{\mu\mu} > 0.9$	0.24	$(2.6 \pm 0.3) \cdot 10^{-2}$	
$L_{xy} > 0.5$mm	0.26	$(1.4 \pm 0.1) \cdot 10^{-2}$	$(1.0 \pm 0.7) \cdot 10^{-3}$
$\alpha < 0.017$ rad	0.23	$(8.5 \pm 0.2) \cdot 10^{-3}$	
Mass in $[-\sigma, 2\sigma]$	0.76	0.079	
TOTAL	0.04	$0.24 \cdot 10^{-6}$	$(2.0 \pm 1.4) \cdot 10^{-6}$
Events yield	5.7		14^{+13}_{-10}

5 Systematic uncertainties

There are several sources of uncertainty in this analysis. Some of them are relevant only for the Monte Carlo study, whilst others should be taken into account with the real data analysis as well.

In this presented analysis, the expected number of signal and background events is estimated by counting directly instead of the normalisation procedure described in Section 3, which is supposed to be used in a real experiment. Consequently the dimuon trigger and reconstruction efficiencies, and acceptance, are not canceled by those from the reference channel and must explicitly be taken into account. Using the methods developed by ATLAS [12] this systematic uncertainly is estimated to be of about few percent.

There is a theoretical uncertainty of a factor of two in the b-production cross-section at LHC energies, which clearly affects the Monte Carlo predictions. Consequently all numbers of events from Table 5 scale accordingly.

The difference between the real and simulated kinematic properties of detected particles (e.g., due to not fully accounting for misalignment or material effects) can also introduce a bias in our predictions. However Figure 2 shows that the most of muons from $B_s^0 \to \mu^+\mu^-$ have a p_T in the region of the efficiency plateau so the possible deformation of p_T (as well as η) spectra could change the resulting efficiency by not more than a few percent. The uncertainty from the cuts factorisation hypothesis is assumed to be approximately 50%.

Some uncertainties will, to a large extent, cancel if we use a normalisation channel $B^+ \to J/\psi K^+$ to estimate the $\mathscr{B}(B_s^0 \to \mu^+\mu^-)$ as the dimuon trigger conditions are similar for both channels. Without experimental data, it is difficult to estimate the uncertainty in the number of background events in a given mass range. In the D0 analysis [17], the sideband extrapolation method is estimated to give an uncertainly of 20-30%. Indeed, this is the main source of uncertainty in the D0 analysis of $B_s^0 \to \mu^+\mu^-$. Corrections should also be made for the contribution of $B_d^0 \to \mu\mu$ decay in the experimental sample.

In total, the uncertainty from the systematic errors discussed in this Section is approximately $\pm$25%. In addition, the procedure adopted to estimate backgrounds via cut factorisation has large uncertainties, which are estimated to be of the order of 50%, as discussed above. In addition, a 70% uncertainty arises from Monte Carlo statistics. Overall, we choose to combine these in quadrature to obtain an indicative overall uncertainty on the background of +90%/-75%.

6 Start-up strategy

Already at 1 fb^{-1}of integrated luminosity, ATLAS can have $O(10^6)$ of dimuon events in a mass window 4 GeV $< M(\mu\mu) <$ 7 GeV (after vertexing and quality cuts). It will allow tuning of the selection procedure either for the cut-based analysis or for the multivariate methods for the background discrimination. Events that survive background suppression will be used to estimate the background contribution to the signal search region. The contribution from combinatorial background will be estimated using the sidebands interpolation procedure. The contribution from exclusive backgrounds due to fake dimuons from hadronic two-body B decays or from $B_s^0 \to K^-\mu^+\nu$, will be determined on the basis of the study of the hadron/muon misidentification probability. The background estimation will be compared with the number of events observed in the signal region. Following this information an upper limit on the number of signal events N_B corresponding to certain confidence level will be determined, using appropriate statistical methods. Finally, the value of N_B will be used to extract the upper limit on the $B_s^0 \to \mu^+\mu^-$ branching fraction, $\mathscr{B}(B_s^0 \to \mu^+\mu^-)$, using a reference channel $B^+ \to J/\psi K^+$. In this procedure a ratio of geometric and kinematical acceptances of the signal and the reference channels will be determined from the Monte Carlo simulation. Trigger and offline reconstruction efficiencies largely cancel for dimuons in these channels. The reference channel $B^+ \to J/\psi K^+$ will also be used to check the Monte Carlo simulation. The efficiency of the final selection cuts on discriminating variables for the signal $B_s^0 \to \mu^+\mu^-$ will be determined using Monte Carlo simulation (validated with the reference channel).

7 Conclusions

We have presented the strategy for searching for the rare decay $B_s^0 \to \mu^+\mu^-$ with the ATLAS detector. Whilst we do not expect to observe this decay during the early stages of the LHC, as more luminosity becomes available and our understanding of the backgrounds improves, it should be possible to identify a signal for the process. There are uncertainties due to the relatively unknown beauty production cross-section at the LHC, and also the limited Monte Carlo statistics available for this study. Within these limitations, assuming the Standard Model, we expect a signal of 5.7 events with a background of 14^{+13}_{-10} events for an integrated luminosity of 10 fb^{-1}. It is evident that the background uncertainties are large in this study. However, background estimates based on real data will be able to make use of much higher statistics and these will provide reduced uncertainties, as well as allowing the evaluation of more sophisticated methods of analysis.

References

[1] R.Ammar et.al., Phys. Rev. Lett. **71** (1993) 674.

[2] M.S. Alam et.al., Phys. Rev. Lett. **74** (1995) 2885.

[3] Heavy Flavor Averaging Group (HFAG) Collaboration, arXiv:hep-ex/0704.3575.

[4] B.Aubert et.al. [BABAR Collaboration], Phys. Rev.D **73** (2006) 092001.

[5] M.Iwasaki et.al.[Belle Collaboration], Phys. Rev. D **72** (2005) 092005.

[6] CDF Collaboration, Search for $B_s^0 \to \mu^+\mu^-$ and $B_d^0 \to \mu^+\mu^-$ Decays in $2fb^{-1}$ of $p\bar{p}$ Collisions with CDF II, CDF Public Note 8956, 2007.

[7] Bobeth, C. and Ewerth, T. and Kruger, F. and Urban, J., Phys. Rev. **D64** (2001) 074014.

[8] M. Misiak and J. Urban, Phys. Lett. **B 451**, 161 (1999); G. Buchalla and A.J. Buras, Nucl. Phys. **B 548**, 309 (1999).

[9] The Tevatron Electroweak Working Group, For the CDF and D Collaborations, Combination of CDF and D0 Results on the Mass of the Top Quark, arXiv:hep-ex/0608.032v1.

[10] ATLAS Collaboration, Introduction to B-Physics, this volume.

[11] W.-M.Yao et al. (Particle Data Group), J. Phys. **G 33** (2006).

[12] ATLAS Collaboration, Triggering on Low-p_TMuons and Di-Muons for B-Physics, this volume.

[13] ATLAS Collaboration, Performance Study of the Level-1 Di-Muon Trigger, this volume.

[14] S. Hassani et.al., Nuclear Instruments and Methods in Physics Research **A572** (2007) 77–79.

[15] V. Kostyukhin, VKalVrt - package for vertex reconstruction in ATLAS, ATLAS Note ATL-PHYS-2003-031, 2003.

[16] Y. Freund and R. Schapire, Journal of Computer and System Science **55** (1997) 119–139.

[17] The D0 Collaboration, A new upper limit for the rare decay $B_s^0 \to \mu^+\mu^-$ using $2fb^{-1}$ of Run II data, D0 Note 5344-CONF, 2007.

Trigger and Analysis Strategies for B_s^0 Oscillation Measurements in Hadronic Decay Channels

Abstract

The capabilities of measuring B_s^0 oscillations in proton-proton interactions with the ATLAS detector at the Large Hadron Collider are evaluated. B_s^0 candidates in the $D_s^- \pi^+$ and $D_s^- a_1^+$ decay modes from semileptonic exclusive events are simulated and reconstructed using a detailed detector description and the ATLAS software chain. For the measurement of the oscillation frequency a Δm_s sensitivity limit of 29.6 ps^{-1} and a five standard deviation measurement limit of 20.5 ps^{-1} are derived from unbinned maximum likelihood amplitude fits for an integrated luminosity of 10 fb^{-1} . The initial flavour of the B_s^0 meson is tagged exclusively with opposite-side leptons. Trigger strategies are proposed for scenarios of different instantaneous luminosities in order to maximise the signal channel trigger efficiencies.

1 Introduction

As tests of the Standard Model the CP–violation parameter $\sin(2\beta)$ will be measured with high precision (at the percent level) as well as properties of the B_s^0-meson system, like the mass difference of the two mass eigenstates Δm_s, the lifetime difference $\Delta\Gamma_s/\Gamma_s$ and the weak mixing phase ϕ_s induced by CP-violation, with $\phi_s \approx 2\lambda^2\eta$ in the Wolfenstein parametrisation. The different masses of the CP–eigenstates B_s^L (CP–even) and B_s^H (CP–odd) give rise to B_s mixing. The observed B_s^0 and $\bar{B}_s^0$ particles are linear combinations of these eigenstates, where transitions are allowed due to non–conservation of flavour in weak–current interactions and will occur with a frequency proportional to Δm_s. B_s^0 oscillations have been observed at the Fermilab Tevatron collider by the CDF collaboration [1] measuring a value of $\Delta m_s = (17.77 \pm 0.10\,(\mathrm{stat}) \pm 0.07\,(\mathrm{sys}))\,\mathrm{ps}^{-1}$ and D0 collaboration [2] reporting a two-sided bound on the B_s^0 oscillation frequency with a range of 17 ps^{-1} $< \Delta m_s <$ 21 ps^{-1}. Both results are consistent with Standard Model expectations [3]. In ATLAS, the Δm_s measurement is an important baseline for the B-physics program and an essential ingredient for a precise determination of the phase ϕ_s. CP–violation in B_s^0-$\bar{B}_s^0$ mixing is a prime candidate for the discovery of non–standard–model physics. For the channel $B_s^0 \to J/\psi\phi$, which has a clean experimental signature, a very small CP-violating asymmetry is predicted in the Standard Model. The measurement of any sizeable effect of the weak–interaction–induced phase ϕ_s in the CKM matrix, which lies above the predicted value, would indicate that processes beyond the Standard Model are involved. Furthermore, the determination of important parameters in the B_s^0 meson system will be valuable input for flavour dynamics in the Standard Model and its extensions.

In this note an estimation of the sensitivity to measure the B_s^0-$\bar{B}_s^0$ oscillation frequency with the ATLAS detector is presented. The signal channels considered are the hadronic decay channels $B_s^0 \to D_s^- \pi^+$ and $B_s^0 \to D_s^- a_1^+$ with $D_s^- \to \phi\pi^-$ followed by $\phi \to K^+K^-$. In the case of $B_s^0 \to D_s^- a_1^+$ the a_1^+ decays as $a_1^+ \to \rho\pi^+$ with $\rho \to \pi^+\pi^-$. Including the sub-decay $D_s^- \to K^{*0}K^-$ [4] would increase the event statistics by about 30%. However, for these sub-channels, which require an additional trigger signature, the increase of the overall trigger rate would be unacceptable. Detailed information of the signal and the exclusive background channels is given in Section 2. The high event rate at the Large Hadron Collider (LHC) imposes very selective requirements onto the B-physics trigger strategies, reducing the rate by about six orders of magnitude for recording events. Since an initial “low-luminosity” running period is scheduled with a luminosity starting at 10^{31} cm^{-2}s^{-1} and rising to $2 \cdot 10^{33}$ cm^{-2}s^{-1}, followed later on by the design luminosity of the LHC of 10^{34} cm^{-2}s^{-1}, the B-trigger must be flexible enough to cope with the increasing luminosity conditions. The overall B-trigger strategy as well as the different strategies dealing with the luminosity scenarios in the initial running periods are discussed in Section 3. An important part of the mixing measurement is to identify the flavour at production, i.e., whether the observed B_s meson initially contained a b or a $\bar{b}$ quark. A detailed description of an opposite-side lepton flavour tag and of the various sources of the wrong tag fractions is given in Section 4. The selection of B_s^0 candidates with kinematic cuts as well as mass resolutions of the B_s^0, are explained and shown in Section 5. A luminosity of 10^{33} cm^{-2}s^{-1} and no pileup is considered for the detailed analysis of signal and background channels. Strategies for lower and higher luminosities are also discussed in the same section. The results of the signal-candidate selection are used as input to a toy Monte Carlo simulation generating a sample of B_s^0 candidates, which is used for the amplitude fit method [5] to obtain the Δm_s measurement limits. The construction of the likelihood function, the Monte Carlo sample and the extraction of the Δm_s sensitivity are discussed in Section 6.

2 Simulated Data Samples

Simulated b-quark pairs are generated using PYTHIA [6], with the $\bar{b}$-quark required to decay to one of the specified signal channels. The b-quark decays semileptonically producing a muon with $p_T > 6$ GeV within $|\eta| < 2.5$. Details on generation, simulation and reconstruction of the simulated data samples are given in the introduction of the B-chapter [7].

In addition to the simulated signal samples $B_s^0 \to D_s^-(\phi\pi^-)\pi^+$ and $B_s^0 \to D_s^-(\phi\pi^-)a_1^+$, corresponding exclusive background channels that give an irreducible contribution to the selected B_s^0 signal were investigated. Two B_d^0 decay channels, $B_d^0 \to D^-\pi^+/a_1^+$ and $B_d^0 \to D_s^+\pi^-/a_1^-$, and one B_s^0 channel, $B_s^0 \to D_s^{*-}\pi^+/a_1^+$, were simulated for both hadronic decay channels. The dedicated trigger studies described in Section 3 require additional samples, such as the inclusive background channels $b\bar{b} \to \mu 6X$, $b\bar{b} \to \mu 4X$ and $c\bar{c} \to \mu 4X$ containing semileptonic b or c decays requiring one muon with a generated $p_T > 4$ GeV (or 6 GeV) and further decay products (X). Also, one particular signal sample (as a choice $B_s^0 \to D_s^- a_1^+$) requiring one muon with a generated $p_T > 4$ GeV (identified by $(\mu 4)$) is used for the trigger studies. A sample of minimum bias events is used for the determination of overall trigger rates. See Table 1 for the number of events generated and the cross-sections calculated from the values given by PYTHIA and the appropriate branching ratios [8]. Errors on the cross-sections include statistical errors and contributions from the uncertainties on the branching ratios.

Effects of pileup and B-meson mixing were not included in the simulation of any of the samples.

3 Trigger Strategies

The trigger strategy used for the $B_s^0 \to D_s^-\pi^+$ and $B_s^0 \to D_s^- a_1^+$ channels is to identify the $D_s^\pm$ decaying to $\phi(\to K^+K^-)\,\pi$, which is common to both decay channels. At level one (LVL1) a muon is required to enrich the content of the triggered data sample with B-events. The high level trigger (HLT) is split into level two (LVL2) and Event Filter (EF). A search for a $D_s^\pm$ is performed following one of two strategies. The first method, the FullScan approach, performs reconstruction of tracks within the entire Inner Detector. It is an efficient method, but time consuming and its feasibility depends on the background event rate. The second method performs track reconstruction in a limited volume of the Inner Detector only, which is defined by a low-p_T jet region of interest (RoI) identified at LVL1. This RoI-based method is faster but there is a loss in efficiency due to the requirement of a LVL1 jet RoI in the event and the geometrical restriction to the RoI.

The increase of the luminosity after LHC startup affects the trigger in two ways: the trigger rates for the jet and muon trigger will increase, seeding the HLT $D_s^\pm$ algorithm more frequently, and combinatorial

Table 1: Number of events generated and calculated cross-sections for the different signal and exclusive background simulated data samples for the $B_s^0 \to D_s^- \pi^+$ and $B_s^0 \to D_s^- a_1^+$ analysis and particular samples used for dedicated trigger studies. Branching ratios for particle decays into final states are included. $^{*)}$The branching fraction has not been measured yet, only an upper limit exists.

	Channel	Events	Cross-section [pb]
Signal	$B_s^0 \to D_s^- \pi^+$	88 450	10.4 ± 3.5
	$B_s^0 \to D_s^- a_1^+$	98 450	5.8 ± 3.2
Background	$B_d^0 \to D_s^+ \pi^-$	43 000	0.2 ± 0.1
	$B_d^0 \to D^- \pi^+$	41 000	6.2 ± 1.1
	$B_s^0 \to D_s^{*-} \pi^+$	40 500	9.1 ± 2.8
	$B_d^0 \to D_s^+ a_1^-$	50 000	$< 8.9\ ^{*)}$
	$B_d^0 \to D^- a_1^+$	50 000	3.7 ± 2.1
	$B_s^0 \to D_s^{*-} a_1^+$	100 000	12.1 ± 2.7
Trigger	$B_s^0 \to D_s^- a_1^+$ ($\mu4$)	50 000	13.6 ± 7.6
	$b\bar{b} \to \mu 6X$	242 150	$(6.14 \pm 0.02) \cdot 10^6$
	$b\bar{b} \to \mu 4X$	98 450	$(19.08 \pm 0.30) \cdot 10^6$
	$c\bar{c} \to \mu 4X$	44 750	$(26.28 \pm 0.09) \cdot 10^6$
	minimum bias	2 623 060	$70 \cdot 10^9$

background from pileup affects the performance of the selection algorithm. Therefore, trigger menus corresponding to different LHC luminosities are discussed in Sections 3.4 to 3.6.

The trigger efficiencies are presented for the $B_s^0 \to D_s^- a_1^+$ channel. Results for the $B_s^0 \to D_s^- \pi^+$ channel are expected to be similar within a few percent (see Section 3.2).

3.1 LVL1 Trigger Selection

The ATLAS hardware allows three LVL1 low-p_T muon trigger thresholds to be defined at once, which can only be adjusted between runs by reconfiguring the lookup tables implemented in the muon trigger firmware. In order to study more than three thresholds we investigated the two available, pre-defined menus (named A and B) with respect to the low-p_T muon trigger thresholds[1].

The three implemented low-p_T thresholds for trigger menu A are: 0 GeV[2] (named `MU00`), 5 GeV (`MU05`) and 6 GeV (`MU06`). For trigger menu B, the three low-p_T thresholds are 6 GeV (`MU06`), 8 GeV (`MU08`), and 10 GeV (`MU10`). Figure 1 shows the efficiencies of the low-p_T LVL1 muon trigger signatures as a function of the true p_T of the muon with the highest p_T in the event.

The LVL1 trigger efficiency depends strongly on the threshold chosen for the transverse momentum of the muon as shown in Table 2. Note that there is a discrepancy between the `MU06` efficiencies from both trigger menus, which will be taken as a systematic uncertainty of the current implementation. Although these dedicated trigger studies have been performed with the $B_s^0 \to D_s^- a_1^+$ sample, the LVL1 efficiencies for $B_s^0 \to D_s^- \pi^+(\mu 6)$ have been checked and agree well with those in Table 2.

The input to the LVL1 calorimeter trigger is a set of ~7 200 trigger towers with granularity $\Delta\phi \times \Delta\eta \approx 0.1 \times 0.1$ formed by the analogue summation of calorimeter cells. There are separate sets of trigger towers for the EM and hadronic calorimeters. The LVL1 jet algorithm employed here uses a

[1]All presented trigger thresholds are meant to be inclusive, i.e. to include all events fulfilling a trigger signature with a p_T threshold equal to or higher than the indicated one.

[2]This requires a coincidence between the muon chambers without an actual threshold applied. Due to the detector geometry this corresponds to an effective transverse momentum threshold of about 4 GeV.

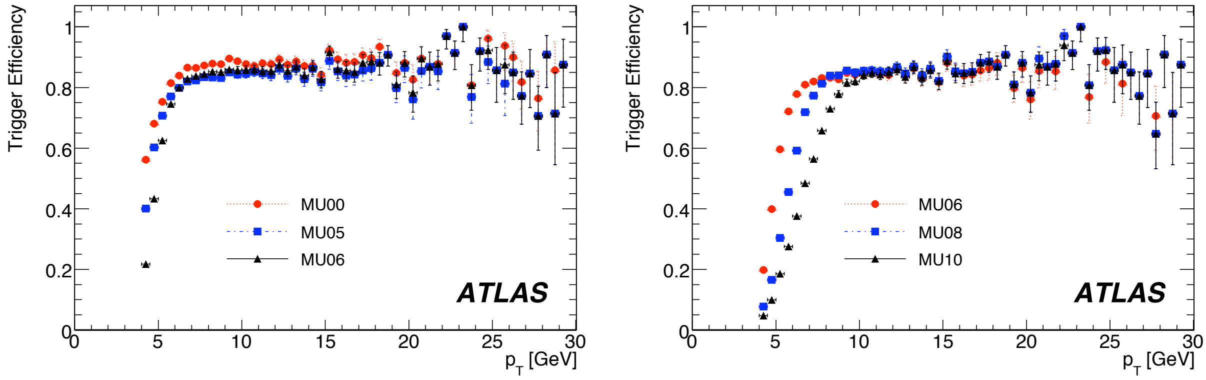

(a) Thresholds for menu A [9]

(b) Thresholds for menu B

Figure 1: Muon trigger efficiency as a function of the true p_T of the muon with the highest p_T in the event for the $B_s^0 \to D_s^- a_1^+(\mu 4)$ for (a) trigger menu A and (b) trigger menu B.

Table 2: LVL1 muon trigger efficiencies for the signal datasets $B_s^0 \to D_s^- a_1^+(\mu 4)$ and $B_s^0 \to D_s^- a_1^+(\mu 6)$ and the exclusive background samples. The first three lines refer to trigger menu A [9], while the last three lines refer to trigger menu B. For $b\bar{b} \to \mu 4X$, $b\bar{b} \to \mu 6X$ and $c\bar{c} \to \mu 4X$, the Monte Carlo data samples are only available using trigger menu A.

Menu	Threshold	Efficiency [%]				
		$B_s^0 \to D_s^- a_1^+$ $(\mu 4)$	$B_s^0 \to D_s^- a_1^+$ $(\mu 6)$	$b\bar{b} \to \mu 4X$	$b\bar{b} \to \mu 6X$	$c\bar{c} \to \mu 4X$
A	MU00	75.65 ± 0.19	86.77 ± 0.15	71.74 ± 0.14	86.60 ± 0.07	70.42 ± 0.22
	MU05	68.41 ± 0.21	82.60 ± 0.17	63.51 ± 0.15	81.91 ± 0.08	62.05 ± 0.23
	MU06	58.93 ± 0.22	81.90 ± 0.17	52.28 ± 0.16	81.00 ± 0.08	50.44 ± 0.24
B	MU06	61.15 ± 0.22	83.83 ± 0.16	—	—	—
	MU08	44.78 ± 0.22	77.64 ± 0.19	—	—	—
	MU10	34.89 ± 0.21	65.47 ± 0.21	—	—	—

cluster of $\Delta\phi \times \Delta\eta$ of approximately 0.4×0.4 (corresponding to 4×4 trigger towers). The projections of the vectors of the energy depositions onto the plane perpendicular to the beam axis (transverse energy, E_T) are summed over both the electromagnetic and the hadronic layers. The jet algorithm moves the cluster template in steps of 0.2 across the $\phi \times \eta$ plane. An RoI is produced if the 4×4 cluster is a local E_T maximum (as defined in [10]) and the cluster E_T sum is greater than the required threshold. The jet RoI is usable if the average number of RoIs per event (RoI multiplicity, see Fig. 2 and Table 3) is small, ideally about 1-2. Clearly, a compromise is required as an increased threshold will reduce the multiplicity, but will also give a reduced efficiency for finding the B jet in an event.

For a transverse energy threshold of 4 GeV, which is implemented to initiate the LVL2 $D_s^\pm$ trigger in trigger menus A and B, the jet trigger has an acceptance of $(98.36 \pm 0.06)\,\%$ based on all events in the $B_s^0 \to D_s^- a_1^+$ sample.

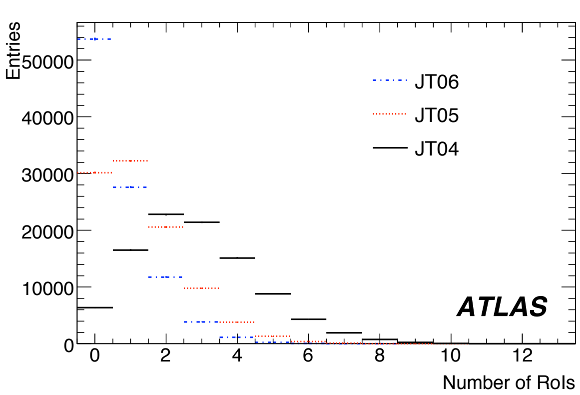

(a) $b\bar{b} \to \mu 4X$

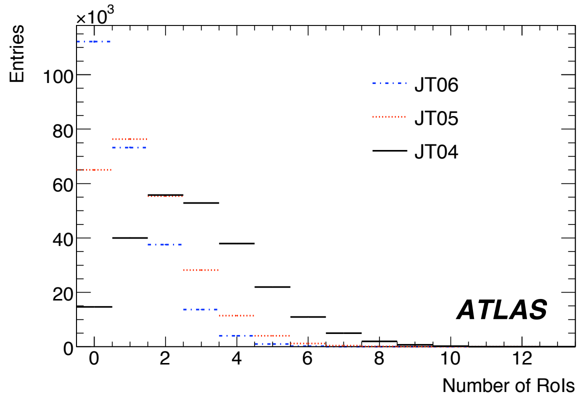

(b) $b\bar{b} \to \mu 6X$

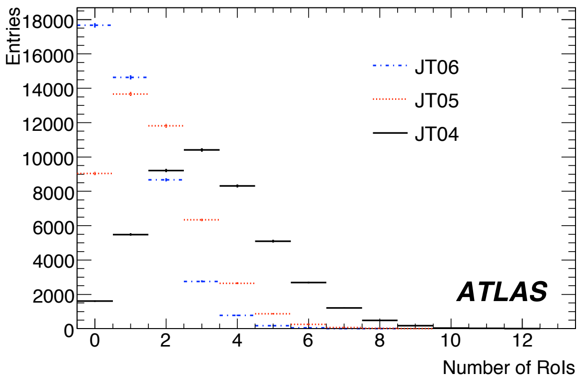

(c) $c\bar{c} \to \mu 4X$

Figure 2: RoI multiplicity distributions for the background samples (a) for $b\bar{b} \to \mu 4X$, (b) for $b\bar{b} \to \mu 6X$ and (c) for $c\bar{c} \to \mu 4X$ as a function of the jet RoI energy threshold [9]. Only RoIs with $\eta < 2.4$ have been taken into account. This corresponds to the requirement that the RoI is to be contained within the solid angle covered by the Inner Detector.

Table 3: Mean and root mean square of the RoI multiplicity distributions (Figure 2) for the background samples as a function of the jet RoI transverse energy (E_T) threshold [9]. Only RoIs with $\eta < 2.4$ have been taken into account. A strong anticorrelation between the E_T threshold and the mean RoI multiplicity is observed.

Threshold	$b\bar{b} \to \mu 4X$		$b\bar{b} \to \mu 6X$		$c\bar{c} \to \mu 4X$	
[GeV]	Mean	RMS	Mean	RMS	mean	RMS
4	2.847	1.746	2.883	1.754	3.235	1.759
5	1.301	1.244	1.441	1.295	1.643	1.300
6	0.703	0.952	0.881	1.046	0.998	1.048
7	0.454	0.786	0.634	0.911	0.703	0.900

3.2 LVL2 Trigger Selection

The first step of LVL2 is to confirm the LVL1 muon trigger decision using more precise muon momentum measurement. Secondly, information from Inner Detector and muon chambers are combined to give a further improvement in the momentum measurement.

As described above, the LVL2 tracking can be run in either FullScan or RoI-guided modes. In both cases, the same algorithm (named `DsPhiPi`) is used to combine the reconstructed tracks and search first for a ϕ and then for a $D_s^{\pm}$. In the RoI-guided approach tracks are reconstructed in a region $\Delta\phi \times \Delta\eta = 1.5 \times 1.5$ around all jet RoIs with E_T above a certain programmable threshold [11]. A p_T cut of 1.4 GeV is applied to all reconstructed tracks.

Opposite sign track pairs are considered as a ϕ candidate if they pass the following cuts: $|\Delta z| < 3$ mm, where z is the distance along the beam line of the track's point of closest approach to the centre of the detector, $|\Delta\phi| < 0.2$ and $|\Delta\eta| < 0.2$.

The tracks are combined using a K mass hypothesis and a cut around the ϕ mass $m_{\phi}(\text{PDG}) = 1019.46$ MeV [8] is applied. Track pairs passing the cut are then combined with all other tracks assuming a π mass for the third track. An event is selected if the mass of the track triplet is close to the $D_s^{\pm}$ mass $m_{D_s}(\text{PDG}) = 1968.2$ MeV. The mass cuts used are $1005\ \text{MeV} < m_{KK} < 1035\ \text{MeV}$ for the ϕ candidates and $1908\ \text{MeV} < m_{KK\pi} < 2028\ \text{MeV}$ for the D_s candidates.

The LVL2 track fit masses are shown in Figure 3 and Table 4 for the RoI-guided approach and FullScan. The standard deviations obtained from the Gaussian fits show that the mass cuts used correspond to 3.0 standard deviations for the ϕ mass distribution and 2.8 standard deviations for the $D_s^{\pm}$ mass distribution [9]. The results for the RoI-based approach and those for FullScan agree well.

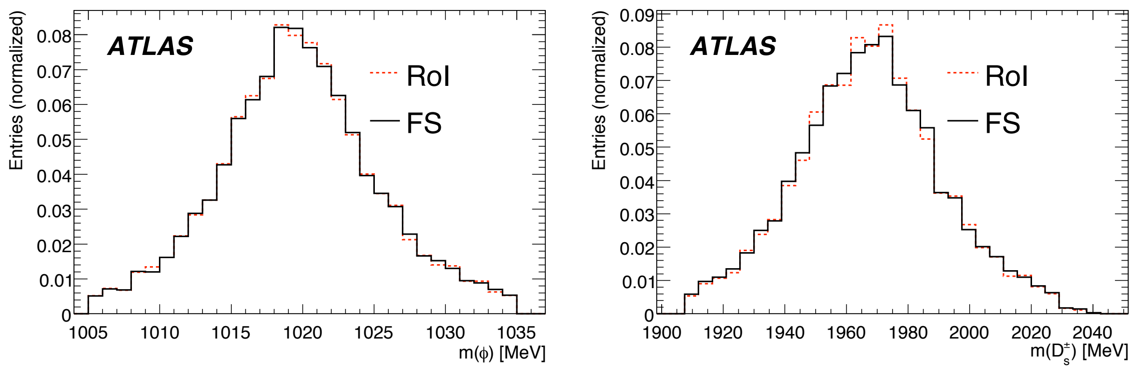

(a) True ϕ candidates (b) True $D_s^{\pm}$ candidates

Figure 3: LVL2 track fit mass distributions of (a) ϕ and (b) $D_s^{\pm}$ candidates (corresponding to a ϕ or $D_s^{\pm}$ particle from the signal decay in the Monte Carlo truth information) for the FullScan- and RoI-based LVL2 trigger signatures from $B_s^0 \to D_s^- a_1^+$ events fulfilling the respective LVL2 $D_s^{\pm}$ trigger signature and `MU06` [9].

The acceptances of possible trigger strategies up to LVL2 are given in Table 5 for the signal samples and in Table 6 for the background datasets. The LVL2 trigger rates for the $B_s^0 \to D_s^- \pi^+$ channel are expected to be lower by a few percent since the average p_T of the B_s^0 candidates and consequently the average p_T of the D_s candidates is smaller for the $B_s^0 \to D_s^- \pi^+$ channel than for the $B_s^0 \to D_s^- a_1^+$ channel due to different track selections (see Fig. 5 and Section 5.1).

Table 4: LVL2 track fit masses for the FullScan- and RoI-based LVL2 trigger signatures (only candidates corresponding to a ϕ or $D_s^{\pm}$ particle from the signal decay in the Monte Carlo truth information) from $B_s^0 \to D_s^- a_1^+$ events fulfilling the respective LVL2 $D_s^{\pm}$ trigger and MU06. The table shows the results of Gaussian fits within the trigger mass windows to the mass distributions from Fig. 3. The results for both trigger strategies agree within statistical errors.

	FullScan-based LVL2 trigger [9]	RoI-based LVL2 trigger
m(ϕ): mean [MeV]	1019.55 ± 0.05	1019.52 ± 0.05
m(ϕ): std. dev. [MeV]	5.07 ± 0.06	5.04 ± 0.05
m($D_s^{\pm}$): mean [MeV]	1966.9 ± 0.3	1967.0 ± 0.3
m($D_s^{\pm}$): std. dev. [MeV]	21.7 ± 0.3	21.5 ± 0.3

Table 5: Acceptances of LVL2 (RoI and FullScan, FS) for the $B_s^0 \to D_s^- a_1^+$ sample for trigger menus A and B.

Menu A			Menu B		
Trigger scenario	Passes (in %) ($\mu6$)	Passes (in %) ($\mu4$)	Trigger scenario	Passes (in %) ($\mu6$)	Passes (in %) ($\mu4$)
Events	50 000	50 000		50 000	50 000
L2_mu0	85.19±0.16	72.05±0.20	L2_mu6	77.13±0.19	35.03±0.21
L2_mu5	79.65±0.18	49.39±0.22	L2_mu8	45.54±0.22	18.96±0.18
L2_mu6	75.66±0.19	34.41±0.21	L2_mu10	26.04±0.20	10.91±0.14
FS & L2_mu0	32.98±0.21	22.93±0.19	FS & L2_mu6	29.99±0.21	12.71±0.15
FS & L2_mu5	30.79±0.21	16.75±0.17	FS & L2_mu8	19.14±0.18	10.91±0.14
FS & L2_mu6	29.38±0.20	12.49±0.15	FS & L2_mu10	11.83±0.15	4.92±0.10
RoI & L2_mu0	28.74±0.20	19.14±0.18	RoI & L2_mu6	26.19±0.20	11.10±0.14
RoI & L2_mu5	26.88±0.20	14.26±0.16	RoI & L2_mu8	17.09±0.17	7.05±0.12
RoI & L2_mu6	25.68±0.20	10.91±0.14	RoI & L2_mu10	10.80±0.14	4.56±0.09

Table 6: Acceptances of LVL2 (RoI and FullScan) for the background samples $b\bar{b} \to \mu4X$, $b\bar{b} \to \mu6X$ and $c\bar{c} \to \mu4X$ (trigger menu A).

Trigger scenario	passes (in %) ($b\bar{b} \to \mu4X$)	passes (in %) ($b\bar{b} \to \mu6X$)	passes (in %) ($c\bar{c} \to \mu4X$)
events	98 450	242 150	44 750
FS & L2_mu0	2.00±0.05	3.73±0.05	2.71±0.08
FS & L2_mu5	1.47±0.04	3.48±0.05	1.93±0.06
FS & L2_mu6	1.11±0.03	3.32±0.05	1.43±0.05
RoI & L2_mu0	1.73±0.04	3.34±0.05	2.34±0.07
RoI & L2_mu5	1.30±0.04	3.12±0.05	1.73±0.06
RoI & L2_mu6	1.01±0.03	2.99±0.05	1.32±0.05

3.3 Event Filter Selection

The muon confirmation at the Event Filter (EF) employs a muon track reconstruction algorithm using muon detector data only, similar to the algorithm used for offline reconstruction.

The EF $D_s^{\pm}$ selection is very similar to that at LVL2. The track reconstruction can be performed in FullScan or RoI-guided modes, which share a common EF signature. The search for ϕ and $D_s^{\pm}$ particles currently uses the same mass cuts as at LVL2, even though better mass resolutions are expected for the EF than for LVL2. In the future the mass cuts might be tightened and additional selection cuts will be added as discussed in section 3.5. EF output rates, which are only available for the minimum bias sample, are discussed in the following subsections.

3.4 Trigger Strategies for Early Running

At the lowest luminosities (10^{31} cm^{-2}s^{-1} and 10^{32} cm^{-2}s^{-1}), the trigger selection needs to be as efficient as possible, which means running a loose trigger. To estimate rates and perform timing studies a trigger menu with a different set of muon thresholds [12] is applied to the minimum bias sample. Table 7 shows the expected trigger rates for muons at LVL1 and after confirmation at LVL2. The output rates of the `DsPhiPi` trigger at LVL2 and the EF are given in Table 8 for 10^{31} cm^{-2}s^{-1}. For a luminosity of 10^{33} cm^{-2}s^{-1} and higher, the rates are expected to increase because of event pile-up and cavern background events.

Table 7: Muon rates based on $2.6 \cdot 10^6$ minimum bias events. Rates set in *italics* are based on an interpolation using an exponential approximation of the rate dependence on the muon threshold concerned. Effects caused by event pile-up and cavern-background events are not included.

Luminosity [cm^{-2}s^{-1}]	LVL1				
	L1_MU00		L1_MU06		L1_MU10
10^{31}	1.3 ± 0.02 kHz		480 ± 10 Hz		266 ± 8 Hz
10^{32}	13.0 ± 0.2 kHz		4.8 ± 0.1 kHz		2.7 ± 0.1 kHz
$1 \cdot 10^{33}$	130 ± 2 kHz		48 ± 1 kHz		27 ± 1 kHz
$2 \cdot 10^{33}$	260 ± 4 kHz		96 ± 2 kHz		54 ± 2 kHz
	LVL2				
	L2_mu0	L2_mu5	L2_mu6	L2_mu8	L2_mu10
10^{31}	450 ± 11 Hz	*213* Hz	120 ± 6 Hz	*50* Hz	25 ± 3 Hz
10^{32}	4.5 ± 0.1 kHz	*2.1* kHz	1.20 ± 0.06 kHz	*500* Hz	250 ± 30 Hz
$1 \cdot 10^{33}$	45.0 ± 1.1 kHz	*21* kHz	12.0 ± 0.6 kHz	*5* kHz	2.5 ± 0.3 kHz
$2 \cdot 10^{33}$	90.0 ± 2.2 kHz	*42* kHz	24.0 ± 1.2 kHz	*10* kHz	5.0 ± 0.6 kHz

In addition to the overall allowed output rate, the time constraints of the HLT system are limiting the `DsPhiPi` trigger. The maximum allowed average computing times are 40 ms at LVL2 and 1 s at the EF. Most of the time is taken in the tracking algorithms as can be seen in Table 9 which shows the average CPU time used by the tracking and hypothesis algorithms at LVL2 and EF.

Table 10 summarises the LVL2 efficiencies and the expected numbers for $B_s^0 \to D_s^- a_1^+(\mu 4)$ events before and after the application of event selection cuts in the analysis as well as the estimated LVL2 and EF trigger rates for different luminosity scenarios and different trigger choices. The L2 and EF output rates shown in this table are deduced from the rate information given in Tables 7 and 8. The LVL2 muon trigger efficiency estimates presented in Table 10 are based on the LVL2 results obtained with the $B_s^0 \to D_s^- a_1^+(\mu 4)$ sample shown in Table 5.

Table 8: Output rates for the `DsPhiPi` trigger based on $2.6 \cdot 10^6$ minimum bias events at 10^{31} cm^{-2}s^{-1}. Rates set in *italics* are based on an interpolation using the results from Table 7.

	LVL2		EF	
Muon input trigger	RoI	FullScan	RoI	FullScan
L1_MU00	23 ± 3 Hz	31 ± 3 Hz	14 ± 2 Hz	19 ± 2 Hz
L1_MU06	11 ± 2 Hz	13 ± 2 Hz	6.4 ± 1.3 Hz	7.5 ± 1.4 Hz
L2_mu0	15 ± 2 Hz	18 ± 2 Hz	6.1 ± 1.3 Hz	6.9 ± 1.4 Hz
L2_mu5	*9.5* Hz	*9.9* Hz	*4.5* Hz	*4.5* Hz
L2_mu6	6.7 ± 1.3 Hz	6.4 ± 1.3 Hz	3.5 ± 1.0 Hz	3.2 ± 0.9 Hz
L2_mu8	*3.9* Hz	*3.3* Hz	*2.1* Hz	*1.7* Hz
L2_mu10	*2.5* Hz	*2.0* Hz	*1.2* Hz	*0.9* Hz

Table 9: Average CPU times on an HLT computing node (Dual core Intel(R) Xeon(R) CPU 5160 @ 3.00 GHz) using 900 $b\bar{b} \to \mu 6X$ events.

		Algorithm	Time/RoI	Time/event
LVL2	tracking	Idscan_RoI	15 ms	23 ms
		Idscan_FullScan		91 ms
	hypothesis	`DsPhiPi`		< 1 ms
Event Filter	tracking	RoI	130 ms	208 ms
		FullScan		470 ms
	hypothesis	`DsPhiPi`		< 1 ms

At 10^{31} cm^{-2}s^{-1}, once the improvements discussed in Section 3.5 have been applied to the EF algorithms, it should be possible to run the FullScan-based trigger at the LVL1 4 GeV muon rate and to remain within the constraints given by available trigger resources. As the luminosity is increased to 10^{32} cm^{-2}s^{-1}, we will need to raise the muon threshold for the FullScan-based trigger or to move to a RoI-based trigger. However, the muon threshold should be kept as low as possible in order to achieve the highest possible trigger efficiency and to allow for as many $B_s^0 \to D_s^- a_1^+$ events as possible to pass. Compared to earlier publications like [13] the $b\bar{b}$ cross-section as shown in [7] is at the upper limit of what is expected and therefore the muon rates are likely to be overestimated.

3.5 Trigger Strategies for Running at 10^{33} cm^{-2}s^{-1}

At 10^{33} cm^{-2}s^{-1} the trigger needs to remain as efficient as possible while operating within the constraints of the trigger system's resources. The EF output rate is expected to be about 10-20 Hz for B-physics.

The muon rates expected at LVL1 and LVL2 for different thresholds and luminosities are included in Table 7. The LVL2 muon rates are the input rates for the LVL2 tracking algorithms. Using the information on jet RoI multiplicities from Figure 2 and Table 3, the computing times from Table 9 and the muon rates in Table 7, trigger strategies are determined for different luminosities.

For a luminosity of 10^{33} cm^{-2}s^{-1}, a LVL1 trigger muon in combination with the RoI-based D_s trigger will be used. It is planned to use thresholds of 6 GeV for the trigger muon and 5 GeV for the jet RoI trigger. It is clear from Table 8 that in order to run such a trigger the LVL2 and EF selections will have to be tightened. This may be achieved by introducing vertex fitting and by reconstructing the B_s^0 at the

Table 10: LVL2 and EF output rates for minimum bias events, LVL2 trigger efficiencies and numbers of expected $B_s^0 \to D_s^- a_1^+(\mu 4)$ events without or with selection cuts. Rates set in *italics* are estimates based on the interpolated and extrapolated rates given in Table 7. LVL2 output rates marked by † are downscaled by a factor two, the estimated rate reduction for a D_s vertex requirement at LVL2. For EF output rates marked by ‡, an estimated rate reduction factor of 60 accounting for EF B_s^0 reconstruction is applied. (See section 3.5 for details.) The results in the columns "LVL2 eff." and $N_{LVL2\ output}^{B_s^0 \to D_s^- a_1^+}$ (without and with selection cuts applied) are based on the $B_s^0 \to D_s^- a_1^+(\mu 4)$ Monte Carlo data sample. Numbers marked by # are corrected for the estimated efficiency loss by a D_s vertex requirement at LVL2. The integrated luminosities and expected event numbers correspond to one year running at the given instantaneous luminosity (10^7 seconds).

$\mathscr{L}$ [cm^{-2}s^{-1}]	$\int \mathscr{L} dt$ [pb]$^{-1}$	Trigger set	LVL2 eff. [%]	$N_{LVL2\ output}^{B_s^0 \to D_s^- a_1^+}$ no sel. cuts	$N_{LVL2\ output}^{B_s^0 \to D_s^- a_1^+}$ incl. sel. cuts	LVL2 rate [Hz]	EF rate [Hz]
10^{31}	100	L2mu0FS	22.93 ± 0.19	308	63	18 ± 2	6.9 ± 1.4
		L2mu5FS	16.75 ± 0.17	225	47	*9.9*	*4.5*
		L2mu6FS	12.49 ± 0.15	168	35	6.4 ± 1.3	3.2 ± 0.9
10^{32}	1 000	L2mu6FS	12.49 ± 0.15	1 678	351	64 ± 13	32 ± 9
		L2mu5RoI	14.26 ± 0.16	1 916	267	*95*	*45*
		L2mu6RoI	10.91 ± 0.14	1 466	322	67 ± 13	35 ± 10
10^{33}	10 000	L2mu5RoI	$12.01 \pm 0.13^{\#}$	16 134#	3 582#	*475*†	*7.5*‡
		L2mu6RoI	$9.19 \pm 0.12^{\#}$	12 344#	2 709#	$335 \pm 93^\dagger$	$5.8 \pm 2.0^\ddagger$
		L2mu8RoI	$5.94 \pm 0.10^{\#}$	7 976#	1 757#	*196*†	*3.5*‡
		L2mu10RoI	$3.84 \pm 0.08^{\#}$	5 159#	1 132#	*126*†	*2.0*‡
$2 \cdot 10^{33}$	20 000	L2mu6RoI	$9.19 \pm 0.12^{\#}$	24 687#	5 418#	$670 \pm 187^\dagger$	$11.7 \pm 4.0^\ddagger$
		L2mu8RoI	$5.94 \pm 0.10^{\#}$	15 953#	3 517#	*392*†	*7.1*‡
		L2mu10RoI	$3.84 \pm 0.08^{\#}$	10 318#	2 264#	*252*†	*4.1*‡

EF level.

Preliminary studies at LVL2 show that a requirement for a vertex fit to the 3 tracks of the D_s candidate can achieve a factor 2 rate reduction for a drop in efficiency from 38% to 32%. This estimate is applied to cells marked by # and † in Table 10. Also, it might be an option to further reduce the rate by tightening the acceptance windows for m_ϕ and m_{D_s} on LVL2, but the resulting rate reduction and the expected signal efficiency loss will need to be studied.

A considerable rate reduction at the EF level may be achieved by reconstructing the B_s^0. A preliminary study using offline selection cuts (see Section 5.1), which have been relaxed to simulate wider mass window and vertexing requirements for the reconstructed particles, has been performed with the $b\bar{b} \to \mu 4X$ and $c\bar{c} \to \mu 4X$ samples. The resulting rate reduction factor, estimated to be approximately 60, is applied to cells marked by ‡ in Table 10. According to this study, the overall trigger and reconstruction efficiency for the $B_s^0 \to D_s^- a_1^+$ signal events will be reduced by about 55%. Although these estimates will need to be confirmed by an implementation of a simplified B_s^0 reconstruction at the EF level, reasonable EF output rates are expected to be achievable.

The numbers of expected $B_s^0 \to D_s^- a_1^+(\mu 4)$ events for 10 fb^{-1} of data for a luminosity of 10^{33} cm^{-2}s^{-1} are given in Table 10. It will be necessary to establish a muon trigger threshold as low as possible to maximise the signal event yield.

3.6 Trigger Strategies for Higher Luminosities

As luminosity increases, it is necessary to stay within the limits of the LVL2 trigger processing times and allowable output rates. As Table 10 shows, this will require increasing the muon threshold to 8 GeV or

10 GeV and to add additional trigger elements in the EF as discussed at the end of Section 3.5. Another option, however a less efficient one, is to prescale the 6 GeV rate before running the track reconstruction.

4 Flavour Tagging

The measurement of B_s^0 oscillations needs the knowledge of the flavour of the B_s^0 meson at production time and at decay time in order to classify events as mixed or not mixed. The tagging algorithm tries to determine the flavour at production time, whereas the decay particles of the signal B_s^0 determine the flavour at decay time. In this analysis soft muon tagging (see B-physics chapter of [4]) is used and the general application on the simulated data samples is shown in Section 4.2 without applying trigger conditions or any selection cut. Tagging results specific for the hadronic channels under investigation including trigger and selection cuts for B_s^0 candidates are given in Section 5.3.

4.1 Soft Muon Tagging

In proton-proton collisions b quarks are produced in pairs leaving the signal B_s^0 and the opposite side b hadron with the opposite flavour. In the case of a semileptonic decay as shown in Fig. 4, the charge of the produced lepton is correlated with the flavour of the signal B_s^0 meson at production time. The charge of the muon with the highest reconstructed p_T is used for the determination of the flavour. Because of the muon trigger, in hadronic B_s^0 decay channels soft muon tagging has a high tagging efficiency $\varepsilon_{tag} = N_{tag}/N_{all}$ limited by the muon reconstruction efficiency. Details on the aspects of muon reconstruction and identification in ATLAS can be found in [14].

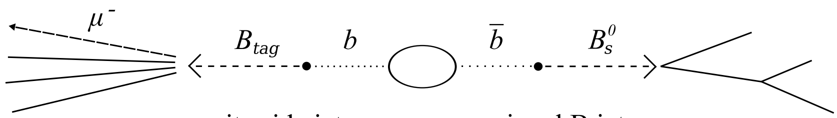

Figure 4: In the case of a signal B_s^0, the associated opposite side b hadron decaying semileptonically produces a negatively charged lepton.

The dilution factor is defined as $D_{tag} = \frac{N_c - N_w}{N_c + N_w}$ where N_c is the number of events correctly tagged and N_w is the number of events with a wrong tag. These wrong tags arise from mixing of the tagging b hadron, muons from decays $b \to c \to \mu$, additional c pairs and various particles decaying into muons. The wrong tag fraction $\omega = N_w/(N_c + N_w)$ is the ratio of wrongly tagged events to all tagged events. As the generation of the simulated data does not include B meson oscillations, mixing of the tagging side hadron is introduced artificially using the integrated mixing probabilities χ_d and χ_s [8]:

$$\chi_d = \frac{\Gamma(B_d^0 \to \bar{B}_d^0 \to \mu^+ X)}{\Gamma(B_d^0 \to \mu^\pm X)} = 0.188 \pm 0.003 \qquad \chi_s = \frac{\Gamma(B_s^0 \to \bar{B}_s^0 \to \mu^+ X)}{\Gamma(B_s^0 \to \mu^\pm X)} = 0.49924 \pm 0.00003$$

4.2 Application to Signal Samples

In Fig. 5 the transverse momentum of the signal B_s^0 mesons is compared for the two B_s^0 decay channels, the vertical lines show the mean values of the two distributions. This difference arises from the different kinematical configuration due to the condition on all charged final state particles $p_T > 0.5$ GeV at Monte

Carlo generation. As $B_s^0 \to D_s^- a_1^+$ has a total number of six final state particles, the mean transverse momentum of the signal B_s^0 is higher compared to $B_s^0 \to D_s^- \pi^+$ with a total number of four final state particles. The difference in the B_s^0 transverse momentum spectrum is also expected at offline reconstruction level due to the different p_T selection cuts for the π and the a_1 combinations (see Section 5.1). This leads in the case of the $B_s^0 \to D_s^- \pi^+$ sample to an overall wrong tag fraction of $\omega = 20.29 \pm 0.14$ % and in the case of the $B_s^0 \to D_s^- a_1^+$ channel to a wrong tag fraction $\omega = 21.05 \pm 0.11$ %, which is higher compared to the $B_s^0 \to D_s^- \pi^+$ channel (see all events in Table 11 in Section 5.3).

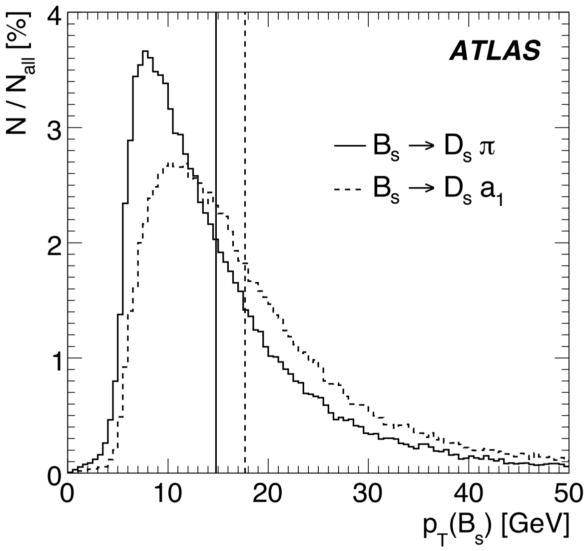

Figure 5: Normalised distributions of signal B_s^0 transverse momentum p_T of the two channels $B_s^0 \to D_s^- \pi^+$ and $B_s^0 \to D_s^- a_1^+$. The vertical lines represent the mean values of the distributions, in the case of $B_s^0 \to D_s^- \pi^+$ the mean is 14.80 ± 0.03 GeV, in the case of $B_s^0 \to D_s^- a_1^+$ 17.68 ± 0.03 GeV. The observed difference is due to the different particle selections.

In Fig. 6 the wrong tag fractions and the sources of these wrong tags are compared for both B_s^0 decays channels. The wrong tag fraction is shown as a function of the tagging muon's transverse momentum $p_T(\mu)$, in Fig. 6(a) for $B_s^0 \to D_s^- \pi^+$ and in Fig. 6(b) for $B_s^0 \to D_s^- a_1^+$. In the regime $p_T(\mu) < 11$ GeV the $B_s^0 \to D_s^- a_1^+$ wrong tag fraction is higher. As mentioned above this difference arises from the different track selections of the two decay channels. In both channels the two main sources of wrong tags are mixing of neutral B mesons on the tagging side and muons from cascade decays $b \to c \to \mu$. As the overall wrong tag fraction is decreasing with the muon p_T, also the part with a wrong tag due to the cascade $b \to c \to \mu$ is decreasing at the same rate. A further source of mistags are additional $c\bar{c}$-pairs. The wrong tag fraction of this part stays about constant with increasing $p_T(\mu)$. A small part of the wrong tag fraction originates from J/ψ, ϕ, ρ, η or τ particles decaying into muons. Additional sources like muons from kaons and pions or hadrons misidentified as muons can be neglected [12].

A $b\bar{b}$ pair produced in proton proton collisions has a transverse momentum equal to zero at first order. Going through fragmentation and hadronisation, the p_T of the signal B_s^0 meson and the opposite side b hadron are still correlated, and therefore a muon coming from a semileptonic decay of the b hadron also is correlated with the signal B_s^0. Hence a muon from a cascade $b \to c \to \mu$ is more likely to pass the LVL1 muon trigger when B_s^0 meson has a higher p_T, leading to the increase in wrong tag fraction with $p_T(B_s^0)$. This behaviour is shown in the Fig. 6(c) and 6(d).

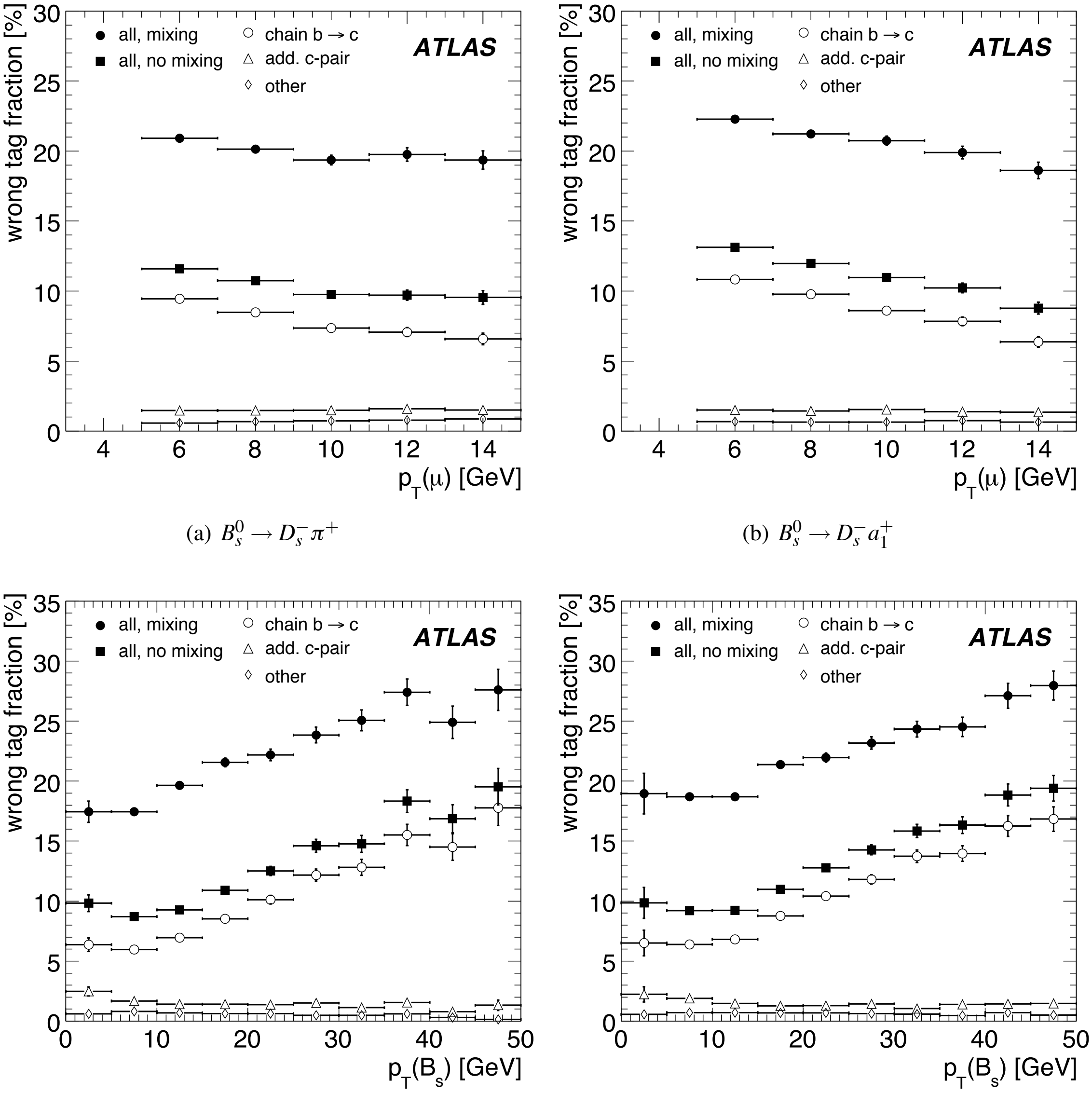

(a) $B_s^0 \to D_s^- \pi^+$

(b) $B_s^0 \to D_s^- a_1^+$

(c) $B_s^0 \to D_s^- \pi^+$

(d) $B_s^0 \to D_s^- a_1^+$

Figure 6: Wrong tag fraction as functions of tagging muons transverse momentum $p_T(\mu)$ in (a) and (b) and wrong tag fractions as functions of signal Monte Carlos B_s^0 transverse momentum $p_T(B_s^0)$ in (c) and (d). The wrong tag fraction is shown with mixing of the tagging side b hadron and without mixing. Without mixing, the different sources of wrong tags are shown. The main contribution is coming from $b \to c \to \mu$ followed by additional c pairs. Additional sources shown are muons coming from J/ψ, ϕ, ρ, η and τ.

4.3 Systematic Uncertainties of Soft Muon Tagging

The calibration of the soft muon tagger will be done with events from the exclusive decay channel $B^+ \to J/\psi(\mu^+\mu^-)K^+$. The high branching ratio and the simple event topology allows the measurement of this channel during the initial luminosity phase at the LHC. Without mixing on the signal side, these events can be used to estimate the systematic uncertainties of soft muon tagging.

For an integrated luminosity of 1 fb^{-1} 160 000 events of the decay channel $B^+ \to J/\psi(\mu^+\mu^-)K^+$ are expected [15] at ATLAS. About 13.5 % events are estimated to have an additional third muon for flavour tagging. Requiring a minimum transverse momentum of 6 GeV for this additional muon, the number of events will be reduced by a factor of three. Assuming that the wrong tag fraction in this channel behaves like in the hadronic B_s^0 decay channels, the expected statistical error of the wrong tag fraction would be of the order of 0.1 % for 1 fb^{-1} integrated luminosity.

5 Event Selection

For the following analysis selecting B_s candidates the default trigger choices are to require MU06 and JT04 trigger elements at LVL1 and to perform a search for the $D_s \to \phi(K^+K^-)\pi$ decay within a jet RoI at LVL2. Resulting event numbers and plots are given for 10 fb^{-1} unless indicated otherwise.

5.1 Signal Event Reconstruction

For the reconstruction of the B_s vertex only tracks with a pseudo-rapidity $|\eta| < 2.5$ are used proceeding via the following steps. The ϕ decay vertex is first reconstructed by considering all pairs of oppositely-charged tracks with $p_T > 1.5$ GeV for both tracks. Kinematic cuts on the angles between the two tracks, $\Delta\varphi_{KK} < 10°$ and $\Delta\theta_{KK} < 10°$, are imposed, where φ denotes the azimuthal angle and θ the polar angle. The two-track vertex is then fitted assigning the kaon mass to both tracks. Combinations passing a fit-probability cut [16] of 1% ($\simeq \chi^2$/dof = 7/1) with the invariant mass within three standard deviations of the nominal ϕ mass are selected as ϕ candidates. The plots in Fig. 7 show the invariant mass distribution for all m_{KK} combinations overlaid with the ϕ candidates matching a generated ϕ from the signal decay (grey filled area) fitted with a single Gaussian function. For the $B_s^0 \to D_s^-\pi^+$ channel the mass resolution is $\sigma_\phi = (4.30 \pm 0.03)$ MeV and for the $B_s^0 \to D_s^- a_1^+$ channel $\sigma_\phi = (4.28 \pm 0.03)$ MeV. This mass window for accepted ϕ candidates is shown by the vertical lines. No trigger selections are applied for the mass plots shown in Fig. 7 to Fig. 9.

From the remaining tracks, a third track with $p_T > 1.5$ GeV is added to all accepted ϕ candidates. The pion mass is assigned to the third track and a three-track vertex is fitted. Three-track vertex candidates which have a fit probability greater than 1% ($\simeq \chi^2$/dof = 12/3) and an invariant mass within three standard deviations of the nominal D_s mass are selected as D_s candidates. The plots in Fig. 8 show the invariant mass distribution for all $m_{KK\pi}$ combinations overlaid with the D_s candidates matching a generated D_s from the signal decay (grey filled area) fitted with a single Gaussian function. For the $B_s^0 \to D_s^-\pi^+$ channel the mass resolution is $\sigma_{D_s} = 17.81 \pm 0.13$ MeV and for the $B_s^0 \to D_s^- a_1^+$ channel $\sigma_{D_s} = 17.92 \pm 0.13$ MeV. The $3\sigma_{D_s}$ mass range for accepted D_s candidates is shown by the vertical lines.

For the $B_s^0 \to D_s^- a_1^+$ channel a search is performed for $a_1^\pm$ candidates using three-particle combinations of charged tracks for events with a reconstructed D_s meson. In a first step ρ^0 mesons are reconstructed from all combinations of two tracks with opposite charges and with $p_T > 0.5$ GeV, each particle in the combination being assigned a pion mass. A kinematic cut $\Delta R_{\pi\pi} = \sqrt{\Delta\phi_{\pi\pi}^2 + \Delta\eta_{\pi\pi}^2} < 0.650$ is used to reduce the combinatorial background. The two selected tracks are then fitted as originating from the same vertex; from the combinations passing a fit probability cut of 1% ($\simeq \chi^2$/dof = 7/1), those with an invariant mass within 400 MeV of the nominal ρ^0 mass are selected as ρ^0 candidates. Next a third track with $p_T > 0.5$ GeV from the remaining charged tracks is added to the ρ^0 candidate, assuming the pion hypothesis for the extra track. A kinematic cut $\Delta R_{\rho\pi} < 0.585$ is applied. The three tracks are fitted to a common vertex without any mass constraints. Combinations with a fit probability greater than 1% ($\simeq \chi^2$/dof = 12/3) and with an invariant mass within 325 MeV of the nominal a_1 mass are selected as $a_1^{\pm}$ candidates.

The B_s^0 candidates are reconstructed combining the $D_s^{\pm}$ candidates with $a_1^{\mp}$ candidates with opposite charge and different tracks. A six-track vertex fit is performed with mass constraints for the tracks from ϕ and D_s; due to the large a_1 natural width the three tracks from the a_1 are not constrained to the a_1 mass. The total momentum of the B_s^0 vertex is required to point to the primary vertex and the momentum of the D_s vertex to the B_s^0 vertex. Only six-track combinations with a vertex fit probability greater than 1% ($\simeq \chi^2$/dof = 27/12) are considered as B_s^0 candidates.

For the $B_s^0 \to D_s^- \pi^+$ channel for each reconstructed D_s meson a fourth track from the remaining tracks in the event is added. This track is required to have opposite charge with respect to the pion track from the D_s and $p_T > 1$ GeV. The four-track decay vertex is fitted including ϕ and D_s mass constraints, and requiring that the total momentum of the B_s^0 vertex points to the primary vertex and the momentum of D_s vertex points to the B_s^0 vertex. In order to be selected as B_s^0 candidates, the four-track combinations are required to have a vertex fit probability greater than 1% ($\simeq \chi^2$/dof = 20/8).

For both channels, $B_s^0 \to D_s^- \pi^+$ and $B_s^0 \to D_s^- a_1^+$, the signed separation between the reconstructed B_s^0 vertex and the primary vertex is required to be positive (the momentum should not point backward to the parent vertex). To improve the purity of the sample, further cuts are imposed: the proper decay time of the B_s^0 has to be greater than 0.4 ps, the B_s^0 impact parameter (shortest distance of the reconstructed B_s^0 trajectory from the primary vertex in the transverse plane to the reconstructed B_s^0 decay vertex) is required to be smaller than 55 μm and p_T of the B_s^0 must be larger than 10 GeV. The plot in Fig. 9(a) shows the invariant mass distribution for all $m_{KK\pi\pi}$ B_s candidates matching a generated B_s from the signal decay for the $B_s^0 \to D_s^- \pi^+$ channel fitted with a single Gaussian function and giving a mass resolution of $\sigma_{B_s} = 52.80 \pm 0.68$ MeV. For the $B_s^0 \to D_s^- a_1^+$ channel Fig. 9(b) shows the invariant mass distribution for all $m_{KK\pi\pi\pi\pi}$ B_s candidates matching a generated B_s and giving a mass resolution of $\sigma_{B_s} = 40.82 \pm 0.53$ MeV. The difference in the B_s^0 mass resolutions is caused by the p_T spectrum of the π in the $B_s^0 \to D_s^- \pi^+$ decay being harder than the p_T spectra of the three pions in the $B_s^0 \to D_s^- a_1^+$ decay, as the pion momentum resolution is worse for higher p_T. A final mass cut of two standard deviations on the B_s^0 candidates is applied for further analysis (see vertical lines in Fig. 9). For some events more than one B_s^0 candidate is reconstructed and in that case the candidate with the lowest χ^2/dof from the vertex fit is selected for further analysis.

No relevant effects induced by the trigger selections on fit variables of the mass plots or the kinematic distributions of the B_s candidates are found (discussed in Section 6.3). All differences are within the fit errors.

5.2 Background Channels

Two main sources of background are considered: irreducible background coming from a decay channel that closely mimics the B_s^0 signal and combinatorial background coming from random combination of tracks.

5.2.1 Exclusive Background Channels

The exclusive samples listed in Table 1 are used as irreducible background sources. See Table 12 in Section 6 for the numbers of reconstructed candidates after applying the same selection cuts as for the signal samples. The histograms in Fig. 10 show the invariant mass spectrum of reconstructed B_s^0 candidates for the $B_s^0 \to D_s^- \pi^+$ and $B_s^0 \to D_s^- a_1^+$ channel respectively (no trigger selection cut applied). The different contributions are scaled with the cross-section given in Table 1.

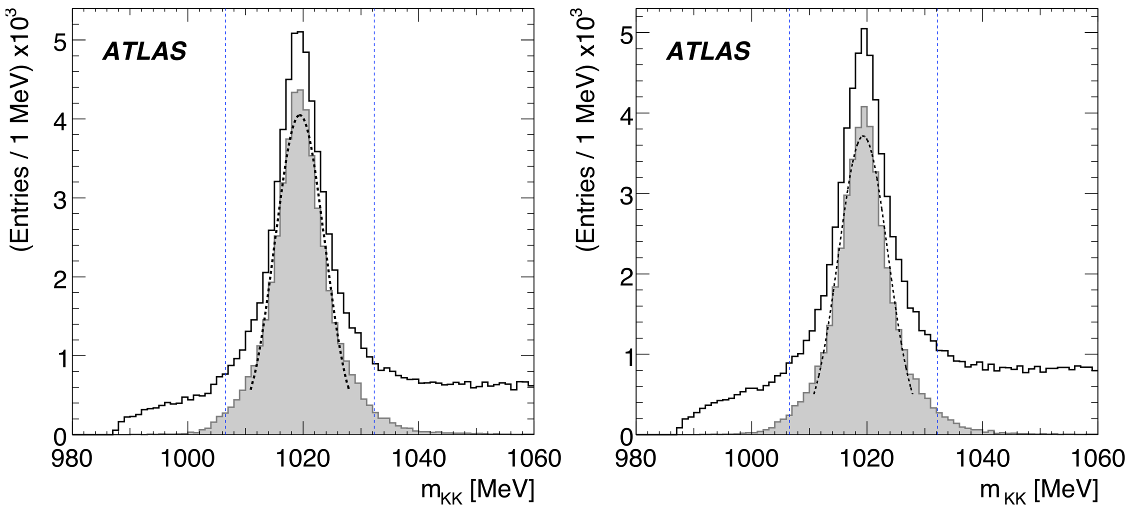

(a) $B_s^0 \to D_s^- \pi^+$ (b) $B_s^0 \to D_s^- a_1^+$

Figure 7: Reconstructed mass m_{KK} for all combinations within the signal sample (black line) and KK candidates corresponding to a ϕ particle from the signal decay in the Monte Carlo truth information (grey filled). The standard deviation obtained from a fit within two standard deviations of a Gaussian function (dashed) to the distribution defines the three standard deviation cut range (vertical dashed). No trigger conditions are applied.

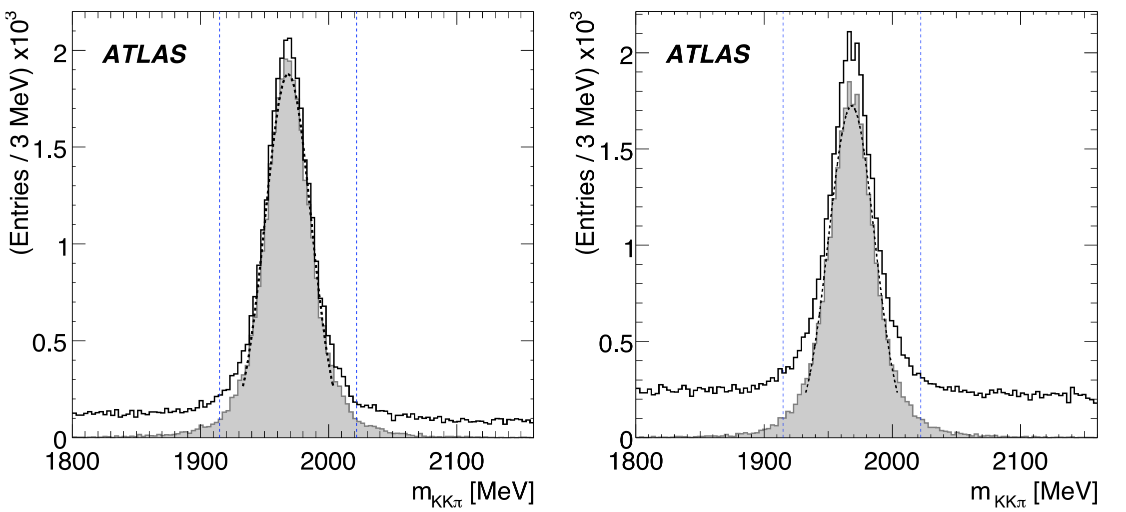

(a) $B_s^0 \to D_s^- \pi^+$ (b) $B_s^0 \to D_s^- a_1^+$

Figure 8: Reconstructed mass $m_{KK\pi}$ for all combinations within the signal sample (black line) and $KK\pi$ candidates corresponding to a D_s particle from the signal decay in the Monte Carlo truth information (grey filled). The standard deviation obtained from a fit within two standard deviations of a Gaussian function (dashed) to the distribution defines the three standard deviation cut range (vertical dashed). No trigger conditions are applied.

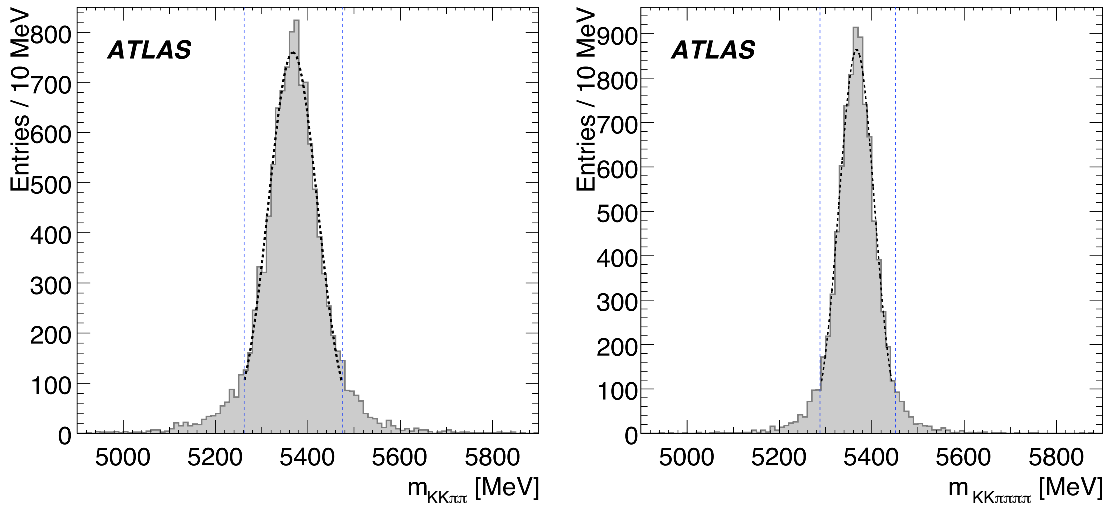

(a) $B_s^0 \to D_s^- \pi^+$ (b) $B_s^0 \to D_s^- a_1^+$

Figure 9: $m_{KK\pi\pi}$ (a) and $m_{KK\pi\pi\pi\pi}$ (b) reconstructed mass and fit of a Gaussian function to the distribution. Each $KK\pi\pi$ ($KK\pi\pi\pi\pi$) candidate displayed corresponds to a B_s particle in the Monte Carlo truth information. The two standard deviation cut range is shown by the vertical dashed lines. No trigger chain applied.

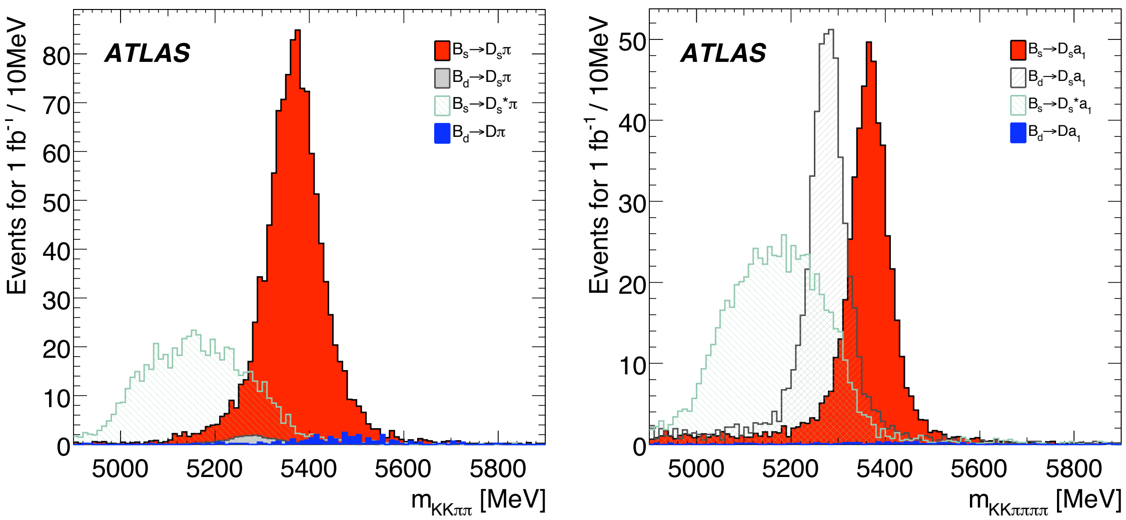

(a) $B_s^0 \to D_s^- \pi^+$ (b) $B_s^0 \to D_s^- a_1^+$

Figure 10: $m_{KK\pi\pi}$ (a) and $m_{KK\pi\pi\pi\pi}$ (b) reconstructed mass for signal and background channels. In (b) the upper limit for the branching fraction of the channel $B_d \to D_s a_1$ is used.

In the case of $B_d^0 \to D_s^+ a_1^-$, there is no measurement of the branching fraction available. The current upper limit is therefore used as a conservative estimate. The similarity to the $B_d^0 \to D_s^+ \pi^-$ channel indicates that the $B_d^0 \to D_s^+ a_1^-$ cross section could be in the same order as the one of the $B_d^0 \to D_s^+ \pi^-$ channel and therefore the $B_d^0 \to D_s^+ a_1^-$ contribution in Fig. 10 (b) could be much smaller.

The $B_s \to D_s^* \pi$ and $B_s \to D_s^* a_1$ channels are treated as a background source, since the momentum and hence the lifetime estimation for this decay is flawed due to the missing photon from the decay of the D_s^*.

5.2.2 Combinatorial Background

The limited statistics of the combinatorial background samples (e.g. 242 150 events for $b\bar{b} \to \mu 6X$) do not allow us to give a reasonable estimate for the signal to background ratio. This ratio as well as kinematic properties of the combinatorial background, like the shape of the proper time distribution will be studied once early data are available.

5.3 Tagging Results

Soft muon tagging is applied on all available simulated data of the two hadronic signal channels $B_s^0 \to D_s^- \pi^+$ and $B_s^0 \to D_s^- a_1^+$. Table 11 shows the number of events, the tagging efficiency and the wrong tag fractions. The tagging efficiency corresponds to the fraction of events where muon candidates have been successfully reconstructed. The events with at least one muon are separated into events with a good tag and events with a wrong tag resulting in a wrong tag fraction.

Comparing the results for all simulated events between the two signal channels, the difference in the wrong tag fraction is of the order 1 % due to the different kinematical topology. As the RoI trigger applies a p_T cut of 1.4 GeV on all reconstructed tracks, low p_T B_s^0 mesons are rejected leading to an increased wrong tag fraction for the triggered events (see Fig. 6(c) and 6(d)). After event reconstruction overall wrong tag fractions of $\omega = 22.30^{+0.56}_{-0.55}$ % for the channel $B_s^0 \to D_s^- \pi^+$ and $\omega = 23.31^{+0.56}_{-0.55}$ % for the channel $B_s^0 \to D_s^- a_1^+$ are observed. Effects of mixing are included as described in Section 4.1.

Table 11: Tagging efficiencies and wrong tag fractions for the signal channels $B_s^0 \to D_s^- \pi^+$ and $B_s^0 \to D_s^- a_1^+$ are shown for three different stages: all simulated events, all triggered events passing the LVL1 muon trigger and the LVL2 RoI trigger, and finally the numbers for the reconstructed events. The errors are statistical only.

Process	Type of Events	Number of Events	Tagging Efficiency [%]	Wrong Tag Fraction [%]
$B_s^0 \to D_s^- \pi^+$	all events	88450	96.08 ± 0.07	20.29 ± 0.14
	triggered	21613	98.77 ± 0.07	22.96 ± 0.29
	reconstructed	5687	$98.79^{+0.14}_{-0.15}$	$22.30^{+0.56}_{-0.55}$
$B_s^0 \to D_s^- a_1^+$	all events	98450	95.93 ± 0.06	21.05 ± 0.13
	triggered	27118	98.55 ± 0.07	23.91 ± 0.26
	reconstructed	5757	$98.47^{+0.16}_{-0.17}$	$23.31^{+0.56}_{-0.55}$

6 Determination of Δm_s

6.1 Methods for the Determination of Δm_s and its Measurement Limits

For the determination of the B_s^0 oscillation frequency the maximum likelihood method is used. The likelihood $\mathscr{L}$ is a function of the proper time t and the mixing state μ, parametrised by Δm_s and $\Delta\Gamma_s$, applied to five classes of events simultaneously: mixed and unmixed B_s^0, mixed and unmixed B_d^0, and background with lifetime but no mixing. The B_s^0 and B_d^0 classes have characteristic wrong tag fractions ω, which are determined on event-by-event basis as described previously. By maximising the likelihood $\mathscr{L}$ for a given event sample one can then extract the model parameters.

For obtaining the $5\,\sigma$ discovery and 95% exclusion measurement limits on Δm_s the amplitude fit method is used because the maximum likelihood method was found to have some disadvantages in that case [5]. The estimation of the maximum value of Δm_s measurable with the ATLAS detector is using B_s^0 candidates from the $B_s^0 \to D_s^- \pi^+$ and $B_s^0 \to D_s^- a_1^+$ hadronic channels. The numbers of reconstructed events after applying the trigger selection (L1_MU06 and LVL2 RoI) and the B_s^0 selection cuts as well as the expected numbers for an integrated luminosity of 10 fb^{-1}are given in Table 12 for all signal and background channels. The effective cross-sections for the various processes can be found in Table 1. Significant background comes from the $\bar{B}_d^0 \to D_s^- \pi^+/a_1^+$ and $B_s^0 \to D_s^{*-} \pi^+/a_1^+$ channels, and from the combinatorial background. Due to limited sample size the estimation of the combinatorial background is very approximate.

The relative fractions of the signal and the background contributions will be determined by a fit of mass shape templates to the reconstructed B_s^0 mass distribution employing a wider mass window than used here for the final extraction of Δm_s, similar to the method used by CDF [1]. The mass shape templates will be determined from Monte Carlo mass distributions of the individual channels. Uncertainties in the knowledge of the shapes will be taken into account as part of the systematical uncertainty.

Table 12: Signal and background samples used for the study of B_s^0-$\bar{B}_s^0$ oscillations and number of events as obtained from the analysis as well as expected numbers for an integrated luminosity of 10 fb^{-1}.

Process	Simulated events	Rec. events	Rec. events for 10 fb^{-1}
$B_s^0 \to D_s^- \pi^+$	88 450	5 687	6 657
$B_d^0 \to D_s^+ \pi^-$	43 000	1 814	99
$B_d^0 \to D^- \pi^+$	41 000	23	35
$B_s^0 \to D_s^{*-} \pi^+$	40 500	495	1 116
$B_s^0 \to D_s^- a_1^+$	98 450	5 757	3 368
$B_d^0 \to D_s^+ a_1^-$	50 000	1 385	$< 2\,454$
$B_d^0 \to D^- a_1^+$	50 000	49	36
$B_s^0 \to D_s^{*-} a_1^+$	100 000	870	1 052

6.2 Construction of the Likelihood Function

The probability density to observe an initial B_j^0 meson ($j = d,\ s$) decaying at time t_0 after its creation as a $\bar{B}_j^0$ meson is given by

$$p_j(t_0,\ \mu_0) \;=\; \frac{\Gamma_j^2 - (\Delta\Gamma_j/2)^2}{2\Gamma_j}\, \mathrm{e}^{-\Gamma_j t_0} \left(\cosh\frac{\Delta\Gamma_j t_0}{2} + \mu_0 \cos(\Delta m_j t_0)\right) \tag{1}$$

where $\Delta\Gamma_j = \Gamma_{\mathrm{H}}^j - \Gamma_{\mathrm{L}}^j$, $\Gamma_j = (\Gamma_{\mathrm{H}}^j + \Gamma_{\mathrm{L}}^j)/2$ and $\mu_0 = -1$.

For the unmixed case (an initial B_j^0 meson decaying as a B_j^0 meson at time t_0), the probability density is obtained by setting $\mu_0 = +1$ in Eq. 1. Here the small effects of CP violation are neglected. Unlike $\Delta\Gamma_d$, which can be safely set to zero, the width difference $\Delta\Gamma_s$ in the B_s^0-$\bar{B}_s^0$ system could be as much as 20% of the total width [17].

However, the above probability is modified by experimental effects. The probability as a function of μ_0 and the reconstructed proper time t is obtained as the convolution of $p_j(t_0,\ \mu_0)$ with the proper time resolution $\mathrm{Res}_j(t\,|\,t_0)$:

$$q_j(t,\mu_0) = \frac{1}{N}\int_0^\infty p_j(t_0,\mu_0)\,\mathrm{Res}_j(t \mid t_0)\,\mathrm{d}t_0 \tag{2}$$

with the normalisation factor

$$N = \int_{t_{\min}}^{\infty}\left(\int_0^\infty p_j(t',\mu_0)\,\mathrm{Res}_j(t \mid t')\,\mathrm{d}t'\right)\mathrm{d}t\ . \tag{3}$$

Here $t_{\min}$ = 0.4 ps is the cut on the B_s^0 reconstructed proper decay time. Plots in Fig. 11 show the proper time resolutions, which are parametrised with the sum of two Gaussian functions around the same mean value. The widths from the fit are σ_1 = (68.4±3.3) fs for the core fraction of 53.2% and σ_2 = (157.2±5.7) fs for the rest of the tail part of the distribution for the $B_s^0 \to D_s^-\pi^+$ channel. The values for the $B_s^0 \to D_s^- a_1^+$ channel are σ_1 = (72.5±4.3) fs for the core fraction of (58.0±6.8) % and σ_2 = (144.7±7.3) fs for the tail part.

Assuming a fraction ω_j of wrong tags occurring at production and/or decay, the probability becomes

$$\tilde{q}_j(t,\mu) = (1-\omega_j)q_j(t,\mu) + \omega_j q_j(t,-\mu) \tag{4}$$

where μ_0 has been replaced by μ in order to indicate that now we are talking about the experimental observation of same or opposite flavour tags. For each signal channel, the background is composed of oscillating B_d^0 mesons, with probability given by Eq. 4, and of non-oscillating combinatorial background, with probability given by Eq. 5, which results from Eq. 1 and Eq. 4 by setting $\Delta m = 0$ and $\Delta\Gamma = 0$:

$$\mathrm{p_{cb}}(t,\mu) = \frac{\Gamma_{\mathrm{cb}}}{2}\,\mathrm{e}^{-\Gamma_{\mathrm{cb}}t}\left[1 + \mu\,(1-2\omega_{\mathrm{cb}})\right] \tag{5}$$

For a fraction f_{kj} of the j component ($j = s$, d, and combinatorial background cb) in the total sample of type k, one obtains the probability density function

$$\mathrm{pdf}_k(t,\mu) = \sum_{j=s,d,\mathrm{cb}} f_{kj}\tilde{q}_j(t,\mu)\ . \tag{6}$$

The index $k = 1$ denotes the $B_s^0 \to D_s^-\pi^+$ channel and $k = 2$ the $B_s^0 \to D_s^- a_1^+$ channel. The likelihood of the total event sample is written as

$$\mathscr{L}(\Delta m_s, \Delta\Gamma_s) = \prod_{k=1}^{N_{\mathrm{ch}}}\prod_{i=1}^{N_{\mathrm{ev}}^k}\mathrm{pdf}_k(t_i,\mu_i) \tag{7}$$

where N_{ev}^k is the total number of events of type k, and $N_{\mathrm{ch}} = 2$. Each pdf_k is properly normalised to unity.

Figure 12 shows how the experimental effects, as parametrised in Eqs. 2, 4, and 6, modify the distribution of the proper time t of a Monte Carlo data sample.

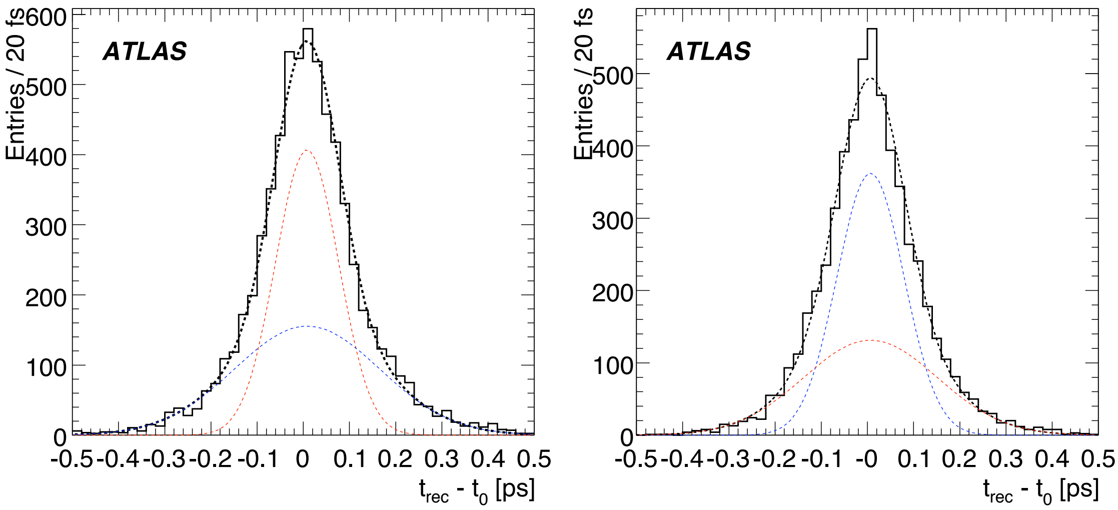

(a) $B_s^0 \to D_s^- \pi^+$ (b) $B_s^0 \to D_s^- a_1^+$

Figure 11: The resolution σ_t of the proper time of simulated B_s^0 fitted with two Gaussian functions (dashed lines). Both Gaussian functions use a common mean value.

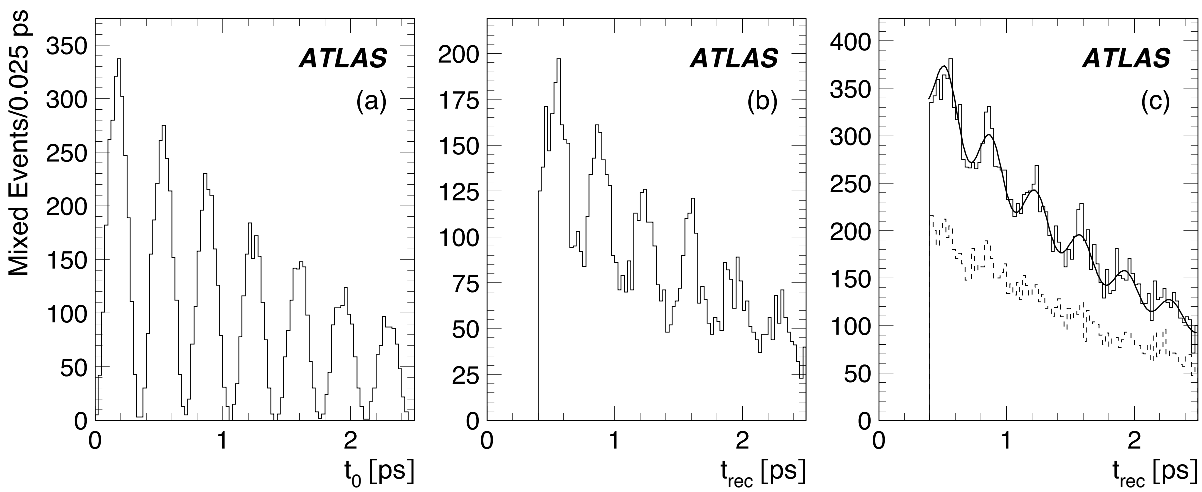

Figure 12: A sequence of plots showing how a true B_s^0 oscillation signal with $\Delta m_s^{\mathrm{gen}} = 17.77\ \mathrm{ps}^{-1}$ (a) is diluted first by the effect of a finite proper time resolution (b) and then by adding background events and including the effect of wrong tags (c). The plots contain samples of events equivalent to 10 fb^{-1} of integrated luminosity. They were generated using the Monte Carlo method described in Section 6.3. Only the case of mixed events is shown. For illustration a χ^2-fit of the function $C\exp(-t/\tau)(1-D\cos(\Delta m_s t))$ is overlaid to the solid histogram in (c), where D can be interpreted as the combined dilution factor: $D \approx 0.1$ here. Note that this is different from the unbinned maximum likelihood fit to the total event sample of mixed and unmixed events which is actually used to derive results in this study. The dashed histogram in (c) describes the contribution from all background sources.

6.3 Monte Carlo Data Sample

For the amplitude fit method a simplified Monte Carlo method is applied to generate a B_s^0 sample using the following input parameters: for each signal channel k the number of reconstructed signal events $N_{\text{sig}}^{(k)}$ for an integrated luminosity of 10 fb^{-1} and the number of background events $N_{B_{d,s}^0}^{(k)}$ from $B_{d,s}^0$ decays is given in Table 12. For the combinatorial background the ratio $N_{\text{sig}}^{(k)}/N_{\text{cb}}^{(k)}$ is taken to be 1. The wrong tag fraction is assumed to be the same for both B_s^0 and B_d^0 mesons in a specific signal channel ($\omega_s = \omega_d$), however, the values are slightly different for the two signal channels (see Table 11).

A Monte Carlo sample with $N_{\text{sig}} = N_{\text{sig}}^{(1)} + N_{\text{sig}}^{(2)}$ signal events oscillating with a given frequency Δm_s (e.g. Δm_s = 100 ps^{-1}, which is far off the expected value for Δm_s), together with $N_{B_{d,s}^0} = N_{B_{d,s}^0}^{(1)} + N_{B_{d,s}^0}^{(2)}$ background events oscillating with frequency $\Delta m_{d,s}$ and $N_{\text{cb}} = N_{\text{cb}}^{(1)} + N_{\text{cb}}^{(2)}$ combinatorial events (no oscillations) is generated according to Eq. 1.

The uncertainty on the measurement of the transverse decay length, $\sigma_{d_{xy}}$ (see Fig. 13), and the true value of the g-factor g_0 ($g := m/p_T$) as seen in Fig. 14(a), are generated randomly according to the distributions obtained from the simulated samples, fitted with appropriate combinations of Gaussian and exponential functions. For the $B_s^0 \to D_s^- a_1^+$ channel the true p_T^0 distribution shown in Fig. 14(b) is fitted with a combination of a parabola function in the low p_T^0 region and a sum of two exponential functions in the high p_T^0 region. The g_0 values are obtained by converting generated p_T^0 values at random.

From the computed true decay length, $d_{xy}^0 = t_0/g_0$, the corresponding reconstructed decay length is generated as $d_{xy} = d_{xy}^0 + \sigma_{d_{xy}} \cdot (\mu_{dxy} + S_{d_{xy}}\Omega)$. t_0 is the proper time of the generated B_s. $S_{d_{xy}}$ is the width and μ_{dxy} the mean value of the Gaussian shape of the pull of the transverse decay length $\frac{d_{xy}-d_{xy}^0}{\sigma_{d_{xy}}}$ shown in Fig. 15. The fitted values are $S_{d_{xy}} = 1.099 \pm 0.011$ and $\mu_{dxy} = (8.76 \pm 1.47) \cdot 10^{-2}$ for the $B_s^0 \to D_s^- \pi^+$ channel respectively $S_{d_{xy}} = 1.113 \pm 0.011$ and $\mu_{dxy} = (5.40 \pm 1.48) \cdot 10^{-2}$ for the $B_s^0 \to D_s^- a_1^+$ channel. The reconstructed g-factor is generated as $g = g_0 + g_0\mu_g + g_0 S_g \Omega'$. The distribution of the fractional g-factor $\frac{g-g_0}{g_0}$ as shown in Fig. 16 is fitted with a Gaussian resulting in a width of $S_g = (0.89 \pm 0.01) \cdot 10^{-2}$ and a mean value of $\mu_g = (0.27 \pm 0.12) \cdot 10^{-3}$ for the $B_s^0 \to D_s^- \pi^+$ channel respectively $S_g = (0.82 \pm 0.01) \cdot 10^{-2}$ and $\mu_g = (0.56 \pm 0.11) \cdot 10^{-3}$ for the $B_s^0 \to D_s^- a_1^+$ channel. Both Ω and Ω' are random numbers distributed according to the normal distribution. From the transverse decay length and g-factor, the reconstructed proper time is then computed as $t = g d_{xy}$. The probability for the event to be mixed or unmixed is determined from the t_0 and Δm_s (or Δm_d) values using the expression $(1 - \cos(\Delta m_j t_0)/\cosh(\Delta\Gamma_j t_0/2))/2$ which is left from Eq. 1 after the exponential part has been separated.

For a fraction of the events, selected at random, the state is interchanged between mixed and unmixed, according to the wrong tag fraction ω_{tag}. Half of the combinatorial events are added to the mixed events and half to the unmixed events.

For the exclusive $B_{d,s}^0$ background channels as well as the combinatorial background, the reconstructed proper time is generated assuming that it has the same distribution as the one for signal B_s^0 mesons coming from the $D_s^- \pi^+$ and $D_s^- a_1^+$ sample respectively, no mixing included.

The Δm_s measurement limits are obtained applying the amplitude fit method [5] to the sample generated as described in the previous section. According to this method a new parameter, the B_s^0 oscillation amplitude $\mathscr{A}$, is introduced in the likelihood function by replacing the term '$\mu_0 \cos \Delta m_s t_0$' with '$\mu_0 \mathscr{A} \cos \Delta m_s t_0$' in the B_s^0 probability density function given by Eq. 1. The new likelihood function, similar to Eq. 7, again includes all experimental effects. For each value of Δm_s, this likelihood function is minimized with respect to $\mathscr{A}$, keeping all other parameters fixed, and a value $\mathscr{A} \pm \sigma_{\mathscr{A}}^{\text{stat}}$ is obtained. One expects, within the estimated uncertainty, $\mathscr{A} = 1$ for Δm_s close to its true value, and $\mathscr{A} = 0$ for Δm_s

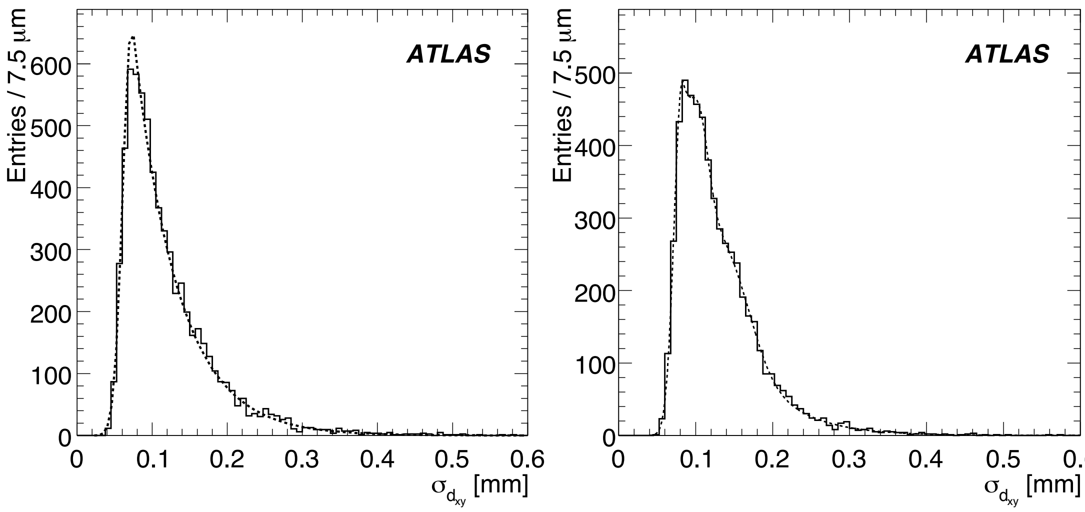

(a) $B_s^0 \to D_s^- \pi^+$

(b) $B_s^0 \to D_s^- a_1^+$

Figure 13: The uncertainty on the measurement of the transverse decay length, $\sigma_{d_{xy}}$ including trigger selection.

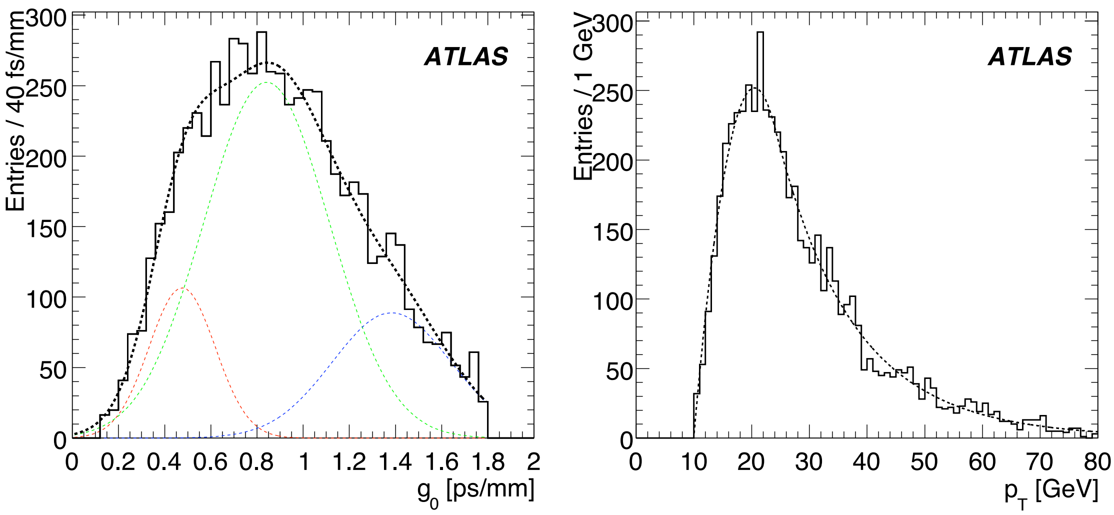

(a) $B_s^0 \to D_s^- \pi^+$

(b) $B_s^0 \to D_s^- a_1^+$

Figure 14: The true value of the g-factor $g_0 = t_0/d_{xy}^0$ of simulated B_s^0 from the $B_s^0 \to D_s^- \pi^+$ sample (a) fitted with the sum of three Gaussian functions (dashed lines) and the true transverse momentum distribution p_T^0 of simulated B_s^0 from the $B_s^0 \to D_s^- a_1^+$ sample (b) including trigger selection.

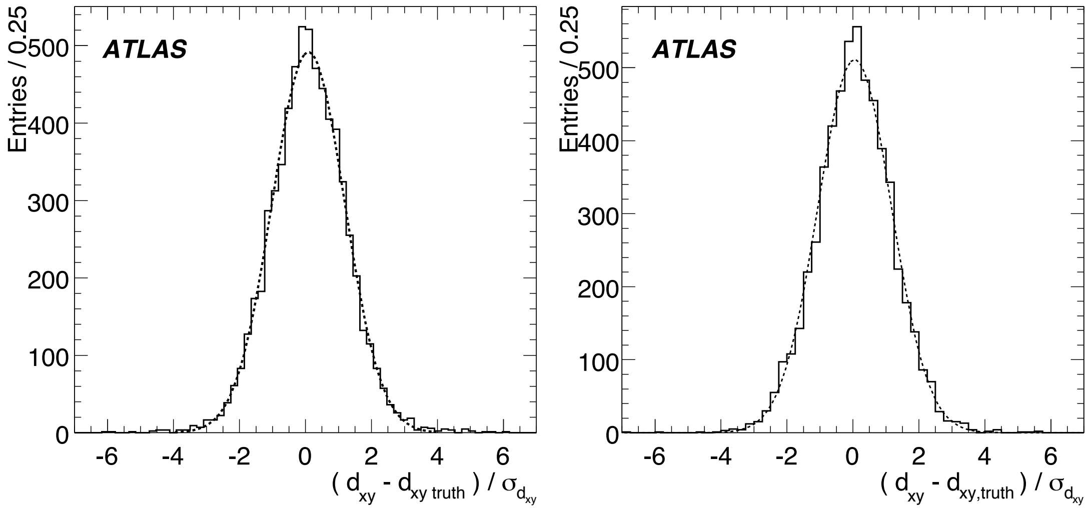

(a) $B_s^0 \to D_s^- \pi^+$ (b) $B_s^0 \to D_s^- a_1^+$

Figure 15: The pull of the measurement of the transverse decay length, $\frac{d_{xy}-d_{xy}^0}{\sigma_{d_{xy}}}$ and fit of a Gaussian function (dashed) to the distribution including trigger selection.

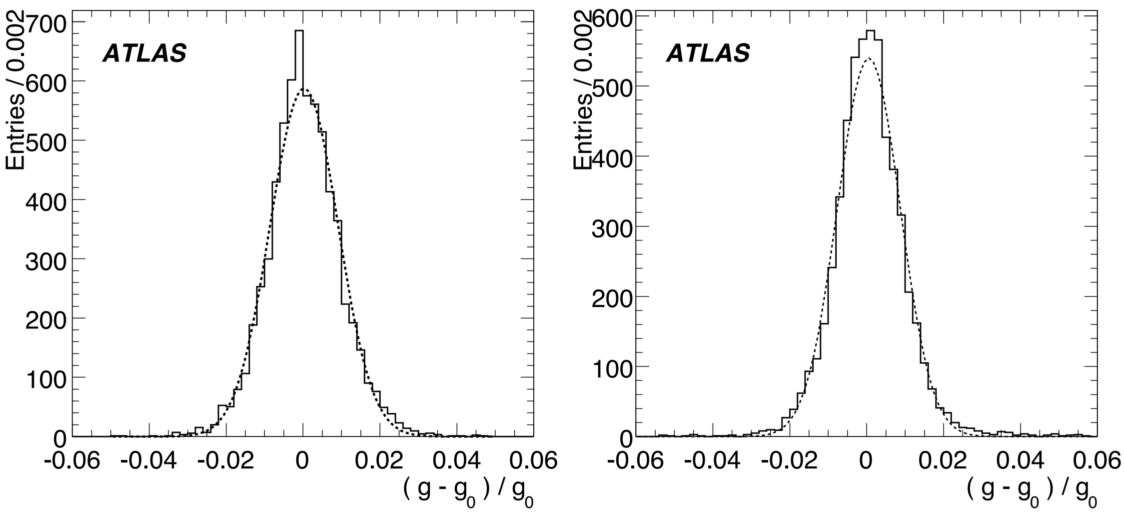

(a) $B_s^0 \to D_s^- \pi^+$ (b) $B_s^0 \to D_s^- a_1^+$

Figure 16: The fractional resolution of the g-factor $\frac{g-g_0}{g_0}$ of simulated B_s^0 fitted with a single Gaussian function including trigger selection.

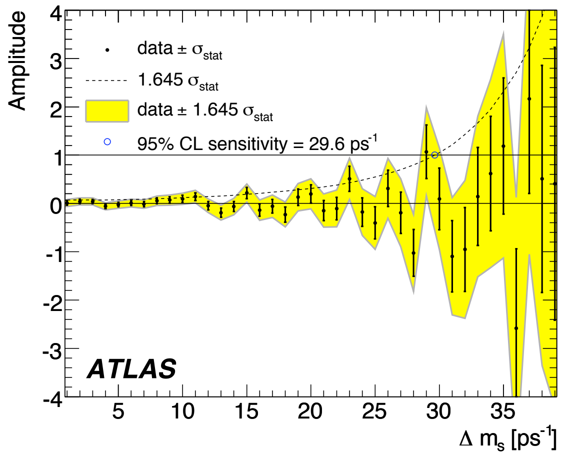

(a) Amplitude vs. Δm_s

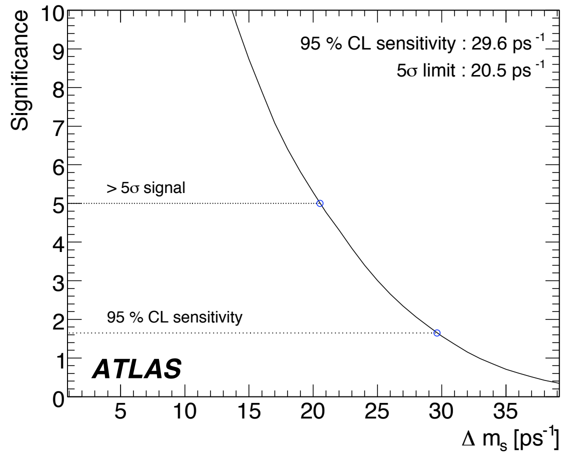

(b) Significance vs. Δm_s

Figure 17: The B_s^0 oscillation amplitude (a) and the measurement significance (b) as a function of Δm_s for an integrated luminosity of 10 fb^{-1} for a specific Monte Carlo experiment with $\Delta m_s^{\mathrm{gen}}$ = 100 ps^{-1} .

far from the true value. A five standard deviation measurement limit is defined as the value of Δm_s for which $1/\sigma_{\mathscr{A}} = 5$, and a sensitivity at 95% C.L. as the value of Δm_s for which $1/\sigma_{\mathscr{A}} = 1.645$. Limits are computed with the statistical uncertainty $\sigma_{\mathscr{A}}^{\mathrm{stat}}$. A detailed investigation on the systematic uncertainties $\sigma_{\mathscr{A}}^{\mathrm{syst}}$, which affects the measurement of the B_s^0 oscillation, is presented in [18].

6.4 Extraction of the Δm_s Sensitivity

For the nominal set of parameters (as defined in the previous sections), $\Delta\Gamma_s = 0$ and an integrated luminosity of 10 fb^{-1}, the amplitude $\pm 1\sigma_{\mathscr{A}}^{\mathrm{stat}}$ is plotted as a function of Δm_s in Fig. 17(a). The 95% C.L. sensitivity to measure Δm_s is found to be 29.6 ps^{-1}. This value is given by the intersection of the dashed line, corresponding to 1.645 $\sigma_{\mathscr{A}}^{\mathrm{stat}}$, with the horizontal line at $\mathscr{A} = 1$.

From Fig. 17(b), which shows the significance of the measurement $S(\Delta m_s) = 1/\sigma_{\mathscr{A}}$ as a function of Δm_s, the 5σ measurement limit is found to 20.5 ps^{-1}.

The dependence of the Δm_s measurement limits on the integrated luminosity is shown in Fig. 18(a), with the numerical values given in Table 13.

Table 13: The dependence of Δm_s measurement limits on the integrated luminosity $\mathscr{L}$.

$\mathscr{L}$ [fb^{-1}]	5 σ limit [ps^{-1}]	95% C.L. sensitivity [ps^{-1}]
3	14.5	25.0
5	17.0	27.0
10	20.5	29.6
20	23.7	32.0
30	25.3	33.2
40	26.4	34.1

The dependence of the Δm_s measurement limits on $\Delta\Gamma_s/\Gamma_s$ is determined for an integrated luminosity

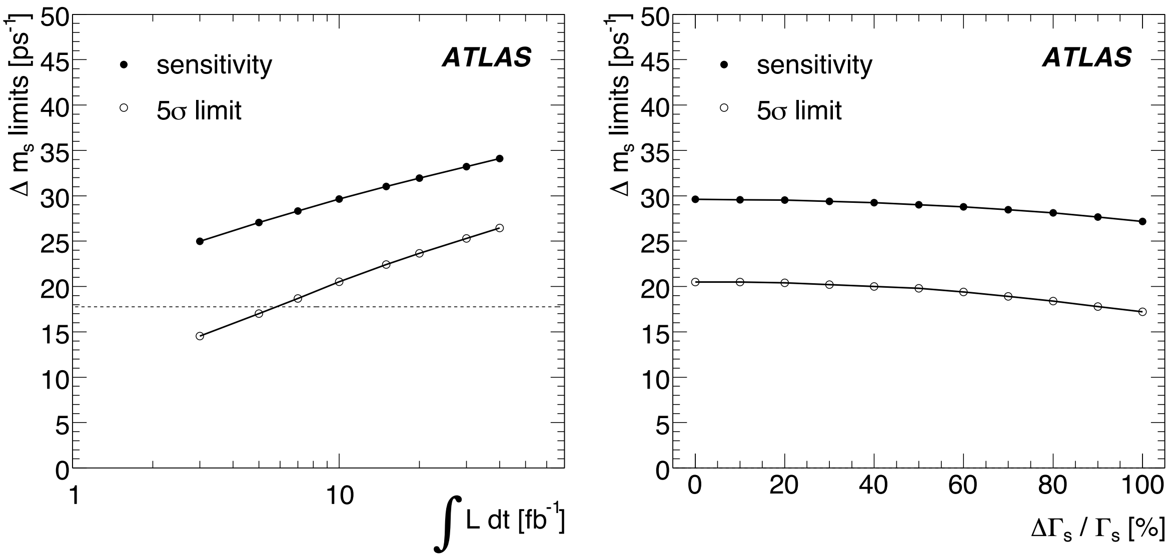

(a) Δm_s limits vs. $\int Ldt$ (b) Δm_s limits vs. $\Delta\Gamma_s/\Gamma_s$

Figure 18: The dependence of Δm_s measurement limits (a) on the integrated luminosity and (b) on $\Delta\Gamma_s/\Gamma_s$ for an integrated luminosity of 10 fb^{-1}. The dashed horizontal line in (a) denotes the CDF measurement.

of 10 fb^{-1}, other parameters having their nominal value. The $\Delta\Gamma_s/\Gamma_s$ is used as a fixed parameter in the amplitude fit method. As shown in Fig. 18(b) no sizeable effect is seen up to $\Delta\Gamma_s/\Gamma_s \sim 30\%$.

6.5 Extraction of the Δm_s Measurement Precision

Whereas the Δm_s measurement limits are obtained by using the amplitude method (see previous section), in case of the presence of an oscillation signal in the data the value of the oscillation frequency Δm_s and its precision are determined by minimising the likelihood (given by Eq. 7) with respect to Δm_s. In this fit $\Delta\Gamma_s$ is fixed to 0, because a study has shown that the systematic uncertainties resulting from varying $\Delta\Gamma_s/\Gamma_s$ in the range 0 to 0.2 (suggested by the present uncertainty) are practically negligible.

An example of the likelihood function is given in Fig. 19(a), in which the Δm_s^{gen} in the Monte Carlo sample has been set to the value measured by CDF for illustration. From this type of graphs the precision of the measurement of Δm_s is extracted and plotted in Fig. 19(b) as a function of the integrated luminosity for three values of Δm_s^{gen}.

6.6 Discussion of Results

In this note it is shown that with an integrated luminosity of 10 fb^{-1} ATLAS is able to verify the CDF measurement of $\Delta m_s = (17.77 \pm 0.10\,(\text{stat}) \pm 0.07\,(\text{sys}))\,\text{ps}^{-1}$ at the five standard deviation level. For these parameters the statistical error on Δm_s is calculated to be about 0.065 ps^{-1}.

In a preceding study [18] it was found that over a wide range of values for Δm_s and integrated luminosity the systematic uncertainty on the measured value of Δm_s was smaller by at least a factor of 10 compared to the statistical uncertainty. The list of contributions to that systematic error estimation included the wrong tag fraction with a relative error of 5% compared to 2.5% found in this study. For the reasons mentioned above, the evaluation of systematic effects has not been repeated here. The study of the effect of varying $\Delta\Gamma_s$ (as explained in the previous section) is new, but the contribution to the systematic uncertainty is also very small.

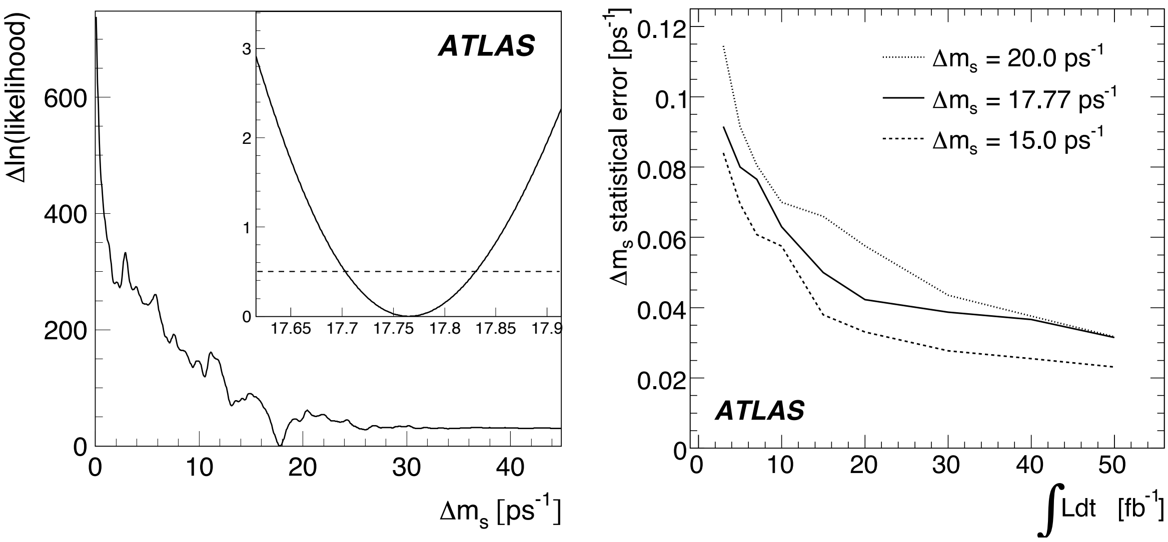

(a) $\Delta\ln$(likelihood) vs. Δm_s (b) $\sigma_{\text{stat}}(\Delta m_s)$ vs. $\int L dt$

Figure 19: (a) The negative natural logarithm of the likelihood for a specific Monte Carlo data sample for an integrated luminosity of 10 fb^{-1} and a true value of Δm_s^{gen} = 17.77 ps^{-1}. The inset shows a zoom around the minimum. (b) The statistical error $\sigma_{\text{stat}}(\Delta m_s)$ as a function of the integrated luminosity for values of Δm_s^{gen} of 15, 17.77 and 20 ps^{-1}. For comparison: the CDF statistical error on their Δm_s measurement is 0.10 ps^{-1}.

Systematic uncertainties on the overall trigger efficiencies mainly effect the statistics available for the analysis. However, an important systematic effect for the Δm_s measurement would be introduced in case different trigger efficiencies for positively and negatively charged muons are observed. In order to constrain this effect, dimuon events from a calibration channel like $B^+ \to J/\psi K^+$ with $J/\psi \to \mu^+\mu^-$ which are triggered by a single muon trigger could be used.

Clearly LHCb can measure Δm_s more precisely than ATLAS ($\sigma_{\text{stat}}(\Delta m_s) \sim 0.01$ ps^{-1} with 2 fb^{-1} of data [19]), but the Δm_s measurement with ATLAS is needed for the simultaneous fit of all parameters of the weak sector of the B_s^0-$\bar{B}_s^0$ system (weak mixing phase ϕ_s, Δm_s, Γ_s and $\Delta\Gamma_s$). This will be performed by a combined analysis of the channels described in this note and the $B_s^0 \to J/\psi\,\phi$ channel [20]. The ATLAS measurement is an independent cross-check of the measurements performed by other experiments.

7 Summary and Conclusions

We have studied the capabilities of the ATLAS detector to measure B_s^0 oscillations in pp collisions at 14 TeV using the purely hadronic decay channels $B_s^0 \to D_s^-(\phi\pi^-)\pi^+$ and $B_s^0 \to D_s^-(\phi\pi^-)a_1^+$. For an integrated luminosity of 10 fb^{-1} a Δm_s sensitivity limit of 29.6 ps^{-1} and a five standard deviation measurement limit of 20.5 ps^{-1} is obtained from a likelihood fit employing the amplitude fit method. This result depends only weakly on the lifetime difference $\Delta\Gamma_s$. The trigger is based on a single muon trigger with adjustable muon p_T thresholds between 4 and 10 GeV on all trigger levels and an active search for $D_s \to \phi\pi$ decays by the High Level Trigger. For 10^{31} cm^{-2}s^{-1} we will be able to afford a muon trigger with the loosest p_T threshold combined with a FullScan $D_s \to \phi\pi$ search. For 10^{32} cm^{-2}s^{-1}, we will need to increase the muon p_T threshold to 6 GeV and possibly employ the RoI-based LVL2 trigger. In both cases, the trigger rates can be kept at an acceptable level. For higher luminosities, we need to implement additional constraints in the HLT in order to reduce the event output rates further.

The offline event reconstruction searches for the hadronic decay of the B_s^0 and requires a muon with a minimum p_T of 6 GeV for each event. While the flavour of the B_s^0 at decay time is determined from the charge of the D_s particle, the identification of the initial B_s^0 flavour at production time is extracted from the charge of the soft muon in the event, taking effects of B_s^0 mixing into account. An overall tagging efficiency of $98.8 \pm 0.2\%$ and $98.5 \pm 0.2\%$ as well as average wrong tag fractions of $22.3 \pm 0.6\%$ and $23.3 \pm 0.6\%$ for the $B_s^0 \to D_s^- \pi^+$ and the $B_s^0 \to D_s^- a_1^+$ channels, respectively, are obtained.

About 100 000 Monte Carlo events of each sample have been produced without B_s^0 oscillations. Monte Carlo events for several exclusive B_s^0 and B_d^0 background channels as well as for inclusive background like $b\bar{b} \to \mu X$ and $c\bar{c} \to \mu X$ have been used. The hadronic decay of the signal side B_s^0 is reconstructed constraining the masses of intermediate particles in the decay chain. A B_s^0 mass resolution of 52.8 ± 0.7 MeV and 40.8 ± 0.5 MeV is obtained and after the application of all analysis cuts, 6 657 and 3 368 events are expected for an integrated luminosity of 10 fb^{-1} for the $B_s^0 \to D_s^- \pi^+$ and the $B_s^0 \to D_s^- a_1^+$ decay channels, respectively. We have considered several exclusive background channels, contributing to the background inside the B_s^0 mass window. The $B_d^0 \to D^- \pi^+/a_1^+$ channels hardly contribute (percent level of the signal), but the $B_s^0 \to D_s^{*-} \pi^+/a_1^+$ make a considerable contribution of about 16% ($B_s^0 \to D_s^- \pi^+$) and 31% ($B_s^0 \to D_s^- a_1^+$). While the $B_d^0 \to D_s^- \pi^+$ channel is expected to contribute with about 1.5% relative to the $B_s^0 \to D_s^- \pi^+$ signal, we can only estimate the $B_d^0 \to D_s^- a_1^+$ contribution to be less than about 70% of the $B_s^0 \to D_s^- a_1^+$ signal, given that this decay channel has not yet been observed.

In future, the $B_s^0 \to D_s^{*-} \pi^+/a_1^+$ channels may be considered signal rather than background. An estimate of the combinatorial background is severely limited by the available Monte Carlo event statistics. We plan to use early data to obtain a realistic estimate. For an integrated luminosity of 100 pb^{-1} at 10^{32} cm^{-2}s^{-1} we only expect about 90 events in the $B_s^0 \to D_s^- \pi^+$ and $B_s^0 \to D_s^- a_1^+$ channels, while the $B^+ \to J/\psi(\mu\mu)K^+$ decay channel, which has a large branching ratio, may be used to calibrate the soft muon tagging with early data. On LVL2 the processing time for the $D_s \to \phi\pi$ trigger may be reduced by restricting the track reconstruction to Regions of Interest (RoI), seeded by a LVL1 jet energy trigger. This typically leads to a reduction of the trigger efficiency by a few percent. At an instantaneous luminosity of $2 \cdot 10^{33}$ cm^{-2}s^{-1} several options will be considered to achieve acceptable Event Filter output rates. Besides further constraining the mass windows of the $D_s \to \phi\pi$ trigger, other improvements are obtained by checking for a good reconstruction quality of the D_s vertex or the implementation of a trigger element in the Event Filter which searches for the full B_s^0 decay chain. However, there is an uncertainty of a factor two in the overall $b\bar{b}$ cross-section at the centre-of-mass energy of 14 TeV and therefore the trigger rates may vary.

Due to the achieved sensitivity limit to measure the B_s^0 oscillations we expect to be able to verify the CDF measurement of $\Delta m_s = 17.77 \pm 0.10\,(\mathrm{stat}) \pm 0.07\,(\mathrm{sys})$ ps^{-1} at the five standard deviation level with a statistical error on Δm_s of about 0.065 ps^{-1}. This will provide a reasonable precision which allows us to combine the measurement described in this note with the analysis of the $B_s^0 \to J/\psi\phi$ channel [20] in a simultaneous fit for all parameters of the weak sector of the B_s^0-$\bar{B}_s^0$ system.

References

[1] A. Abulencia et al. [CDF Collaboration], Phys. Rev. Lett. **97** (2006) 242003.

[2] V.M. Abazov et al. [D0 Collaboration], Phys. Rev. Lett. **97** (2006) 021802.

[3] M. Battaglia et al. arXiv:hep-ph/0304132 (2003).

[4] ATLAS Collaboration, ATLAS Detector and Physics Performance TDR 15, Vol. 2, (CERN/LHCC/99-15, May 1999).

[5] H.G. Moser and A. Roussarie, Nucl. Instr. Meth. A **384** (1997) 491.

[6] T. Sjöstrand, S. Mrenna and P. Skands, JHEP **05** (2006) 026.

[7] ATLAS Collaboration, Introduction to B-Physics, this volume.

[8] W.-M. Yao et al., Journal of Physics G **33** (2006 and 2007 partial update for the 2008 edition) 1+.

[9] H. v. Radziewski, Trigger Considerations for the Measurement of $B_s^0 \to D_s^- a_1^+$ with the ATLAS Experiment, Master's thesis, University of Siegen, 2007 (SI-HEP-2008-05).

[10] ATLAS Collaboration, ATLAS Level-1 Trigger TDR 12, (CERN/LHCC/98-14, June 1998).

[11] C. Schiavi, Real Time Tracking with ATLAS Silicon Detectors and its Applications to Beauty in Hadron Physics, Ph.D. thesis, Genoa University and INFN Genoa, 2005 (CERN-THESIS-2008-028).

[12] ATLAS Collaboration, Triggering on Low-p_TMuons and Di-Muons for B-Physics, this volume.

[13] P. Nason et al., arXiv:hep-ph/0003142v2 (2001).

[14] ATLAS Collaboration, Muons in the Calorimeters: Energy Loss Corrections and Muon Tagging, this volume.

[15] ATLAS Collaboration, Production Cross-Section Measurements and Study of the Properties of the Exclusive $B^+ \to J/\psi K^+$ Channel, this volume.

[16] Upper Tail Probability of Chi-Squared Distribution, CERNLIB - CERN Program Library, routine entry PROB (G100), CERN.

[17] M. Beneke, G. Buchalla and I. Dunietz, Phys. Rev. D **54** (1996), 4419, M. Beneke et al., Phys. Lett. **B459** (1999) 631.

[18] B. Epp, V.M. Ghete, A. Nairz, EPJdirect CN3, SN-ATLAS-2002-015 (2002) 1–23.

[19] S. Barsuk [LHCb Collaboration], LHCb 2005-068 (2005).

[20] ATLAS Collaboration, Physics and Detector Performance Measurements for $B_d^0 \to J/\psi K^{0*}$ and $B_s^0 \to J/\psi \phi$ with Early Data, this volume.